

Design of an Industrial Precision Ceramic Grinding Machine

by

Paul Albert Scagnetti

M.S.M.E. Boston University (1992)
B.F.A. Rhode Island School of Design (1990)

Submitted to the Department of Mechanical Engineering
in partial fulfillment of the requirements for the degree of

Doctor of Philosophy in Mechanical Engineering

at the

MASSACHUSETTS INSTITUTE OF TECHNOLOGY

April 1996

© Massachusetts Institute of Technology 1996. All rights reserved.

Author

.....
Department of Mechanical Engineering
April 22, 1996

Certified by

.....
Alexander H. Slocum
Associate Professor
Thesis Supervisor

Accepted by

.....
Ain A. Sonin
Chairman, Department Committee on Graduate Students

MASSACHUSETTS INSTITUTE
OF TECHNOLOGY

JUN 27 1996

ARCHIVES

LIBRARIES

Design of an Industrial Precision Ceramic Grinding Machine

by

Paul Albert Scagnetti

Submitted to the Department of Mechanical Engineering
on April 22, 1996 in partial fulfillment of the
requirements for the degree of
Doctor of Philosophy in Mechanical Engineering

Abstract

In order to effectively grind ceramic components, more accurate, rigid, and wear resistant machine tools are needed. Ceramic materials often have many performance advantages compared with other materials such as steel or aluminum. However, machining costs are comparatively expensive for ceramic components. Part of the machining cost is capital equipment which must be frequently replaced or rebuilt because abrasive ceramic dust quickly penetrates seals and destroys conventional bearings. Additionally, the low stiffness of conventional machines limits the material removal rate. Removal rates for ceramic components are currently lower than equivalent steel components. Conventional grinding machines, used to process steel components, are insufficient for ceramic grinding even though they are frequently used in industrial processes. Such machines lack the stiffness, motion resolution, and wear resistance required to process ceramic materials efficiently. New design strategies are therefore required for precision grinding machines to process ceramic materials. The unique demands of ceramic grinding have not yet driven new designs, as the machine tool industry has largely ignored this potential market for a new class of machine tools.

This dissertation presents the results of a project aimed at developing a machine specifically for finishing ceramic components. There are two sections to this dissertation. The first section focuses on the development, experimental characterization, and design methods for three new machine tool technologies which are appropriate for ceramic grinding processes. The second section describes the synthesis (or design integration) of these technologies into a production machine.

The tangible result of this thesis is a production grinding machine which will be used full time in a ceramic component factory. This thesis will be a "proof-of-concept" to encourage new machine designs, and a "design manual" for use in future machine development projects.

Thesis Supervisor: Alexander H. Slocum
Title: Associate Professor

ACKNOWLEDGEMENTS

My graduate studies have been an enjoyable and significant experience because of the support and input of many people and organizations. The work has been financially supported by Wilbanks International, the National Science Foundation, and the Office of Naval Research.

Alex Slocum has been an enthusiastic, supportive, and driven advisor throughout this thesis. Most important, Alex always demanded that my thesis would be significant to industry as well academia. There are not many advisors who would (and could) arrange to send their graduate student to a company for their thesis project. Many advisors develop graduate students into good researchers, Alex has also helped develop me as an engineer. Industrial experience and distance from M.I.T. forced me to solve the daily micro-problems with only "training wheels" (i.e. his email question and answer service)

Wilbanks International sponsored the building of the grinding machine described in this thesis. Several people at Wilbanks were critical to completing the project and to my overall education.

Reg Maas has been my "mentor away from M.I.T.". He has been one of the most significant parts of my graduate studies. Our partnership on this project worked well (especially our frequent "micro-design-arguments"), both in solving problems and pushing new ideas. I have learned from Reg because he has been patient in explaining new ideas and unfamiliar concepts. He has a strong combination of knowledge and practical building common sense.

Steve Williams' late night working sessions helped me battle through the last year of this project. His ambitious approach to sales and customer service at Wilbanks were an inspiration for my efforts.

Lee Harder was my manager during this project. He supported the project even when it conflicted with production schedules and made all efforts to leave me free to complete this project.

Roger Egberg is the reason that the production drawings for the endgrinder were immaculate and free of errors. Roger took numerous sketches (calling some of them a sketch is generous) and turned out detailed, production ready prints.

Jim Groth was the main technician in charge of the assembly and lapping of the endgrinder components. Jim's experience with high accuracy assembly was absolutely critical to making the machine work and is one of the main reasons that the machine exhibited high performance.

Jim Alberton (electrician from Oregon Electric Group) played a critical role in the endgrinder project. He worked on the design of the electronic cabinet and with the endless troubleshooting.

Bob Argue produced most of the hardware components, and worked on assembling the coolant guard components. His good humor and willingness to act quickly was important, especially in the final stages of the project.

Other critical people in the precision products group include Tad Boone, Dennis Sohler, Vo Huynh, Richard Wiltse, Bob Santesson, Gary Gray, George Meyers, John Schuh, Matt Sauter, Rollie Boggs, Dave Kemper, Gene Paddock, Larry Fox, Randy Wachner, Rod Worthington, Marshall Miller, Mark Martin, Roy Jensen, Howard Davis, Dan King, Bill Rowe, Randy Brown, Travis Grant, and Nun Nguyen.

Aside from the precision products group, the project involved: Kris Vanaken (who was responsible for scheduling in the ceramic component work even though it effected the usual production schedule), Kat Cunningham (purchasing), Bill Czaplinski (general manager of Wilbanks), and Mike Cherney (who edited portions of the thesis and added late night humor on swing shift).

Critical vendors included: Bruce Beakley (Trilogy Systems) supplied and supported the linear motor, Whit Rappole (Convolve) helped debug the electronics and wrote the motion control programs, and Clark Frone (Lee's Industrial) built the tanks and coolant pans.

Before starting my work at Wilbanks, I was fortunate to spend a summer in Tokyo working at Sumitomo Heavy Industries. The opportunity was provided by the National Science Foundation and the Japanese Agencies M.I.T.I. and C.G.P. The time spent there was an important (and interesting) part of my graduate studies. I would especially like to thank Yoshiyuki Tomita (research engineer at Sumitomo Heavy Industries who worked with me during the summer), and Prof. Miyashita (Ashikaga Institute of Technology).

My initial research was done at the Laboratory for Manufacturing and Productivity at M.I.T. I gained a lot from the members of Alex's group including Eric Marsh (who helped with the modal analysis and ShearDamping portions of this thesis), and Nathan Kane (hydrostatic bearings, particularly the spreadsheets).

The members of my committee, Prof. Thomas Bifano, Prof. Woodie Flowers, and Prof. Michael Cima, provided a diverse background with helpful suggestions and questions along the way at our meetings.

My family has been loving and supportive throughout my entire graduate student career. My parents have always wanted the best for me and worked hard to provide the opportunity. There have been a number of times when they chose the more difficult route for themselves to provide an opportunity for me. My sister, Anne, housed me during my first year of graduate school (the ultimate sacrifice for a sibling) and brought her homemade food to the lab at the critical times. My brother Robb has long been my best friend. His parallel effort (with my father) to turn the family business into an enjoyable success has been a good reminder that all goals worth achieving require hard work and something else, rational thinking.

Finally, I am most grateful to my wonderful-beyond-belief fiance Michelle Meagher. Her love, enthusiasm, genuine interest, and "power-editing" skills made the completion of this project enjoyable. Our upcoming wedding (and future together) has made this work even more worthwhile.

"Have you ever looked for the root of production? Take a look at an electric generator and dare tell yourself that it was created by the muscular effort of unthinking brutes. Try to grow a seed of wheat without the knowledge left to you by men who had to discover it for the first time. Try to obtain your food by means of nothing but physical motions - and you'll learn that man's mind is the root of all the goods produced and of all the wealth that has ever existed on earth."

"If you asked me to name the proudest distinction of Americans, I would choose -because it contains all the others- the fact that they were the people who created the phrase 'to *make* money'. No other language or nation had ever used these words before; man had always thought of wealth as a static quantity - to be seized, begged, inherited, shared, looted, or obtained as a favor. Americans were the first to understand that wealth has to be created. The words 'to make money' hold the essence of human morality".

- Ayn Rand
Atlas Shrugged

CONTENTS

| | |
|---|-----------|
| Chapter 1: Introduction | 8 |
| 1.1 Background | 9 |
| 1.2 Machine Tool Requirements for Grinding Ceramic Materials | 10 |
| 1.3 Conventional and State-of-the Art Ceramic Grinding Machines | 16 |
| 1.4 Thesis Definition | 18 |
| 1.5 References | 21 |
| Chapter 2: Advanced Ceramics for Precision Machine Design | 22 |
| 2.1 List of Variables | 23 |
| 2.2 Introduction | 23 |
| 2.3 Material Properties of Advanced Ceramics | 24 |
| 2.4 Types of Engineered Ceramics | 31 |
| 2.5 Production of Precision Machine Ceramic Components | 32 |
| 2.6 Design Strategies for Ceramic Structural Beams | 47 |
| 2.7 Design Strategies for Multiple Component Structures | 51 |
| 2.8 Conclusions | 57 |
| 2.9 References | 57 |
| Chapter 3: Design of Self-Compensated, Water-Hydrostatic Linear Bearings | 58 |
| 3.1 List of Variables | 59 |
| 3.2 Overview of Linear Hydrostatic Bearings | 59 |
| 3.3 Self-Compensating Hydrostatic Bearing Operating Principles | 62 |
| 3.4 Squeeze Film Damping in Hydrostatic Bearings | 67 |
| 3.5 Design Considerations | 69 |
| 3.6 Experimental Results | 73 |
| 3.7 Conclusions | 82 |
| 3.8 Acknowledgements | 82 |
| 3.9 References | 83 |
| Chapter 4: Fluid Circuit Design Method for Hydrostatic Bearing Systems | 84 |
| 4.1 List of Variables | 85 |
| 4.2 Introduction | 85 |
| 4.3 Bond Graph Diagrams of Hydrostatic Bearing Systems | 86 |
| 4.4 Simulation Results of Hydrostatic Bearing Noise | 93 |
| 4.5 Experimental Results of Hydrostatic Bearing Noise | 96 |
| 4.6 Conclusions | 97 |
| 4.7 References | 98 |

| | |
|---|------------|
| Chapter 5: ShearDamping of Advanced Ceramic Structures | 99 |
| 5.1 List of Variables | 100 |
| 5.2 Introduction to ShearDamping Theory | 102 |
| 5.3 Single Cell Prototype Design and Experimental Evaluation | 103 |
| 5.4 Multiple Cell Prototype Design and Experimental Evaluation | 110 |
| 5.5 Conclusions | 117 |
| 5.6 Future Work | 117 |
| 5.7 References | 118 |
| | |
| Chapter 6: Design of the Wilbanks Precision Grinding Machine (WPGM)..... | 119 |
| 6.1 Introduction | 120 |
| 6.2 Design Overview | 124 |
| 6.3 Structural Design Description | 127 |
| 6.4 Hydrostatic Bearing System Description | 135 |
| 6.5 Hydrostatic Bearing Pump System Description..... | 140 |
| 6.6 Crossfeed Overtravel Stops..... | 142 |
| 6.7 Temperature Control System Description | 143 |
| 6.5 Electronics and Drive Systems Description | 144 |
| 6.6 Coolant Distribution System Description | 148 |
| | |
| Chapter 7: Experimental Characterization of the WPGM | 150 |
| 7.1 Straightness of Motion | 151 |
| 7.2 Modal Analysis | 155 |
| 7.3 Noise Measurements | 161 |
| 7.4 Stiffness Measurements | 163 |
| 7.5 Hydrostatic Bearing Flows and Pressures | 168 |
| 7.6 Conclusions | 171 |
| | |
| Chapter 8: Grinding Experiments on the WPGM | 172 |
| 8.1 Grinding Set-Up | 173 |
| 8.2 Straightness Results | 173 |
| 8.3 Modulus of Rupture Experiment | 175 |
| 8.4 Summary of Grinding Results | 177 |
| | |
| Chapter 9: Conclusions and Recommendations for Future Work | 178 |

CHAPTER 1

INTRODUCTION AND

CONTRIBUTIONS OF THE DISSERTATION

In order to effectively grind ceramic materials, more accurate, rigid, and wear resistant machine tools are needed. Conventional grinding machines, used to process steel components, are insufficient for ceramic grinding even though they are frequently used in industrial processes. Such machines lack the stiffness, motion resolution, and wear resistance required to process ceramic materials efficiently. New design strategies are therefore required for precision grinding machines to process ceramic materials. The unique demands of ceramic grinding have not yet driven new designs, as the machine tool industry has largely ignored this potential market for a new class of machine tools.

This dissertation presents the results of a project aimed at developing a machine specifically for finishing ceramic components. There are two sections to this dissertation. The first section focuses on the development, experimental characterization, and design methods for three new machine tool technologies which are appropriate for ceramic grinding processes. The second section describes the synthesis (or design integration) of these technologies into a production machine.

The goal of this research has been to demonstrate the benefits and resolve the initial design issues for this new class of machines. The tangible result is a production grinding machine which will be used full time in a ceramic component factory. This thesis will be a “proof-of-concept” to encourage new machine designs, and a “design manual” for use in future machine development projects.

1.1 - Background

Ceramic materials often have many performance advantages compared with other materials such as steel or aluminum. However, machining costs are comparatively expensive for ceramic components. In many applications, machining costs account for 18% (mass produced electronics packages and substrates) to 80% (precision bearing components) of the final cost [1]. Part of the machining cost is capital equipment which must be frequently replaced or rebuilt because abrasive ceramic dust quickly penetrates seals and destroys conventional bearings. Additionally, the low stiffness of conventional machines limits the material removal rate. Removal rates for ceramic components are currently lower than equivalent steel components.

1.1.1 - Grinding ceramic materials

Grinding of advanced ceramic is done almost exclusively with superabrasive wheels. Grinding is by definition a fixed abrasive process which uses the relative motion between a fixed workpiece and a moving grinding wheel to remove material. It is an inherently complex process in which many aspects of the process effect the quality and production rates [2]. Several researchers [3] have summarized the various factors which dominate the grinding process. Figure 1.1 diagrams the parameters and results of common grinding processes.

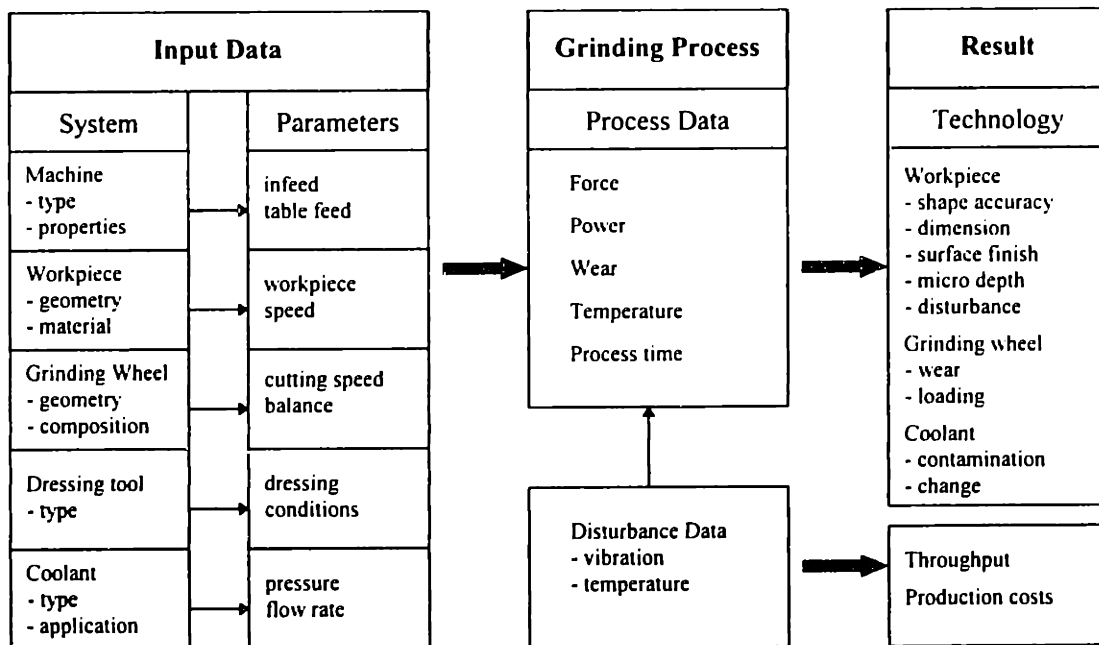


Figure 1.1 Diagram of the significant process parameters and measurable in grinding processes.

From a process point of view, there are two primary differences between grinding ceramic materials and steel. First, grinding forces are higher in ceramic materials given the same removal rate. The increase in grinding forces is primarily due to the higher

hardness of ceramic materials. Second, ceramic materials are subject to fracture when ground beyond the critical depth of cut. The critical depth of cut is a parameter which explains how large the depth of grinding can be without causing damage to the ceramic. In most industrial grinding applications, some fracture is induced into the workpiece during grinding because typical critical depths of cut are $0.1\mu\text{m}$. Most conventional grinding machines are incapable of infeeds this small. However, the machine stiffness and infeed resolution have a strong impact on the amount of fracture caused by grinding.

All methods of ceramic grinding depend heavily upon the quality of the machine tool. For example, creep-feed grinding of ceramics [2] is particularly promising because of the potential for higher removal rates and because the workpiece experiences compressive forces which minimize damage. However, any improvements in the finishing process depend heavily upon current machine tool technology. Creep feed grinding, for example, requires an extremely stiff, machine, capable of withstanding greater forces with minimal deflection [3, 4].

1.2 - Machine Tool Requirements for Grinding Ceramic Materials

Even though the application of ceramic materials is not widespread, there are thousands of grinding configurations for various components. Therefore, defining the proper characteristics for ceramic grinding machines depends strongly upon the configuration. However, four characteristics are essential for all ceramic grinding machines; (1) durability to withstand ceramic particles from the grinding process, (2) high stiffness and high damping, (3) high motion resolution to control the depth of cut, and (4) excellent coolant distribution and filtration.

1.2.1 - Durability

In terms of the economics of grinding in industrial applications, the most noticeable requirement is durability. The entire performance of a machine tool effects the productions costs, yet none is more obvious than durability. A machine requiring rework every 6 months costs thousands of dollars and weeks of downtime. During grinding, ceramic particles are often blasted about the machine by high pressure coolant. This wears seals and particles get by them, even the most minute quantities of these particles damages slideway and spindle bearings, particularly rolling element bearings. Note that sub-micron particles are extremely difficult to remove from the environment.

Figure 1.2 shows the rails of a machine used to grind ceramic components. The lighter gray stripe down the middle is the result of wear from grinding. In this particular machine, the roller bearings trap small ceramic particles and the relative motion of the roller to the rail causes both to wear. Remember that the rails and roller bearings of all conventional machines are made of steel which is significantly less hard than advanced ceramics such as aluminum oxide and silicon nitride. Other conventional bearing systems also fail to withstand the abrasive wear from ceramic particles. Sliding contact (also referred to as hydrodynamic) bearings are frequently used in grinding machines. These bearings use a film of oil to support the table weight. However, since the oil film is not

pressurized between the table and the base, ceramic particles can enter the bearing surface and scratch both the table and the base. These scratches remove the scrape marks which are critical to the accuracy of the bearing. Figures 1.3 and 1.4 show the distinctive scrape marks worn away by small ceramic particles trapped in the bearing.

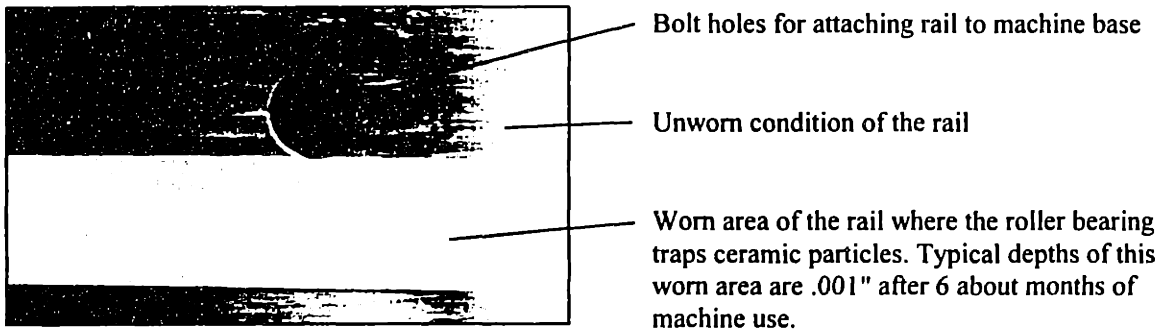


Figure 1.2 A roller bearing rail which has been worn away by ceramic dust in between the roller and the rail. The lighter gray line is the region where the roller travels and has been worn away over a period of about 6 months.

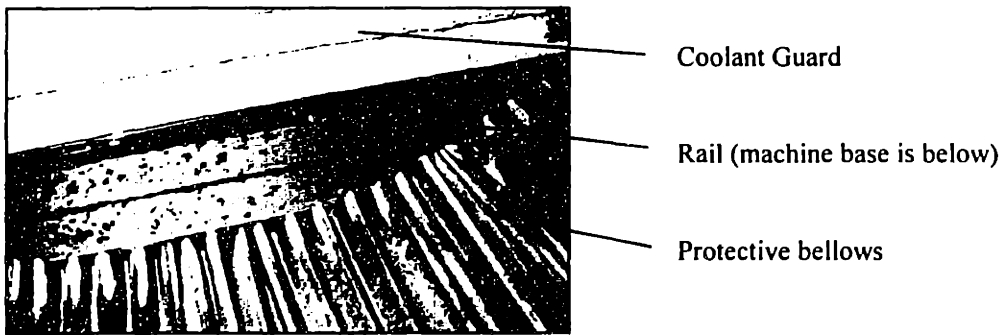


Figure 1.3 A rail of a hydrodynamic bearing shown with bellows and coolant guard moved (for photographic purposes). Wear shown on this rail has occurred in 6 months since last machine rebuild.

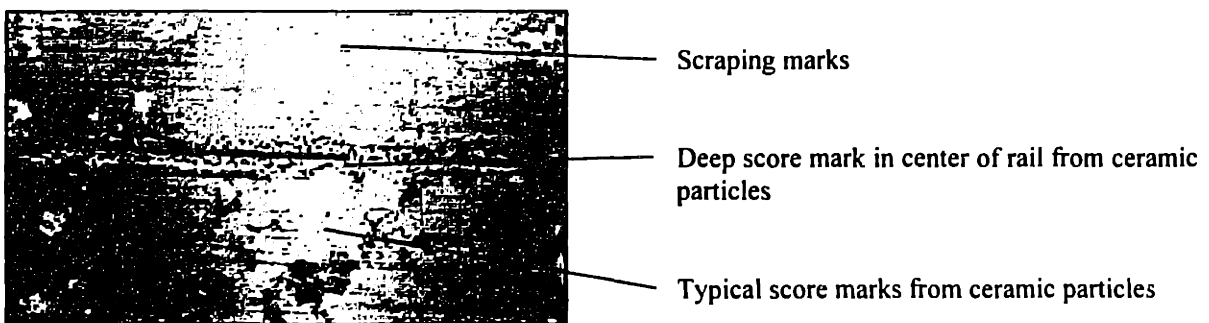


Figure 1.4 Close-up of rail (10" from rail) in Figure 1.3.

The wear on machine tools for grinding ceramic is not limited to the bearings. Actuators experience a similar type of wear. The most frequently used actuators in conventional grinding machines are hydraulic cylinders and ballscrews.

In many ceramic grinding facilities, leaking oil is a continual problem. Hydraulic actuators are used in applications which require fast movement and acceleration, but not accurate positioning. Crossfeed of a table in grinding is one frequent application for hydraulic actuators. In these applications, the seals which prevent the oil from leaking between the piston and the cylinder wear away quickly. Leaking oil from the pistons is a maintenance expense and also forces the pump to work harder to create the same force. More heat is generated which is thermally undesirable for the machine tool. Figure 1.5 shows a machine which has worn cylinders after 1 year of use.



Figure 1.5 A surface grinding machine which leaks oil continually due to wear of the hydraulic seals from ceramic particles. A bucket (lower left) is installed in order to capture the loose oil. This level of wear often occurs within 2 years of machine use.

Ballscrew actuators are typically used in applications where fine motion resolution over a long range of travel is required. Virtually all infeed actuators on conventional grinding machines are ballscrews or leadscrews. In ceramic grinding applications, ceramic particles wear the balls and screw quickly which increases backlash. A typical machine used full time for grinding ceramics might develop .010" backlash within 2 years of service.

The overall effect of machine tool wear is detrimental for two main reasons. First, the machine requires rebuilding frequently. Rebuilding machine tools is expensive, and reduces productive time in the factory. Second, during the wear cycle, the machines performance (and therefore component quality) degrades. Components take longer to

grind because the machine rigidity decreases. Components ground on older machines must be dwelled¹ for longer periods of time.

1.2.2 - Stiffness and Damping

Stiffness and damping are both critical to the performance of a grinding machine. They determine how well a machine will withstand the grinding forces. Accuracy directly depends upon how much the grinding wheel deflects due to a given grinding force. The grinding force, in turn, depends directly upon the material removal rate. Therefore, the stiffness limits (though there are other limiting factors) the material removal rate for a given machine tool.

Stiffness has become a somewhat vague term in the machine tool industry. Many manufacturers quote extremely large stiffness in conventional machine tools. However, there is an important distinction to be made with the specification. Static stiffness and dynamic stiffness are not the same for a given machine tool. In most cases, machine tool manufacturers quote the static stiffness of a machine rather than the dynamic stiffness (which is often much lower). Figure 1.6 is a frequency response plot for two systems with identical static stiffness but very different dynamic stiffness.

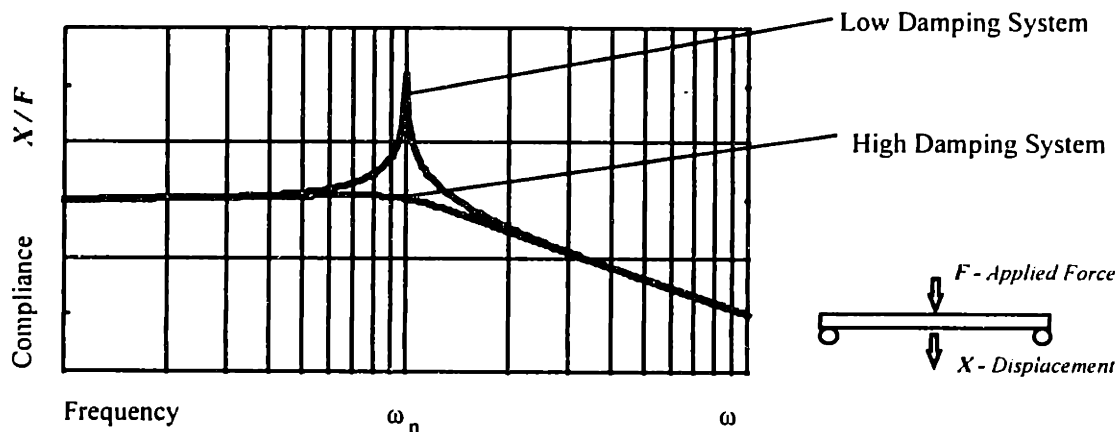


Figure 1.6 Frequency response example of two systems that have the same static stiffness yet very different dynamic stiffness. The difference is particularly obvious at the resonant frequency ω_n where the low damped system is much more compliant.

Therefore, stiffness must be considered over a range of frequencies rather than just at $\omega = 0$ (static stiffness). Dynamic stiffness must be viewed as a frequency response plot not just a single number (or the worst case number can be used). The difference in performance between different machines depends partially upon the static stiffness, and also upon the damping. Damping refers to a system's ability to dissipate vibration energy. A system that is well damped will not vibrate, which is critical for ceramic grinding

¹ Dwelling refers to the final stage of the grinding process in which the the infeed is zero. Contact between the grinding wheel and component still occurs because the machine has finite stiffness and therefore stores elastic energy during each infeed.

applications where vibration greatly decreases the component quality. The most commonly used measurement of damping in systems is the loss factor (denoted by the symbol η). A loss factor of 1 would mean that a system could not vibrate (the loss factor will be discussed more in chapter 5). A typical value for a system loss factor for a machine tool might be 0.1.

Therefore, a prime goal for ceramic grinding machine design (and most machine tools) is to have high stiffness and high damping. The measurement of stiffness and damping which most accurately reflects how the machine will grind is the loop stiffness. Figure 1.7 is a diagram of loop stiffness measurement. In this measurement, the entire structure, bearings, and all actuators between the grinding wheel and the workpiece are measured together as one spring-mass-damper system.

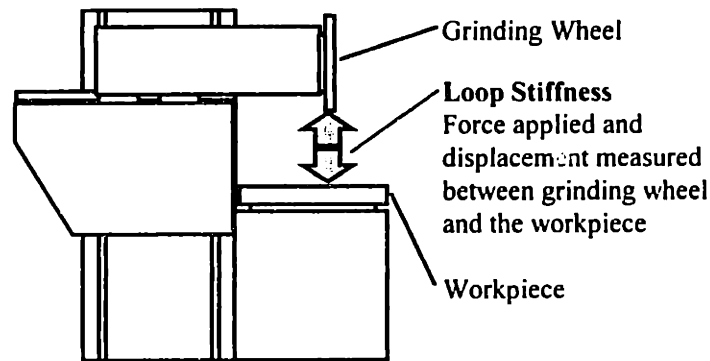


Figure 1.7 Diagram of the configuration for measuring loop stiffness in a surface grinding machine.

1.2.3 - High motion resolution

Motion resolution refers to the smallest controlled movement for a machine tool system. A typical motion resolution for a conventional machine tool is approximately 0.0001".

Motion resolution in ceramic grinding machines has an effect on the system performance for two reasons. First, ceramic materials are often ground at low depths of cut in order to reduce the amount of fracture in the final component. As mentioned previously, ceramic materials have been found to grind in a ductile mode when machined below their critical depth of cut (this parameter is a material property and can be calculated according to expressions developed by Bifano [need reference]). Typical values are $.01\mu\text{m}$ to $.1\mu\text{m}$. Though the lower end of this limit is often difficult to realize in industrial situations, a lower depth of cut will result in less damage to the component. Second, the motion resolution of a system will have a large impact on the system stiffness for small deflections. In order to control deflection on the order of $1\mu\text{m}$, the machine must have resolution of about 10 times this amount or $0.1\mu\text{m}$. The resolution is effected by both the actuator and the feedback sensor.

1.2.4 - Coolant Distribution and Filtration

In grinding operations, coolant serves to (1) lubricate and (2) cool the part during the grinding operation. In ceramic grinding, coolant is particularly important because the cutting forces and the specific grinding energy are generally higher than steel grinding.

For machine tools, the coolant system must provide adequate coolant velocity (and flow), maintain the temperature of the coolant (in order to reduce thermal errors in the workpiece and the machine), and filter particles. Filtration is particularly difficult in because ceramic particles are not as dense as steel. Therefore, they do not settle out as quickly, and cannot be filtered with cyclonic type filters effectively. Filters in line have generally not been used because they reduce the pressure of the coolant (by acting as a fluid resistor) and require more maintenance.

The most common filtration technique is a simple settling tank. Particle filtration is only somewhat effective in settling tanks even if baffles are used to force the settling process. If the tank is sufficiently large, the thermal stability is not a problem. In general, if the tank volume is at least 5 times larger than the flow rate, then thermal issues will be minimal. In other words, the water should not circulate more than once every 5 minutes (this assumes that the grinding room is temperature controlled). Figure 1.8 is a photograph of a typical machine tool settling tank.



Figure 1.8 Typical settling tank (bottom left) for an industrial grinding machine.

There are three general goals for a coolant system for ceramic grinding. First, the fluid should be filtered such that the ceramic particles are removed with at least 99% efficiency even though some of the smallest particles (below $.5\mu\text{m}$) would be difficult to remove. The only exception to this rule is when synthetic coolants (which have additives which would be strained out at about $3\mu\text{m}$ or less) are used for the coolant. In this case, the fluid should be filtered thoroughly to the additive size. The filtration is definitely the most difficult issue for the grinding coolant and will be addressed in this thesis. Second, thermal stability of the fluid should be within $\pm 2^\circ\text{F}$ of the ambient temperature. This can

either be done by using a large enough tank to ensure sufficient heat transfer between the coolant and the environment or by using a temperature controller. Third, the coolant velocity in the grinding area must be at least 10% higher than the surface speed of the wheel. This velocity is a function of the coolant pump power (and pressure characteristics) and the nozzle design. Figure 1.9 is a surface grinding application in which the coolant is aimed at a point on the grinding wheel directly in front of the grinding.

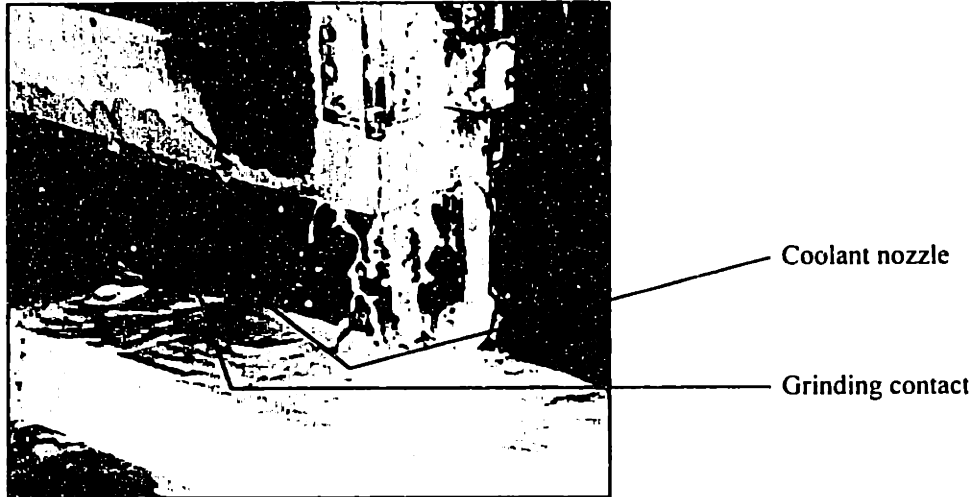


Figure 1.9 Photograph of the coolant spray onto a surface grinding operation.

1.3 - Conventional and State-of-the-Art Ceramic Grinding Machines

Conventional steel grinding machines are used in production grinding of ceramics materials. Such machines lack the stiffness, damping, and durability required for machining ceramics. They have less than half the lifetime of a similar machine used to machine metals because their performance degrades quickly due to sub-micron ceramic particles which permeate the manufacturing environment. Such machines typically have sliding contact bearings and either hydraulic actuators or ballscrews (usually a combination of these two actuators is used). At this time, there are no grinding machines produced specifically for grinding ceramic materials. Some manufacturers produce machines with slight modifications in order to improve durability. For example, one major machine tool manufacturer produces a grinding machine with positive pressure in the bellows. Thus, the current manufacturing strategy for grinding ceramics uses conventional grinding machines with slight modifications until the machines wear. The ceramic industry has long accepted the additional cost associated with rebuilding machine tools. However, it is this cost that has helped prevent the use of ceramic components in several applications such as automotive engine components and turbine blades.

The optics industry uses state of the art machine tools to make lenses. The design of these machines usually includes oil hydrostatic bearings, granite structures, and lapped

leadscrews or friction drives. An example of one such machine is the Nanoform produced by Cranfield Precision and is shown in Figure 1.10.

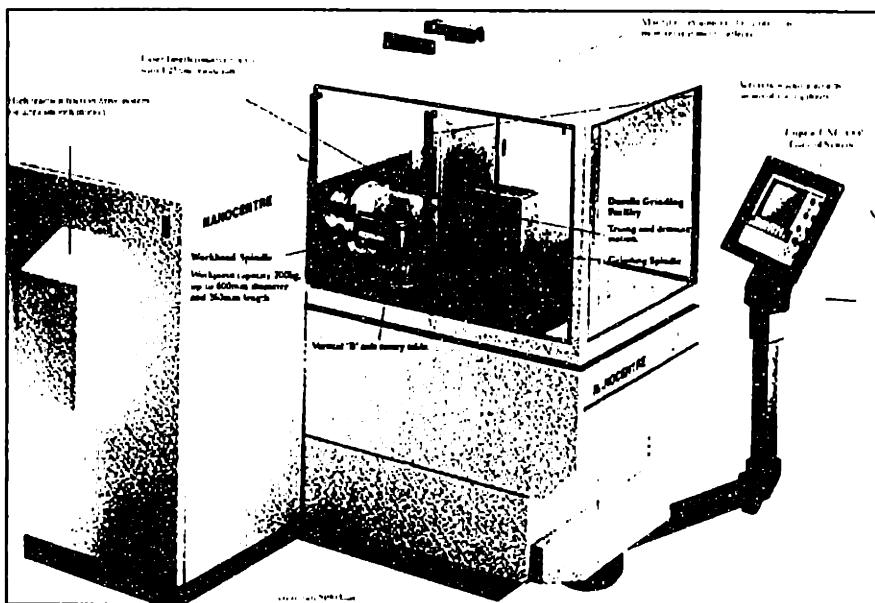


Figure 1.10 The Nanoform optics grinding machine from Cranfield Precision.

The machines used in the optics industry for grinding glass and sapphire have excellent characteristics for the type of grinding which they typically perform. The tolerances are on the order of 10nm, and the production is not high volume. In many ways, these machine represent the state of the art for grinding brittle materials.

However, these machines are not suited for most production facilities. They require a laboratory environment with substantial maintenance (often 5-10% of the production time per year) and somewhat delicate operation. Furthermore, there is not an equivalent machine which can accommodate parts of larger size. Most optical grinding machines are designed to produce parts under 6" in diameter.

Aside from optical grinding machines, several machines have been developed as instruments to test new concepts in grinding brittle materials. Table 1.1 is a summary of some of the most significant machines build for grinding ceramic materials.

Table 1.1 Recent grinding machines developed for grinding ceramic materials.

| Company | Machine | Principles | Completed |
|---------------------------|-----------------------------|----------------------------------|----------------------|
| Weldon Machine | Cylindrical Grinder | G. Dice and J. Flinchbaugh | 1st Prototype - 1994 |
| Nissin Machine | Wafer Grinder | M. Miyashita K. Abe, M. Daito | 1st Machine - 1993 |
| Boston University PERL | Ductile Grinding Machine | T. Bifano A. Yi | Completed 1991 |
| EATON | Centerless Grinder | J. Kovak | Estimated 1997 |

1.4 - Thesis Definition

In order to effectively grind ceramic materials, more accurate and wear resistant machine tools are needed. Next generation machines for grinding of ceramic materials will require improvements in structural components, actuators, and bearings as well as a means to address the inability of seals to effectively prevent rapid wear of the machines. An ideal machine tool for precision grinding of ceramics would have high stiffness, high damping, high motion resolution, and be insensitive to fine ceramic dust. High stiffness is required in order to withstand large infeed rates which are currently increasing in industrial practice. Current practice involves material removal rates of 1 cubic inch per minute, however, it is expected that this rate will triple within the next few years and this will require a commensurate increase in machine performance (e.g., dynamic stiffness). High damping is required in order to dissipate the inherent vibrations of the cutting process, because vibrations directly reduce surface quality. High motion resolution is required because the infeed of the grinding wheel must be precisely controlled.

As illustrated in Figure 1.11, developing next generation machines for grinding of ceramics will require improvements in structural components, actuators, and bearings. Ceramics, such as alumina and silicon carbide, hold great potential as a next generation structural material for machine tools. These materials have high stiffness, hold their form accurately over time, have a low coefficient of thermal expansion, and are resistant to most forms of chemical attack. The inherent disadvantage of structural ceramics, poor damping, can be overcome with the use of passive shear damping devices [5]. Linear motors are being developed into powerful actuators which could be used for fast, accurate positioning without mechanical contact and the associated wear problems. To eliminate bearing wear problems and to provide high dynamic stiffness, hydrostatic bearings are required [6].

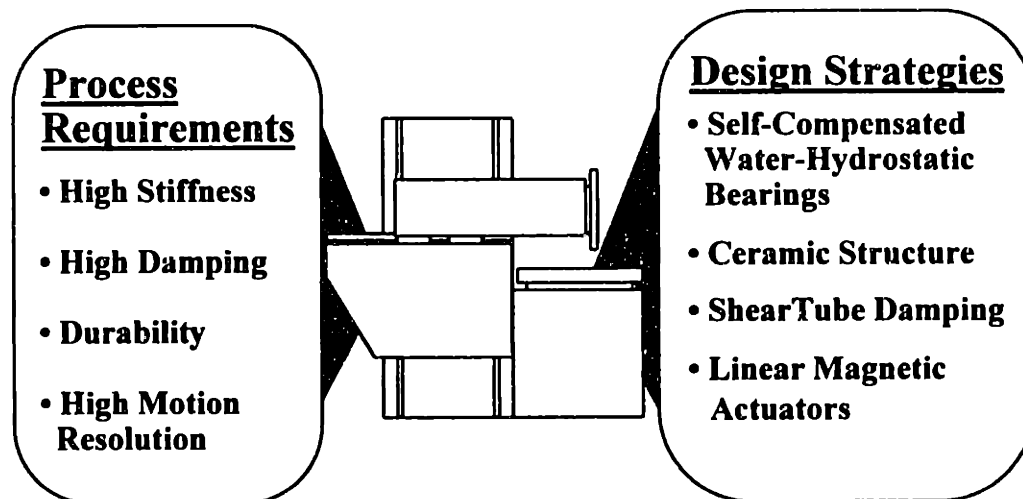


Figure 1.11 Diagram of machine tool requirements (left) and new technologies (right) for ceramic grinding machines.

1.4.1 - Thesis definition and Goals

The goal of this thesis is to develop a new design strategy for ceramic grinding machines. The thesis has two sections; (1) a series of three design manuals on new machine tool technologies intended for use by design engineers, and (2) a description and characterization of the machine tool developed for the Precision Products Group at Wilbanks International.

The largest goal of this thesis is to encourage machine tool manufacturers to consider designing and producing machine tools specifically for grinding ceramic materials. Such machines would be well suited for grinding steel as well. The widespread use of structural ceramic components is hinged upon such new machines. Hopefully, this thesis (mainly the machine at Wilbanks) will encourage new thinking and debate over the best type of bearings, actuators, and structures for ceramic grinding machines.

1.4.2 - Research Issues

When this thesis was started, Prof. Slocum (and colleagues at the Precision Engineering Research Group at M.I.T.) had already developed prototypes for linear water-hydrostatic bearings and ShearDamped™ structures. This thesis (1) develops these technologies to the point where they can be used in an industrial production facility, and (2) synthesizes these technologies into a complete machine design.

This thesis focuses on the development of three new technologies for precision machines tools; (1) self-compensated, water-hydrostatic, linear bearings, (2) ceramic structures for precision machines, and (3) ShearDamping™ to increase the dynamic stiffness of ceramic structures.

Each technology required a separate research initiative before being integrated into the framework of a complete grinding machine prototype. For each new technology, the following issues are addressed; (1) design tools for implementing the technology into a real industrial machine tool, and (2) advantages and disadvantages of the new technology versus the conventional technology. As an example, design tools for implementing hydrostatic bearings into grinding machines include models for predicting dynamic stiffness, and reducing pressure vibrations from the pump source.

The following summarizes each new technology and the research issues which were addressed in this thesis.

Self-Compensated, Water-Hydrostatic Bearings

The bearings for precision machines must have high dynamic stiffness and damping characteristics as well as high motion resolution. Rolling element bearings often have high stiffness, but are ineffective in damping vibrations and have limited motion resolution. Aerostatic bearings are effective dampers, yet are not stiff and crash resistant enough for many production applications. A bearing with good stiffness, damping,

motion resolution, and robustness is the self-compensated, hydrostatic bearing². Optimization of these bearings is an important research topic.

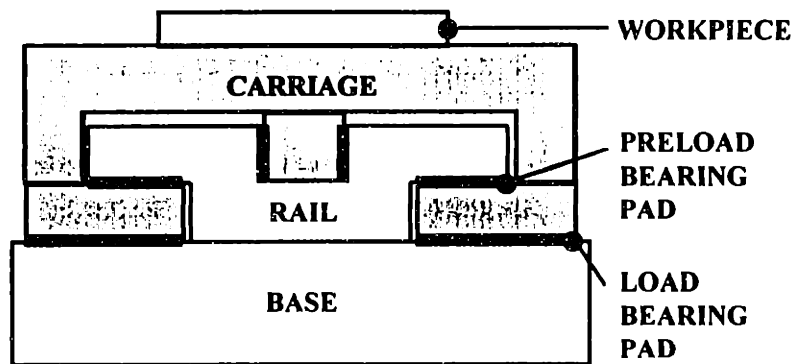


Figure 1.12 Diagram of machine tool axis with hydrostatic Bearing Pads

This thesis examines the following design issues related to hydrostatic bearing design; (1) an accurate model of the bearing in order to predict the dynamic stiffness before prototyping, (2) an accurate model in order to predict pressure fluctuations (which cause error motions of the carriage) in the bearing pad before prototyping. The thesis also presents results of two prototype hydrostatic bearing systems as well as the bearing system used in the grinding machine at Wilbanks.

Ceramic Structural Components

Historically, new materials have placed difficult demands on conventional machines. These demands have often been met by incorporating the new material itself into the machines. Early machine builders switched to iron machines from wood in order to machine iron. They also found that iron was generally more stable, and thus it also machined wood more efficiently. It is likely that such a change will take place with regard to ceramics. Ceramic materials such as alumina have several advantageous features including high stiffness, good thermal stability, and strong resistance to wear and to corrosion.

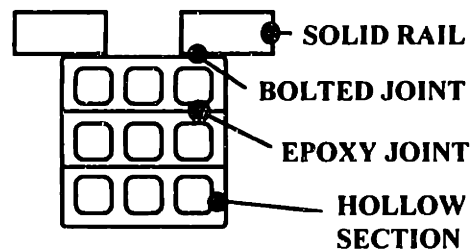


Figure 1.13 Cross-section of a ceramic machine tool base structure.

² There are many self-compensated, hydrostatic bearing design concepts. One which uses water as the working fluid for ergonomic and thermal advantages has been patented by Prof. A.H. Slocum, U.S. Patent # 5,104,237. This design concept will be used as the basis of the hydrostatic bearings developed in this thesis.

This thesis presents a "design manual" for developing ceramic, precision machine structures. This design manual is a means of educating design engineers about the possibilities of ceramic structures rather than the standard weldments or cast iron structures.

ShearTube[™] Structural Damping

The damping of the structure of the machine itself is another area of research. A method of passive damping of machine tool structures has been developed by E. Marsh and A. Slocum [6]. This method involves utilizing a thin film of viscoelastic material as shown in figure 1.14. As the structure vibrates, the film layer is sheared and energy is dissipated. This technique has the potential to compensate for the poor material damping characteristics of ceramic materials.

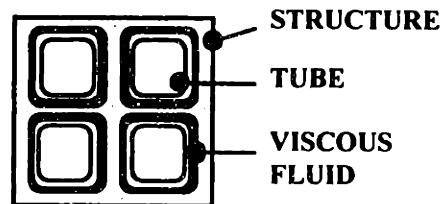


Figure 1.14 Diagram of the ShearTube structural damping technique.

In this thesis, the ShearTube concept has been applied to ceramic structures in order to increase their dynamic stiffness. Experimental modal analysis of the structures is presented. This thesis will also develop simple and effective strategies for machine tool designers to implement ShearTube dampers.

1.5 - References

- [1] NIST Special Publication 834, *Ceramic Machining: Assessment of Current Practice and Research Needs in the United States*, June, 1992.
- [2] Metzger, J.L., *Superabrasive Grinding*, Butterworths, Cambridge, UK, 1986.
- [3] NIST Special Publication 847, *Machining of Advanced Ceramics, Proceedings of the International Conference on Machining of Advanced Materials*, Gaithersburg, MD, July 20-22, 1993,
- [4] Abe, K., Yasunaga, N., Miyashita, M., Yoshioka, J., Daito, M., *Development of an Ultraprecision Grinding Equipment for Ductile Mode Surface Finishing of Brittle Materials*, International Conference on Precision Engineering, Kobe, Japan, May, 1993.
- [5] Salmon, S.C., "Modern Grinding Technology", Lecture notes given for SME Conference on "Using Advanced Ceramics in Manufacturing Applications", Cincinnati, OH, June 1991.
- [6] Slocum, A.H., Marsh, E.R., Smith, D.H., "A New Damper Design for Machine Tools and Components: The Replicated Internal Viscous Damper", *Precision Engineering*, Vol. 16, No. 3, July, 1994.

CHAPTER 2

ADVANCED CERAMICS FOR PRECISION MACHINE DESIGN

This chapter will present a modular approach to ceramic structural design for precision machine tools. The production process and design issues will be described. Examples will be presented from coordinate measuring machines, rails for machining centers, and machine tool bases.

In order to improve the accuracy of conventional machine tools, structures with improved stiffness, thermal stability, and durability are needed. Ceramic materials such as aluminum oxide are ideal candidates for precision machine tool structures.

Using ceramic beams with internal cells as modular machine tool components is a cost effective method of producing large machine tool structures. Accuracy is easier to attain on simple components. Precision prismatic beams, accurate to within $1.0\mu\text{m}$ or better, can be economically produced. These can be assembled into large, stiff, highly accurate structures.

2.1 - List of Variables

K_{Ic} - fracture toughness

MOR - modulus of rupture

P - applied force

E - elastic modulus

a - critical flaw length

γ - specific weight

2.2 - Introduction

Historically, machining new materials has placed difficult demands on machine tools. These demands have often been met by incorporating the new material into the machine tool. Ceramic materials are ready for such application into the next generation of precision machine tools. Ceramic materials (particularly aluminum oxide and silicon carbide) often have advantages compared with steel machine components including higher specific stiffness, improved thermal stability, and increased wear resistance.

Precision machine tools have typically been constructed of cast iron steel weldments, and granite. Ceramic components have not been widely integrated into machine tools because of the relative cost, the brittleness of most ceramic materials, and the lack of design knowledge among machine tool engineers. Table 3.1 is a summary of the general advantages and disadvantages of ceramic components for precision machine tools.

Table 2.1 Summary of advantages and disadvantages of ceramic materials for precision machine tool applications.

| General Advantages | General Disadvantages |
|-----------------------------|------------------------------|
| High stiffness / Weight | Low toughness |
| Thermal stability | Low tensile strength |
| Corrosion resistance | Brittleness |
| High hardness | Low thermal shock resistance |
| Elastic burr free material | Low material damping |
| Non-hydroscopic | |
| High temperature capability | |
| High compressive strength | |

2.3 - Material Properties of Advanced Ceramics for Structures

Ceramic materials are often distinguished by what they are not; they are non-metallic, and non-organic. However, ceramic materials can be more specifically defined based on the bonding of the atoms. Ceramic materials have ionic and covalent bonds between the atoms rather than metallic bonds. The following is a description of each type of bond:

- The metallic bond consists of atoms surrounded by an electron cloud which holds them together. This bond provides a closely packed structure with many “slip planes”. The result is a ductile material with a wide range of melting points.
- The ionic bond results from the coulomb attraction between metallic atoms losing outer electrons and becoming positive ions and the nonmetallic atoms gaining electrons to form negative ions.
- The covalent bond is the result of a pair of electrons being shared by two atoms. This type of bond is characteristic of materials with low densities, high brittleness, and high melting temperatures. The bond also prevents dislocations which provides high hardness.

For precision engineering applications, there are three main types of advanced ceramic materials are likely to be used; oxides, non-oxides, and composites.

- Oxides consist of oxygen in an atomic bond with a metal to form a stable compound. Examples of oxides are alumina and zirconia.
- Non-oxides consist of carbides and nitrides which bond with metal to form a stable compound. Examples of non-oxides include silicon nitride, silicon carbide, boron carbide, and boron nitride.
- Composites consists of blends of two or more ceramic materials which are combined in order to improve material properties. Examples of composites include zirconia toughened alumina and silicon carbide whisker reinforced alumina.

Before considering the process of producing ceramic components, it is important to have an understanding of the significant properties of advanced ceramics. Some characteristics of metal do not translate to ceramics, and one needs to be cautious when trying to use test data from tests designed for metals and applying them directly to ceramics. Properties are defined below for reference.

2.3.1 - Strength

Ceramics are known to have very high compressive strength. For most advanced ceramics, the compressive strength is far higher than needed for a given application. It is nearly impossible to cause a ceramic to fail in compression. The typical mode of failure for ceramics is tensile or shear.

The strength of ceramics is most easily measured using a four point flexural test. The test specimen is simply loaded in flexure and the tensile stress at the time of breakage of the outer surface is calculated as shown in Figure 2.1. This test measures tensile strength which, in ceramic, is much lower than compressive strength.

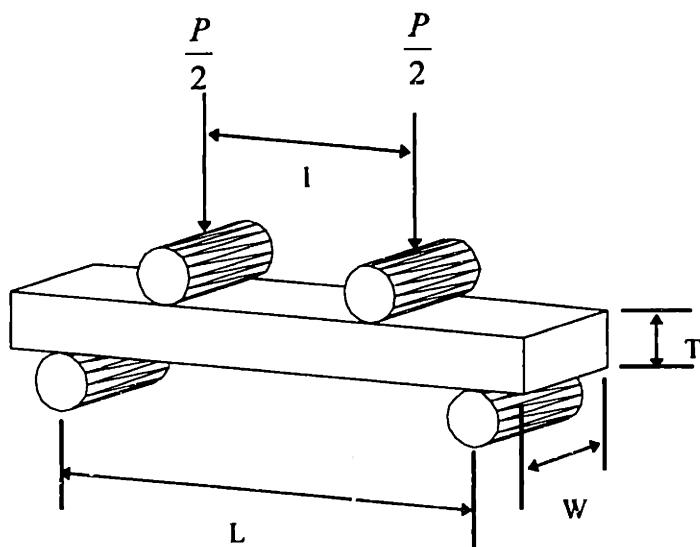


Figure 2.1 Diagram of a four-point flexural test with main parameters.

After experiments are performed, the modulus of rupture of can be calculated using the following expression:

$$MOR = \frac{3P(L - l)}{2WT^2} \quad (2.1)$$

2.3.2 - Fracture Toughness

Ceramics are known to be extremely sensitive to cracks or flaws. In brittle materials like ceramics, crack tips do not get blunted by ductile flow as they do in metals. If cracks are subjected to stresses sufficient to make them grow, they will simply propagate until they reach the end of the part. The ultimate strength of a given ceramic is highly dependent on the shape and concentration of flaws within its microstructure.

Prior to about 1975, it was a goal to make ceramic completely dense and free of flaws to achieve maximum strength. However, there are practical limits to the level of perfection in a ceramic. Also, production methods for achieving perfection do not yet exist.

Current methods for producing high-strength ceramics try to control rather than eliminate the flaw structure in ceramics. Stress analysis of a typical crack in ceramic

leads to a formula for computing the stress intensity at a crack tip. Figure 2.2 shows this formula. The toughness depends on the stress applied and the length of the flaw. Therefore, if we could create a myriad of extremely small flaws in the matrix, we raise the critical stress required to fracture the part. This is a simplified description of microcracking—a process used by ceramists to actually toughen ceramics.

The toughness of ceramics is measured by creating a controlled crack in the surface of the ceramic and measuring the force necessary to propagate the crack. The K_{IC} value is the critical force/flaw relationship required to propagate a crack. A typical classical ceramic such as a porcelain dinner plate has a K_{IC} value of about 1, while an aluminum oxide such as a spark plug insulator has a K_{IC} value of about 3.

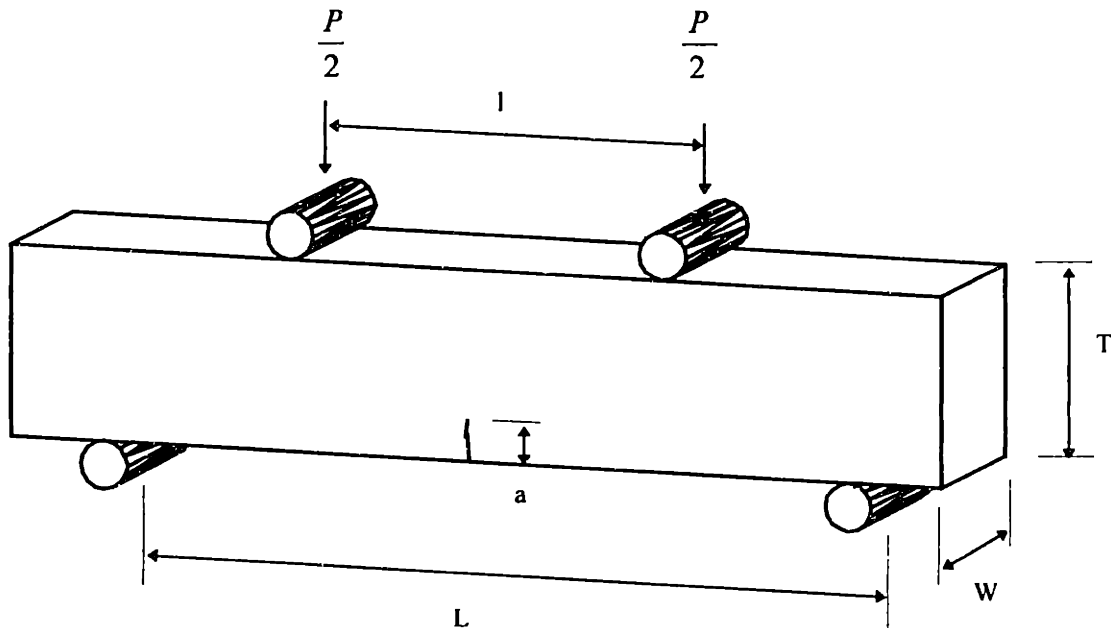


Figure 2.2 Testing schematic for fracture Toughness K_{IC} .

$$K_{Ic} = \gamma \frac{3P(L-l)}{2WT^2} a^{\frac{1}{2}} \quad (2.2)$$

Highly toughened ceramics such as a partially stabilized zirconia can have K_{IC} values as high as 11 to 13. For comparison, imagine throwing a porcelain saucer from a third-story window onto a cement parking lot. The porcelain would shatter. If that same saucer were made of aluminum oxide, it would break. If it were made of toughened zirconia, the cement parking lot would be dented.

2.3.3 - Elastic Modulus

Many ceramics are known to have a very high specific stiffness. They tend to be lighter than metals and yet have a very high modulus of elasticity. This makes them ideal for structures that need to move with minimum acceleration and minimum deflection.

The modulus of elasticity is easy to measure in most ceramics since they follow Young's law. Most elasticity data is run using the same four point bending load as that used for measuring flexural strength.

A related property to elastic modulus is the Poisson's ratio. This is the amount of increase or decrease in cross sectional area for a given amount of strain. Most ceramics have a Poisson's Ratio between .2 and .3. They can be subjected to extensive modeling with various finite element analysis programs.

2.3.4 - Hardness

Hardness is a difficult trait to test since many of the tests used for evaluating metal hardness are not valid for ceramics. The most common test for measuring hardness on metals is the Rockwell Indentation Test. Here, a carbide ball is pressed down on the surface of the material and the depth of the indent is compared to the load applied to the ball. Unfortunately, this test doesn't work for ceramics since they will not accurately deform in compression without shattering. Any Rockwell hardness numbers which have been published for ceramics are merely comparative guesses based on the perceived equivalency to known metals.

The most common hardness test for ceramics is the MOHS Hardness Scale. This is an old geological scale for identifying minerals by their ability to scratch one another.

Presently, the best compromise between these tests is the Knoop Hardness Test. Here, a diamond point is pressed into the surface until a measurable flaw occurs. The load applied is then divided by the cross sectional area of the flaw to give a comparative value.

One needs to be careful when using hardness numbers to predict wear resistance. Numerous tests exist to evaluate wear and abrasion which are normally specific to the application being pursued. These types of test data are available from most ceramic manufacturers and must be studied carefully before drawing any conclusions as to specific applications. Figure 2.3 shows comparative wear resistance of several common ceramic materials using three different testing methods. The information demonstrates that wear resistance is strongly test dependent.

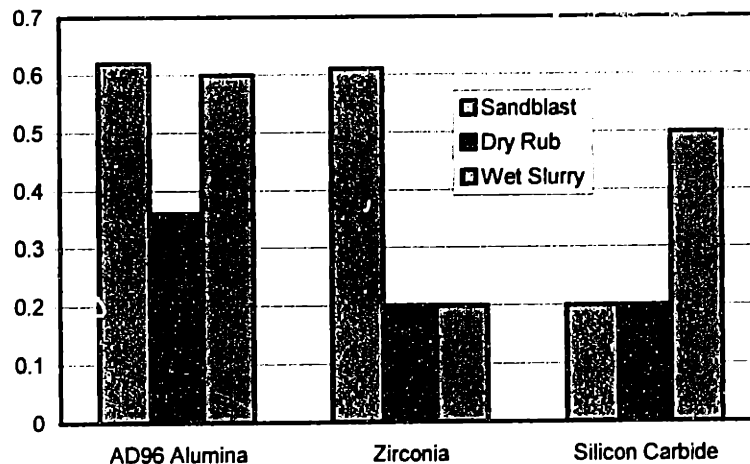


Figure 2.3 Wear test comparison of various ceramic materials. Wear index is the weight loss compared to an 85% Alumina specimen.

2.3.5 - Thermal Properties

Designers are often drawn to ceramics because of their high melting points. When designing for high temperature operation, it is important to understand the material limitations.

The melting point of a ceramic is different than its ultimate use temperature. As with metals, ceramics begin to lose their stability and strength when they are heated above one half their melting point. For example, the melting point of aluminum oxide is approximately 2000 °C. At 1250 °C, there is evidence that the material will creep under prolonged load.

Thermal shock must be considered when designing components which are subjected to heating cycles. Ceramics are most susceptible to thermal shock when they are rapidly cooled. The thermal shock resistance of a given material evolves from many properties. The size and shape of the component has a tremendous effect on the ability to withstand thermal shock. A small round component will have much higher resistance to thermal shock than a large irregular object. A vessel with a uniform wall thickness and a smooth symmetrical shape will withstand shock better than a part with adjoining thick and thin cross sections.

Some ceramics can be formulated to have a very low thermal expansion coefficient. Among many structural ceramic materials, there is a tendency for the thermal expansion coefficient to increase at higher temperatures. It is important to know how the material behaves over the full temperature range in order to design the differential expansion. Most oxide ceramics are fairly poor conductors of heat. By contrast, materials such as aluminum nitride conduct heat an order of magnitude more efficiently.

2.3.6 - Chemical Properties

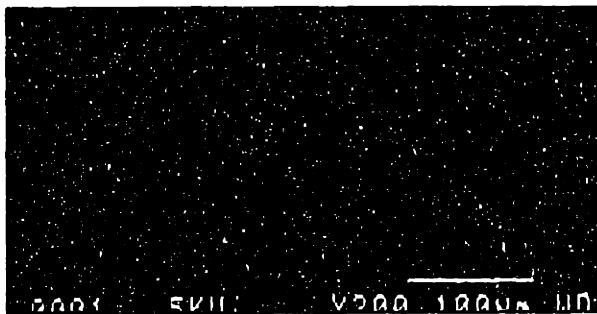
Most ceramic materials are chemically inert, which means that they are suitable for corrosive environments. The most common way to evaluate chemical resistance is to expose the material to a chemical at various temperatures and measure the weight loss as a function of time. When designing for corrosive environments, the designer should try to get as much detailed information from the ceramic manufacturer as possible or design a test to carefully evaluate the materials' suitability.

2.3.7 - Surface and Grain Properties

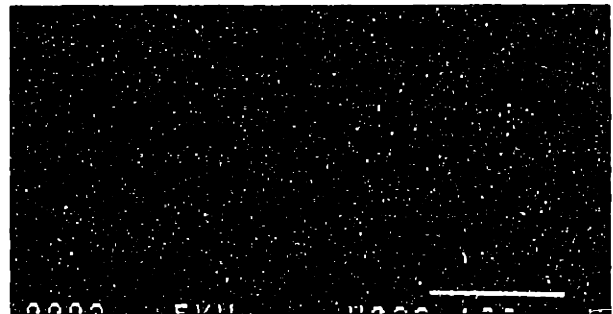
The grain size of ceramic materials depends upon the firing cycle, the material preparation process, and the material properties. For the precision machine designer, the most important consideration is that the surface finish depends slightly on the material property and firing cycle. A typical grain size for aluminum oxide is about 2-20 μm . Therefore, the final stages of finishing a component involve shearing the grains of the material.

The following photographs in Table 2.2 give a qualitative description of the surface of some of the more commonly used ceramics for precision machine design applications.

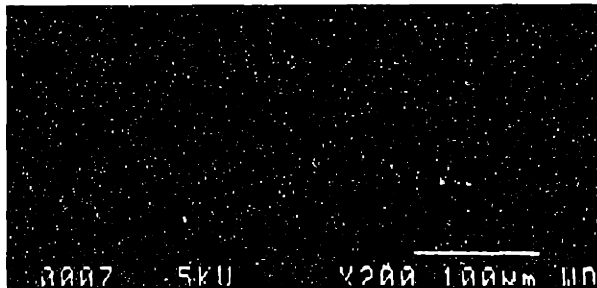
Table 2.2 Photographs of the surface, and grain structure of four commonly used ceramic materials.



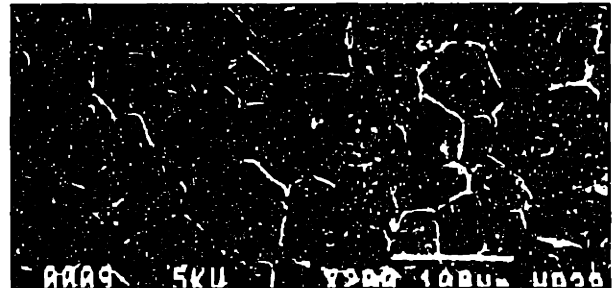
Alumina 96%



Alumina - 99.5 - Fine Grain



Zirconia Toughened Alumina



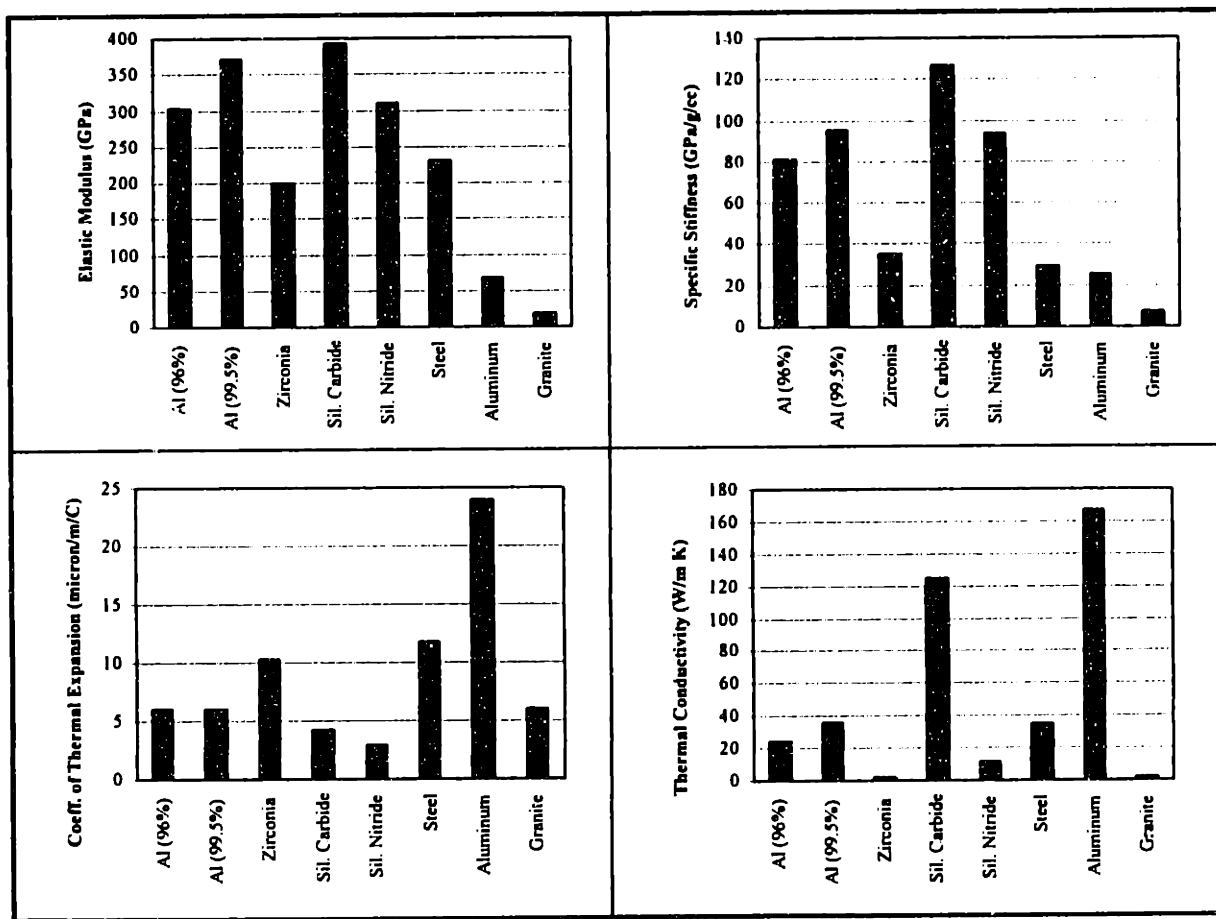
Zirconia

2.3.8 - Summary Tables of Material Properties

Table 2.3 Material Properties for commonly used advanced ceramic materials.

| Property | Units | Aluminum Oxide 96% | Aluminum Oxide 99.5% | Silicon Carbide | Silicon Nitride | Zirconia | Tool Steel |
|-------------------------------|--|--------------------|----------------------|-----------------|-----------------|-------------|-------------|
| Density | g/cc lb/cu in | 3.72 .13 | 3.89 .14 | 3.10 .11 | 3.31 .12 | 5.60 | 7.75 .28 |
| Elastic Modulus | GPa Mpsi | 303 44 | 372 54 | 393 57 | 311 45 | 200 29 | 230 34 |
| Weight / Stiffness | Gpa/ g/cc | 81 | 96 | 127 | 64 | 33 | 30 |
| Flexural Strength | Mpa Kpsi | 358 52 | 379 55 | 462 67 | 906 132 | 900 | |
| Knoop Hardness | GPa | 11 | 14 | 27 | 15 | 13 | 9-14 |
| Thermal Expansion Coefficient | $\mu\text{in/in}/^\circ\text{F}$ $\mu\text{in/in}/^\circ\text{C}$ | 3.4 6.0 | 3.4 6.0 | 2.4 4.3 | 1.7 3.0 | 5.8 10.3 | 6.7 11.8 |
| Thermal Conductivity | W/m $^\circ\text{K}$ | 24.7 | 35.6 | 125 | 12 | 2.2 | 35 |

Table 2.4 Property graphs for commonly used advanced ceramic materials. Al (96%) and Al (99.5%) refer to Alumina (96% and 99.5% purity respectively).



2.4 - Types of Engineered Ceramics

In terms of price, size, and availability, *Alumina* and *Zirconia* are of particular interest to the precision machine designer. These are the most commonly used in coordinate measuring machines, machine tools, and gaging products.

2.4.1 - Zirconium Oxide

Zirconium oxide is made in three forms: fully stabilized, partially stabilized tetragonal (Y-TZP), and partially stabilized transformation toughened (TTZ).

Structural ceramic components are made by adding carefully controlled amounts of various impurities such as calcium oxide, magnesium oxide, yttrium oxide and cerium oxide, and allowing the material to undergo phase transformations under controlled conditions. A transformation toughened zirconia, for example, is produced by adding just enough impurity to freeze the material in its high temperature form. As the material cools, it is heat treated so the material starts to precipitate a second phase. On further cooling, these precipitates have a tendency to transform to the low temperature phase but are held by the matrix so they can't undergo the discontinuous expansion. This situation tends to toughen the material because a crack front hitting one of these precipitates causes a sudden expansion of the precipitate. This tends to compress the crack front and deflect it in other directions. This mechanism is analogous to a martensitic phase transformation used to harden steel.

Another type of partially stabilized zirconia controls the phase transformation by forcing the entire matrix to crystallize in the middle temperature form which happens to be tetragonal. This material also transforms when a crack occurs, although not as dramatically as TTZ. Normally, yttrium oxide is the impurity used to form these composites which are called yttria stabilized tetragonal zirconia polycrystals (Y-TZP).

Zirconium oxide ceramics are used in numerous tough applications such as bearing, extrusion dies, wear surfaces, cutting tools, and forming tools. They are the toughest of the high tech ceramics and extremely useful because they can be sharpened to a keen, stable edge. Since most steel cutting surfaces are dulled by corrosion rather than abrasion, zirconia cutting edges have shown some remarkable results when tested in side by side edge life experiments.

2.4.2- Aluminum Oxide

Aluminum oxide is the oldest and most widely used of the engineering ceramic materials. It is relatively inexpensive and can be manufactured into many forms. Therefore, it should be the first material considered when choosing a ceramic material.

Aluminum oxide (Alumina) or Corundum, is probably the oldest true engineering ceramic. It is extremely hard and has good mechanical strength. Generally, alumina is sold in purities such as 96% and 99.5%. Cost is a function of purity.

Alumina has approximately 40% of the density of steel, yet is nearly twice as stiff. Additionally, it has better wear characteristics, lower thermal expansion coefficient, and is corrosion resistant.

2.5 - Production of Precision Machine Ceramic Components

Ceramic components are formed either by slip casting or isostatic pressing of the ceramic material. Slipcast components can be formed into more unusual shapes but will be approximately 25% less stiff than a comparable isostatically pressed component.

Slipcasting integrates most of the features into a single ceramic component. Hobby ceramics utilize slip casting methods and thus there is a greater familiarity with this method. Slipcasting can be divided into (1) drain casting, and (2) solid casting as described by Norton [1]. In drain casting, the slip is poured into a mold long enough for a layer of solid material to build against the outside wall. At this time, the remaining slip is poured out. In solid casting, the slip remains until the solid layer completely fills the mold. Slipcast machine tool bases have been produced for research machines such as those built by Furukawa et al. [2] and Ueno [3] and Tsutsumi et al. [4].

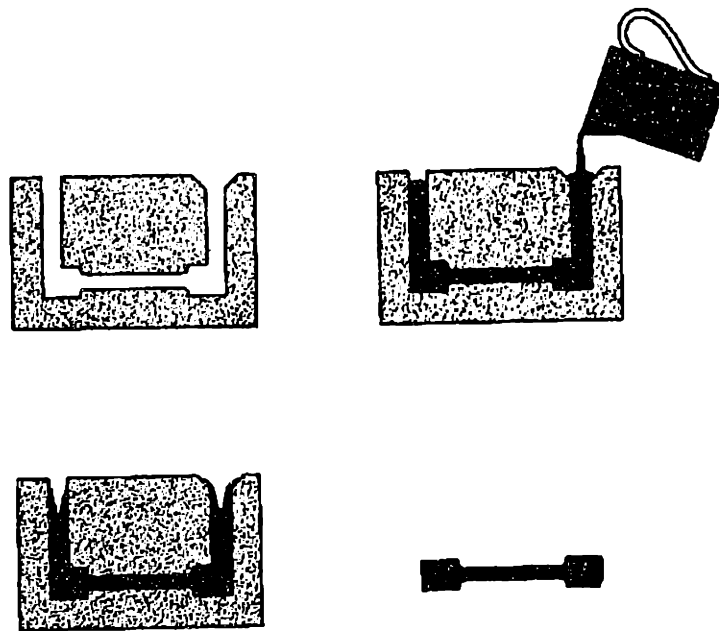


Figure 2.4 Diagram of the slipcasting process (from Norton [1]).

In order to reduce the cost associated with ceramic components, and increase the range of component shapes which can be inexpensively produced to high accuracy, a modular approach has been developed. This approach uses simple, isostatically pressed prismatic beams with internal cells as building blocks which can be combined to form larger, more complicated structures. The beams are processed to high accuracy, then assembled, then finished. This approach is different from the slipcasting approach.

The modular approach has several advantages compared with slipcasting. First, the components can be densified under isostatic pressure which generally increases the final elastic modulus of the fired ceramic component. Second, the components can be ground and brought close to final tolerance as simple prismatic shapes before assembly. Thus, a significant portion of the after fired machining can be done on subcomponents rather than

on the assembly. Third, the tooling for the modular approach is more flexible and generally less expensive to change. For prismatic beams, tooling is generally simple and can be easily reconfigured. Finally, the design is less sensitive to firing problems because of changes in thickness and slumping in unsupported areas.

The prismatic beams used as modular components often have internal cells in order to decrease the structural weight. The beams can have a single internal cell or multiple cells. Figure 2.5 shows some common cross-sections for prismatic beams.

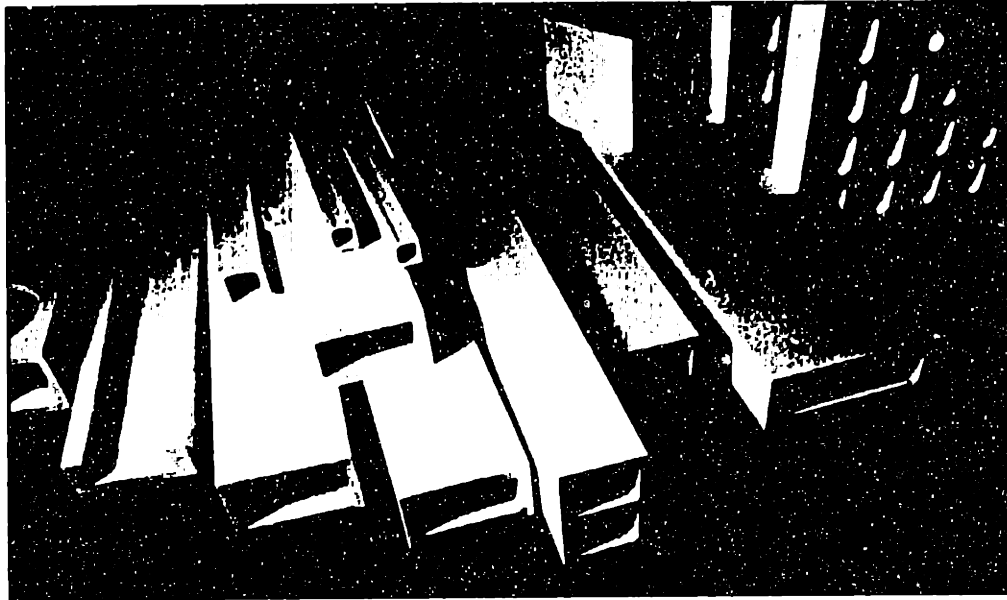


Figure 2.5 Examples of prismatic aluminum oxide beams which are isostatically pressed with hollow interiors.

Constructing beams with hollow internal cells is advantageous for structural and thermal reasons in particular. Many precision applications are concerned with the bending stiffness and the weight. The most efficient way to increase the stiffness of a beam without increasing the weight is to have material far away from the neutral axis of the beam. Furthermore, since many ceramic materials (for example aluminum oxide) have relatively low thermal conductivity, it is advantageous to design a beam which has as much surface area as possible in order to increase heat convection. Any areas with significant thickness should be carefully considered in order to make certain that thermal gradients are minimal.

This configuration is also efficient for manufacturing. Thick ceramic parts are susceptible to cracking during the firing process. Hollow parts, by contrast, fire efficiently. The center webs in a multiple cell configuration must be designed such that the density does not vary significantly throughout the cross-section.

Structures which are modular in design generally follow a standard production process. The components are pressed, green formed, fired, and finished to within approximately 25-100 μ m of their final form. The components are then assembled and machined to final form. It is preferable, though often difficult, to design a precision

machine structure or component such that no final machining will be required after assembly. Figure 2.6 is a flow chart of the basic steps in producing large scale, high precision, ceramic components.

In general, controlling accuracy is easier at the component level. Simple prismatic beams can be lapped to within $0.5\mu\text{m}$ of a nominal dimension over a large area. However, once components are joined together, the task of bringing accuracy to both parts increases substantially. For example, consider two beams joined in a T shape. If the beams were machined separately, they could be produced to a high degree of accuracy, then joined. However, if the beams were joined when rough, machining the area close to the joint would be extremely difficult. Moreover, positioning the part on a grinding machine bed would require careful shimming techniques in order to machine a reference surface.

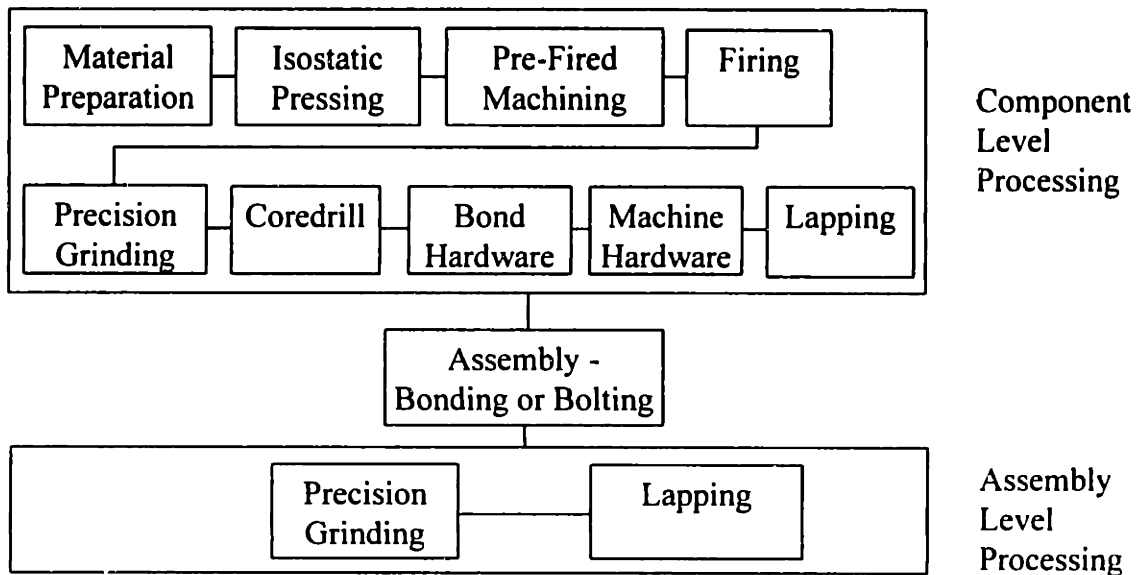


Figure 2.6 Flow chart of the main manufacturing steps involved in producing a precision ceramic machine tool component.

2.5.1- Material Preparation

The process of preparing the ceramic powder has a strong effect on both the material properties of a finished component and the processing parameters. Aluminum oxide is made from bauxite that has been chemically purified using the Bayer process. In this process, the bauxite ore is chemically dissolved under heat and pressure to form a soluble salt of aluminum. This salt is then chemically reacted and precipitated into a chemically pure aluminum trihydrate. The hydrate is calcinated in a rotary kiln similar to a cement kiln or lime kiln to produce aluminum oxide.

Pure aluminum oxide has to be further treated to make it a pressable powder. It is first, made into a slurry by mixing the powder with water and adding an organic binder. Talcs, clays, and other alloying ingredients are added to adjust the sintering properties. The slurry is ball milled for several hours to achieve proper mixing and particle size distribution. This wet slurry may be processed by slip casting or isostatic pressing.

Material prepared for isostatic pressing feeds the wet slurry into a spray dryer, where it is sprayed into tiny droplets which are dried as they fall through a hot steam of air. This produces a free flowing powder that can be poured into molding cavities and dies. Spray drying produces a uniform body that aids in automation of subsequent operations.

2.5.2 - Isostatic Pressing of Prismatic Ceramic Components

Densifying the powder can be done in an isostatic press. This consists of placing the powder into a rubber bag and sealing it. The bag is then placed into vessel and water pumped around it to 70 MPa. Figure 2.7 shows the press geometry. This produces a soft machinable block (Figure 4) referred to as “green” ceramic which has to be handled carefully.

Typical production presses allow parts to be manufactured to monolithic fired lengths of 2.25 meters and widths to 0.5 meters. The type of tooling used will influence the size of the machinable block available for a given press size. The tooling will also strongly influence the material flow during the densifying process. Typical tooling examples are; solid slug, single mandrel, or multiple mandrel.

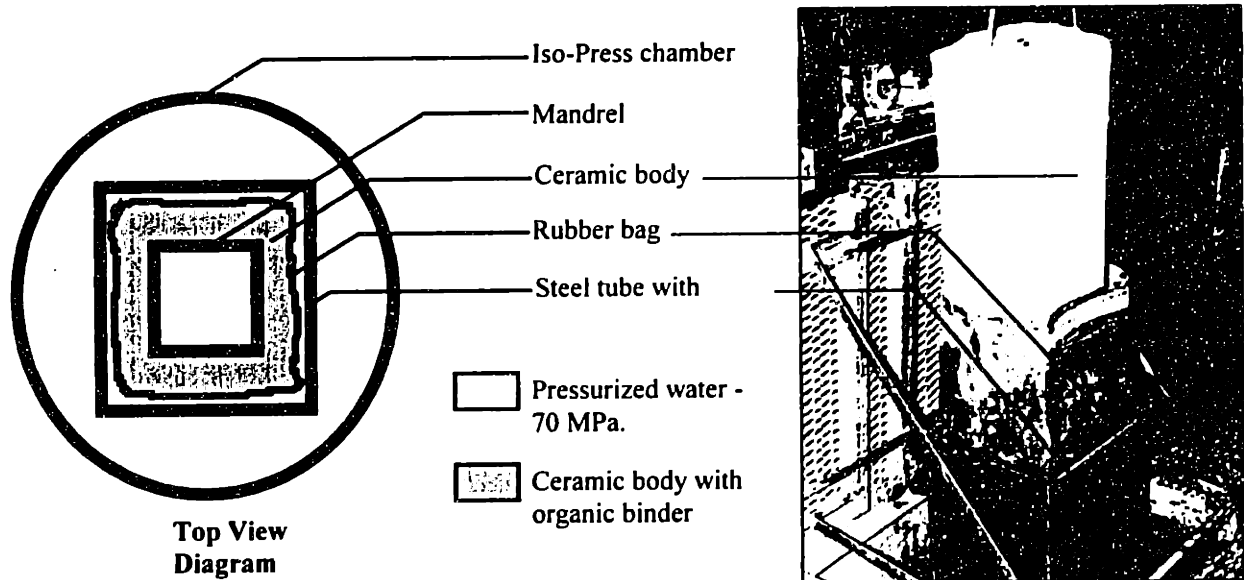


Figure 2.7 Top view diagram (left) and a photograph (right) of the main components in the isostatic pressing of a hollow prismatic beam.

It is good practice to maintain as much symmetry as possible in press tooling design. Pressing long, slender mandrels in large bags is a common pressing problem due to slight variations in the density of the powder poured into the tooling. The filled tooling is vibrated to minimize the powder density variation. Additionally, pressing large internal steps on a mandrel can create problems during the pressing process. In general, complicated features are not generally added to components in the isostatic press. External features such as slots are usually added to a component by green machining or grinding after firing.

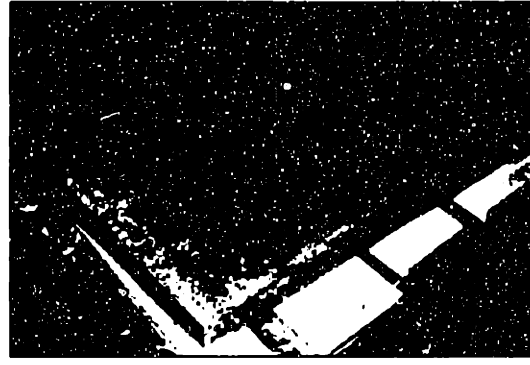
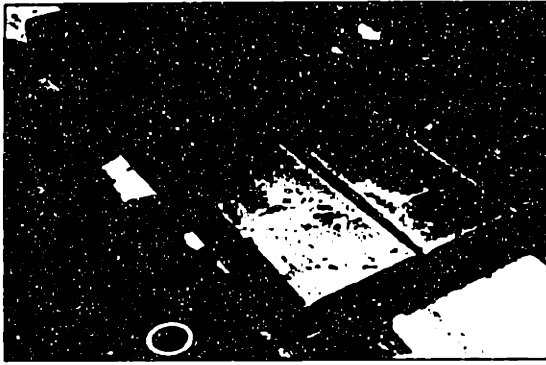


Figure 2.8 Examples of pressed ceramic parts. The parts on the left are multiple cell beams (dimensions: outside 8" x 3" x 60", each cell is approx. 1.5" x 1.5"). The part on the right is a solid plate (dimensions: 20" x 30" x 2").

2.5.3 - Machining of "Green" Ceramic Components

Green ceramic can be milled, sawed, and sanded much like wood. Figure 2.9 shows a green ceramic component being milled. The green ceramic has the feel and hardness of a bar of soap. This allows rapid machining although the material is extremely abrasive. Therefore, the tooling is usually diamond coated or solid carbide. Green ceramic is routinely processed on numerically controlled machinery so that intricate features may be incorporated into the part. However, accuracy may be limited to 1.0% in some cases due to variations in material preparation, and pressing.

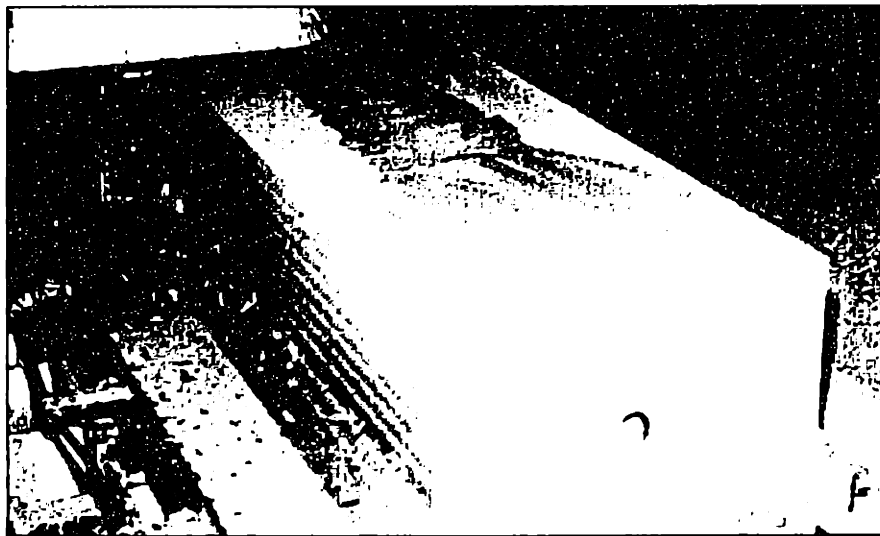


Figure 2.9 The green ceramic is milled with conventional machines. The material behaves similar to wood when being machined.

2.5.4 - Firing Ceramic Components

Alumina can be sintered in either periodic or tunnel kilns with cycles up to 6 days. This cycle is usually dependent on the thickness of the components being fired. This cycle also transforms the green "soap-like" material into a hard, stiff material with hardness characteristics close to those of sapphire. The firing operation is similar to an oven. The material is heated to 3000 °F. The material is still well below the melting point for alumina, yet there is sufficient energy to cause the material to bind to adjacent particles.

Similar to the material preparation process, the firing cycle has a significant effect on the material properties of the final component. A part which is not fired at a sufficiently high temperature will not fully densify and will have minute flaws. Such flaws have a substantial effect on the part. For example, in some cases 1% excess porosity can reduce the tensile strength of a part by 60%. The final strength of a fired component is dependent upon the grain size and density of the material. A firing cycle which is too long or too high in temperature results in oversized grain structure.

During the firing cycle, dimensions will be effected by shrinkage. Typical shrinkage values for alumina are close to 15%-20% (but may be as high as 30%), depending upon the type of ceramic. Additionally, parts can slump and distort during the firing cycle. The amount of distortion depends upon the design of the part, as well as the orientation of the part while in the kiln. For example, the shrinkage of a long slender beam, fired standing on end, would shrink in length substantially more than the same beam if hung in the kiln, due to the effect of gravity on the part. In many cases, parts must be specifically designed so that they do not distort too significantly while being fired. For example, the webs in multiple cell beams must be designed to minimize such distortion.

When manufacturing larger single and multiple cell beams, slumping is a consideration. As the ceramic approaches peak temperature, it deforms quite easily. Thus, a thin wall suspended over a wide span can droop considerably during firing. A maximum span to thickness ratio of 6-8 is advised. A way of minimizing this slump on thin, square beams is firing in V furniture. For larger or more irregular shapes, green or fired furniture may be used inside the component. Slumping can be utilized in certain designs. For example, a curved beam can be manufactured by firing a straight beam on curved refractory.

Another consideration is the design of transitions between thin and thick sections. In general, such transitions should be streamlined as much as possible. Similarly, sharp radii between adjoining surfaces should be avoided.

Straightness can be improved by more frequent kiln rebuilds. In general, there is a tradeoff between the additional cost of rebuilding the kiln and the cost of removing additional grind stock. Straightness is usually not worse than 0.001% of the component length. This will also cover the slight necking which occurs from drag on long parts.

The large reduction in volume causes any crack or defect to become more evident as it is fired. Thus, defects are easier to identify after firing than one might expect. Inspection is most frequently done with a dye or a fluorescent penetrant.

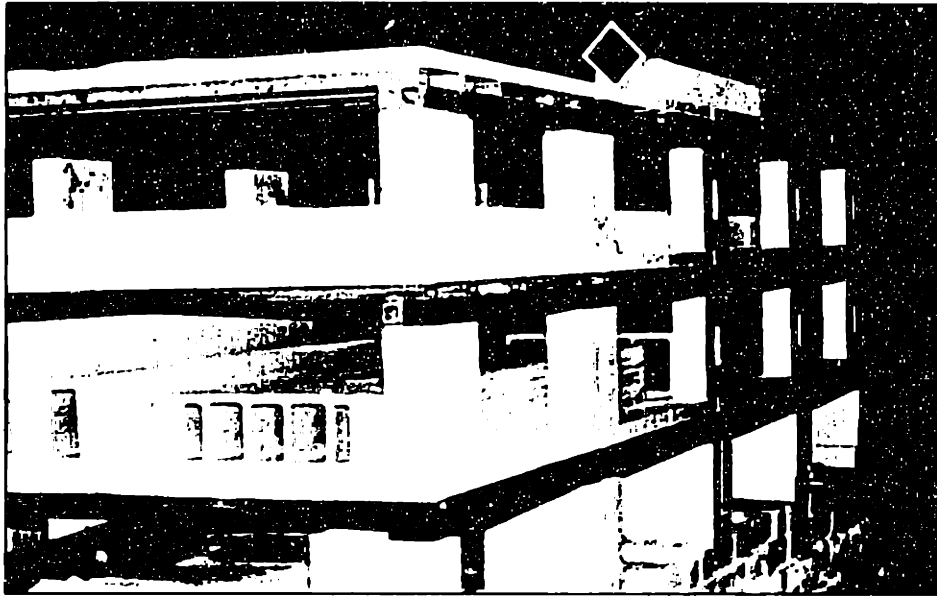


Figure 2.10 Green components being loaded into a kiln.

2.5.5 - Grinding Ceramic Components

Grinding is done almost exclusively with diamond wheels. Grinding may be separated into rough grinding and precision grinding. For the most part, grinding is done with 180 grit or finer diamond wheels. The coolant is generally a combination of water and a lubricant. A typical mixture might include 95% water and 5% lubricant. The depth of cut is often approximately $3.0\mu\text{m}$ and the relative velocity of the wheel with respect to the workpiece is often about 0.5m/sec . Overall, the material removal rate of a grinding machine aggressively finishing a ceramic component is about 16cm^3 of material per minute. Since grinding is an expensive part of producing ceramic components, industry is pushing hard to increase this rate.

The overall finish of a ground part depends heavily upon the dynamic stiffness of the machine, the ability to control the thermal distortion of the part and the machine during grinding, and the processing parameters such as the grinding wheel finish and the feed rates. Flatness of approximately $3.0\mu\text{m}$ over 1.0m is reasonable for a well tuned process. Figure 2.11 shows a surface grinder working on an alumina, multiple cell beam with coolant flooding the grinding area.

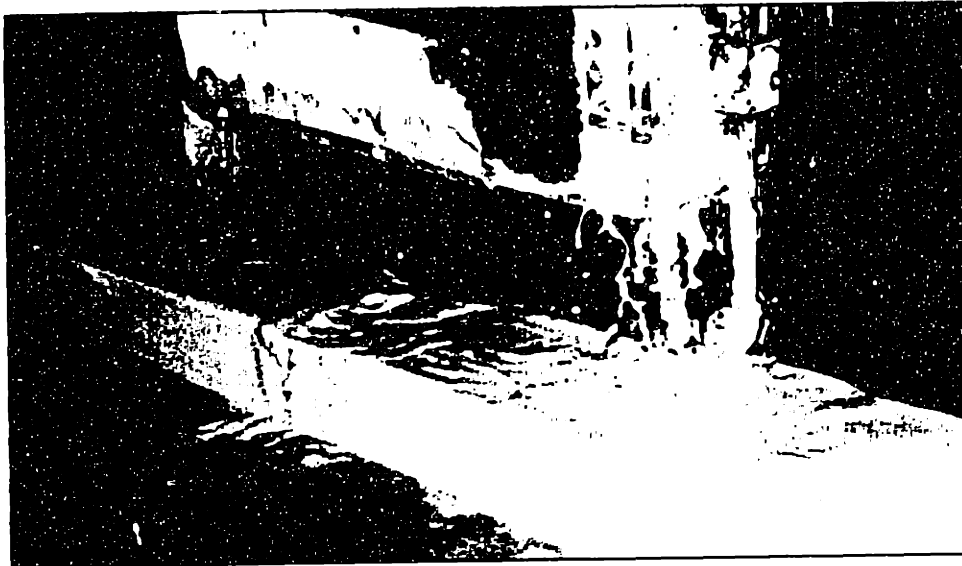


Figure 2.11 Fired components are ground on a surface grinder with coolant flooding the surface. The machine is operated in a thermally controlled room in order to improve accuracy.

2.5.6 - Coredrilling Fired Ceramic Components

Coredrilling operations are done on numerically controlled equipment so that complex shapes can also be ground using the same set-up. Coredrills have diamond plated surfaces, which cut through the ceramic on the outside of a hole, leaving the center of the hole uncut. Counterbored holes can be manufactured with coredrills, and small diamond wheels to finish the counterbore seat.

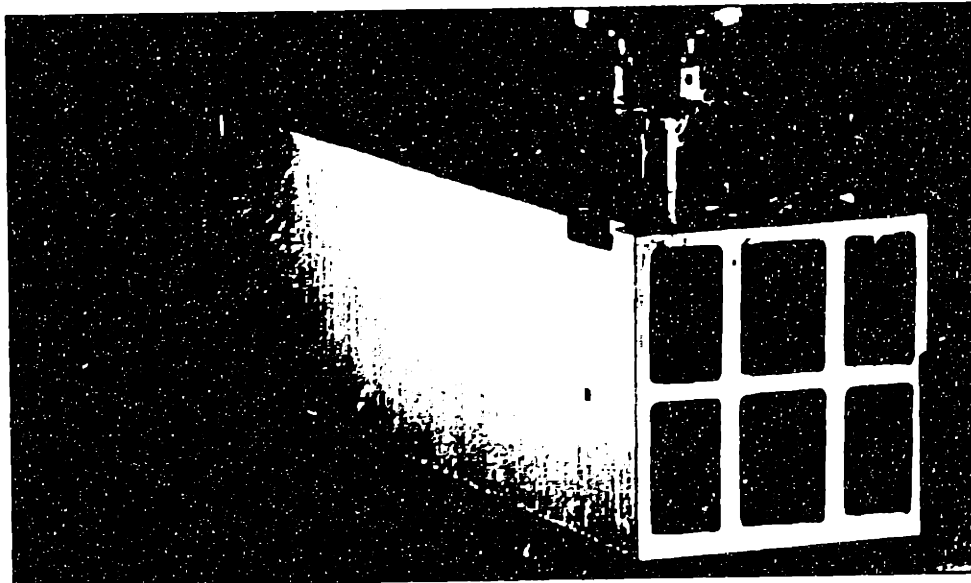


Figure 2.12 The fired component is coredrilled using diamond coated drills. Feed rates of 9 mm/min. have been achieved.

Since high pressure coolant is used, the underside of coredrilled holes may be damaged by the process of drilling when the pressure across the core exceeds the strength of the thin ring of material holding the core. When this happens, small chips along the underside rim can result. Holes are usually placed in positions where such chipping is not critical. In cases where fractured edges could be a problem, the hole can be halfway drilled from each side. Figure 2.12 shows the coredrill of a hole on a multiple cell alumina beam.

Unlike steel components, ceramic holes are difficult to thread internally, unless the threads are large and can be done in the green forming stage. Even then, they are brittle, so they are only used for low-strength, high temperature situations. For precision machine applications, threaded steel inserts are bonded in coredrilled holes. For precise thread locations, solid inserts are bonded then drilled and tapped.

2.5.7 - Lapping of Precision Ceramic Components

Precision finished ceramic components fully exploit the material's properties because they can be lapped to almost any accuracy and they will remain stable. Lapping of large precision structures is done by hand as shown in Figure 2.13, by skilled lappers who have developed their abilities over years.

Large ceramic parts are lapped on cast iron lapping plates which are embedded with small diamonds. Plates are prepared by spreading diamond powder then rolling the diamond into the plate with a hardened steel wheel. The plate is referred to as "charged" once the diamonds have been embedded. The charged plate is rubbed against the ceramic part with varying degrees of pressure depending upon how much stock needs to be removed.

It is possible to use diamond in a slurry form rather than as a diamond powder. However, diamond slurry requires clean up rather than charging time as with dry diamond powder.

The parts are inspected before, during, and after lapping in order to measure the geometry of the part. However, the part has to thermally stabilize before measurement can be done. For final inspection, the part is allowed to thermally soak in the temperature controlled room for 24 hours.

The lapping process for ceramic is distinct from lapping of granite parts in several ways. First, stock removal is harder with ceramic because of the hardness of the material. Second, stock removal is more predictable with ceramic. Third, ceramic components are more capable of holding an edge than the granite.

Accuracy of lapped components is generally limited by the measurement resolution rather than the ability to control the material removal rate. A typical part leaving lapping will have a surface finish of approximately 0.4 μ m RA. It is difficult to achieve rough surface finishes unless unusually large diamond grains are used. Since ceramic has a negative skewness on the surface, finish readings are dependent upon the diameter of the stylus point. Typical stylus diameters are 15.0 μ m.

Parts which require lapping should be made as rectangular as possible. Lapping one face of a beam parallel to another is not difficult. However, lapping an incline into a beam is fairly involved. Additionally, lapping into the corner of a part is difficult if there

is no clearance zone allowed. Typically, 1.5mm is sufficient as a clearance zone for lapped components. Finally, lapping thin walled components is difficult because the part will tend to deflect under the load of the lapping plate and may have significant thermal distortions since there is less volume to absorb the lapping energy. Thus, thin walled surfaces must be lapped with low material removal rates and allowed to thermally stabilize during the lapping process.

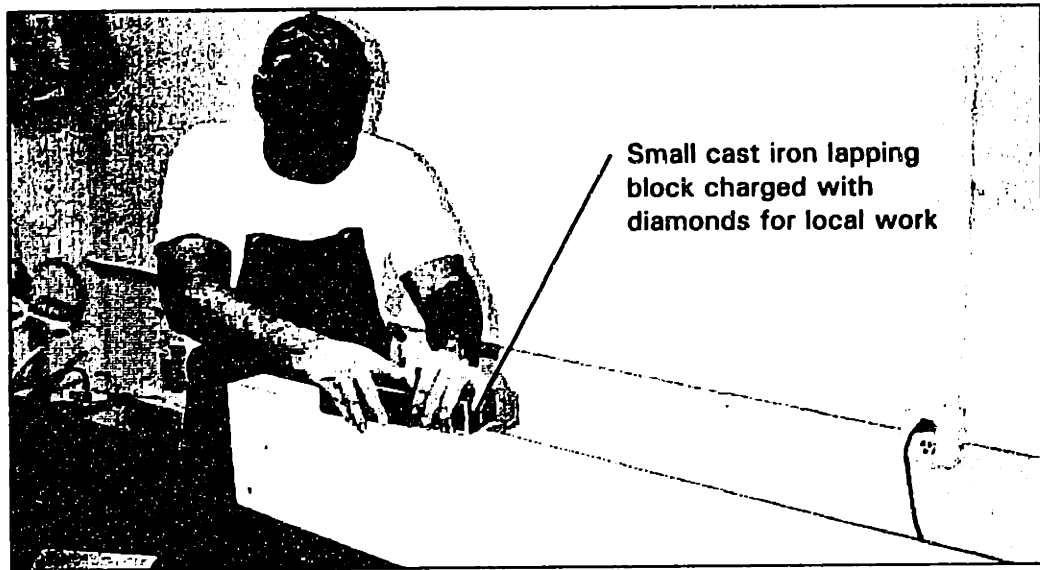


Figure 2.13 Lapping of ceramic beams is done using cast iron plates which are "charged" with diamond particles.

2.5.8 - Metrology of High Precision Ceramic Components

One of the most important aspects of producing high precision components, regardless of material, is the method of inspection. Precision machine designers always need to be concerned with how components are inspected.

One of the main advantages of ceramic materials, when compared to steel or aluminum, is that they can be lapped or machined to high accuracy. The thermal stability and the hardness of ceramic makes this possible. As an example, steel rails for precision machine tools are often ground to flatness and parallel tolerances of approximately $5\mu\text{m}$ (for lengths up to 5 meters). If higher accuracy is required, they are generally scraped by hand so that high spots are removed. The resulting product is not necessarily flat over every part of the rail. However, the average of the high and low spots of a region of several millimeters may be very flat. With ceramic components, the resulting product is very different. A ceramic rail can be machined or hand lapped to a flatness and parallel tolerance of approximately $1\mu\text{m}$ for the same length (assuming excellent production environment and gauging capability). The resulting ceramic rail will be flat to within the stated tolerance over a much smaller area than the equivalent steel rail. This is an extremely important advantage for fluid film bearing rails such as air bearings and hydrostatic.

All of the possible accuracy advantages of ceramic components depend on the ability to inspect the part. In many cases, where skilled lapping capabilities are developed, the measurement accuracy limits the process of achieving ever better tolerances.

The following descriptions explain common measurement techniques for precision ceramic components. The descriptions are taken from one particular manufacturing facility (Precision Products Group at Wilbanks International). They are intended to give a qualitative sense of metrology performed in a successful production facility.

Typical Environmental Conditions

- All gaging is performed in a temperature controlled room. The temperature is controlled to $\pm 1^\circ\text{F}$. The nominal temperature is 68°F .
- All parts are “soaked” in the temperature controlled room for 24 hours prior to final gaging in order to ensure that the measured component is at thermal equilibrium.
- The gaging is performed on granite surface tables which are typically about 10' x 5' x 2' in size. The tables are kinematically mounted on the gaging room floor. The total flatness variation of the table surface is .0002" (over the entire surface as measured by a Federal™ level system).
- The foundation of the gaging room is separated from the rest of the production facility in order to isolate the gaging room from vibration.

Measuring Straightness

Straightness measurements are made with a Leitz® autocollimator. The autocollimator has 2 main components, a stationary source/read unit, and a travelling reflector mirror.

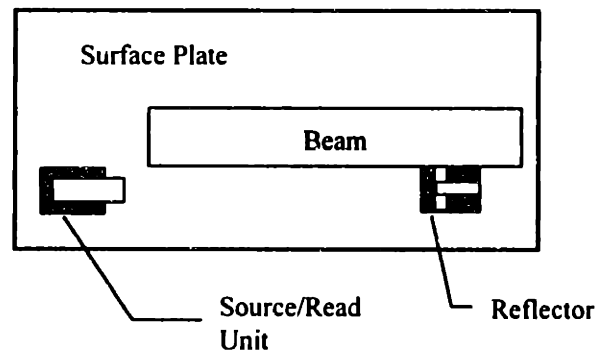


Figure 2.14 Top view diagram of the straightness measuring set-up. The reflector is moved along the beam to collect a series of readings.

The autocollimator is a standard measurement system which has been used in the precision industry for over 20 years. The autocollimator integrates (discrete integration) a series of angular measurements to arrive at the straightness for the beam. The following photographs give a clearer idea of the equipment set-up for a straightness measurement.

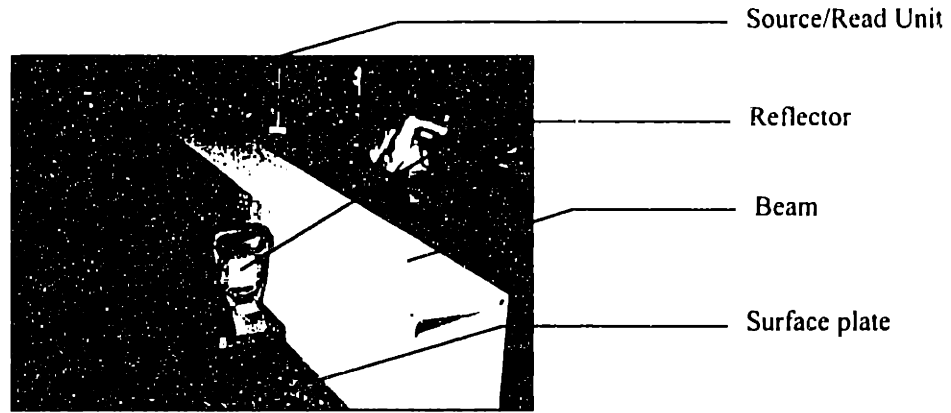


Figure 2.15 Photograph of the main components in an autocollimator measurement.

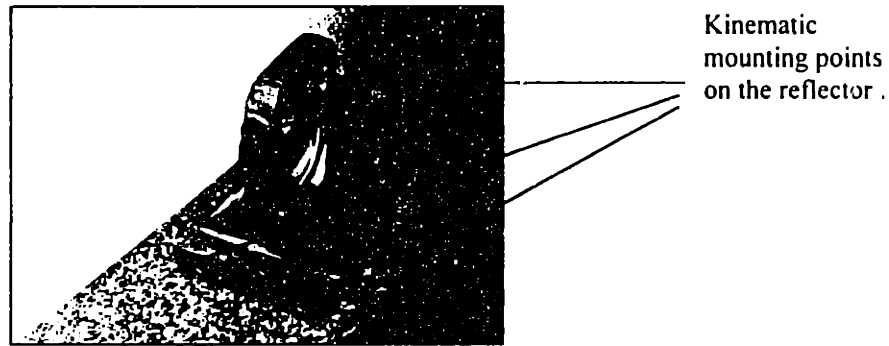


Figure 2.16 Photograph of the reflector unit with the kinematic mounts, which register the reflector against the beam in order to ensure that the location of the reflector is stable and repeatable.

The stated uncertainty of the autocollimator is provided by the manufacturer and is usually expressed as a function of the length of the component:

$$U = (.000002 / 4) * L \quad (2.3)$$

where L is the length of the beam in inches. The uncertainty U accounts for only errors in the measurement system and assumes no thermal errors, vibrations, or operator errors. For a 100" beam, the uncertainty is 0.00005" which is less accurate than the lapping accuracy for the same length.

Parallelism

Parallelism between two surfaces is measured using a surface plate and an LVDT gage head. The LVDT is adjusted to the height of the top surface of the beam, then the beam is moved underneath the gage in order to check the parallelism of the entire surface. This measurement technique is the primary measurement used by lappers when bringing components into high precision tolerances. The following diagram and photographs illustrate the measurement set-up.

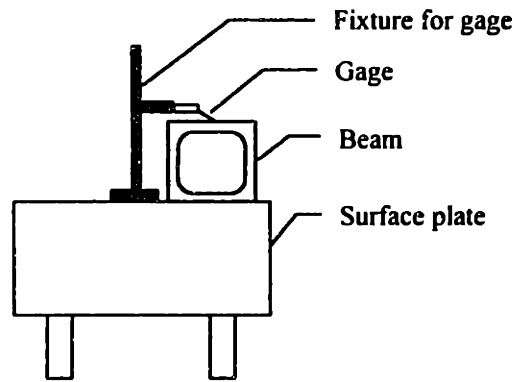


Figure 2.17 Side view diagram of the parallelism measurement set-up.

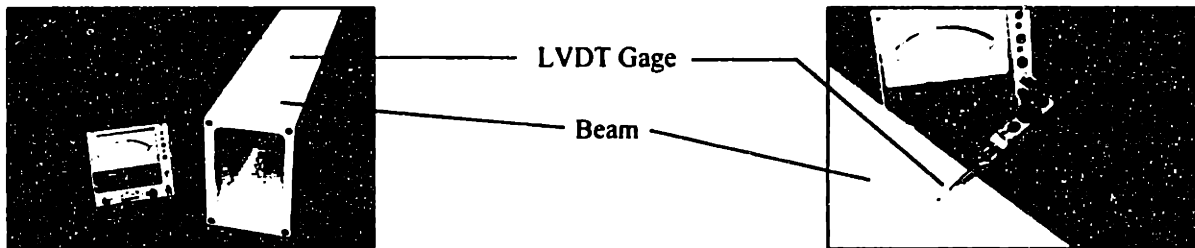


Figure 2.18 Photographs of the LVDT gage head being used to measure parallelism between two surfaces.

The uncertainty of the set-up depends upon the flatness of the surface plate underneath the beam and the uncertainties of the LVDT gage. The combined uncertainty for 60" beams has been experimentally determined as .000010".

Squareness

Squareness is checked with a reference master square and a Squarol gaging set-up. In this set-up, the squareness of the master square with respect to the surface plate is first checked in order to establish a datum. The component is checked with one of the two sides on the surface plate. Figure 2.18 and 2.19 show the squareness checking process.

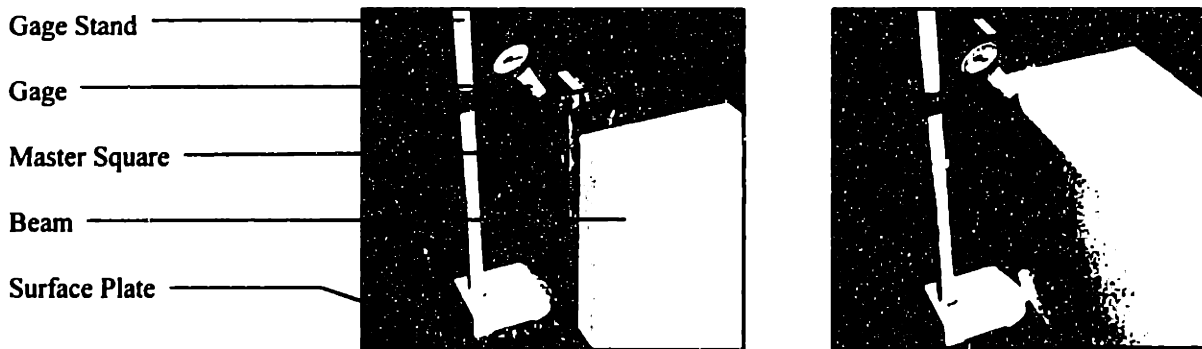


Figure 2.19 Photographs of the Squarol gaging set-up. The gage is zeroed out using a master square (left) then positioned against the beam (right) to establish squareness between the gaged surface and the surface plate side of the beam.

The gage stands are alumina ceramic in order to increase the stiffness and thermal stability. The uncertainty of this measurement has been experimentally evaluated at .000020" over a 12" wide beam side.

2.5.9 - Fixing Defects in Ceramic Components

The goal of this section is to describe the sources of defects and methods for patching small defects in large precision ceramic components.

In manufacturing large ceramic components, it is currently possible to have defects in the component even in a well controlled production facility. The process of producing a 4 meter long beam to tolerances of 2µm flatness without visual defects is extremely demanding. Ceramics, which are generally white, easily reveal small contaminates. Large, high precision ceramic components such as beams and polishing plates have significant value even before they are ground and lapped to final tolerance. Therefore, in order to keep the price of these components reasonable, it is important to fix these defects (if it will not effect performance) rather than start production of a new component. It is usually possible to patch small defects without effecting the performance of the component. Performance includes characteristics such as modulus of rupture, surface finish, stiffness, and aesthetics.

Examples of possible defects include voids, cracks, chips, and material contamination marks. Table 2.5 is a summary of the most common non-geometric defects and possible production causes.

Table 2.5 Summary of non-geometric defects in ceramic components.

| Defect ¹ | Description | Common Causes |
|---------------------|---|--|
| Pits, Pocks | Shallow surface depression (pit) and partially closed surface cavity (pock) | <ul style="list-style-type: none"> • Voids in the isostatically pressed blank. • Excess organic binder particle in powder which burns out during firing leaving a vacant volume. |
| Cracks | Line of fracture without complete separation | <ul style="list-style-type: none"> • Handling. • Stress from machining. • Binder burnout. |
| Chips | Area along edge or corner where material has been broken off | <ul style="list-style-type: none"> • Handling. |
| Inclusions | Embedded foreign material or stain | <ul style="list-style-type: none"> • Concentrated points of impurities such as metal in the ceramic powder. • Material impurity from the firing process. Since air flows over the parts during firing, contaminates are occasionally deposited on the ceramic. |

¹ Defects as defined by the ASTM Standard Designation: F 109 - 91. "Standard Terminology Relating to Surface Imperfections on Ceramics".

Several types of patches have been developed to fix defects in ceramic components such that their performance is not degraded. Even in critical applications, such as airbearing surfaces, patches can be used to repair the component. There are three common patches; (1) "puck" type insets, (2) epoxy, and (3) ceramic core insets. Figure 2.20 shows these common patches in a small ceramic plate.

The "puck" patch is most frequently used on chipped edges, and areas where only a thin layer of the component has been effected. The patch is implemented by milling (with an abrasive diamond tool on a milling machine) a small cylinder which completely removes the defect. The cylinder is then filled with a ceramic cylinder (machined to about .03mm less than the diameter of the machined region). The new ceramic cylinder is bonded into the component with a high strength epoxy. Then it is ground and/or lapped flat to the surface. Usually the cylinder size is about 50% larger than the size of a defect. For example, a 3mm chip might be replaced by a 5mm puck.

The use of epoxy is perhaps the most widely used method for correcting surface defects such as cracks, chips, or contamination spots. In the case of chips, the effected area is prepared (cleaned, and sharp edged removed) then filled directly with epoxy. The epoxy generally has a shear modulus of approximately 35MPa. and a thermal expansion rate similar to the ceramic. Contamination spots and cracks are generally "opened up" with the use of a dental drill, then prepared and filled with epoxy. All epoxy patches are honed flat to the surface.

The use of ceramic cores is common with many defects larger than 2mm which are not on the edges of the component. The defect is coredrilled out of the component then replaced with a matching core. The new core is generally about .03mm smaller than the diameter of the coredrilled hole. The new core is bonded into the component then ground and/or lapped flat to the surface.

Table 2.6 summarizes the advantages and disadvantages of these three patches.

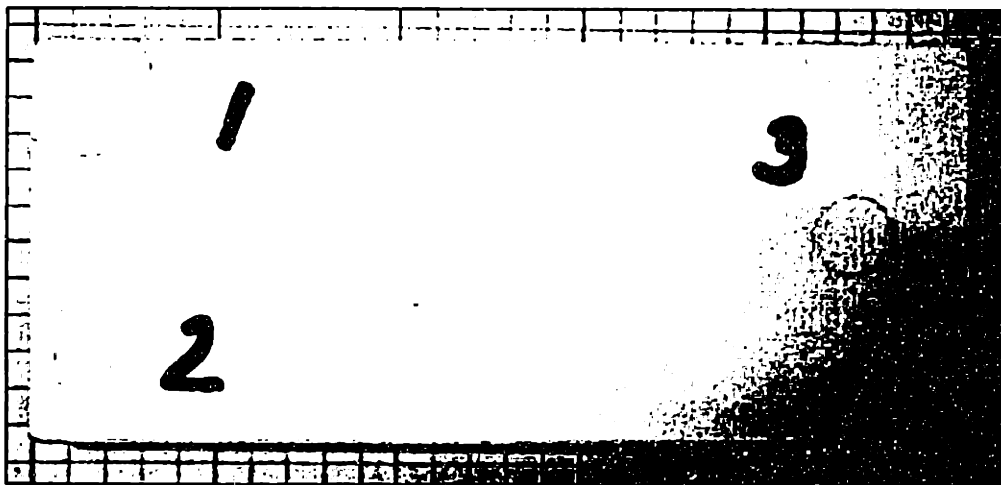


Figure 2.20 A sample plate of aluminum oxide with three different types of patches for small defects. Patch # 1 is referred to as a "hockey puck", patch # 2 is a chip rebonded into the plate, and patch # 3 is a core fill.

Table 2.6 Advantages and disadvantages of common patches.

| Patch | Applications | Advantages | Disadvantages |
|--------------|--|--|--|
| Ceramic puck | Edge chips, voids and cracks which are too large for epoxy fill. | <ul style="list-style-type: none"> • Solid fill of removed area. | <ul style="list-style-type: none"> • Puck must be ground and lapped back into tolerance |
| Epoxy | Small chips and pits and pocks | <ul style="list-style-type: none"> • Quick • Fills defects of any shape. | <ul style="list-style-type: none"> • Epoxy is not as hard as the ceramic. |
| Ceramic core | Non-edge chips and cracks | <ul style="list-style-type: none"> • Solid, strong fill of removed area. | <ul style="list-style-type: none"> • Puck must be ground and lapped back into tolerance |

2.6 - Design Strategies for Ceramic Structural Beams

A simple design problem to consider is the uniform cross-section prismatic, single cell beam. In designing ceramic beams, there are four typical goals: (1) increasing stiffness and the stiffness/weight ratio, (2) ensuring the design will be easy to manufacture (particularly in terms of firing and finishing), (3) designing the details such as edge chamfers and hardware so that the beam will be durable against chipping, and (4) designing for thermal stability.

Figure 2.21 shows the main design parameters of a single cell beam. Although the beam is a simple case in that it has no hardware or holes, there are still seven important design parameters to specify regardless of tolerances; the overall width and height, the width and height of the internal cavity, the internal radius, the external chamfer or radius, and the length.

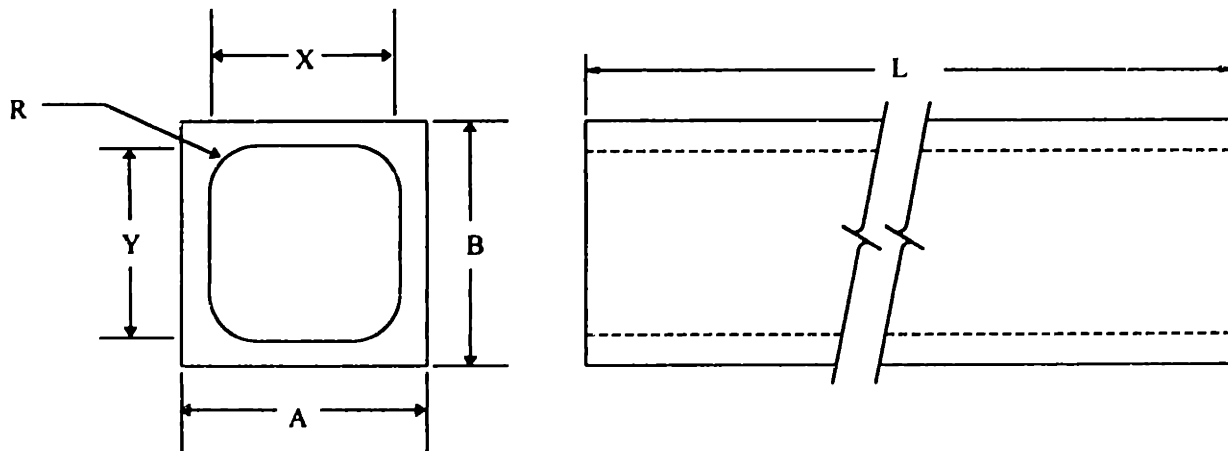


Figure 2.21 Diagram of a single cell, prismatic beam and the main parameters.

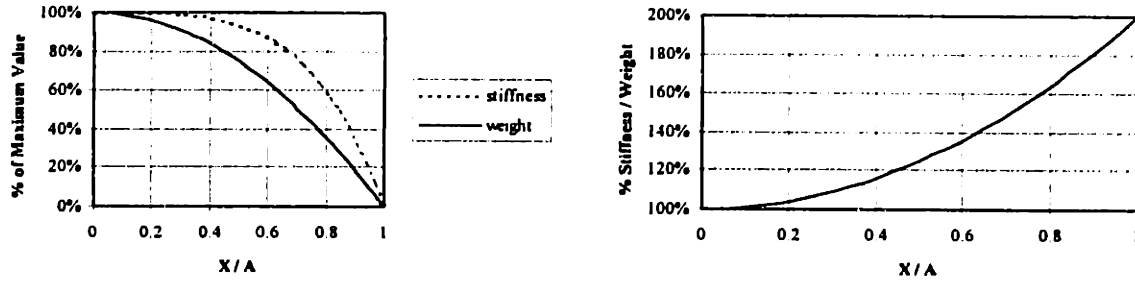


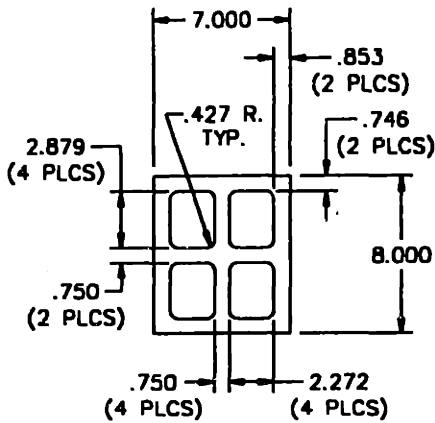
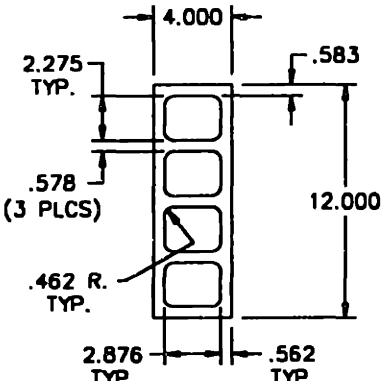
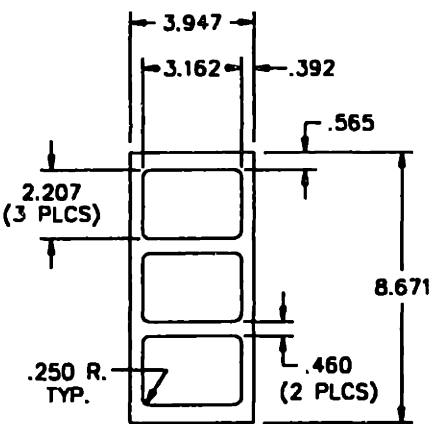
Figure 2.22 Plots of stiffness and weight (left) and stiffness/weight (right) as a function of the internal cell size. Typical values of the X/A ratio are between .6 and .8

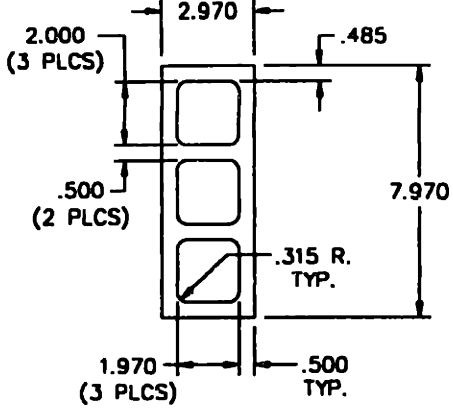
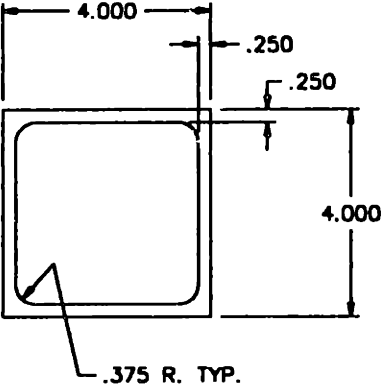
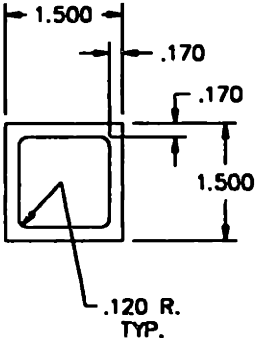
In general, the design process for ceramic beams begins with outside dimensions which must be maintained to fit into the entire machine. Next, the internal dimensions are generally set based upon the required stiffness and weight for the beam. Finally, the design is reviewed from the standpoint of manufacturing. The tooling for the isopress is evaluated, and the thickness of the walls is reviewed in terms of firing. A final design usually evolves from a few iterations of making sure all specifications and manufacturing requirements are satisfied.

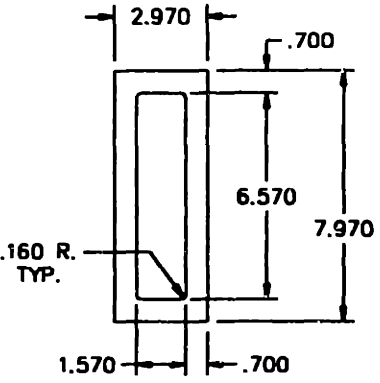
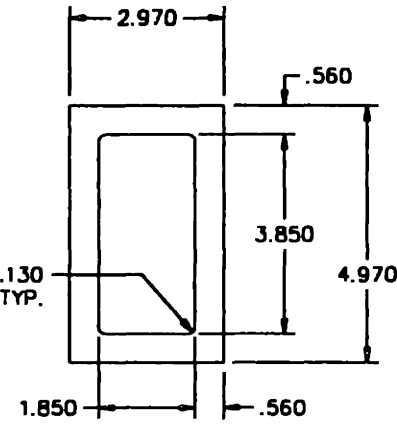
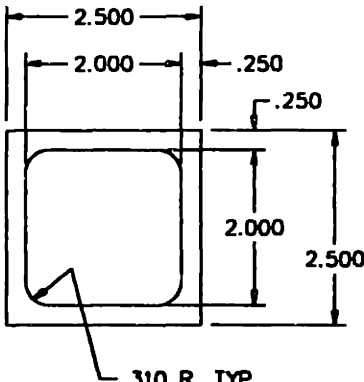
There are “standard” cross-sections for beams which have been tested and verified as manufacturable. The following table shows diagrams of some of the more common shapes.

Table 2.7 Standard single and multiple cell aluminum oxide (isostatically pressed) beams.

| | | |
|---|--|--|
| <p>Technical drawing of a 2x2 grid of ceramic cells. The overall width is 10.636 inches and the overall height is 10.324 inches. Each cell has a width of 4.260 inches (6 PLCS) and a height of 2.920 inches (2 PLCS). The wall thickness is .584 inches (2 PLCS). The corner radius is .250 inches (R. TYP.). There are 4 PLCS (Part Lengths) for the top and bottom walls and 2 PLCS for the side walls. The distance between the centerlines of the cells is 2.394 inches (4 PLCS) horizontally and .764 inches (2 PLCS) vertically. The distance from the centerline to the outer edge is .724 inches (2 PLCS).</p> | <p>Nominal Cross-Section 10.5" X 10.5" Number: 16414</p> <p>Weight / In (lbs.)</p> <p>Moment of Inertia (in^4) - Horizontal - Vertical</p> | <p>5.77</p> <p>512.39</p> <p>553.23</p> |
|---|--|--|

| | | |
|---|--|--|
|  <p>7.000 .853 (2 PLCS) .427 R. TYP. .746 (2 PLCS) 2.879 (4 PLCS) 8.000 .750 (2 PLCS) .750 (4 PLCS) 2.272 (4 PLCS)</p> | <p>Nominal Cross-Section 7.0" X 8.0" Number: 31632</p> <p>Weight / In (lbs.)</p> <p>Moment of Inertia (in⁴) - Horizontal - Vertical</p> | <p>4.08</p> <p>197.65 159.79</p> |
|  <p>4.000 2.275 TYP. .583 12.000 .578 (3 PLCS) .462 R. TYP. 2.876 TYP. .562 TYP.</p> | <p>Nominal Cross-Section 4.0" X 12.0" Number: 16915</p> <p>Weight / In (lbs.)</p> <p>Moment of Inertia (in⁴) - Horizontal - Vertical</p> | <p>3.02</p> <p>306.68 47.27</p> |
|  <p>3.947 3.162 .392 .565 2.207 (3 PLCS) 8.671 .250 R. TYP. .460 (2 PLCS)</p> | <p>Nominal Cross-Section 3.9" X 8.6" Number: 31695</p> <p>Weight / In (lbs.)</p> <p>Moment of Inertia (in⁴) - Horizontal - Vertical</p> | <p>1.80</p> <p>107.60 27.36</p> |

| | | |
|---|--|---|
|  <p>2.000 (3 PLCS)</p> <p>2.970</p> <p>.485</p> <p>.500 (2 PLCS)</p> <p>7.970</p> <p>.315 R. TYP.</p> <p>1.970 (3 PLCS)</p> <p>.500 TYP.</p> | <p>Nominal Cross-Section 2.9" X 7.9" Number: 30372</p> <p>Weight / In (lbs.)</p> <p>Moment of Inertia (in^4) - Horizontal - Vertical</p> | <p>1.62</p> <p>73.40 13.79</p> |
|  <p>4.000</p> <p>.250</p> <p>.250</p> <p>4.000</p> <p>.375 R. TYP.</p> | <p>Nominal Cross-Section 4.0" X 4.0" Number: 32390</p> <p>Weight / In (lbs.)</p> <p>Moment of Inertia (in^4) - Horizontal - Vertical</p> | <p>0.52</p> <p>9.16 9.16</p> |
|  <p>1.500</p> <p>.170</p> <p>.170</p> <p>1.500</p> <p>.120 R. TYP.</p> | <p>Nominal Cross-Section 1.5" x 1.5" Number: 30501</p> <p>Weight / In (lbs.)</p> <p>Moment of Inertia (in^4) - Horizontal - Vertical</p> | <p>0.12</p> <p>0.28 0.28</p> |

| | | |
|---|--|--|
|  | <p>Nominal Cross-Section 2.9" x 7.9" Number: 32586</p> <p>Weight / In (lbs.)</p> <p>Moment of Inertia (in^4) - Horizontal - Vertical</p> | <p>1.79</p> <p>88.43 15.29</p> |
|  | <p>Nominal Cross-Section 2.97" X 4.97" Number: 30700</p> <p>Weight / In (lbs.)</p> <p>Moment of Inertia (in^4) - Horizontal - Vertical</p> | <p>1.03</p> <p>21.64 8.83</p> |
|  | <p>Nominal Cross-Section 2.5" X 2.5" Number: 31733</p> <p>Weight / In</p> <p>Moments of Inertia • Horizontal • Vertical</p> | <p>0.312</p> <p>1.994 1.994</p> |

2.7 - Design Strategies for Multiple Component Structures

As mentioned previously, the modular approach to large precision ceramic structures considers the prismatic beams as building blocks which can be integrated into a complete structure. Integrating the components is generally done in one of two ways; (1) bonding the components together, (2) bolting the components together. The second method often involves bonding hardware into the structure.

2.7.1 - Bonding Ceramic Components

Bonding ceramic structures gives design engineers tremendous flexibility. Bonding allows the construction of larger "composite" ceramic structures as well as adding features uncommon to ceramic such as threads. Essentially, there are three requirements for a good bond; (1) a good epoxy bonding system, (2) proper surface preparation, and (3) good clamping of the parts.

In terms of the epoxy bonding system, several types can be used. Two types of high temperature epoxy can be used in order to attain maximum bond strength. High temperature epoxy can be used in either film or paste form. Two forms of room temperature epoxy can be used; thick "putty" form epoxy or viscous liquid. Finally, a joint filler, similar to dental epoxy can be used for filling the seam between two joined components in order to attain a flat surface.

The strength of the bond system is dependent upon the surface finish, the clamping, and (mainly) the type of epoxy used. Under controlled conditions, high temperature epoxy can create a joint with shear strengths of 41 MPa. Room temperature bond can create a joint with strength of 27 MPa. However, in both cases, designers should use a safety factor of 2 when designing the joint.

One common configuration for bonded ceramic structures is to bond beams perpendicular to one another in order to gain stiffness in more than one direction. Since a prismatic ceramic beam has high bending stiffness along the main axis, stacking beams in two directions is effective for creating a stiff plate or table. Figure 2.23 is an example of this type of configuration. The top beams and bottom beams each provide bending stiffness along their main axis.

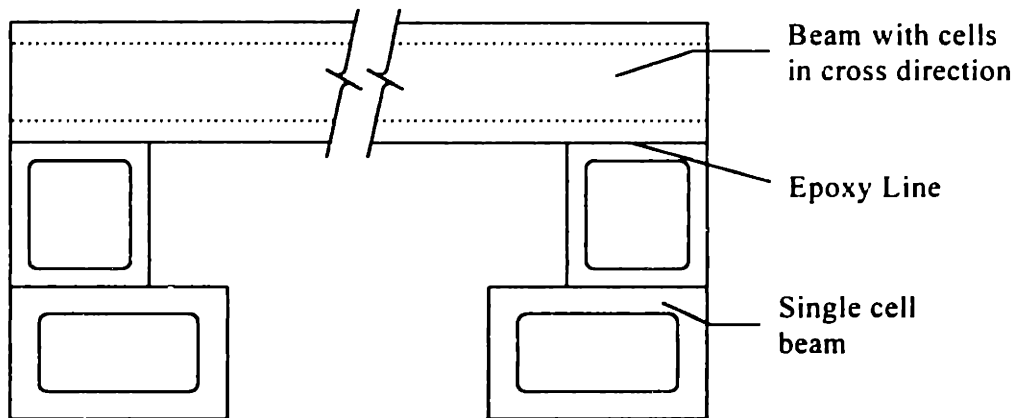


Figure 2.23 End diagram of a bonded ceramic structure which has prismatic beams orthogonally bonded in order to provide high stiffness in more than one axis. Photograph of the structure is Figure 2.26.

Another common configuration which increases bending stiffness along one axis uses several beams in the same direction. An I beam is an example of this configuration. For

ceramic I beams, three beams can be bonded together along the entire length of the beam. Figure 2.24 is an example of a large scale ceramic I beam.

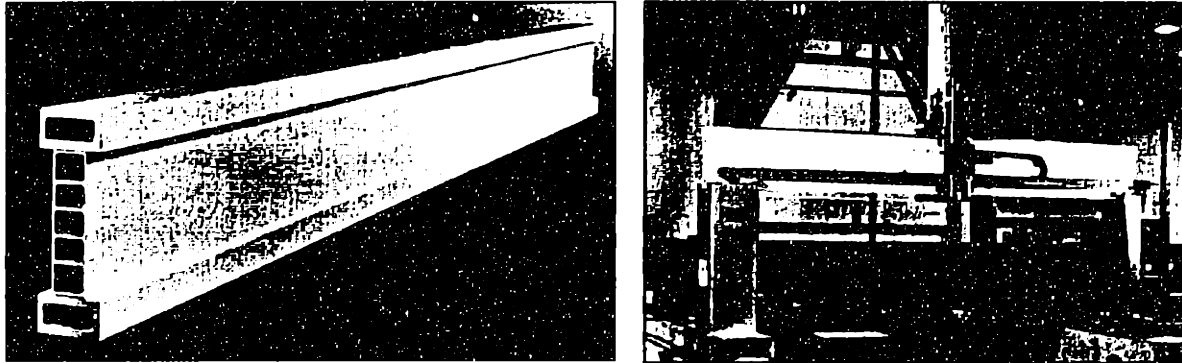


Figure 2.24 A large ceramic I beam (left), approximately 5.25 meters in length. The right photograph shows the I beam in place in a large scale coordinate measuring machine.

2.7.2 - Bolted Ceramic Components

In cases where disassembly is needed, ceramic components should be bolted together. Bolted joints can be extremely stiff with ceramic components because the clamping loads can be made extremely high. Since ceramic components take compressive loads well, bolts can be torqued in excess of 135 Nm (for a 20mm bolt) in order to create clamping loads in excess of 25.0kN. In order to bolt two beams end to end, flanges can be pressed into one end of each beam, or hardware can be bonded into the ends. Two examples of bolted assemblies are shown in Figure 2.25.

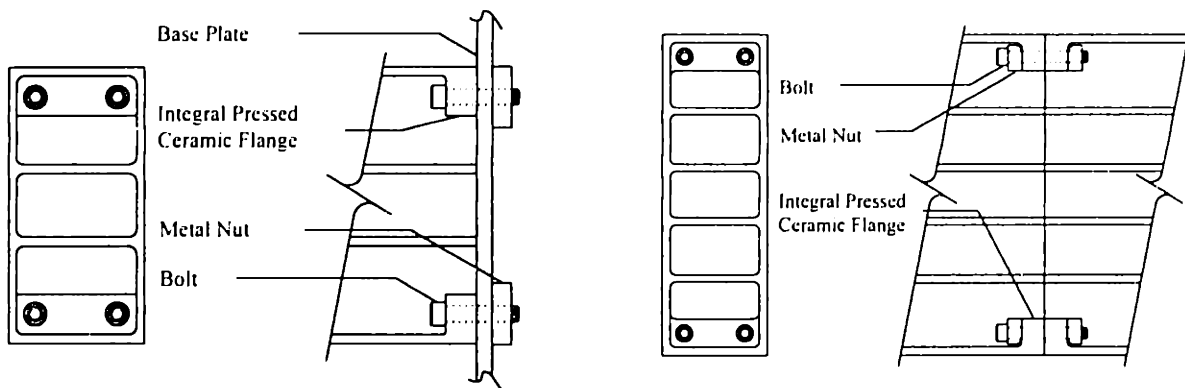


Figure 2.25 Diagrams of two bolted assemblies. A beam endbolted to a plate (left) and two beams bolted end to end (right).

2.7.3 - Ceramic Machine Tool Prototypes

In order to develop the idea of ceramic machine tool structures and components, prototypes are being constructed and tested. One approach for precision machine tools involves ceramic structures and water-hydrostatic bearings [5]. Prototypes of these technologies are shown in Figure 2.26.

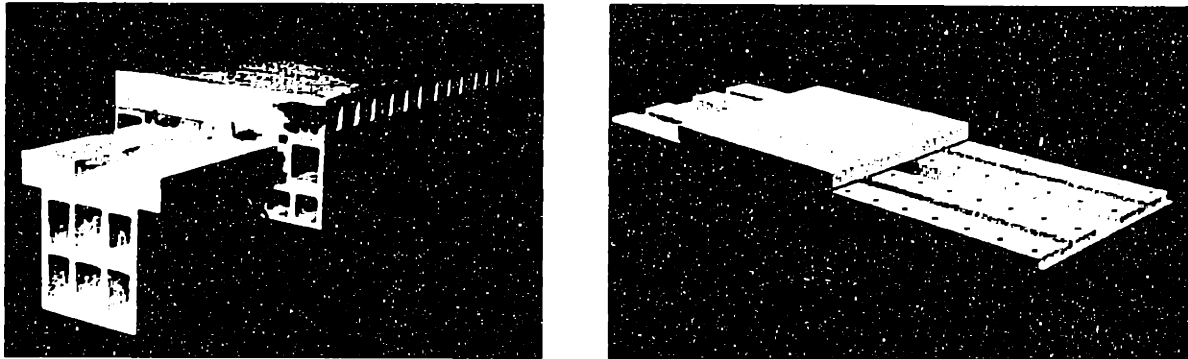


Figure 2.26 Photographs of two ceramic machine tool axis prototypes with self-compensated, water-hydrostatic bearings designed at M.I.T. (left) and Devitt Machinery (right).

The idea of a machine tool with a ceramic structure is now being developed and constructed by the Precision Products Group at Wilbanks International. A two axis grinding machine with water-hydrostatic bearings, and linear motor drive systems, is being constructed in order to research future precision machine design strategies. A photograph of the main structure of the machine is shown in Figure 2.28.

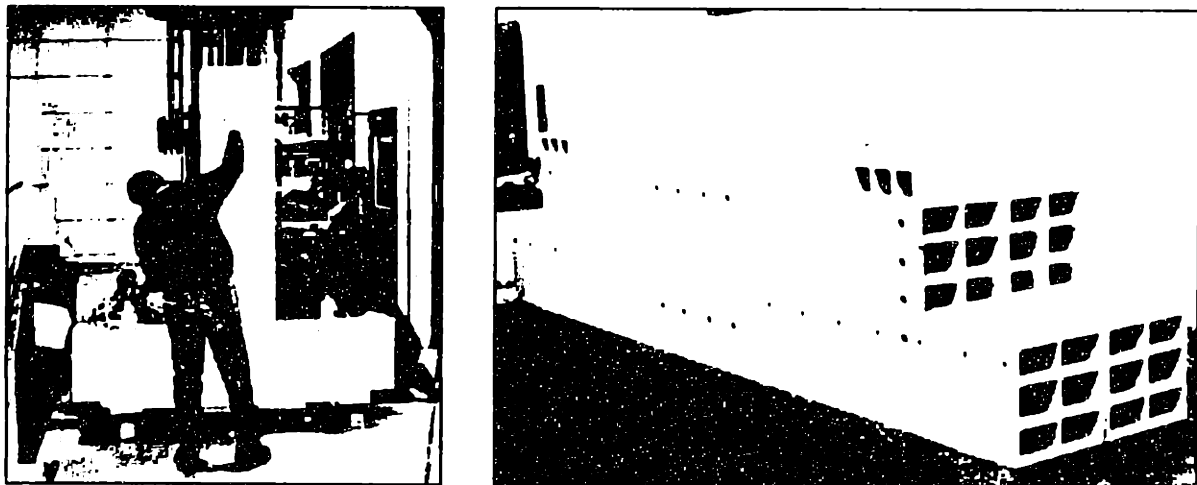


Figure 2.27 Photographs of the base structure of the Wilbanks Precision Grinding Machine (left, structure is shown vertical but will be operated as a horizontal T base machine) and one of the structural components (right).

2.7.4 - Recent Applications of Ceramic Structural Components

In recent years, coordinate measuring machines have been the main application for ceramic structural beams. Other industries have also implemented ceramic structures into machine which either require higher than normal accuracy, or are larger than usual machines (and therefore require long equivalently stiff components). Each application has unique requirements which drive the design. Therefore, the best way to become familiar with the types of designs which have been successful is to look at previous applications. Figures 2.28 through 2.31 are photographs of recent applications of high precision ceramic structures.



Figure 2.28 An air bearing profilometer developed by Reg Maas uses porous ceramic airbearings to guide the table along the rail. The rail was lapped to $2\mu\text{m}$ flatness and parallelism.

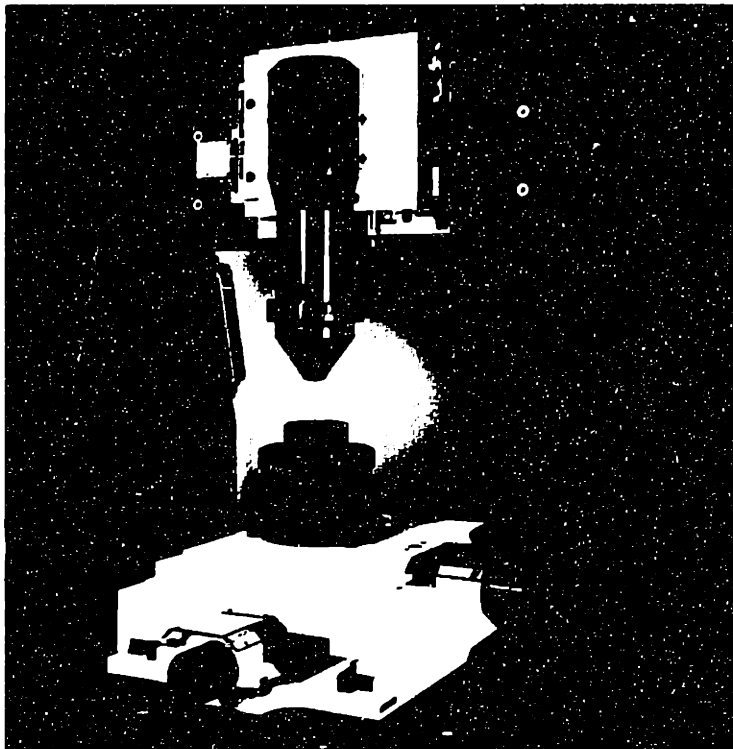


Figure 2.29 Photograph of a robot with ceramic tables on all three axes of motion. The robot was developed by the Dukane Company.

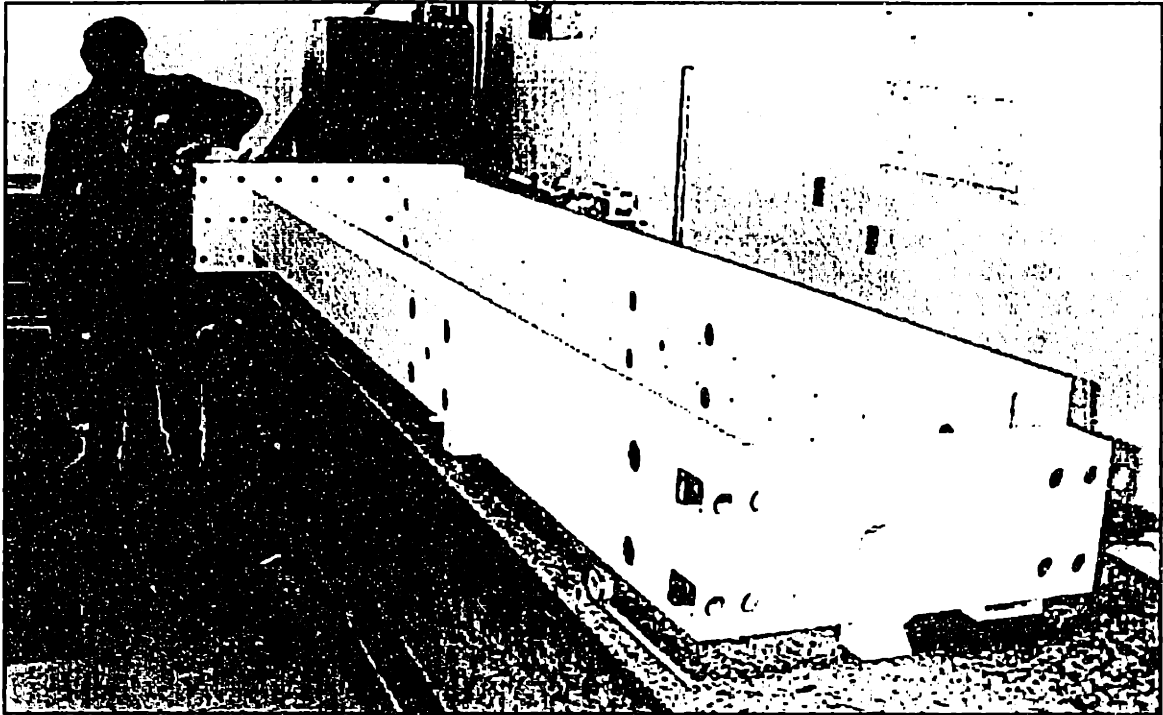


Figure 2.30 A large structure for an automotive inspection system. In this application, the tolerances of the machine were not at micron level, but the large range of motion required high specific stiffness and accurately machined surfaces.

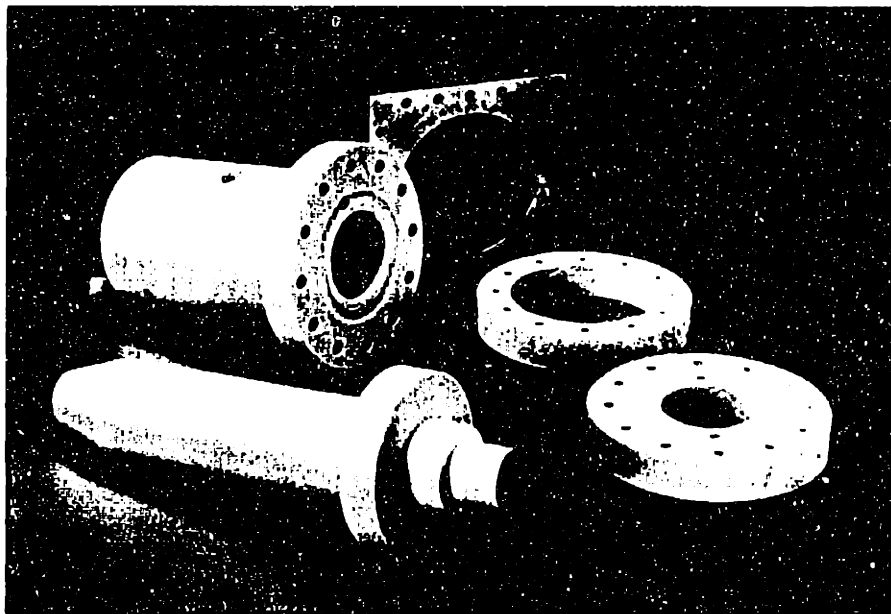


Figure 2.31 Photograph of a ceramic spindle including rotor, sleeves and face plates. This spindle was developed by Alex Slocum (AESOP, Inc.) as a prototype for a water-hydrostatic spindle.

2.7 - Conclusions

In order to improve the accuracy of precision machine tools, structural improvements are required. Ceramic materials are the most appropriate material candidates for next generation machine tool structures. The current challenge is to manufacture ceramic structures to high accuracy in an economical manner.

One strategy for producing large, accurate ceramic structures is to build modular building blocks which can be combined. Prismatic beams with hollow internal cavities are promising building block components because of their strong structural and thermal performance.

2.8 - References

- [1] F.H. Norton, Elements of Ceramics, Addison-Wesley Publishing Co., Reading, MA., 1974.
- [2] Y. Furukawa, N. Moronuki, and K. Kitagawa, "Development of Ultra-Precision Machine Tool Made of Ceramics", Annals of the CIRP, Vol. 35, No. 1, 1986, 279-282.
- [3] S. Ueno, "Development of an Ultra-Precision Machine Tool Using a Ceramics Bed", Fifth International Precision Engineering Seminar, American Society for Precision Engineering, Monterey, CA, September, 1989, 116-132.
- [4] M. Tsutsumi, K. Unno, M. Yoshino, and F. Yamuchi, "New Material Application to Ultraprecision Lathe", Ultraprecision in Manufacturing Engineering, M. Weck and R. Hartel, Eds., International Congress for Ultraprecision Technology, Aachen, FRG, May, 1988, 171-183.
- [5] P.A. Scagnetti., A.H. Slocum, N.R. Kane, "*Design of Self-Compensated, Water-Hydrostatic, Ceramic Structure, Machine Tool Axis*", Proceedings of the Ninth Annual Conference of the American Society for Precision Engineering., October 2-7, 1994, Cincinnati, OH.

CHAPTER 3

DESIGN OF SELF-COMPENSATED, WATER-HYDROSTATIC LINEAR BEARINGS

There are many elements of the machine tool system required for high performance. This chapter describes development work on self-compensating, water hydrostatic linear motion bearings for precision machine tools. The bearing design is discussed in detail, including the analysis of its fundamental mechanics, the tools required to apply such designs, and an evaluation of two full-scale, prototypes.

A new type of hydrostatic bearing for precision machine linear motion axes has been developed and tested. The bearing has many of the traditional benefits of hydrostatic bearing systems including high stiffness (on the order of 2000 N/ μm at a supply pressure of 13.5 atm), excellent straightness characteristics (less than 0.5 μm vertical motion over 100 mm) which can exceed the straightness characteristics of the rails due to the averaging effect of the fluid, high damping, and low noise levels. Additionally, the bearings are modular in design, and use water-based cutting fluids (or pure water) as the hydrostatic fluid so it doesn't have the environmental problems associated with oil based hydrostatic systems. The smallest passage is typically 3-5 mm in diameter which virtually eliminates clogging of the hydrostatic passages. The design of the bearing system is simplified primarily by the deterministic design of the restrictor passages. The restrictors have a linear sensitivity with respect to stiffness. Fixed-compensation restrictors have a gap cubed sensitivity. This also significantly helps manufacturing because hand-tuning of restrictors is eliminated, and the restrictors are less sensitive to manufacturing errors than traditional hydrostatic bearing systems.

Durability is perhaps the most critical issue for ceramic grinding. Ceramic particles are often blasted about the machine by high pressure coolant. This wears seals and particles get by them, even the most minute quantities of these particles damages slideway and spindle bearings, particularly rolling element bearings. Note that sub-micron particles are extremely difficult to remove from the environment. Conventional linear bearing systems on ceramic grinding machines are often reconditioned 2 times per year in order to maintain accuracy.

3.1 - List of Variables

K - stiffness

b - damping factor

h - nominal bearing gap

δ - displacement

μ - viscosity of the bearing fluid

$R_{restrictor}$ - resistance of the restrictor

$R_{bearing}$ - resistance of the bearing pad

r_o - outer radius of restrictor land

r_i - inner radius of restrictor land

F - applied force

P_s - supply pressure

A_{eff} - effective area

K_{shape} - shape factor related to bearing geometry

3.2 - Overview of Linear Hydrostatic Bearings

Linear motion bearings for machine tools used to grind ceramics must have the following properties:

- High motion resolution in order to allow for small infeed rates below the critical depth of cut for reciprocal grinding
- High stiffness
- High damping
- Low friction
- Insensitivity to ceramic dust contamination
- High straightness

Traditionally, linear bearings have excelled in only a few of these categories as shown in Figure 3.1 [2]. Rolling element bearings, for example, have high stiffness, but limited damping characteristics, and have an associated motion resolution due to friction and preload on the bearings. Furthermore, rolling element bearings are especially susceptible to damage from ceramic dust. Aerostatic bearings are very accurate and operate without any friction, so they can operate at virtually any speed without generating much heat. However, the low viscosity of the air limits the loads that can be supported and the damping available. In comparison, hydrostatic bearings generally provide a superior level

of performance in terms of stiffness and damping and are less sensitive to aggressive environmental conditions. As with air bearings, since there is no static friction, motion resolution can be infinite and depends mainly on the actuator and control system. Principle drawbacks of hydrostatic bearings are the expensive support equipment and problems associated with oil as a working fluid. Overall, hydrostatic bearings are most suitable for the described application with its high performance requirements [2].

| Bearing Capacity | Rolling Element Bearings | Air Bearings | Hydrostatic Bearings |
|-------------------|--------------------------|--------------|----------------------|
| Damping | - | ○ | + |
| Stiffness | + | ○ | + |
| Motion Resolution | ○ | + | + |
| Heat Generation | ○ | + | - |
| Durability | - | + | + |
| Cost | + | - | - |

Level of Performance - low, ○ medium, + high

Figure 3.1 Performance comparison of linear bearings.

Hydrostatic bearings utilize a thin film of externally pressurized fluid supplied to the bearing pockets which have a large area and therefore are able to support large external loads. In order to provide the necessary differential pressure to support a varying external load, the inlet flow must be regulated by means of a flow resistance before the fluid enters the bearing pocket. This is generally referred to as *compensation*. The compensation device and the bearing behave like two resistors in series with each other as shown in Figure 3.2.

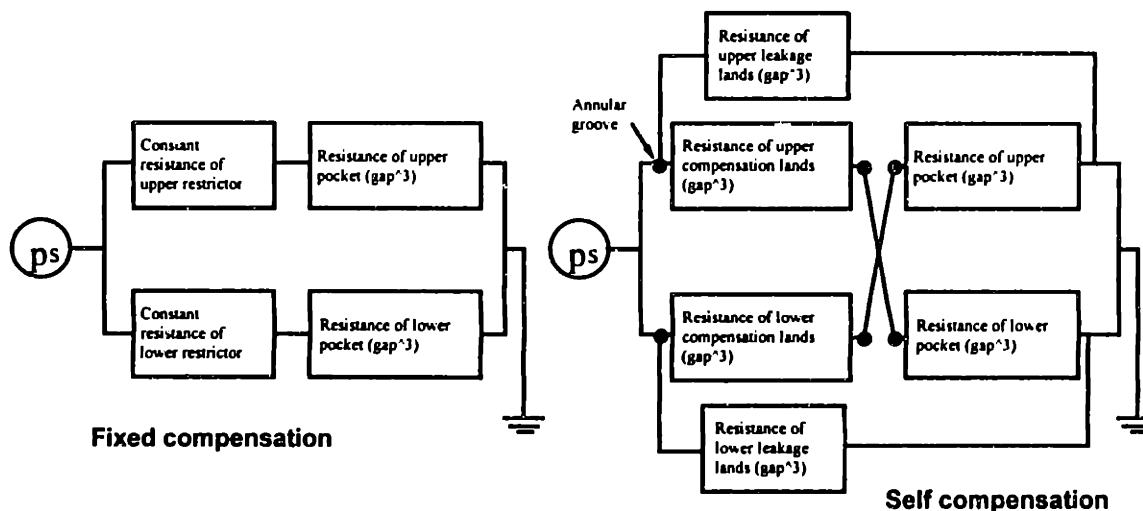


Figure 3.2 Electric circuit analogy for opposed pad hydrostatic bearings. Conventional fixed compensation and self-compensated hydrostatic bearings.

There are four different types of hydrostatic bearings, distinguished by the kind of flow restrictor that regulates the inlet flow into the bearing pocket [3]. Fixed compensation bearings use a device with a constant fluid resistance (e.g., capillary tubes or an orifice). Constant flow compensated bearings use gear pumps or other devices to provide a constant flow to the pocket. Variable compensated bearings (e.g., a diaphragm compensation device) use load dependent flow restrictors where the resistance is inversely proportional to the load applied. Self-compensated bearings use the small bearing gap between the bearing block and the rail to provide the required flow resistance to the opposed bearing pocket. The flow restrictor itself is a pad located at the side of the bearing rail opposed to the corresponding bearing pad. As loads are applied the change in the bearing gap regulates the fluid flow by means of passages on the bearing surface. Overall, especially considering manufacturing ease, self-compensated bearings have the highest performance potential and robustness of the types mentioned.

Conventional fixed or variable compensation hydrostatic bearings have several disadvantages:

- They require hand tuning during installation, due to high (third power) sensitivity of the system to manufacturing tolerances. Thus, oil is often used because it's higher viscosity allows it to be run with larger gaps.
- They require maintenance and support equipment.
- Oil must usually be used as the working fluid because it is easy to keep clean and has high inherent lubricity (in the even of a touchdown). However, the use of oil creates ergonomic and maintenance problems.

Heat is generated by two sources: the pump and viscous shear during high speed motion. The former dominates in linear motion systems, and thus total heat input can be minimized by reducing the flow and increasing the heat capacity of the fluid.

Hand tuning of conventional compensators is often required because the resistances of the bridge circuit elements, shown in Figure 3.2, typically vary with the third power of the dimension (e.g., bearing gap). Small variations in the bearing gap, due to manufacturing errors cause large resistance variations. For example, a 12% gap variation causes the resistance to change by a factor of 2. A self-compensated bearing (as discussed in the following section) does not suffer from this problem, and requires no hand tuning.

All hydrostatic bearings require support equipment, and in particular, filters must be maintained to prevent the restrictors from clogging. Unfortunately, in applications involving ceramic grinding, sub-micron sized particles easily get past filters and can form a clogging paste. However, with the use of a hydrocyclone/cartridge filter system and a self-compensating bearing, cleanliness becomes far less of a problem than is required for conventional hydrostatic or rolling element bearing systems.

Finally, the use of oil as fluid, although ideal from the bearing's point of view, is not desirable from an operator's point of view because of possible cross-contamination with the coolant, clogging problems, oil drips around the machine, and disposing of the oil. Water based coolants are a good alternative, however conventional restrictors can be easily clogged by bacteria formations in the supply lines. A self-compensating bearing is less susceptible to such clogging because the supply lines are larger. Any dirt which does

collect will do so on the bearing surface where it will be broken up by the shearing action of the bearing motion.

3.3 - Self compensating hydrostatic bearing operating principles

Although designing restrictors may appear to be straightforward, the third and fourth-power relationships in some of the calculations make most restrictors extremely sensitive to manufacturing errors. Self-compensation, sometimes called gap compensation, is based on the principle that high-pressure fluid can be regulated through passages on the bearing surface. The fluid flows out of a pocket on the surface of the bearing, across compensation lands, whose area is tuned to that of the opposed pocket's lands, and into a small collection pocket that is connected to a large bearing pocket on the other side of the bearing rail. Figure 3.3 shows the fluid paths for an opposed pad self-compensated, hydrostatic bearing system. As the bearing rail is loaded and the gap on one side begins to close, the flow resistance increases to the pad that generates a force in the direction of the load. Conversely, fluid flows more easily to the pad that is resisting the load. Therefore, a self-compensating design is insensitive to variations in the bearing gap. Changes in gap due to manufacturing errors affect the pocket and the compensator equally; hence the resistance bridge remains balanced. In addition, a properly designed self-compensated bearing is affected less by deflection of bearing components (e.g., keeper rails). Self-compensating designs are also far less sensitive to dirt because there are no small diameter passages.

Although there are many different self-compensated bearing designs [3, 4], previous designs suffered from hydrostatic shorts (leakage flow from the compensators into the bearing pockets or drain grooves), and thus had performance limitations and were not easy to model. Figure 3.4 shows the bearing pad geometry for a novel design [1] for a self-compensated modular hydrostatic bearing. Table 3.1 lists the properties of the novel design.

Table 3.1 Properties of self-compensated, water-hydrostatic bearings.

| Feature | Description | Advantages |
|---------------|-------------------------------|--|
| Compensation | Self-compensation | <ul style="list-style-type: none"> • Less sensitive to manufacturing errors than capillary compensated bearings • More resistant to clogs |
| Bearing Fluid | Water or Cutting Fluid | <ul style="list-style-type: none"> • Low viscosity and friction • High heat capacity • High thermal conductivity • Environmentally friendly • Allows crosstalk between bearing fluid and cutting fluid. |
| Bearing Gap | 10-15 μm - nominal | <ul style="list-style-type: none"> • Modest flow rates • Modest pump power |

The prototypes described in this paper were designed as modular, self-compensating hydrostatic bearing systems which are deterministic and therefore easy to design without excessive modeling and testing. There is no necessity for hand-tuning, the system is assembled without any alignment fixtures and is insensitive to manufacturing errors. It operates reliably under most circumstances because typically there are no passages smaller than 3-5 mm in diameter, and it can use water as the bearing fluid.

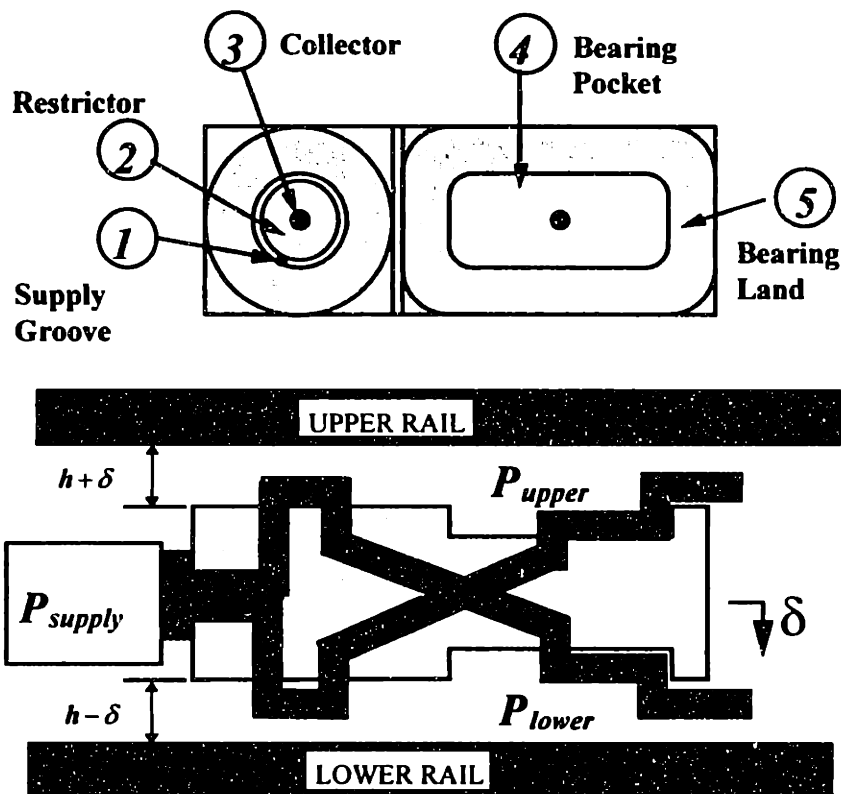


Figure 3.3 Diagram of a self-compensated hydrostatic bearing system. The nominal bearing gap (h) and the displacement (δ) define the position of the bearing block relative to the bearing rails.

When designing hydrostatic bearings, often the two most important factors to consider are the stiffness and the damping. From these factors, an approximate second order system can be modeled in order to predict system behavior. The design process for developing a self-compensated system with the desired specifications has been simplified by: (1) closed form expressions that model system performance, and (2) spreadsheet analysis tools in which the analytical expressions are implemented and applied during the design process.

Designed as a self-compensated bearing, the prototype bearing system's restrictor and bearing lands, as shown in Figure 3.4, are deterministic. To achieve this characteristic, the restrictor is symmetric and the pressure supply groove fully surrounds the restrictor land. The resistance of the restrictor is determined by the viscosity of the fluid, the

bearing gap and the radii of the land geometry. In previous designs, the supply groove did not completely surround the restrictor. This led to a decrease in efficiency and performance, particularly at higher speeds.

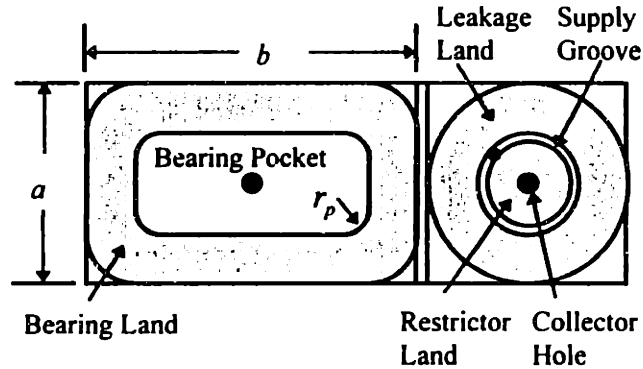


Figure 3.4: Prototype bearing pad geometry.

With the inlet flow restrictor on the bearing surface itself, the restrictor pad resistance can be set to a desired proportion of the bearing pad resistance regardless of the magnitude of the nominal equilibrium gap:

$$\frac{R_{restrictor}}{R_{bearing}} = \gamma \quad (3.1)$$

The load capacity is calculated from:

$$F = A_{effective} (P_{upper} - P_{lower}) = A_{effective} \left(\frac{\frac{1}{(h-\delta)^3}}{\frac{\gamma}{(h+\delta)^3} + \frac{1}{(h-\delta)^3}} - \frac{\frac{1}{(h+\delta)^3}}{\frac{\gamma}{(h-\delta)^3} + \frac{1}{(h+\delta)^3}} \right) \quad (3.2)$$

The stiffness is calculated from:

$$K = 3A_{eff}P_s \left[\frac{\frac{\gamma}{(h-\delta)^4} - \frac{1}{(h+\delta)^4}}{(h+\delta)^3 \left(\frac{\gamma}{(h-\delta)^3} + \frac{1}{(h+\delta)^3} \right)^2} + \frac{1}{(h+\delta)^4 \left(\frac{\gamma}{(h-\delta)^3} + \frac{1}{(h+\delta)^3} \right)} - \frac{\frac{1}{(h-\delta)^4} - \frac{\gamma}{(h+\delta)^4}}{(h-\delta)^3 \left(\frac{1}{(h-\delta)^3} + \frac{\gamma}{(h+\delta)^3} \right)} + \frac{1}{(h-\delta)^4 \left(\frac{1}{(h-\delta)^3} + \frac{\gamma}{(h+\delta)^3} \right)} \right] \quad (3.3)$$

The effective area is calculated from:

$$A_{eff} = (a - 2l)(b - 2l) + r_p^2(\pi - 4) + l(a + b - 4(l + r_p)) + \pi \left(\frac{l(2r_p + l)}{2 \log_e \left(\frac{r_p + l}{r_p} \right)} - r_p^2 \right) \quad (3.4)$$

In order to select the resistance ratio a spreadsheet can be used to make a parametric study of the design variables. Typically, the resistance ratio is in the range of 2-3. Figure 3.5 shows the stiffness of an ideal (e.g., systems with no leakage flows such as the prototypes which will be described in section 6) self-compensating bearing for various values of γ . The nominal bearing gap is 10 microns and the supply pressure 7 atm. The various curves are different values of the resistance ratio γ , from 1 to 10. Note that for the same resistance ratio, the stiffness level will be about twice the value for an equivalent capillary compensated bearing. Figures 3.6 and 3.7 show the effect of manufacturing errors on the stiffness of a self-compensated and a capillary compensated hydrostatic bearing system.

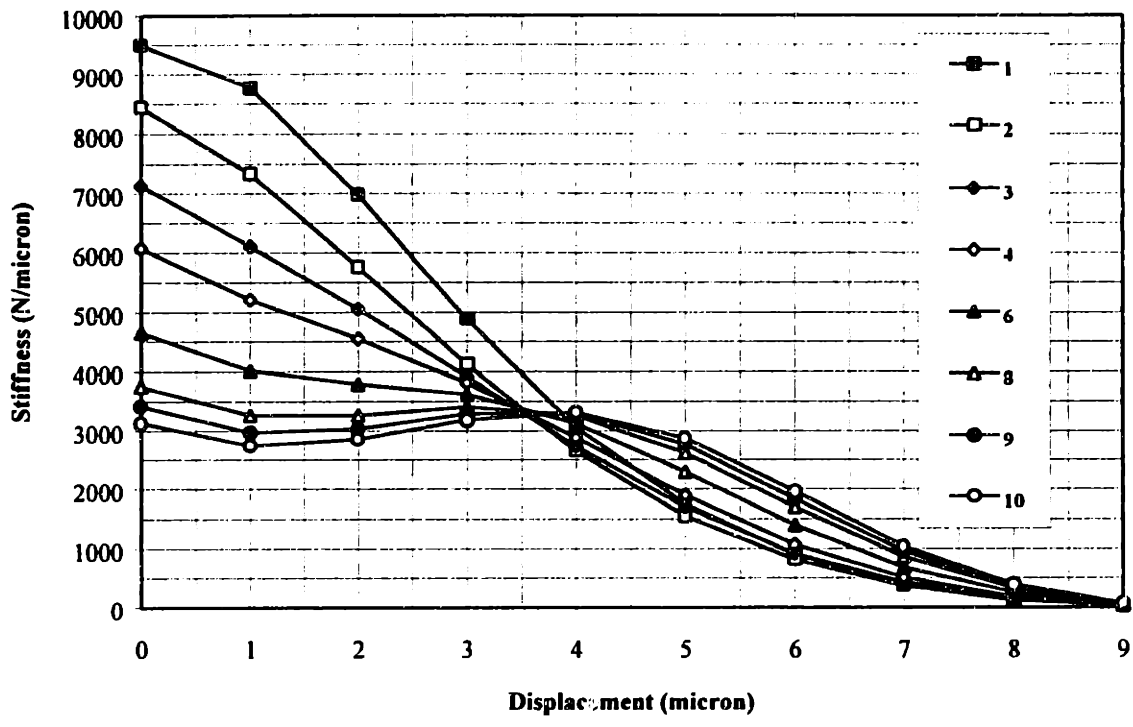


Figure 3.5 Plot of stiffness versus displacement for an ideal self-compensated bearing, consisting of four opposed pads.

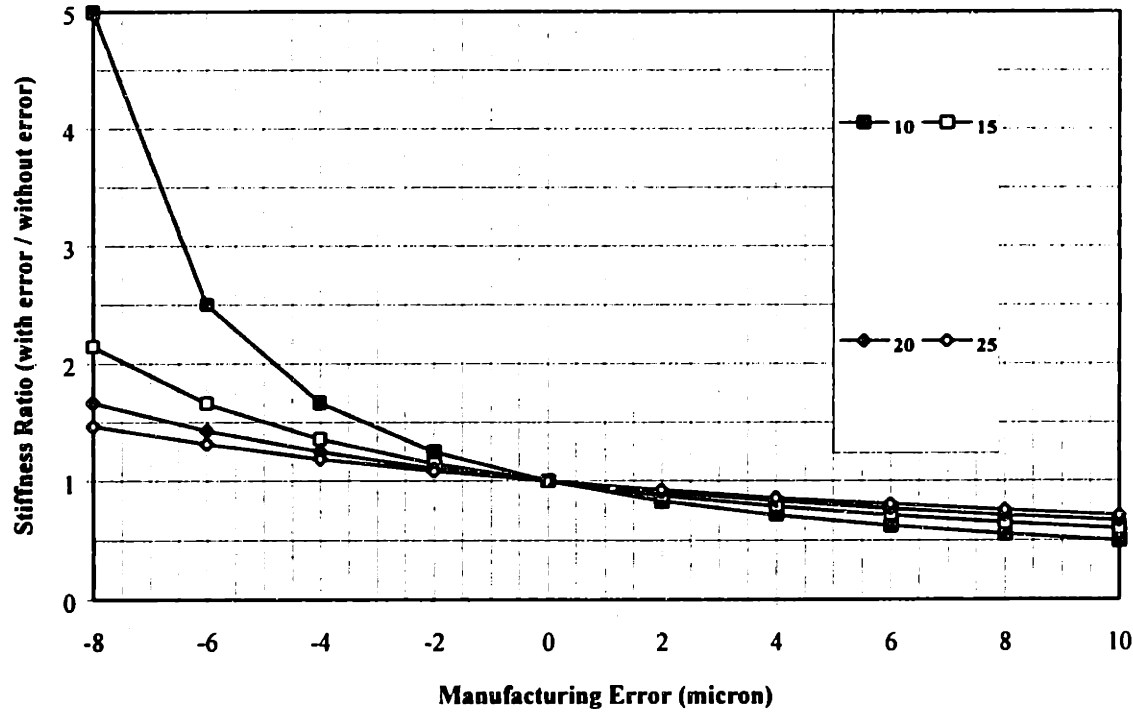


Figure 3.6 Influence of manufacturing errors on capillary compensated bearing performance. The various curves are different bearing gaps, from 10µm to 25µm.

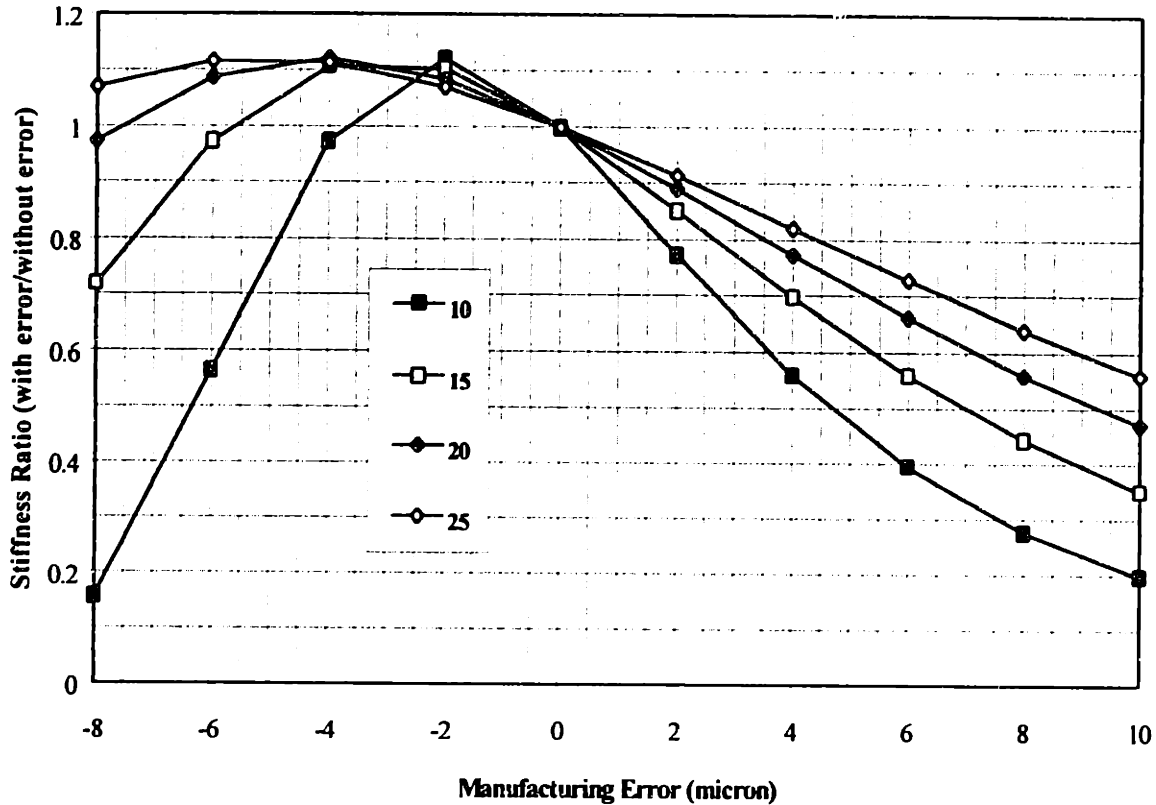


Figure 3.7 Influence of manufacturing errors on self-compensated bearing performance. The various curves are different bearing gaps, from 10 μm to 25 μm .

3.4 - Squeeze film damping in hydrostatic bearings

As the bearing pads approach the rail, the fluid is pushed out of the gap. However, since the fluid is viscous, it slows the approach of the pad. This effect, referred to as squeeze film damping, adds a desirable quality to hydrostatic bearings: high damping. Damping, as noted before, is particularly desirable in ceramic grinding applications, where it is necessary to eliminate vibrations due to the machining process. Figure 3.8 shows a schematic of the major parameters which determine the amount of damping for a squeeze film geometry. The ability of the bearing to damp vibrations can be approximated using closed-form expressions [5, 6, 7, 8]. As the bearing surfaces move towards each other, fluid is squeezed out. As the fluid is squeezed out, it is sheared between the lands by the mechanism of a velocity gradient caused by a pressure differential which dissipates energy. When the gaps are small, the fluid is a liquid, and the area large, very high damping factors (>1) can be obtained [9, 10].

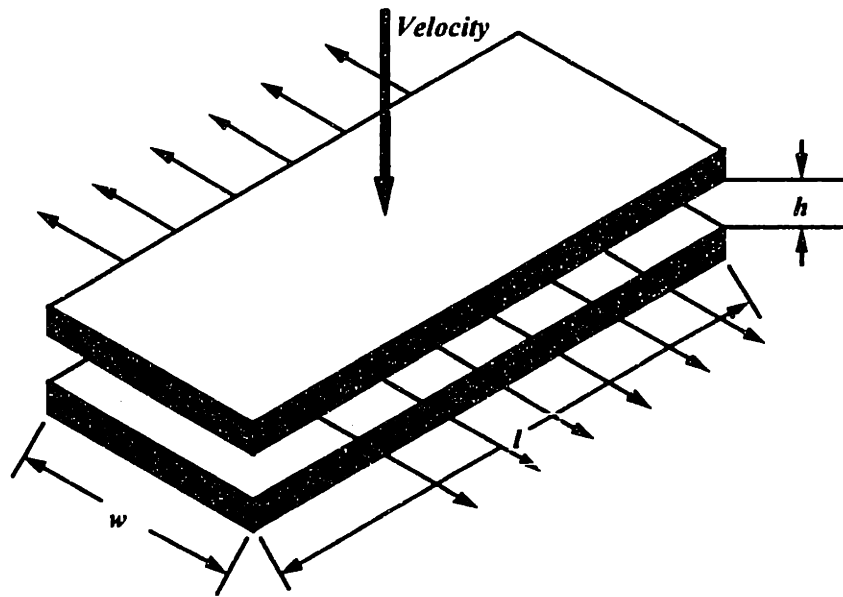


Figure 3.8 Geometric parameters involved in the calculation of the damping constant.

Since most of the damping areas in a hydrostatic bearing are rectangular, the damping factor, b , is calculated from:

$$b_{rec} = K_{shape} \frac{\mu l w^3}{h^3} \quad (3.5)$$

where μ is the viscosity of the bearing fluid and K_{shape} is a geometric factor related to the bearing. For rectangular regions, by fitting a curve to the data in Fuller, the constant K_{shape} can be obtained from:

$$K_{shape} = 0.7925 - \frac{1.1005}{e^{l/w}} + \frac{.0216w}{l} + \frac{.0153l}{w} \quad (3.6)$$

where l is the length of the region, and w is the width, and for $l/w > 10$, $K_{shape} = 1$. For circular regions, the damping factor is:

$$b_{circular} = \frac{3\pi\mu(r_o^2 - r_i^2)}{2h^3} \quad (3.7)$$

Most bearing pads have surface areas which can be analyzed by dividing the bearing into round and rectangular sections. Although, this type of analysis does not account for all damping areas, the excluded regions are usually small. Thus, the calculated damping will be underestimated slightly. The damping capability of the entire bearing pad is calculated by adding the effect of dampers in parallel.

3.5 - Design considerations

There are a large number of variables that must be taken into account while designing hydrostatic bearings. Once the theory is understood, spreadsheets can be written and used to help converge upon a design, which enables the user to quickly respond to new specifications and check the resulting bearing performance immediately. According to the equations described above, stiffness, load capacity, and damping can be readily calculated. Parameter studies, which are readily made using spreadsheets, can be used to optimize and check the sensitivity to parameter variations.

Initially, it is helpful to keep in mind the relationships between the bearing performance and the design parameters of the bearing pads. Table 3.2 is a list of the main characteristics, and the parameters which affect them.

Table 3.2 List of bearing characteristics and the related design issues.

| Characteristics | Related Design Issues |
|------------------------|---|
| Stiffness | <ul style="list-style-type: none"> • Bearing pad geometry • Bearing gap • Pressure supply system |
| Damping | <ul style="list-style-type: none"> • Bearing pad geometry • Bearing gap |
| Straightness | <ul style="list-style-type: none"> • Rail straightness • Bearing pad geometry • System geometry |
| Noise Level | <ul style="list-style-type: none"> • Pressure supply system |

In designing the bearing pads, the main considerations are stiffness, damping, and noise level. In designing the pads, there is a trade-off between “designing for stiffness and damping” and “designing for low noise level” as shown in Table 3.3. In order to design a bearing with high stiffness and damping, the supply pressure the bearing pad area can be increased and the bearing gap can be decreased. However, these design choices make a bearing which is more sensitive to pressure induced noise. Fortunately, the pressure induced noise can be attenuated by proper sizing and placement of accumulators and relief valves (described in chapter 4).

Table 3.3 Table of the relationship between major bearing pad design parameters and system characteristics. The numerical values are presented as typical values from previously designed bearing systems.

| | Supply Pressure 250 psi. | Bearing Area 12 in ² | Nominal Gap 15 μm |
|--|-----------------------------|------------------------------------|-----------------------|
| High Stiffness 2000 N/μm | P | A | h |
| High Damping $\zeta = .7$ | | A² | h³ |
| | | | |
| Low Noise Level $\Delta z < .5\mu\text{m}$ | P⁻¹ | A⁻¹ | h⁻³ |

The bearing gap has an important influence on the stiffness, damping, flow rate, and flow velocities. Unfortunately, high feed rate applications require larger bearing gaps, which decreases the system performance. In addition, with smaller bearing gaps, the fluid flow decreases so less heat is generated by the pump. For ultra-precision machines, where carriage velocities are small, the reduced fluid flow will not cause major problems and the gap can be chosen as small as reasonable to manufacture (e.g., 10 μm). For high speed applications, the bearing must not force air into the pocket; thus the fluid velocity must be higher than the relative velocity between the carriage and the rail.

The bearing pocket should typically be 10-20 times the nominal bearing gap in order to evenly distribute the fluid to the lands and to ensure the structure is lifted when the bearing is started. High speed applications can cause turbulence problems, thus the Reynolds number in the bearing pocket (with the pocket depth the characteristic length) should be smaller than 1000 to ensure that the fluid flow is laminar.

With respect to the land width, the lands must be small enough to allow the pressure in the pocket to provide an initial lift force and sufficient stiffness. They should also be large enough to provide adequate squeeze film damping and withstand sliding loads should the pressure source fail. In addition, if the land width is too small, flow rates will be too high. A good starting point for the land width is 25% of the bearing pad width. The governing equations for the system can be used to seek an optimum value for the situation at hand. If greater damping or sliding support in the case of pressure loss is required, a central island in the pocket can be created.

In order to test the new self-compensating concept, two prototype linear bearings were designed. Parameter studies were carried out using a spreadsheet to determine the input values for the resistance ratio γ , the bearing gap and the pocket depth to optimize

the system. Part of the spreadsheets written for the first linear slide are shown in Tables 3.4 and 3.5. The prototypes are described in section 3.6.

Table 3.4 Input for a spreadsheet for self compensating hydrostatic bearing design.

| | | | |
|-----------------------------------|---|-------|----------|
| General Input: | | | |
| supply pressure | ps (atm, Pa= N/m ²) | 1.36 | 137,857 |
| supply pressure | ps (psi) | | 20 |
| dynamic viscosity | μ [mu] (Nsec/m ²) | 0.001 | |
| density ρ | ρ (kg/m ³) | 997 | |
| pocket depth | hp (μ m, m) | 300 | 0.000300 |
| nominal bearing gap | h (μ m, m) | 15 | 0.000015 |
| carriage weight | wc[N] | 1000 | |
| upper bearing pad: | | | |
| bearing width | au (mm, m) | 45 | 0.045 |
| bearing length | bu (mm, m) | 90 | 0.090 |
| land width | lu (mm, m) | 10 | 0.010 |
| pocket radius | rpu (mm, m) | 5 | 0.005 |
| effective bearing pad area | AAu (mm ² , m ²) | 2686 | 0.002686 |
| lower bearing pad: | | | |
| bearing width | al (mm, m) | 110 | 0.110 |
| bearing length | bl (mm, m) | 110 | 0.110 |
| land width | ll (mm, m) | 15 | 0.015 |
| pocket radius | rpl (mm, m) | 5 | 0.005 |
| effective bearing pad area | AAI (mm ² , m ²) | 8825 | 0.008825 |
| first deviation from nominal gap | del (μ m, m) | 5.47 | 5.47E-06 |
| second deviation from nominal gap | dels (μ m, m) | 7.35 | 7.35E-06 |

Table 3.5 Output from a spreadsheet for self compensating hydrostatic bearing design.

| | | | | | |
|--------------------------------------|--|---------|---------|---------|----------|
| Pocket Pressure: | | | | | |
| pocket pressure in upper bearing pad | | | | | |
| at delta=0 | ppu (atm, Pa=N/m ²) | | 0.35 | | 35,575 |
| at first displacement delta | ppud (atm, Pa=N/m ²) | | 0.09 | | 8,999 |
| at second displacement delta | p _u uds (atm, Pa=N/m ²) | | 0.07 | | 6,693 |
| at -second displacement delta | mppuds (atm, Pa=N/m ²) | | 1.21 | | 122,097 |
| pocket pressure in lower bearing pad | | | | | |
| at delta=0 | ppl (atm, Pa=N/m ²) | | 0.32 | | 32,672 |
| at first displacement delta | ppld (atm, Pa=N/m ²) | | 1.00 | | 101,292 |
| at second displacement delta | pplds (atm, Pa=N/m ²) | | 1.19 | | 120,449 |
| at -second displacement delta | mpplds (atm, Pa=N/m ²) | | 0.06 | | 6,007 |
| load capacity and stiffness | | | | | |
| per bearing block | | | | | |
| displacement | (%) | 0 | 36.46 | 49.00 | -49.00 |
| smallest gap | (μm) | 15 | 9.53 | 7.65 | 7.65 |
| load capacity | F (N) | -193 | 250.01 | 317.02 | -1072.35 |
| | F (lbf) | -43 | 56 | 71 | -241 |
| stiffness | (N/μm) | 116 | 109.49 | 67.50 | 25.85 |
| | (lbf/μin) | 0.7 | 0.63 | 0.39 | 0.15 |
| for the system: | | | | | |
| number of opposed bearing pads | | 4 | | | |
| displacement | (%) | 0 | 36.46 | 49.00 | -49.00 |
| smallest gap | (μm) | 15 | 9.53 | 7.65 | 7.65 |
| load capacity | F (N) | -771.11 | 1000.03 | 1268.09 | -4289.42 |
| | F (lbf) | -173.28 | 224.73 | 284.96 | -963.91 |
| stiffness | (N/μm) | 465.42 | 437.95 | 270.01 | 103.41 |
| | (lbf/μin) | 2.66 | 2.50 | 1.54 | 0.59 |

3.6 - Experimental Results

3.6.1 Prototype # 1: Granite Linear Machine Tool Axis Prototype

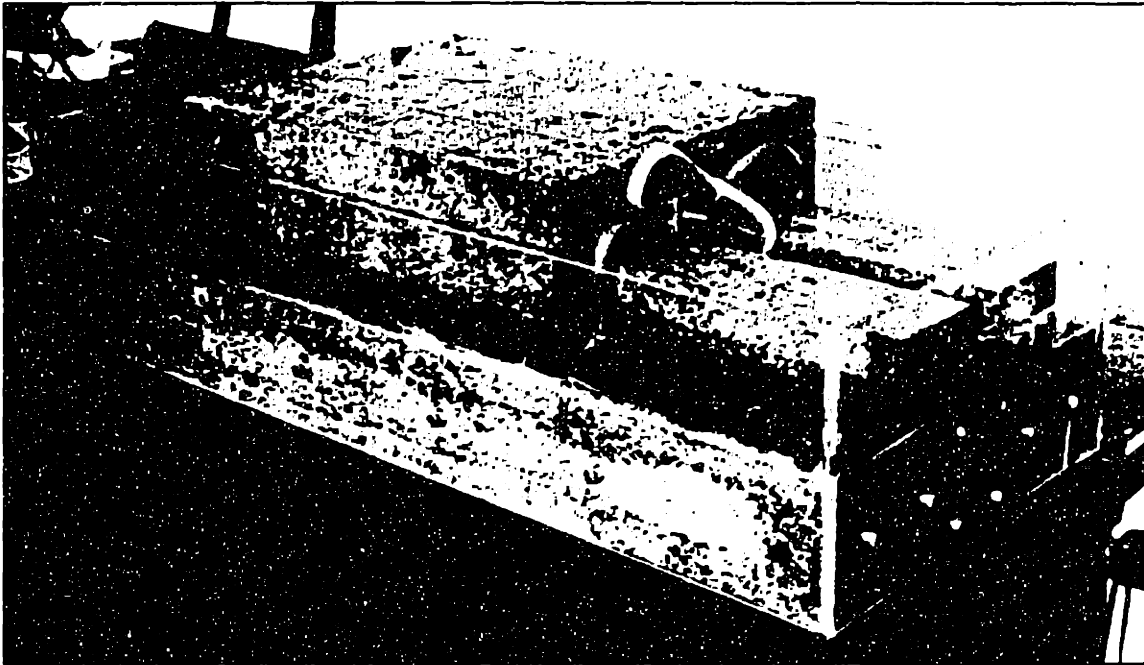


Figure 3.9 Photograph of the first HydroGuide™ prototype.

To test the design theory, the first test bearing was built from granite components for reasons of stability, damping, and economics. This system is shown in Figure 3.9 and Figure 3.10. To prevent water absorption, the granite was treated with a dissolved acrylic. The bearing blocks were made from stainless steel with replicated bearing pad surfaces. The surfaces were replicated using a thermally stable epoxy, which was treated to prevent water absorption.

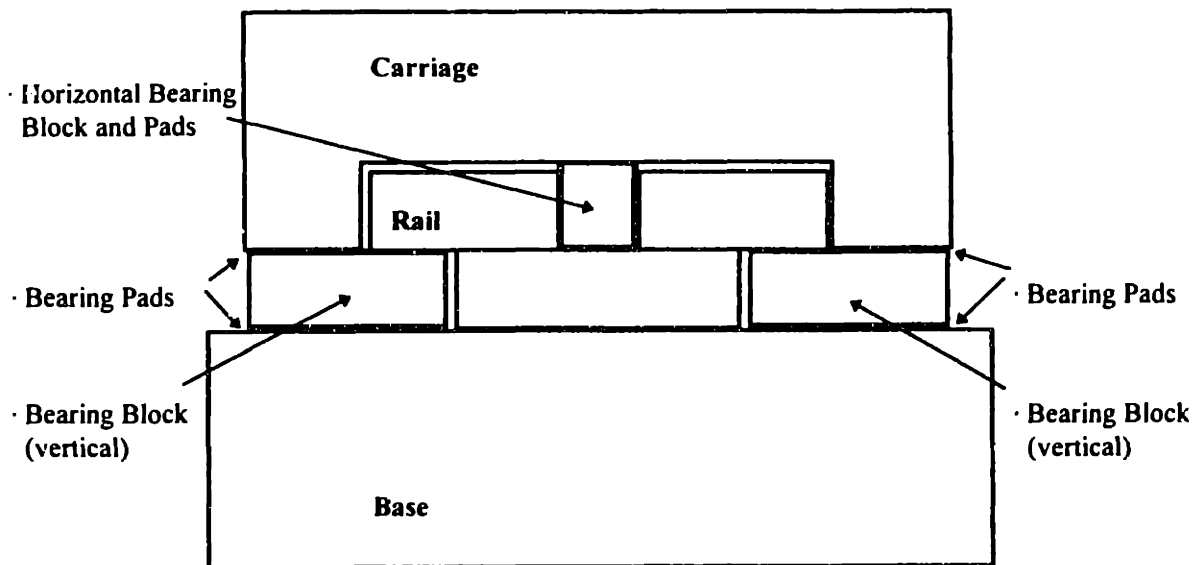


Figure 3.10 Diagram of hydrostatic bearing system prototype.

Many types of preloaded bearing systems can induce deformations into the machine structure. In the case of hydrostatic bearings, unequal bearing areas create a moment on the structure. Figure 3.11 illustrates the shape of hydrostatic pressure induced deformations of the carriage. For the granite system, which has a low modulus but excellent damping properties, the difference in gap between the two sides of the large bearing region was $1.1 \mu\text{m}/\text{atm}$. The prototype was designed to run using the building water lines as a pressure source (about 1.4 atm), causing a variation in gap across the large pad of about 10% at a nominal gap of $15 \mu\text{m}$. It was found that when a pump was added to the system to boost the pressure, the pocket pressure did not increase in a linear fashion, but instead rolled off rapidly as discussed below.

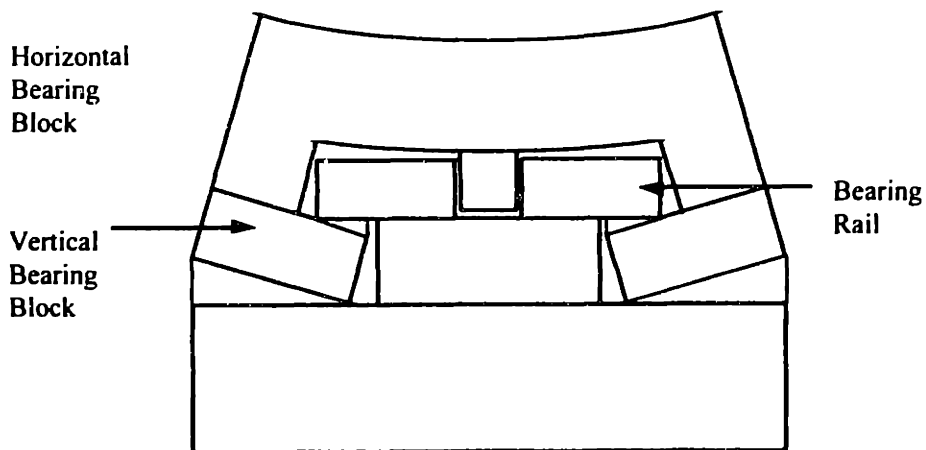


Figure 3.12 Hydrostatic pressure induced system deformations. Gray areas indicate pressurized fluid.

Tests verified the effect of hydrostatic pressure induced deformations on bearing pocket pressure. As shown in Figure 3.12, a supply pressure of 20 psi creates a bearing pocket pressure of 4 psi, which is consistent with the analytical value predicted by the spreadsheet for the bearing designed here. At higher supply pressures, deformations cause a large increase in gap that is not sensed by the compensator, so the pocket pressure drops. Note that if the large bearing region were located on the top of the rail, and the small preload bearing on the bottom, which forms a wrap-around bearing, the deformation effects would be considerably lower. For the test system, which was intended to be run using building line pressure, this design was not practical. A next generation design uses this type of wrap-around bearing concept on a ceramic structure so pressures can be increased for grinding applications.

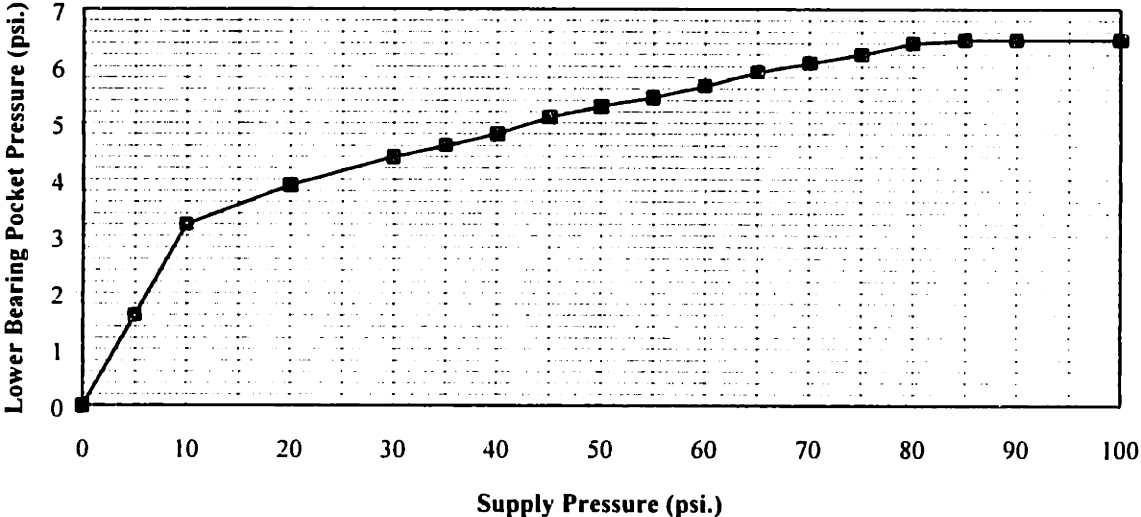


Figure 3.12 Bearing pocket pressure as a function of supply pressure.

The static stiffness was evaluated by loading the carriage with weights and measuring the relative displacement of the carriage with respect to the bearing rails with a capacitance probe. The probe has a nominal resolution of $.05\mu\text{m}$. As shown in Figure 3.13, the results indicated that from zero to the maximum load, the stiffness value was approximately linear, and equal to about $270 \text{ N}/\mu\text{m}$. The value was taken after the carriage settled from the applied load. The reason for the non-linear behavior, when linear behavior is expected, is believed to be due to the tilted bearing pad caused by hydrostatic pressure-induced deformations.

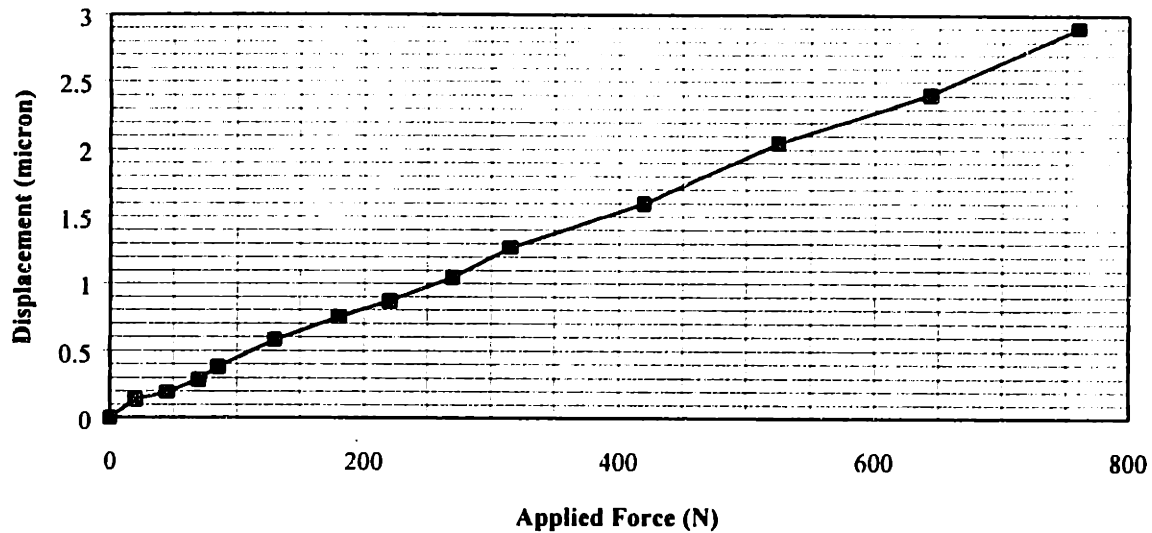


Figure 3.13 Static carriage displacement (relative to the bearing rail) as a function of applied load. The supply pressure was 20 psi.

In order to determine the dynamic stiffness of the system, a modal analysis was performed by taking data at 104 points on the testbed. Since the testbed was made from granite, which is very well damped, any resonances observed would be due to the bearing. The frequency plot, shown in Figure 3.14, indicates several important characteristics of the bearing test prototype. The most important conclusion of the modal analysis work was that there are no distinct modes of the fluid interface. Although the water bearing system supported carriage has a calculated natural frequency of approximately 310 Hz (when modeled as a second order spring mass system), there are no modes in this region. Furthermore, all of the modes found were due to the motions of the granite base on its air isolation system. This large mass/spring system has a rigid body mode at 12 Hz and a bending mode along the long axis at approximately 200 Hz. The remaining modes are also associated with torsional and bending modes of the granite isolating slab. The carriage system motions are relative to these modes. Since the magnitude of the relative motions depends upon the stiffness and damping characteristics of the bearing system, the bearing has a very high dynamic stiffness because the system compliance increases only slightly with the bearing system operating. Most significantly, the carriage/hydrostatic system itself does not show a separate mode because of the high degree of squeeze film damping.

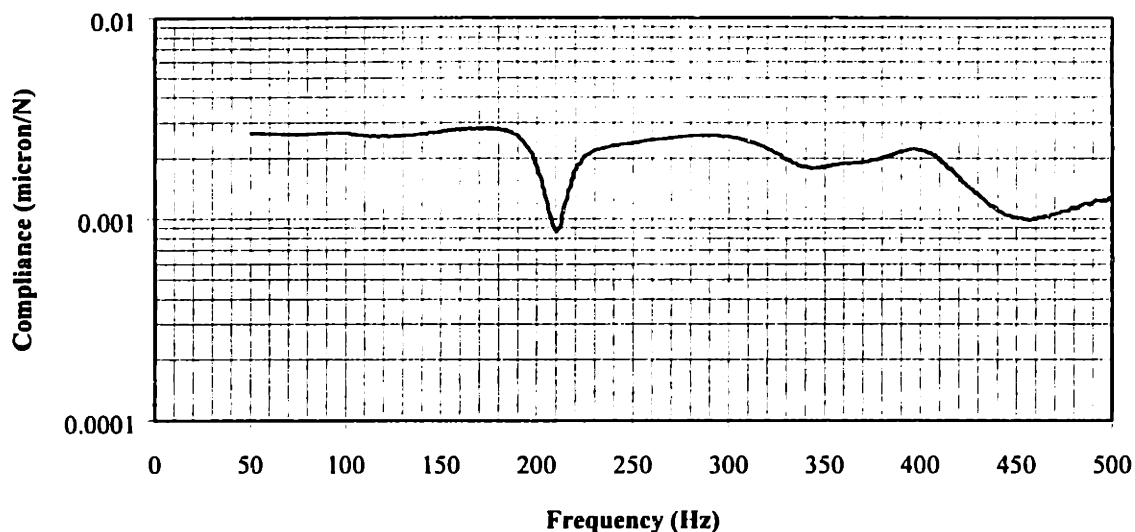


Figure 3.14 Frequency response of the hydrostatic bearing prototype. The excitation point was located on the corner of the carriage. The accelerometer was located near the drive point.

In order to make straightness measurements to evaluate the dimensional performance of the bearing, a differential plane mirror laser interferometer and a $\lambda/12$ straightedge were used with a Zygo Axiom 2/20 system. A linear interferometer was used to measure the axial position during the straightness measurements. Figure 3.15 shows the straightness of the system over 100 mm of travel. Note that the components were initially toleranced at $\pm 5 \mu\text{m}$ over 1 m of length. The repeatability, as measured by moving the bearing back and forth between hard-stops and recording the straightness at the end points, was about 30 nm.

Figure 3.16 shows a small portion of the straightness measurement that shows the effects of ambient vibration and pressure system supply noise. The ambient noise level, with the bearing off, was found to be $.03 \mu\text{m}$. With the building water supply on, the ambient noise level was a total of $.03 \mu\text{m}$. With an impeller pump at 80 psi, the ambient noise level was a total of $.07 \mu\text{m}$. In both cases where pressure was supplied to the bearing, it was pressure filtered using a system shown in Figure 4.1. The ambient noise measurements were taken of the vertical carriage motions relative to the rail. Measurements of the noise level were confirmed by capacitance probe and laser interferometer. The noise level measurements indicate that self-compensated, water hydrostatic bearings can be made to run with essentially no noise due to the pressure supply system.

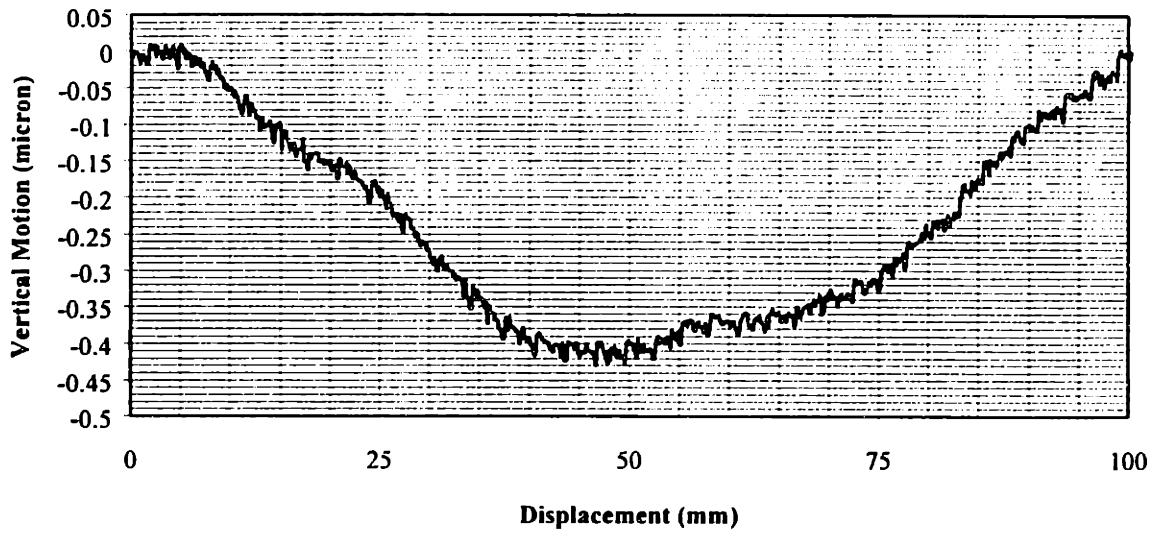


Figure 315 Vertical motions of the carriage over 100 mm travel.

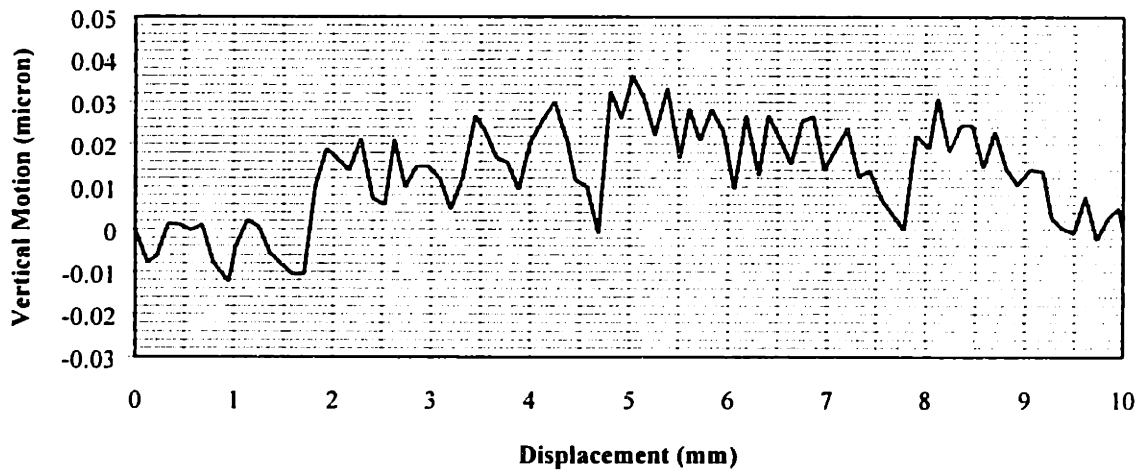


Figure 3.16 Vertical motions of the carriage over 100 mm travel. Note that the noise level in the system with the supply pressure off is $.03\mu\text{m}$.

3.6.2 Prototype # 2: Ceramic Machine Tool Axis Prototype

The second prototype was developed to improve upon the disadvantages of the granite prototype. The system is shown in Figures 3.17 and 3.18.

1. A carriage design which is capable of holding the bearing pads with respect to the rail even when the bearing pressure is high.
2. Thermal stability such that a change in ambient temperature or heat from the fluid will not cause adversely effect the straightness and overall performance of the system.
3. A simplification of the assembly method such that the alignment tolerance of the two rails with respect to one another is decrease. This requirement lead to the design which uses only of the rails for horizontal bearing surfaces.
4. An assembly process in which the bearing pads can be easily installed in a simple yet accurate manner with respect to the rails. This requirement led to a bearing pad design which can be replicated into the carriage assembly with thermally stable epoxy.

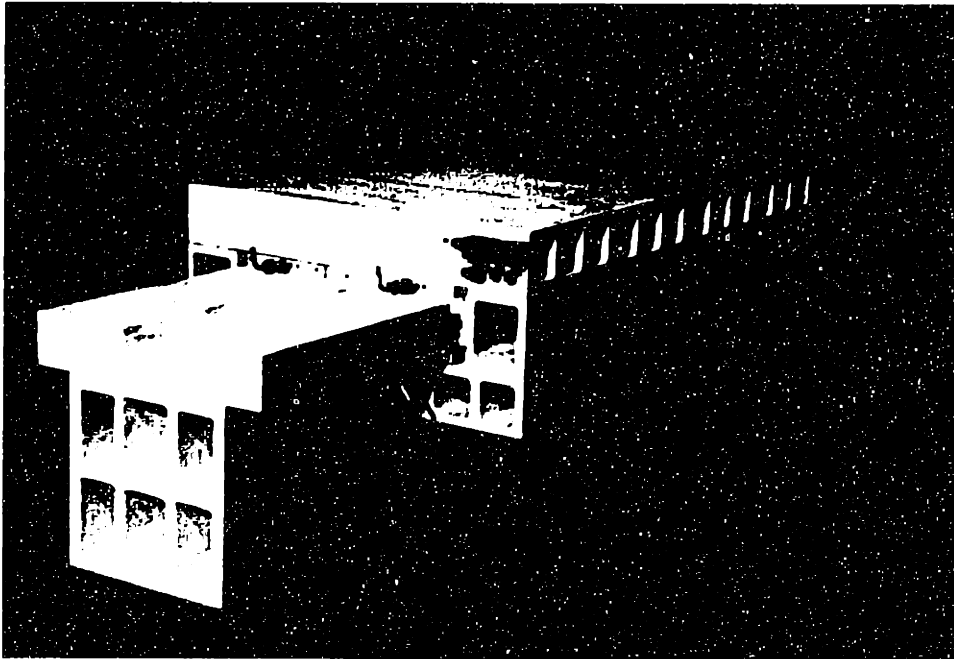


Figure 3.17 Photograph of the prototype ceramic machine tool axis¹. The axis was mounted to an isolated granite table for measurement purposes. Hydraulic supply lines are not shown in this photograph

¹ Assembled at M.I.T. from alumina components built by Wilbanks International, Hillsboro, OR. Hydrostatic bearing pads replicated into assembly by Drew Devitt, Devitt Machinery, Ashton, PA.

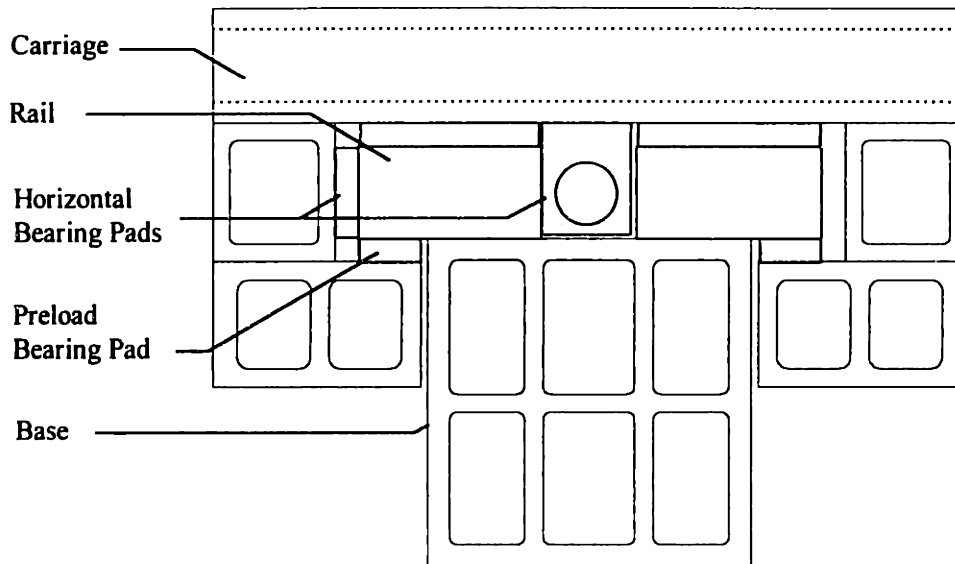


Figure 3.18 Diagram of the prototype machine tool axis. The gray areas indicate the location of bearing pads. All components were constructed of alumina (96% alumina).

The bearing system was evaluated in a similar manner as the first prototype. Measurements were taken of the system straightness, frequency response, and static stiffness. The overall motion of the carriage in the vertical direction along the entire rail was $.55\mu\text{m}$. A typical plot of straightness, as measured in a similar manner as the granite prototype (except with a Zygo ZMI1000 laser interferometer), is shown in Figure 3.21. The frequency response, and modal analysis demonstrated that there was no distinct bearing mode of the carriage moving with respect to the rails. The frequency response plot, Figure 3.19, shows the drive point compliance of the corner of the carriage with respect to the rails. The main modes are a rocking mode of the carriage at 390Hz and a bending mode along the long axis of the system at approximately 600Hz. The system generally achieved an order of magnitude improvement over the first prototype across a range of frequencies from 100Hz to 1000Hz. Similarly, in the static stiffness tests (Figure 3.20), the ceramic axis had a stiffness of approximately $1950\text{ N}/\mu\text{m}$ compared with $270\text{ N}/\mu\text{m}$ for the first prototype. The improvements in stiffness are mainly due to the ability of the prototype to withstand higher supply pressures.

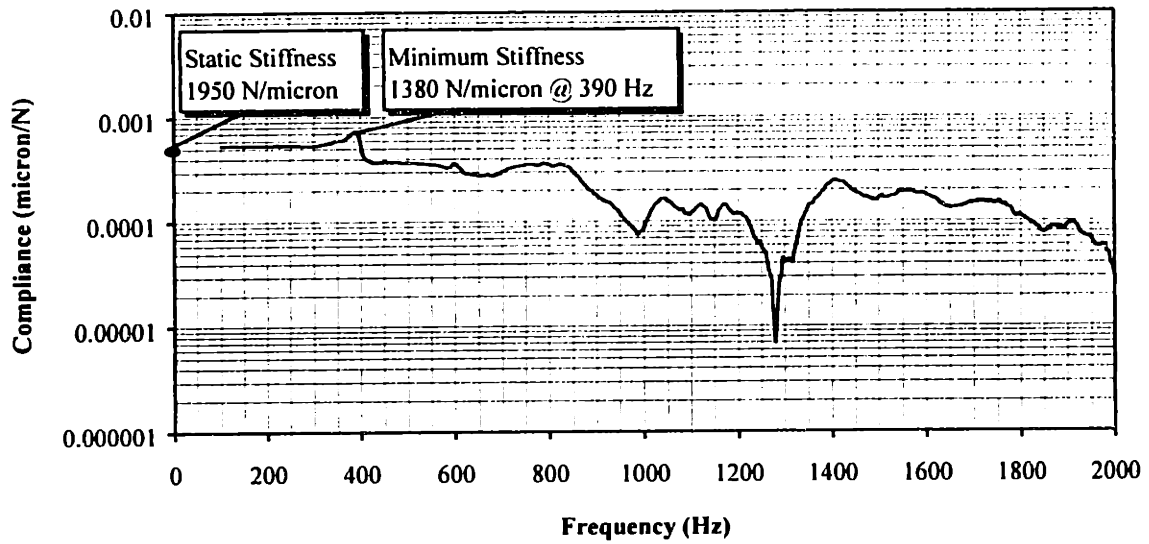


Figure 3.19 Plot of dynamic compliance as a function of frequency for a rolling element bearing / carriage linear axis system and the prototype linear guide system.

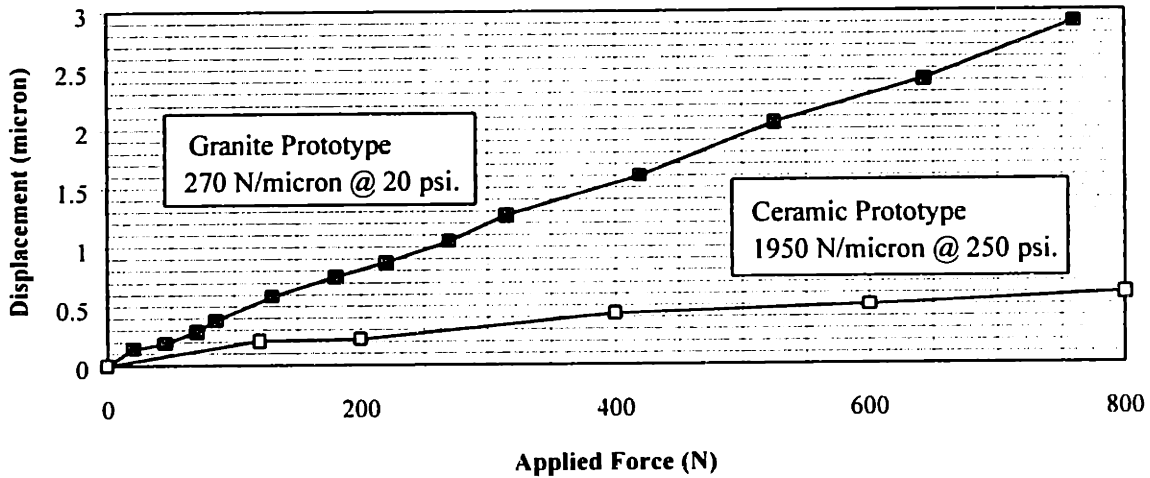


Figure 3.20 Plot of force versus displacement. The stiffness can be estimated by fitting a line to the drive. Using a best fit line, the stiffness is 1950 N/ μm . The spreadsheets used to design the HydroGuide predicted 2000 N/ μm .

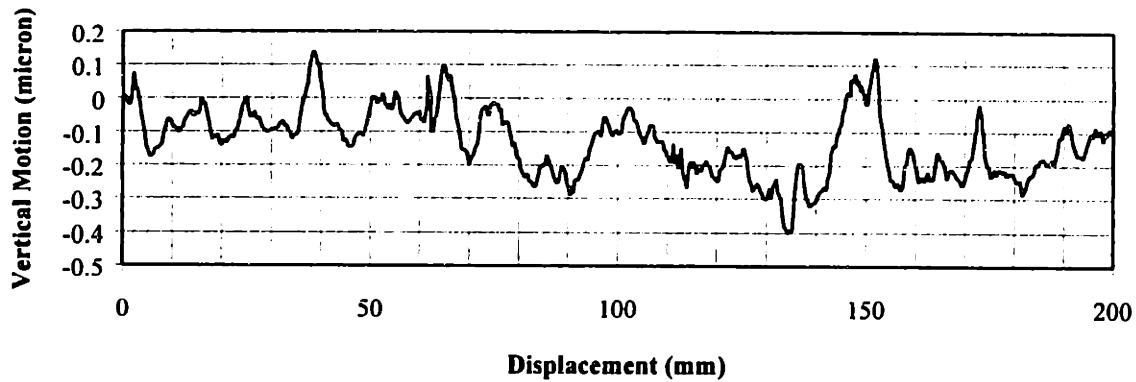


Figure 3.21 Plot of vertical straightness of the axis over 200mm travel. The overall vertical motion is approximately $.55\mu\text{m}$. The data is characteristic of measurements over the entire length.

3.7 - Conclusions

A new type of hydrostatic bearing for precision machine linear motion axes has been developed and tested. The bearing, which is constructed with easy-to-manufacture replicating methods, and is modular in design, has high stiffness (on the order of $1950 \text{ N}/\mu\text{m}$ at a supply pressure of 250psi), excellent straightness characteristics (approximately $0.55 \mu\text{m}$ vertical motion over 200mm), high damping, and low noise levels. The bearing system is environmentally friendly and can use water-based cutting fluids as the hydrostatic fluid. The system requires no hand-tuning of restrictors, and is insensitive to manufacturing errors. Furthermore, the smallest passage is typically 3-5 mm in diameter which virtually eliminates clogging of the hydrostatic passages. The design of the bearing system is simplified by the deterministic design of the restrictor passages, which have a linear sensitivity with respect to stiffness, compared to a gap cubed sensitivity for other types of restrictors. Hence the analysis of bearing performance can be more readily evaluated with simple spreadsheet analysis. Thus, the developed prototypes are well suited for precision linear motion axes of machine tools.

3.8 - Acknowledgments

Support for this research was provided by the National Science Foundation under grant number DDM-9201906. The authors would also like to thank the following people who supplied their time and resources: Kurt Swenson, Jerry Parrott and Mike Caputto of Rock of Ages Corporation saw to the construction of the granite components for the testbed. Reg Maas of Wilbanks International assisted with the design of the second prototype, and supervised the manufacturing of the components. Drew Devitt of Devitt Machinery produced the bearing pads for the first prototype and assembled the bearing pads into the second prototype. Ned Bennett of Zygo Corporation provided the

straightedge for the interferometer measurements and the laser interferometer for the straightness measurements. Mike Bahtarian of A.D.E. Corporation provided the capacitance probe system.

3.9 - References

- [1] Slocum, A.H., "Self-Compensating Hydrostatic Bearing," US Patent #5,104, 237, April 14, 1992.
- [2] Slocum, A.H., *Precision Machine Design*, Prentice Hall, Englewood Cliffs, NJ, 1992.
- [3] Stansfield, F., *Hydrostatic Bearings for Machine Tools*, Machinery Publishing Co., London, 1970.
- [4] Hoffer, "Hydrostatic Bearing," US Patent #2,449,297, Sept., 1948.
- [5] Fuller, D.D., *Theory and Practice of Lubrication for Engineers.*, John Wiley & Sons. New York, NY, 1984.
- [6] Griffin, W.S., Richardson, H.H., Yamanani, S., "A Study of Squeeze Film Damping", *ASME Journal of Basic Engineering*, June, 1966, p. 451-456.
- [7] Hays, D.F., "Squeeze Films for Rectangular Plates", *ASME Journal of Basic Engineering*, June, 1963, p. 243-246.
- [8] Archibald, F.R., "Load Capacity and Time Relations for Squeeze Films", *Transactions of the ASME*, January, 1956, p. 29-35.
- [9] Hahn, R.S., "Some Advantages of Hydrostatic Bearings in Machine Tools", *Journal of the American Society of Lubrication Engineers*, March, 1965, p.89-96.
- [10] Lushington, S.H., Johnson, D.C., "Damping Properties of Thin Oil Films Subjected to High Frequency Alternating Loads", *Journal of Mechanical Engineering Science*, Vol. 5 No. 2, 1963.

CHAPTER 4

FLUID CIRCUIT DESIGN METHOD FOR HYDROSTATIC BEARING SYSTEMS

This chapter will focus on the design issues related to removing pressure fluctuations from hydrostatic bearings. In all cases, conventional hydraulic, and plumbing equipment are used. Simulation techniques will be presented for analyzing the dynamic performance of the bearings.

Hydrostatic bearings are frequently the bearing of choice for precision machine applications. When properly designed, they offer high motion resolution, low friction, high transverse stiffness, and excellent damping [1,2]. They are promising for machine tool applications such as ceramic grinding machines where high stiffness, high damping, and durability are important. However, such bearings have the potential to introduce pressure induced vibrations [3] and thermal errors into machine tools.

Since the stiffness of a hydrostatic bearing system is directly proportional to the supply pressure, high supply pressure is usually beneficial (300psi. is a typical supply pressure). However, in supplying high pressure from a pump, pressure fluctuations and heat will be present. Usually, either piston pumps or diaphragm pumps are used for hydrostatic bearing systems. Such pumps typically produce large fluctuations in pressure, up to 20% of the nominal pressure. Additionally, the high pressure fluid introduces viscous heat into the machine tool as the fluid passes through the hydrostatic bearings.

The fluid circuit which supplies water to the bearings, must accomplish the following tasks; (1) remove pressure fluctuations caused by the pump so the fluid system does not introduce vibrations into the machine tool, (2) maintain the working fluid at constant temperature so the fluid does not cause thermal errors in the machine tool, (3) filter the fluid so that particles do not clog the bearings. The second and third items can be accomplished with conventional equipment such as chillers and filters without modeling. It is the first task which requires the most planning and analysis.

4.1 - List of Variables

Subscripts denote either location or direction

Q - flow

G - transfer function between output and input

P - pressure

C - fluid capacitance

I - fluid inertia

R - resistance

V - volume

ρ - density

A - cross-sectional area

μ - viscosity

l - length

d - pipe diameter

β - bulk modulus

ω - frequency

n - gas constant

K - system gain

4.2 - Introduction

There are three main steps in designing a fluid circuit which is capable of suppressing pressure fluctuations across a range of frequencies. First, a dynamic model must be constructed for simulating the system dynamics. Supplying pressure to the bearings without pressure fluctuations requires careful modeling. A model is useful for the initial design of the fluid supply components. Second, components are selected and integrated including pumps, accumulators, relief valves, needle valves, pipe fittings, filters, and gauges. In selecting components, the dynamic model is an important tool. Additionally, issues such as maintenance, ergonomics, cost, and even aesthetics are resolved during this part of the design process. Third, once the system is operating, the parameters are tuned by experimental monitoring. Dynamic pressure measurements are taken with a piezo-electric type pressure transducer and analyzed with a spectrum analyzer. During this final stage, the settings are tuned in order to compensate for differences between the model and the actual system.

The problem of removing supply pressure fluctuations is an important design issue for hydraulic systems. Viersma [5] developed a method for modeling and removing this type of noise. Many of the lessons learned in this research can be applied to the issues in hydrostatic bearing systems. Typically, the pressure fluctuations are suppressed by placing gas charged accumulators in the transmission line. A simplified schematic of a hydrostatic bearing system and fluid supply system is shown in Figure 4.1.

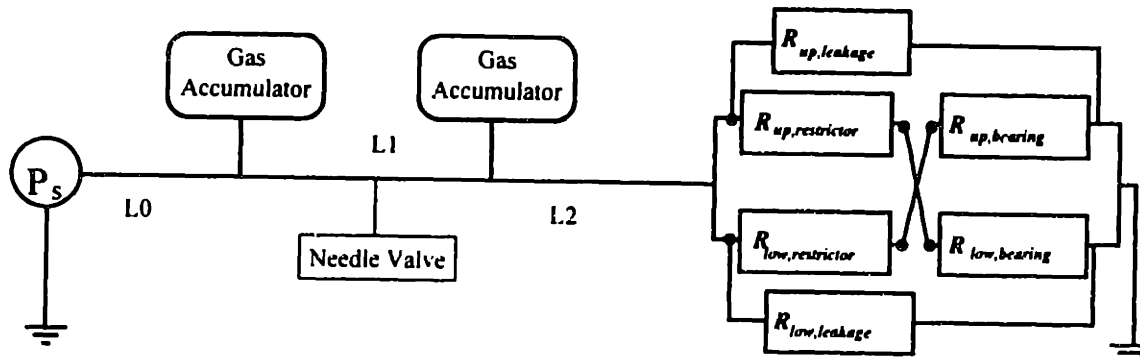


Figure 4.1 Block diagram of the fluid path of a self-compensated, hydrostatic bearing system. The restrictors and bearing lands are represented as fluid resistances.

The main variables which enter into the circuit design are:

- Diameters (D_1 , D_2 , and D_3) of the transmission lines.
- Lengths (L_1 , L_2 , and L_3) of the transmission lines.
- Location of the accumulators.
- Size of the accumulator.
- Charge pressure of the accumulators.

4.3 - Bond Graph Diagrams [6] of Hydrostatic Bearing Systems

In order to eliminate vibrations in the carriage due to pressure fluctuations, it is essential to study the dynamic effect of pressure variations on the system. A simple dynamic model of the bearing system has been developed. The model is capable of predicting system resonances.

The model is developed using bond graph techniques. Bond graphs model the system as a series of capacitances, inertias, and resistances. These elements are joined together with 0 and 1 junctions. A 1 junction indicates equal flow to all adjoining elements. A 0 junction indicates equal pressure in all of the adjoining elements.

A simple lumped parameter model of a fluid transmission line is shown in Figure 4.2.

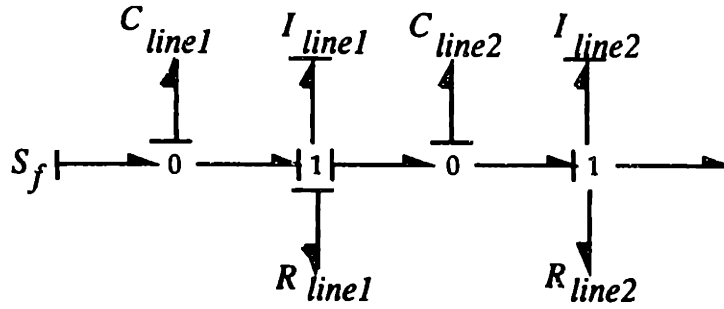


Figure 4.2 Bond graph of a typical transmission line.

The elements in the fluid line can be expressed as:

$$C_{line} = \frac{V_{line}}{B_{fluid}} \quad (4.1)$$

$$I_{line} = \frac{\rho_{fluid} l_{line}}{A_{line}} \quad (4.2)$$

$$R_{line} = \frac{128 \mu_{fluid} l_{line}}{\pi d_{line}^4} \quad (4.3)$$

Thus, the line is modeled as a series of lumped parameters, even though the physical system is continuous. This approximation makes it difficult to capture dynamic events above certain frequencies. For a transmission line, the highest frequency that the model can capture is computed as:

$$\omega = \frac{1}{l_{line}} \sqrt{\frac{B_{fluid}}{\rho_{fluid}}} \quad (4.4)$$

This expression can be used to determine how many lumped elements must be put in series in order to capture the dynamics of the transmission line. In many applications, dynamic events with a frequency greater than 500Hz are not significant. With this highest frequency set, the length of the pipe can be set. In order to model this range of frequencies, the pipe length can be no greater than .5 meters. In many hydrostatic bearing applications, the supply line is approximately 5 meters long, therefore 10 elements are needed to model a typical supply line.

As mentioned previously, gas accumulators are the primary device for reducing the fluctuations in fluid supply fluctuations. A typical accumulator schematic is shown in Figure 4.3.

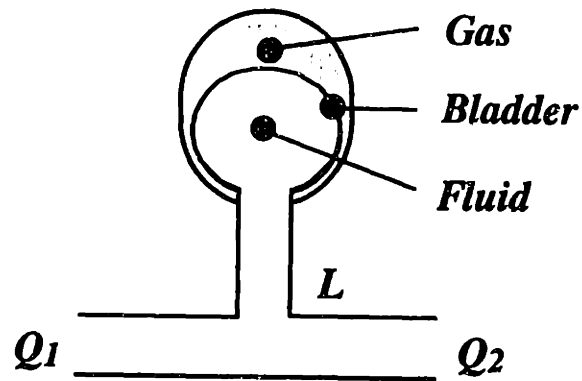


Figure 4.3 Schematic of a gas accumulator. The gas is charged to a prescribed pressure. The fluid supply to the accumulator is provided via a tee from the main supply line.

In order to model an accumulator, the following bond graph (figure 4.4) can be used.

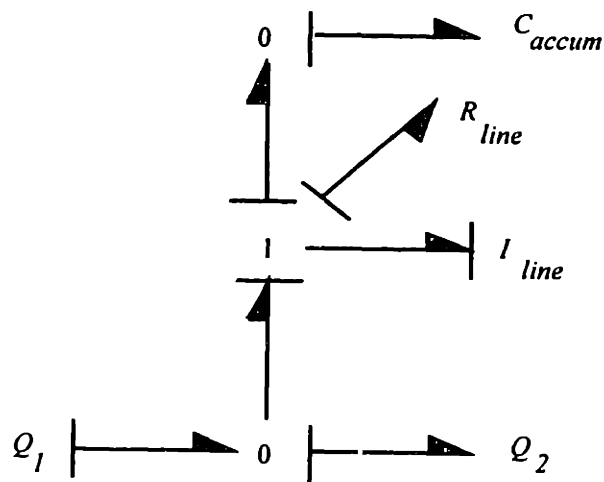


Figure 4.4 Bond graph of an accumulator positioned off of a supply line.

An accumulator effects the supply fluctuations over a range of frequencies. The transfer function of an accumulator is similar to a notch filter. The effect is analyzed by the change in flow entering and leaving the accumulator. The constant associated with the accumulator is calculated as:

$$C_{accum} = \frac{V_{gas}}{nP_{gas}} \quad (4.5)$$

$$G_{accum} = \frac{Q}{P} = \frac{C_{accum} s}{I_{line} C_{accum} s^2 + 1} \quad (4.6)$$

A typical frequency response for an accumulator is shown in figure 4.5.

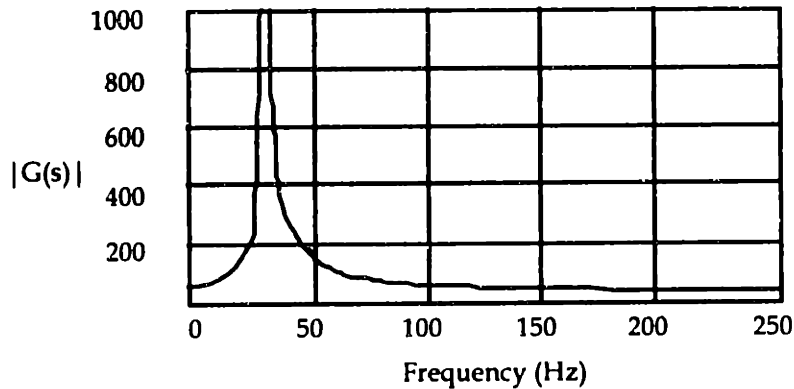


Figure 4.5 Frequency response of a 1gallon gas accumulator charged at 40psi. The accumulator supply line is 1" long and 3/8" diameter.

The expression relating the end conditions to the entrance for an accumulator is:

$$Q_{in} - Q_{out} = C_{accum} \frac{dP_{in}}{dt} \quad (4.7)$$

A pressure relief valve also controls the flow rate through the transmission line. However, this fluid line element is only effective at low frequencies. Typical pressure relief valves have little effect on the system dynamics. Two stage pressure relief valve can act as a low pass filter up to about 10 Hz. Therefore, a pressure relief valve should not be relied upon to reduce pressure fluctuations.

Figure 4.7 is a bond graph of an opposed pad hydrostatic bearing system with a supply line that includes two accumulators. The fluid supply line can have as many degrees of freedom as necessary.

The model of the hydrostatic bearing block can be derived by combining the transmission line model with the electrical diagram of a self-compensated bearing block. The block uses two transmission lines to connect the restrictors to the bearing pads. The bond graph for a bearing block is shown in Figure 4.6. Table 4.1 explains the definition of each variable.

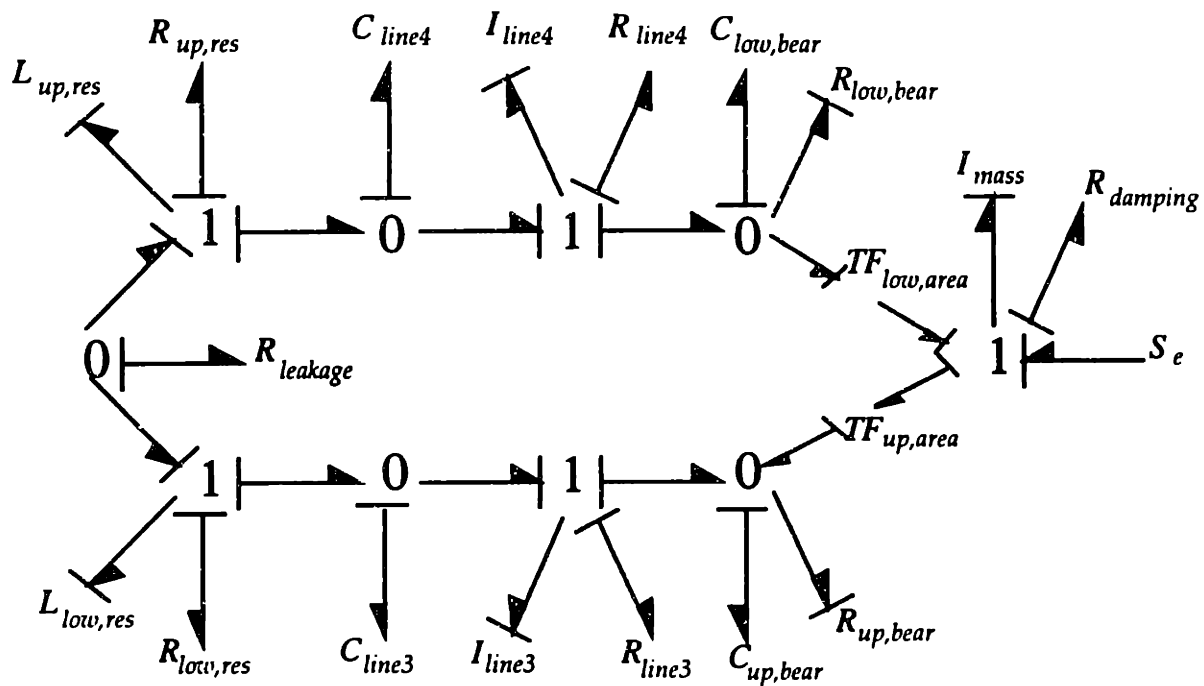


Figure 4.6 Bond graph of a self-compensated, opposed pad hydrostatic bearing pad.

Table 4.1 Description of elements in a hydrostatic bearing bond graph.

| Symbol | Description | Units | Typical Value |
|---------------|---|-------------------------|---------------|
| $R_{low,res}$ | Resistance of the lower restrictor | $\frac{N \cdot S}{m^5}$ | 10^4 |
| $I_{low,res}$ | Inertia of the fluid as it passes over the resistance land, since the gap is on the order of $15\mu m$. The inertia might be high. | $\frac{kg}{m^4}$ | 10^7 |
| C_{line3} | Capacitance of the fluid in the tube between the restrictor and the bearing pocket | $\frac{m^5}{N}$ | 10^{-4} |

Table 4.1 (con't) Description of elements in a hydrostatic bearing bond graph.

| Symbol | Description | Units | Typical Value |
|----------------|--|---------------------|----------------------|
| I_{line4} | Inertia of the fluid in the tube between the restrictor and the bearing pocket | $\frac{kg}{m^4}$ | 10^4 |
| R_{line4} | Resistance of the fluid in the tube between the restrictor and the bearing pocket | $\frac{N * S}{m^5}$ | 10^{-3} |
| $C_{up,bear}$ | Capacitance of the fluid in the bearing pocket. | $\frac{m^5}{N}$ | 10^{-7} |
| $R_{up,bear}$ | Resistance of fluid flow over the bearing lands. | $\frac{N * S}{m^5}$ | 10^4 |
| $R_{leakage}$ | Leakage resistance for flow that goes from the supply groove over the leakage lands. The bearings are designed so that the leakage resistance is much higher than the restrictor land resistance. Leakage flow is detrimental to the performance of the bearing. | $\frac{N * S}{m^5}$ | 10^5 |
| $TF_{up,area}$ | This transformer term translates the bearing pressure into the bearing force. The transformer is the area of the bearing land, since pressure multiplied by area equals a force. | m^2 | 10^{-2} |
| I_{mass} | Mass of the load being supported. | kg | 250 |
| S_e | External force acting on the mass. | N | 150 |

The system model is a combination of the supply line, the accumulator and the bearing block. The fluid supply line can have as many degrees of freedom as necessary. The model only needs to include one bearing pad and mass.

Once a bond graph is developed, differential equations relating the supply pressure to the bearing pocket can be derived. If the resistances of the restrictors and the bearing pads are considered constant, the equations will be linear. If they are modulated based on the position of the carriage, the equations will be nonlinear.

In the nonlinear case, it is not possible to derive a transfer function between the supply pressure and the bearing pocket pressure. In this case, the simulation must calculate the restrictor and bearing pad resistances at each time step based upon the current position of the mass.

Since the restrictor and bearing pad resistances do not vary more than 3% under normal operating conditions, they can be modeled as constant parameters. Therefore, the transfer function between the supply pressure and bearing pressure can be expressed in closed form. However, since there are usually a high number of states, plotting the transfer function is the best description of system performance.

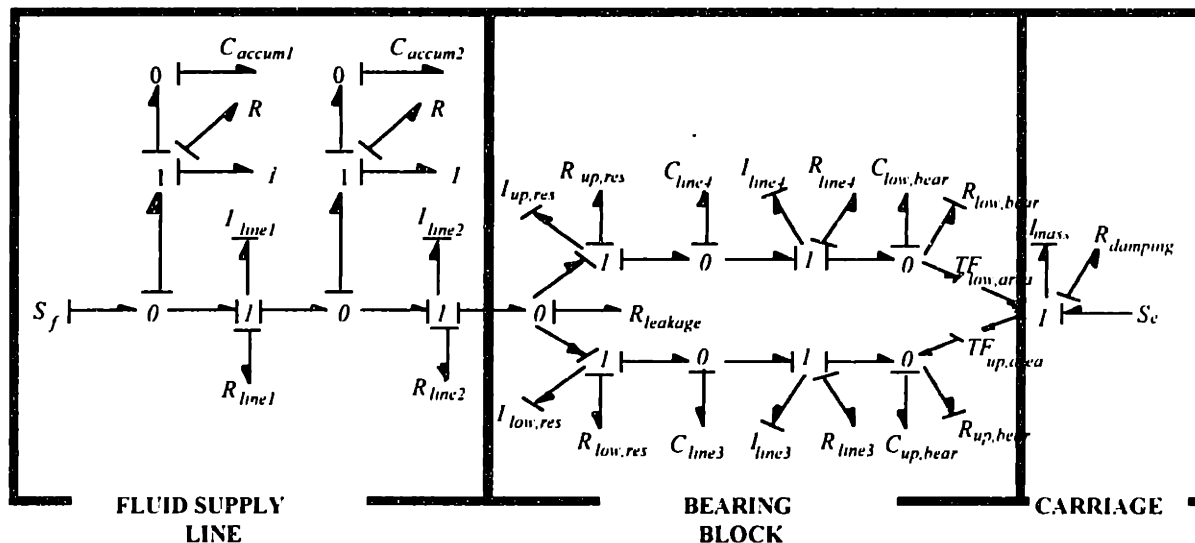


Figure 4.7 Bond graph of a self-compensated, opposed pad hydrostatic bearing system. The model includes one opposed bearing pad and one mass. The model also includes the effect of an external force acting on the carriage, such as a grinding force.

The system as shown will have two inputs; (1) the flow from the pump S_f , and (2) the external grinding force S_c . The number of states is determined by the number of independent energy storage elements. In bond graph notation, it is convenient to choose the efforts associated with capacitances in integral causality and the flows associated with the inertia elements. For systems such as the hydrostatic bearing system, the number of

states will depend upon the length of the supply line leading to the bearing block. Referring to figure 4.7, the bearing block has 8 states. The supply line has 2 states for each .5 meter section of pipe. Thus, a system can easily have 25-40 states.

4.4 - Simulation Results of Hydrostatic Bearing System Noise

The bond graph diagram is translated into differential equations which are then numerically solved on computer. The simulations presented in this thesis were performed with MATLAB. The output of the simulation is a transfer function plot for the output over the input. The output is the bearing pressure and the input is the pump supply pressure. The simulation answers the question: how much does a fluctuation in supply pressure cause a fluctuation in bearing pressure? Since the bearing resistance usually does not fluctuate more than 2% during normal operating mode, the simulation is simplified by modeling the bearings as a single resistor. The following tables show the computer code for a bearing noise simulation.

Table 4.2 MATLAB computer simulation of a simple system similar to Figure 4.1. This section is the system parameter definition and calculation.

| Code | Description |
|--|--|
| Paccum1 = 178800; | Input: Gas pressure in the 1st accumulator |
| Paccum2 = 1378800; | Input: Gas pressure in the 2nd accumulator |
| Vaccum1 = .001; | Input: Volume of the 1st accumulator |
| Vaccum2 = .000757; | Input: Volume of the 2nd accumulator |
| GasConst = 1.4; | Input: Gas constant for the accum. gas |
| bulk = 2.29 * 10 ⁹ ; | Input: Bulk modulus of the working fluid |
| visc = 0.000653; | Input: Viscosity of the working fluid |
| rho = 997; | Input: Density of the working fluid |
| L1 = .2; | Input: Length of the 1st pipe |
| L2 = 5; | Input: Length of the 2nd pipe |
| D1 = .125/39.6; | Input: Diameter of the 1st pipe |
| D2 = .125/39.6; | Input: Diameter of the 2nd pipe |
| Caccum1=Vaccum1/(Paccum1*GasConst); | Output: Capacitance of the 1st accumulator |
| Caccum2=Vaccum2/(Paccum2*GasConst); | Output: Capacitance of the 2nd accumulator |
| z = (rho*a)/(3.14*(D1*D1)/4); | Output: Impedence of 1st pipe |
| RL1 = (128.0*visc*L1)/(3.14*(D1 ⁴)); | Output: Resistance of the 1st pipe |
| RL2 = (128.0*visc*L2)/(3.14*(D2 ⁴)); | Output: Resistance of the 2nd pipe |
| IL1 = (rho*L1*4.0)/(3.14*(D1 ²)); | Output: Inertia of the 1st pipe |
| IL2 = (rho*L2*4.0)/(3.14*(D2 ²)); | Output: Inertia of the 2nd pipe |
| CL2 = (L2*3.14*(D2*D2)*.25)/bulk; | Output: Capacitance of 2nd pipe |
| Rbear = 5*10 ⁹ ; | Output: resistance of the bearing |

Table 4.3 MATLAB computer simulation of a simple system similar to Figure 4.1.
This section is the system parameter definition and calculation.

| Code | Description |
|--|--|
| <pre>a12 = -1/Caccum1; a21 = 1/IL1; a22 = -RL1/IL1; a23 = -1/IL1; a32 = 1/Caccum2; a34 = -1/Caccum2; a43 = 1/IL2; a44 = -RL2/IL2; a45 = -1/IL2; a54 = 1/Caccum2; a55 = -1/(CL2*Rbear);</pre> | <p>Output: The following lines are the calculation of the A matrix in the state space equations.</p> |
| <pre>b11 = 1/Caccum1;</pre> | <p>Output: B matrix calculation</p> |
| <pre>A = [0 a12 0 0 0, a21 a22 a23 0 0, 0 a32 0 a34 0, 0 0 a43 a44 a45, 0 0 0 a54 a55];</pre> | <p>Definition of the A matrix</p> |
| <pre>BB = [1/Caccum1 0 0 0 0]; B = BB' ;</pre> | <p>Definition of the B matrix</p> |
| <pre>C = [0 0 0 0 1]; DD = [0 0 0 0 0]; D = 0;</pre> | <p>Definition of the C matrix Definition of the D matrix</p> |
| <pre>[num,den] = ss2tf(A,B,C,D); w = (1:1:2000); h = freqs(num,den,w); f = w/(2*pi); h1 = abs(h); plot(f(300:2000),h1(300:2000)/z) xlabel('Frequency (Hz)'); ylabel('P/Q'); grid on;</pre> | <p>Calculation of the transfer function and plotting functions</p> |

Table 4.4 Simulation plots of the transfer function between bearing pressure and supply pressure for a hydrostatic bearing systems with and without accumulators.

| | |
|--|--|
| <p>Figure 4.8: Transfer function for a system with no inline accumulators.</p> | |
| <p>Figure 4.9: Transfer function for a system with one accumulator. The accumulator is placed near the hydrostatic bearing with volume of 1/8 gallon and is charged to 60% of the supply pressure.</p> | |
| <p>Figure 4.10: Transfer function for a system with two accumulators. The first accumulator (1/8 gallon) is placed near the hydrostatic bearing. The second accumulator (1 gallon) is placed near the pump. Both are charged to 60% of the supply pressure.</p> | |

4.5 - Experimental Results of Hydrostatic Bearing System Noise

The following figures show noise measurements from a typical bearing system. The pump noise, shown in Figure 4.11, is from a piston pump. The bearing pressure noise is measured by drilling a hole and mounting piezo-electric pressure gauges in the bearing pocket. The successive reduction of pressure fluctuations in the bearing pad is due to the tuning of system parameters (figures 4.12, 4.13, and 4.14). The accumulator pressure has the most significant impact on reducing pressure fluctuations.

Note that it is not possible to get a direct comparison of the bearing pad simulations and the experimental results because the coherence of the measurements is not sufficient. In other words, the input and output measurements of the pressure are not clean enough (except in resonant areas to use them in a cross-power spectrum). However, the bearing pressure results are extremely clean as power spectrum plots. The power spectrum indicates that the simulation correctly predicted the resonances and the effect of the accumulators.

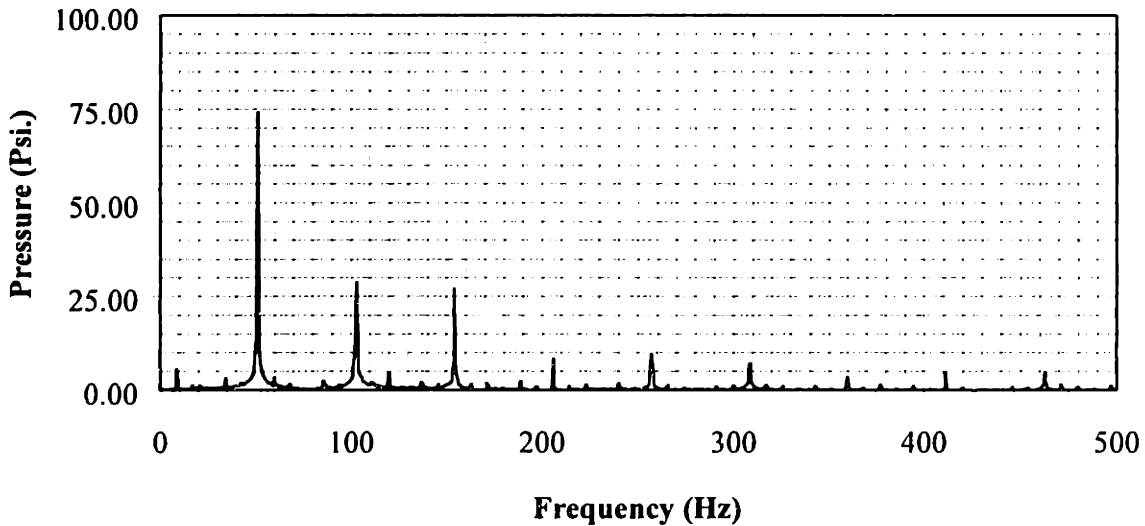
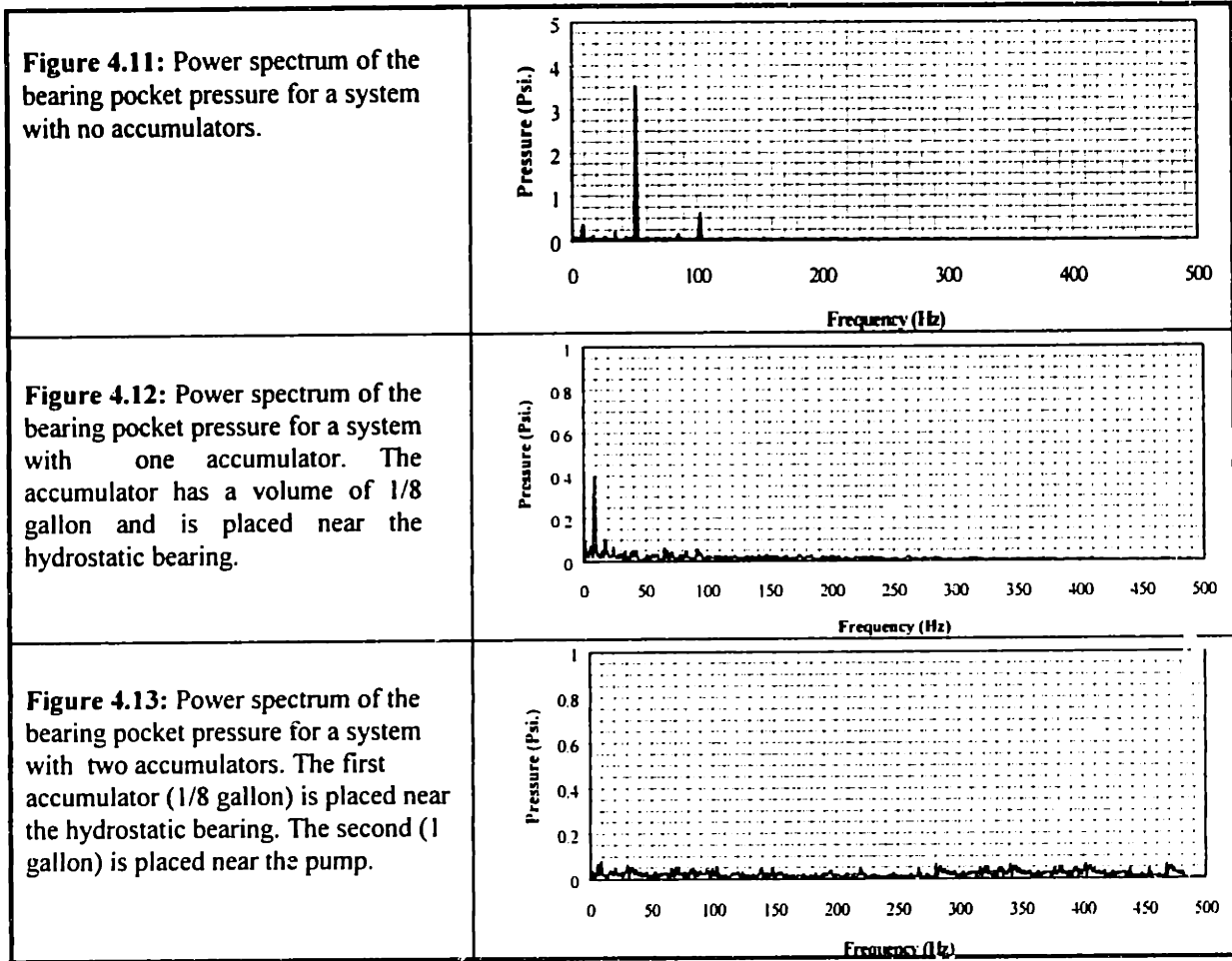


Figure 4.11 Power spectrum of the pressure from a piston pump (three pistons). The nominal supply pressure is 400psi.. Note that the pressure fluctuations are nearly 20% of the nominal supply pressure.

Table 4.5 Experimental power spectrum for the bearing pocket pressure for an opposed pad, self-compensated, water-hydrostatic bearing system with and without accumulators.



4.6 - Results and Conclusions

The simulations and experiments indicate that simple dynamic modeling can capture the dominant system characteristics. Therefore, simulations are an effective method of designing hydrostatic bearing fluid systems. The experimental results shown in figures 4.11, 4.12, and 4.13 demonstrate that the conventional strategy of placing one accumulator in the fluid circuit is not sufficient for precision machine applications. This strategy is the most common industrial method of filtering out pressure fluctuations.

Experiments on the linear guide prototype at M.I.T. have shown that proper selection and placement of accumulators can reduce the vertical error motions of the carriage by more than $.1\mu\text{m}$.

Prior to simulations, the following general rules are useful for choosing the size and location of accumulators:

- Generally two accumulators are required for filtering out supply pressure noise in the 0 Hz to 500 Hz frequency range.
- One accumulator (usually about 1 gallon volume) should be placed as near to the pump as possible and the charge pressure should be set in order to match the natural frequency of the accumulator with the pump.
- The second accumulator (usually about 1/8 gallon volume) should be placed as close to the hydrostatic bearing system as possible. The charge pressure can be set at approximately 60% of the supply pressure.

4.7 - References

- [1] A. Slocum, *Precision Machine Design*, Prentice Hall, Englewood Cliffs, New Jersey 07632, 1992..
- [2] Stansfield, F., *Hydrostatic Bearings for Machine Tools*, Machinery Publishing Co., Ltd., London 1970.
- [3] Nakano, Y., Kato, H., Low, S., "Chatter Marks due to Pulsation of Hydraulic Oil Pressure in Surface Grinding and its Suppression", *Bulletin of the Japan Society for Precision Engineering*, Vol. 20, No. 1 (March 1986), p. 43-44.
- [4] S. Skaistis, *Noise Control of Hydraulic Machinery*, Marcel Dekker, Inc. New York, 1988. Also see,
- [5] T. Viersma, *Analysis, Synthesis, and Design of Hydraulic Servosystems and Pipelines*, Elsevier Publishing Co., New York, 1980.
- [6] Rosenburg, R.C., Karnopp, D. *Introduction to Physical System Dynamics*, McGraw-Hill Publishing Co., New York, NY 1983.

CHAPTER 5

SHEARDAMPING™ OF ADVANCED CERAMIC STRUCTURES

This chapter reviews the theory of ShearDamping then focus on the advantages, difficulties, and design issues related to ShearDamping ceramic structures. ShearDamping uses a thin film of viscoelastic material backed by stiff, elastic components inside a structure. As the structure vibrates, there is relative motion between the embedded component and the structure. This motion shears the viscoelastic layer which dissipates vibration in the form of heat.

One significant disadvantage of ceramic materials when used in structural applications is the low material damping capacity. This has limited their application in high precision machines where high dynamic stiffness is needed. Ceramics, such as aluminum oxide, have high static stiffness. However, the low material damping causes ceramic structures to vibrate significantly at the resonant frequencies of the structure. A new structural damping technology referred to as ShearDamping has increased the low dynamic stiffness of ceramics by increasing the damping.

5.1 - List of Variables

η - loss factor

$W_{dissipated}$ - energy dissipated

W_{total} - total system energy

$\eta_{theo,max}$ - maximum theoretical loss factor

E - elastic modulus

I_{damper} - moment of inertia of the damping structure

$I_{structure}$ - moment of inertia of the structure

ω - frequency

ω_r - resonant frequency

k_{stat} - static stiffness

k_{dyn} - dynamic stiffness

m_{insert} - mass of the damping insert

5.2 - Introduction to ShearDamping Theory

Structural vibration can result from energy sources such as floor noise, actuator activity, cutting forces, and movement of various components. These sources generate relatively wide band excitation which can cause a structure to vibrate if it has a resonant frequency within the same band. Ceramic structures are more susceptible to vibration than cast iron or granite structures because of their relatively low material damping capacity. Although most ceramic structures have high static stiffness, they may not have high dynamic stiffness because of structural resonance.

Designers concerned with vibration have often used cast iron (for heavy structures) and plastic (for light structures) because of their favorable internal damping. Hollow structures filled with other materials such as concrete may provide further vibration reduction. Constrained layer damping has been used extensively to reduce vibration further [1].

ShearDamping was developed through research conducted at M.I.T. by Marsh and Slocum [2,3].¹ This damping technique shears a lossy material to dissipate energy, but unlike traditional constrained layer treatments, the shear medium is inside the structure. The medium is generally a viscoelastic material similar to rubber yet often only 0.1mm thick. Figure 1 shows a sketch of how the shear mechanism works. The thin viscoelastic

¹ Prof. Eric Marsh (Penn. State University) was particularly helpful in developing the ideas presented in this chapter. Eric designed one of the beams and worked on interpreting the modal analysis results.

layer placed between two smooth plates is sheared as the beams move relative to one another (because one face will be in compression and the other will be in tension). As the beams oscillate, energy is dissipated by shearing the viscous layer.

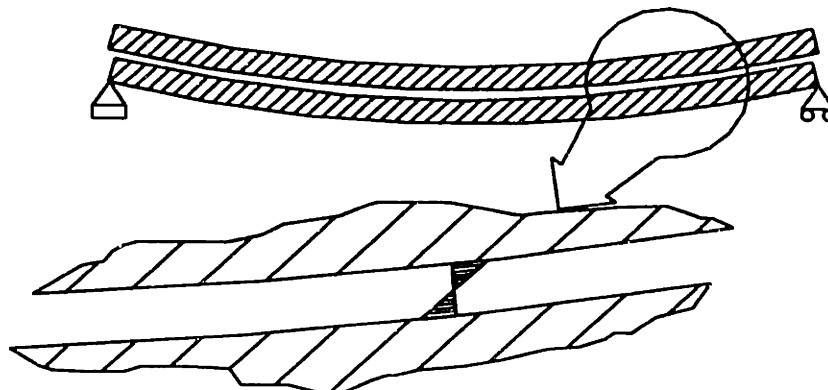


Figure 5.1 Schematic of the damping layer profile in a shear damped beam.

The effectiveness of the damping in a system can be measured in terms of the vibration removed from the system per cycle. The loss factor η is the ratio of energy dissipated versus total system energy system:

$$\eta = \frac{W_{dissipated}}{2\pi W_{total}} \quad (5.1)$$

Thus, a system with a loss factor of 1 would not vibrate. Common steel and ceramic structures might exhibit loss factors on the order of 0.01-0.1 (depending upon the number of joints in the system). Filled structures might achieve a loss factor on the order of 0.01. ShearDamped steel structures with viscoelastic material have achieved a loss factor of 0.2 depending upon weight constraints and available space for shear members. The maximum loss factor for a given configuration can be estimated using the empirical expression from Marsh:

$$\eta_{theo,max} = 0.4 \left(\frac{EI_{damper}}{EI_{structure}} \right) \quad (5.2)$$

This energy dissipation has been modeled analytically and found to be proportional to shear modulus of the layer and inversely proportional to the thickness of the layer. Experiments verify this relationship except that as the layer becomes extremely thin, the shear strain goes to zero. As the layer thickness goes to zero, the structure will have increased stiffness but not increased damping. Figure 5.2 shows the importance of choosing the correct shear layer thickness. In this plot, finite element analysis was performed on a specific configuration in order to determine which shear modulus would

provide the highest loss factor [4]. For this configuration, the highest damping of the first mode occurs when the viscoelastic layer has a shear modulus of approximately 200 MPa and a thickness of 2.5mm.

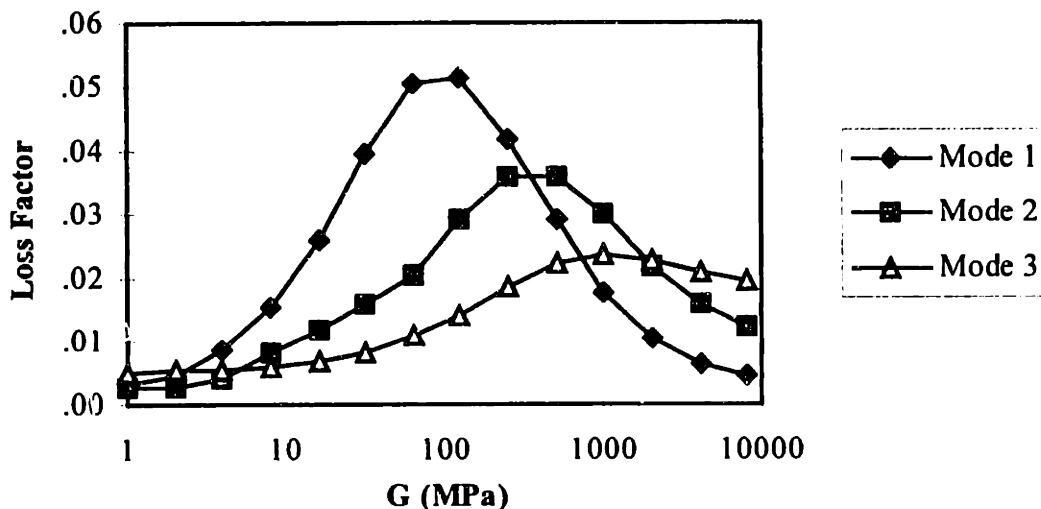


Figure 5.2 Plot of loss factor versus shear modulus of the shear layer.

The design of the ShearDampers also requires a careful regard for geometry. In general, the dampers must be designed such that the neutral axis of the dampers is not the same as the beam itself. If the neutral axes were chosen to be the same, the relative motion would be zero, the shear layer would not be displaced, and therefore no damping would occur.

There are two difficult issues related to ShearDamping of ceramic structures. First, the high stiffness / weight of ceramic structures makes damping more difficult because the shear modulus of viscoelastic materials decreases at higher frequencies. In practical cases investigated, the first bending mode of a typical ceramic beam might be approximately 1500Hz. At this frequency, many viscoelastic materials have a shear modulus which is too low to be effective in damping the structure. Second, the loss factor of the ShearDamped structure depends upon the stiffness ratio of the internal structure to the main structure. With ceramic structures, it is often difficult to design internal dampers which are stiff enough to effect the structure.

5.3 - Single Cell Prototype Design and Experimental Evaluation

5.3.1 - Design of the first ShearDamped single cell ceramic beam

This section discusses the design of single cell ceramic beams with internal ShearDampers. Two types of inserts used; (1) ceramic and (2) carbon fiber composite (CF). The geometry of the inserts and the structure were similar. The internal materials were chosen because of their high stiffness / weight ratio.

Figure 5.3 shows the prototype configuration designed for a ceramic single cell beam. To increase the damping surface while maximizing the distance between the neutral axis

of the inserts and the structure, two c-shape beams were inserted in the single cell beam. Viscoelastic material was wrapped around the inserts and bonded to both along the interface at the neutral axis of the structure. The bond of both c-shapes is very important, since the potential shearing velocity in the damping layer is expected to be the highest there. The gap between the inserts and the inner wall of the single cell beam was filled with epoxy.

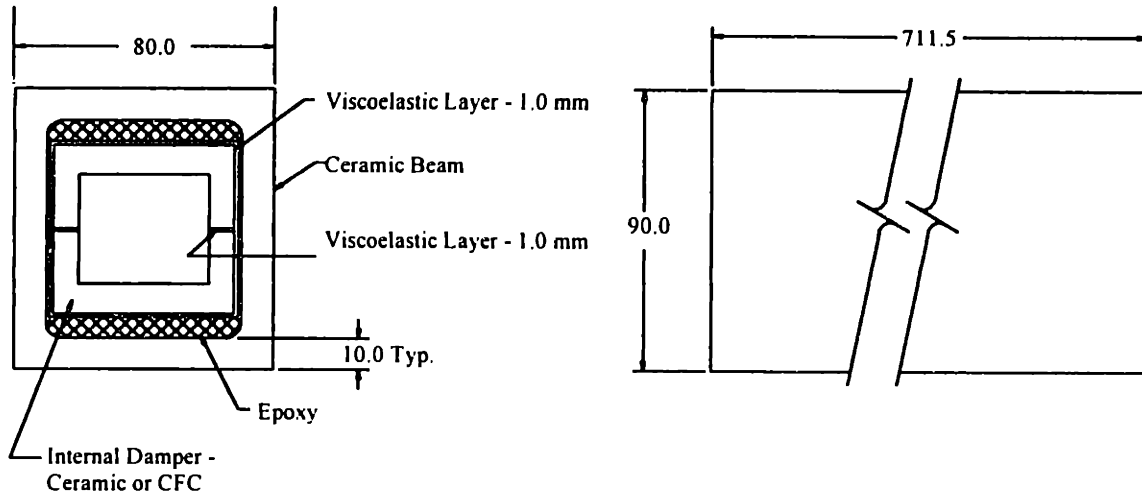


Figure 5.3 ShearDamper design in single cell beam.

Figure 5.4 illustrates the geometry of the ceramic and the carbon fiber composite CF inserts used to damp the ceramic single cell beam. The outer dimensions of both inserts were kept the same, while the wall thickness varied slightly. The wall thickness of each was different in order to compare the damped structures with each other. Reducing the wall thickness of the ceramic insert decreases the mass, the moment of inertia, and consequently the bending rigidity. Conversely, increasing the wall thickness of the CF insert increases the mechanical properties such that the inserts are similar for comparison.

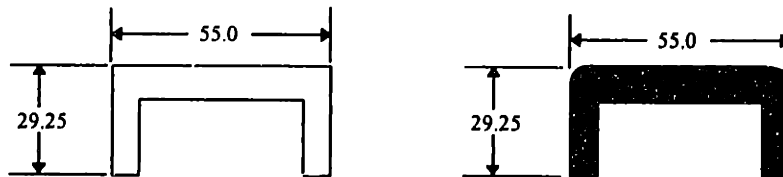


Figure 5.4 Geometry of the ceramic (left) and the CF (right) inserts.

Table 5.1 summarizes the properties of the inserts due to the different material and geometry. The carbon fiber composite (CF) insert was made out of “prepreg” unidirectional laminates that were hand-laid. The content of the carbon fiber (type HS-Carbon) in the matrix system was 60% of the total volume. The ceramic insert was made out of Aluminum Oxide (purity of 96%), the same material as the single cell beam.

Despite the fact that the density of CF is 60% smaller than the density of ceramic, the mass of the inserts differs only by 35%. This is due to the slight geometric differences of the inserts. The same effect may be observed with the stiffness. While the elastic modulus of CF is 52% less than ceramic, the component stiffness is only 32% smaller.

Table 5.1 Characteristic parameters of the ceramic and the CF inserts.

| Property | Symbol | Unit | CF Insert | Ceramic Insert |
|-------------------|--------------|-------------------|-----------------------------|---|
| Material | | | 40% Epoxy / 60% HS Fiber | Alumina 96% Al ₂ O ₃ |
| Density | ρ | kg/m ³ | 1580 | 4000 |
| Elastic Modulus | E | GPa | 145 | 303 |
| Poisson's Ratio | ν | | 0.25 | 0.25 |
| Moment of Inertia | I | mm ⁴ | 63096 | 43840 |
| Stiffness | k_{stat} | N/ μ m | 0.095 | 0.139 |
| Mass | m_{insert} | kg | 1.1 | 1.7 |

The outside beams are both constructed of 96% aluminum oxide (isostatically pressed) which are ground to final dimension with superabrasive wheels. The finished beams with inserts installed are shown in figure 5.5. The inserts are assembled by wrapping the insert with damping tape, placing them inside the beam, then filling the gap between the insert and the beam with epoxy.

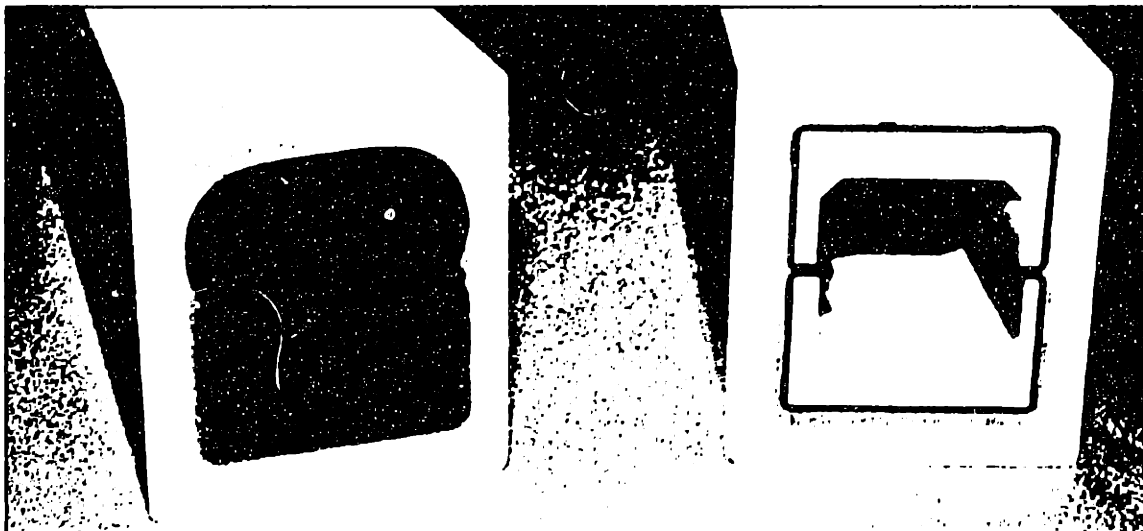


Figure 5.5 Photograph of prototype ceramic beams with the CF inserts (left) and the ceramic inserts (right).

5.3.2 - Performance evaluation of the first ShearDamped single cell ceramic beam

This section describes the performance of the damped beam prototypes. The results are presented in two sections. First, the time response shows the vibration of the system to an impulse force input over time. Second, the frequency response measures the ratio of acceleration to the input force as a function of frequency. The input for all results in this section was an impulse input with a hammer. The force of the hammer force was measured by a piezo-electric force transducer. The structural vibration was measured by a piezo-electric accelerometer.

Figure 5.6 shows the time responses of the undamped and the damped single cell beam. The charts show the acceleration decay over time of the different configurations in both cross-sectional axes of the beam. The difference in horizontal and vertical direction response is due to the difference in stiffness in each direction.

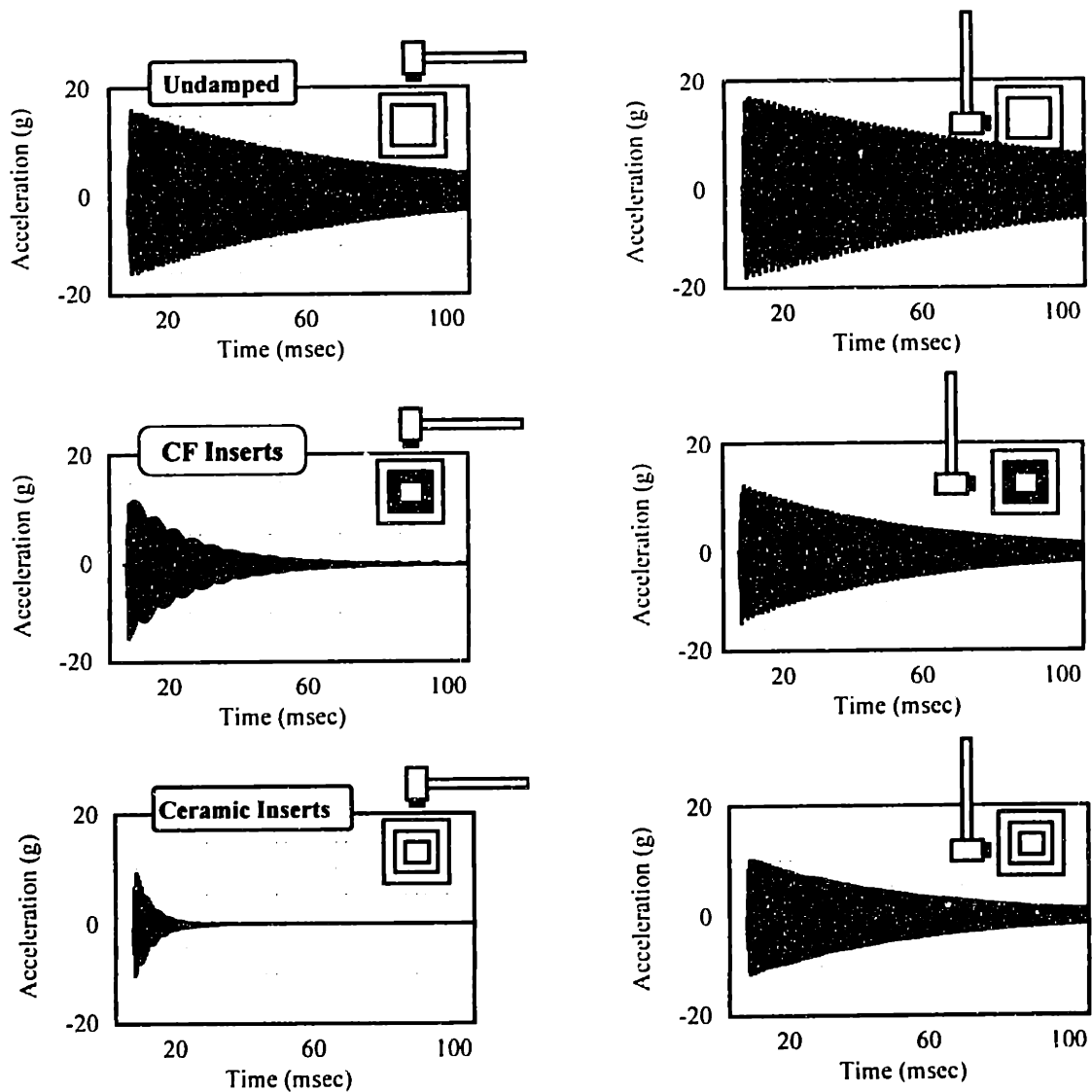


Figure 5.6 Time response charts of undamped and damped beams.

The tremendous improvement of the damping in the cell beam is evident in the time response of the damped single cell beam. Almost all of the damping occurring in the structure is due to the energy dissipation in the damping layer. The damping in the horizontal direction is minimal because the displacement of the insert neutral axis is small. In the vertical direction, where the neutral axis of the insert is displaced from the neutral axis of the beam, the damping is much higher.

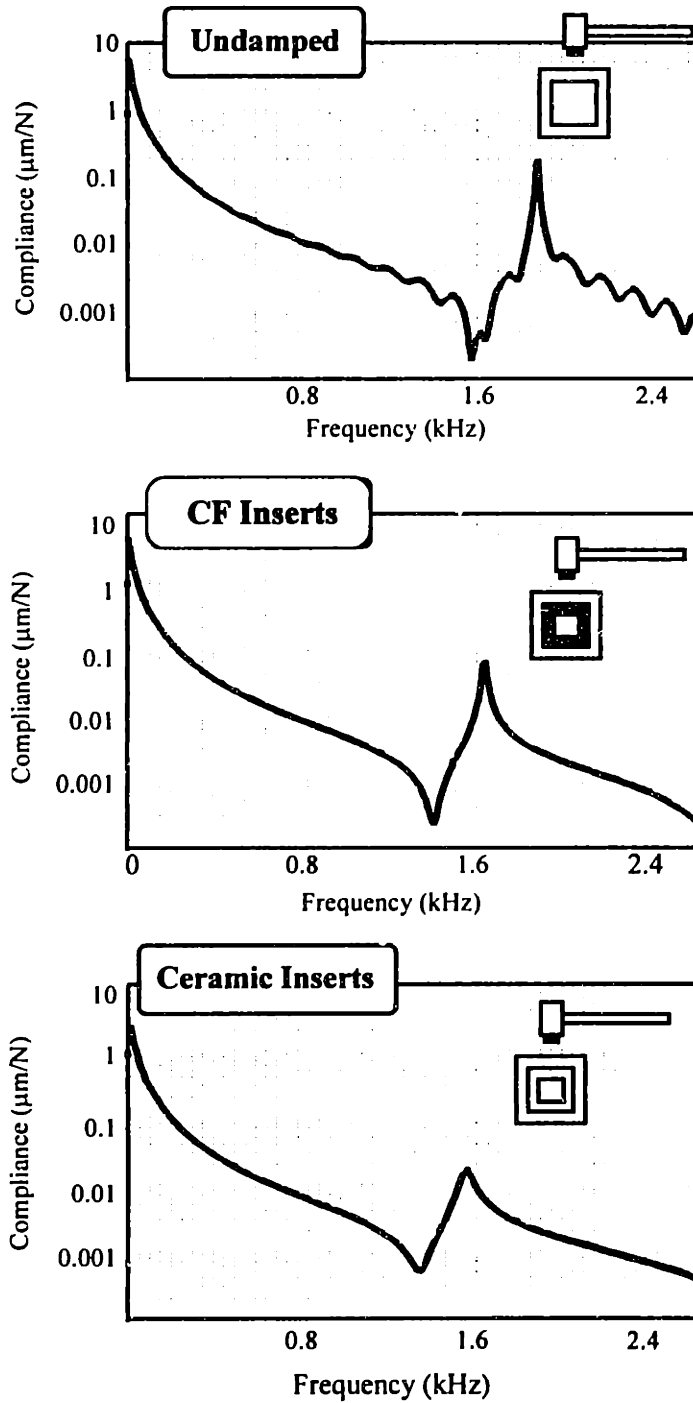


Figure 5.7 Drive point compliance plots of the undamped and damped beams.

The vibration of the damped beam with ceramic inserts decays considerably faster than the vibration of the beam with CF inserts. Since the CF has more material damping than ceramic, it can be concluded that the material damping is insignificant compared to ShearDamping. The higher material damping of CF does not influence substantially the damping of the single cell beam.

Figure 5.7 shows the frequency response of the undamped and damped beams. The charts show the displacement of the resonant frequency in the first mode towards lower frequencies for the damped beams. The beam with the CF inserts has a higher resonant frequency than the beam with ceramic inserts. This may be explained by the higher stiffness/weight ratio of the CF material. The lower resonant peak of the beam with ceramic inserts confirms the improvement in damping compared with the beam with CF inserts.

In order to strengthen the results obtained by the time and frequency response measured at the free end of the single cell beam, data was collected at discrete points on the beam. The modal analysis problem was solved using Star[®] Software² which creates an animation of the vibrating beam at various characteristic frequencies. The animation indicates the type of vibration at each resonance.

Table 5.2 shows the first bending mode shape of the vibrating beam computed by Star[®] Software. In a frequency range of 0-3.2 kHz, the undamped and damped beams show a dominant mode that corresponds to the first bending mode of the beam. The loss factor η is given for the x and y direction of the CF and ceramic damped single cell beam at the resonant frequency ω_r .

Table 5.2 Mode Shape diagram of beam with damping results.

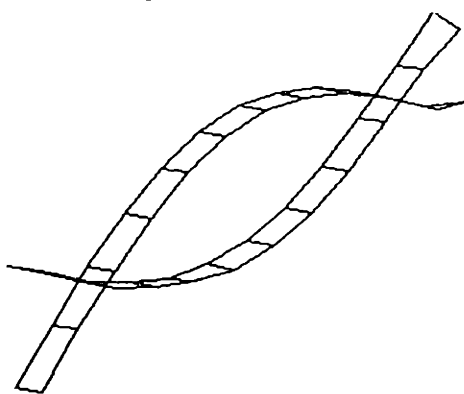
| <u>First Bending Mode:</u> | | ω (Hz) | η |
|---|-----------------------|---------------|--------|
|  | <i>X - direction:</i> | | |
| | Undamped | 1730 | .002 |
| | Damped (CF) | 1527 | .0035 |
| | Damped (Ceramic) | 1494 | .004 |
| | <i>Y - direction:</i> | | |
| | Undamped | 2358 | .002 |
| Damped (CF) | 1668 | .0086 | |
| Damped (Ceramic) | 1586 | .035 | |

Table 5.3 provides an overview of characteristic parameters for all three beams. The dynamic stiffness of the undamped beam increases over 4 times with the CF inserts and over 17 times with the ceramic inserts. The dynamic stiffness corresponds to the minimum stiffness of the component over the range of frequencies sampled. Using equation 7.2, the theoretical maximum loss factor $\eta_{\text{theo,max}}$ of the beam with the ceramic

² Star[®] Software is produced by Structural Measurement Systems, 510 Cottonwood Drive, Milpitas, CA 95035. Tel: (408) 432-8600.

inserts is twice the $\eta_{\text{theo,max}}$ of the CF damped beam. The measured η values show that the ceramic inserts come close to the maximum possible damping of this configuration whereas the η value of the CF damped beam is seven times lower than $\eta_{\text{theo,max}}$.

Table 5.3 Characteristic parameters of the ceramic single cell beam.

| Property | Symbol | Units | Undamped | CF | Ceramic |
|-----------------------------|--------------------------|-----------------|------------------------|------------------------|------------------------|
| Mass | m | kg | 7.8 | 11.0 | 13.3 |
| Moment of Inertia | I | mm ⁴ | 3.11 x 10 ⁶ | 3.24 x 10 ⁶ | 3.21 x 10 ⁶ |
| Static Stiffness | k _{stat} | N/μm | 9.85 | 10.04 | 10.12 |
| Dynamic Stiffness | k _{dyn} | N/μm | 0.020 | 0.09 | 0.35 |
| Loss Factor Theoretical | $\eta_{\text{theo,max}}$ | | - | 0.057 | 0.111 |
| Loss Factor Experimental | η_{exper} | | 0.002 | 0.008 | 0.035 |

5.3.3 - Design of the second ShearDamped single cell ceramic beam

Two significant changes were made to the next prototype. First, the material for the inserts was changed to a higher stiffness ceramic (Aluminum Oxide - 99.5% pure) in order to improve the stiffness ratio presented in Equation 1. The higher purity aluminum oxide has a modulus of elasticity which is 20% higher than that of the external beam but is still economical and readily available. Second, the viscoelastic layer was more precisely tuned with finite element studies in order to determine the most effective shear modulus for the shear layer. Figure 5.2 is an example of such optimization which can have a significant effect on the damping performance of the structure. Figure 5.8 is a photograph and cross-sectional drawing of the second set of damping prototype.

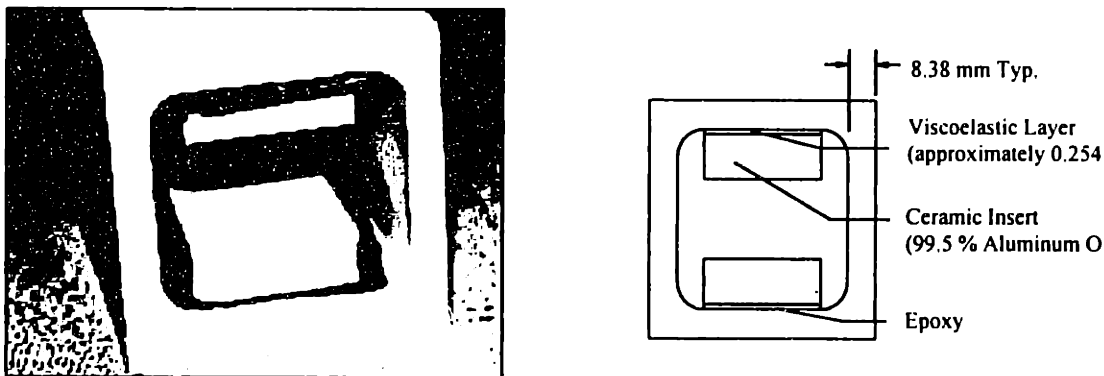


Figure 5.8 Second ShearDamped ceramic beam configuration. The overall dimensions of the beam are 67mm x 67mm x 914mm. The viscoelastic layer is .25mm thick.

Figure 5.9 shows the time response and frequency response of the undamped and damped prototype with 99.5% aluminum oxide inserts. The damping factor is increased from .002 to .02 with the ShearDampers, while the weight is increased from 6.01 to 9.07 kg. Thus, the natural frequency does not decrease as significantly as in the first prototypes.

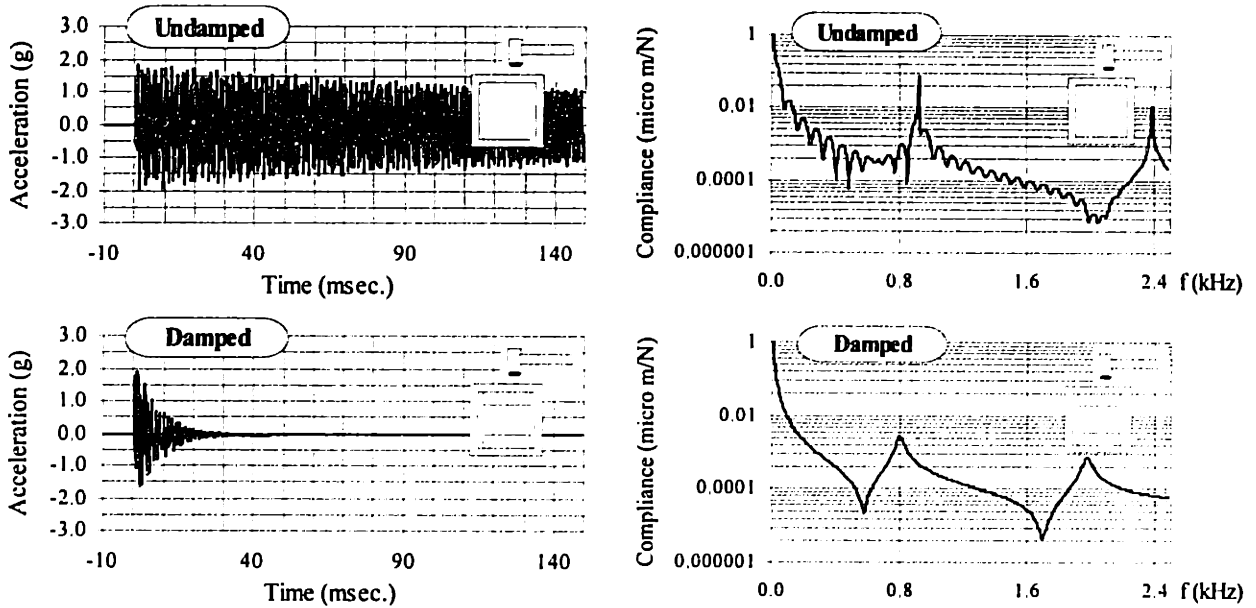


Figure 5.9 Time response and frequency response for damped and undamped single cell beam.

Table 5.4 is a summary of the main characteristics for the second prototype. The results indicate that the damping increases significantly while the additional weight of the internal dampers has been reduced. The increased stiffness of the inserts and the tuning of the shear modulus of the viscoelastic layer are the main factors in the improved performance.

Table 5.4 Characteristic parameters of the ceramic single cell beam.

| Property | Symbol | Units | Undamped | Ceramic |
|------------------------------|----------------|-------|----------|---------|
| Mass | m | kg | 6.01 | 9.07 |
| Elastic Modulus - Inserts | E | GPa | - | 372 |
| Loss Factor - Finite Element | η_{theo} | | - | 0.04 |
| Loss Factor - Experimental | η_{exper} | | 0.002 | 0.04 |

5.4 - Multiple Cell Prototype Design and Experimental Evaluation

5.4.1 - ShearDamper design for a Coordinate Measuring Machine Beam

This section of the chapter will discuss a ShearDamper configuration in a multiple cell ceramic beam for a Coordinate Measuring Machine (CMM). Damping parameters will show the effect of the ShearDampers in the dynamic behavior of the beam. The application requires high damping, and low weight since the beam will be rapidly accelerated. The damping is required mainly in the stiff direction of the beam. The weak direction should also have a higher dynamic stiffness, but it should not reduce the damping performance of the stiff direction.

Figure 5.10 is a diagram of the undamped CMM beam configuration which has become a standard design for high performance CMM's. However, when the beam is used in applications in which high acceleration and deceleration are used in order to increase the system bandwidth, vibration can reduce the system accuracy.

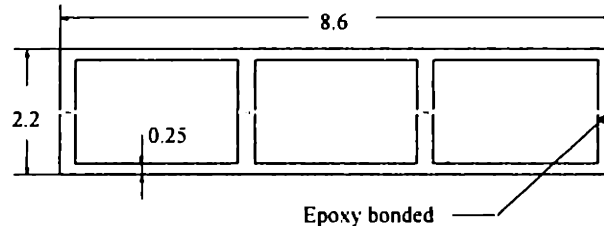


Figure 5.11 Diagram of a typical undamped multiple cell ceramic beam.

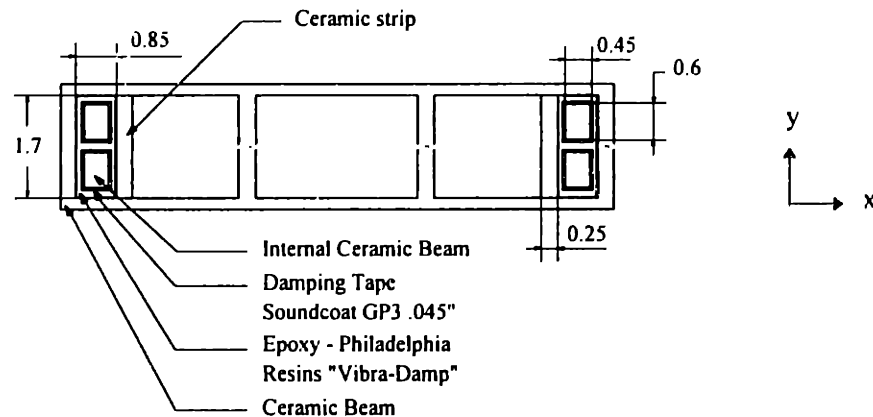


Figure 5.12 Diagram of the ShearDamped multiple cell ceramic beam.

The CMM beam consists of two symmetrical ceramic parts bonded together with epoxy. The goal for this particular beam was to increase the damping of the beam in the x direction. The y direction dynamic stiffness is not as critical in this application. To achieve a high damping in the x-direction, the neutral axis of the ceramic inserts was

displaced as far as possible from the neutral axis of the structure. The inserts were kept small so that the system mass would not increase dramatically. Two rods were designed for each side in order to Sheardamp the y -direction as well. The damping in the y -direction however, will be much smaller than in x -direction.

The rods are wrapped with damping tape then epoxied into the structure. A ceramic strip was used to create a hole for the ceramic rods. The strip minimizes the amount of epoxy and ensures relative motion in the shearing layer.

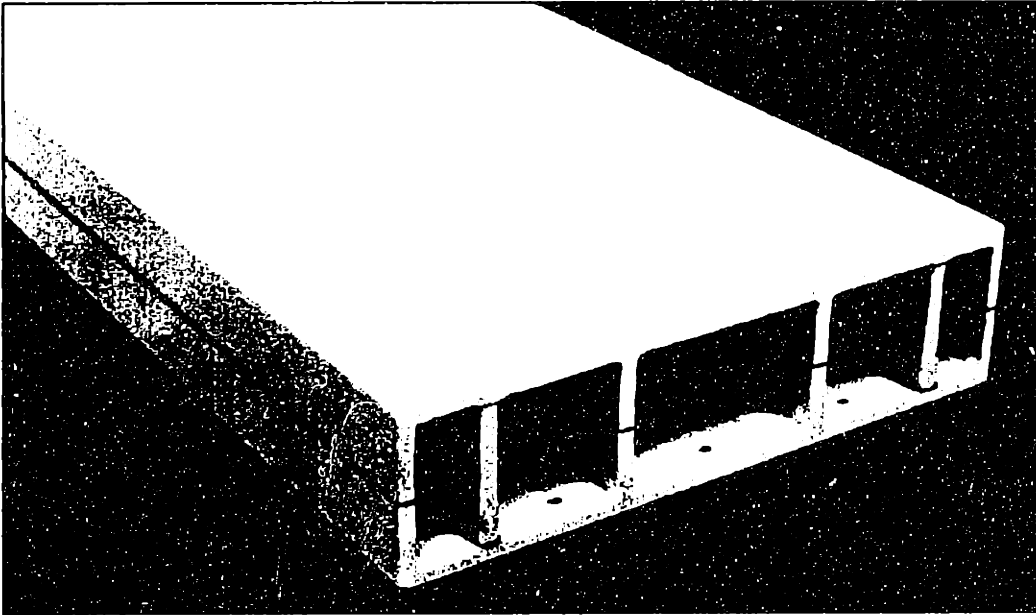


Figure 5.13 Photograph of the CMM beam with the ShearDampers.

5.4.2 - Time Response and Compliance

Figure 5.14 shows the time response of the undamped and damped CMM beam to an impulse excitation. The damped beam in the stiff direction shows a dramatic improvement of the dynamic behavior. While after 45 msec. the acceleration of the damped beam is almost zero, the undamped beam vibrates at over 50% of its maximum acceleration. This may be explained by the overlapping of bending and torsional modes (these modes of vibration will be discussed in the next section of the chapter). The acceleration decays of the damped and the undamped CMM beam in weak direction are similar, where the damped beam shows a better damping than the undamped. The lower damping of the ShearDampers in the weak direction may occur because of the small displacement from the neutral axis of the inserts.

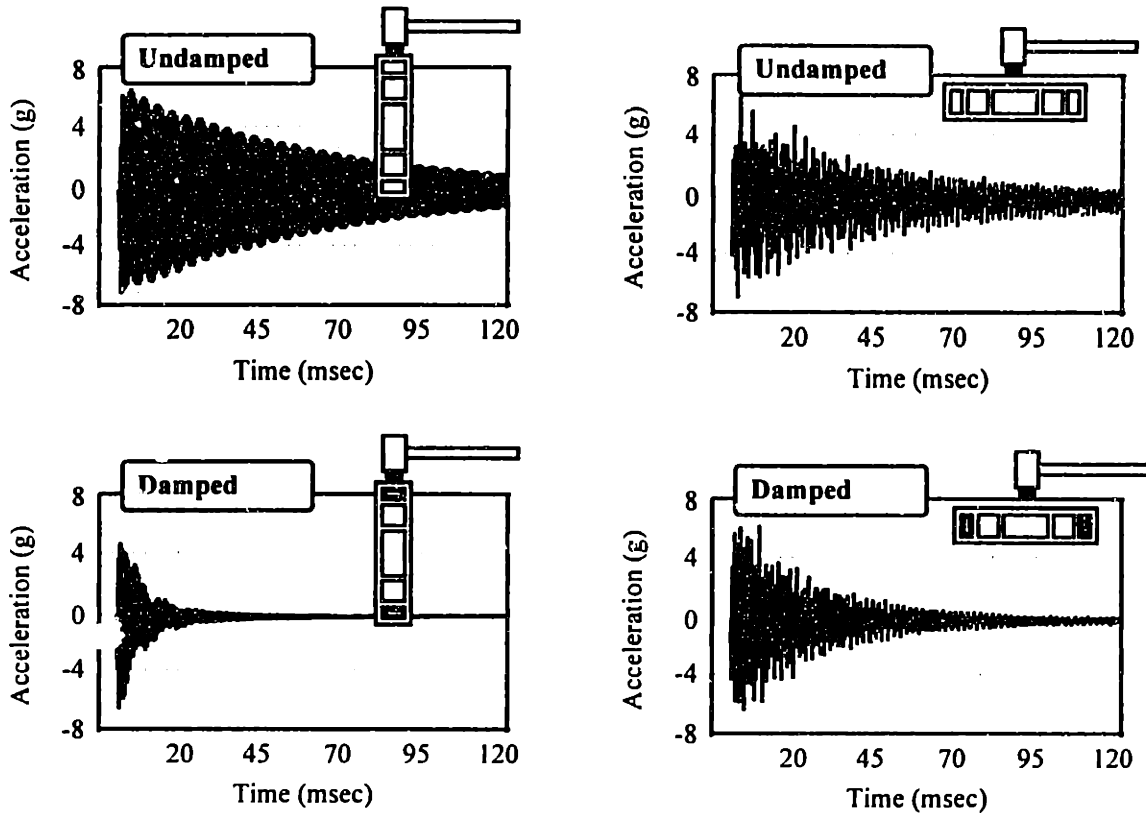


Figure 5.14 Time response of undamped and damped beam.

Figure 5.15 illustrates the frequency responses of the CMM beam for the undamped and the damped configuration. While the ShearDampers show a tremendous improvement of the dynamic stiffness in the first mode of vibration ($\omega = 1596$ Hz), the damping in the second mode at $\omega = 3100$ Hz is nearly as high. The time response demonstrates that the damping in weak direction is not as high as in stiff direction. The modal analysis will show the significant improvement of the dynamic stiffness at all vibration modes even in the weak direction.

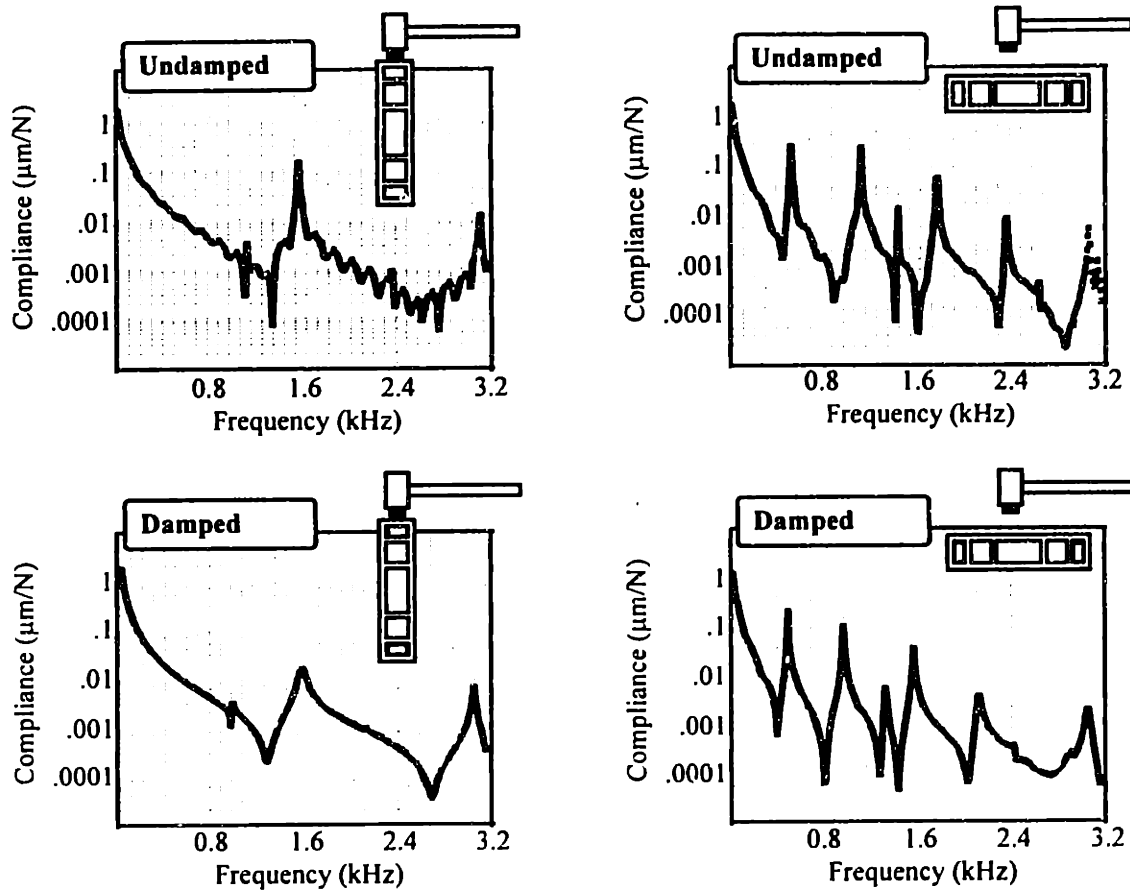


Figure 5.15 Compliance of damped and undamped beam.

5.4.3 - Modal Analysis Results

The experimental modal analysis was performed for both, stiff and weak, directions in order to obtain a better understanding of the vibration occurring in the CMM beam. The emphasis of the evaluation was given to the stiff direction, since the dynamic behavior in this direction is of primary concern for the future application of the CMM beam.

Table 5.5 is an overview of damping parameters for the beam in stiff direction. The static stiffness k_{stat} has been determined assuming no shearing forces in the damping layer for the static case. Therefore, the inserts are assumed to be totally uncoupled from the beam. Since the static stiffness will be the lowest in the uncoupled case, the actual beam has higher stiffness.

The static stiffness of the beam due to the ShearDampers is 18% higher than the undamped beam. The mass increased by 24%. The increased static stiffness in the damped beam is mainly due to the bonded ceramic strip on each side of the beam. The performance of the ShearDampers may be observed in the dynamic behavior of the beam. The dynamic stiffness increased by a factor of 21 times when compared to the undamped

beam. The damping loss factor η increased by a factor of 17. The theoretical maximum possible damping for this configuration (calculated using equation 5.2) is close to the actual measured damping parameters. It is important to note, however, that the calculated and experimental values are not generally within 10%. The theoretical number calculates a maximum, and therefore, the numbers will be similar if the design is carefully manufactured.

Table 5.5 Characteristic parameters of the multiple cell CMM beam in the stiff direction.

| Property | Symbol | Units | Undamped | Damped |
|----------------------------|-----------------------|------------------------|--------------------|--------------------|
| Mass | m | kg | 18.5 | 23 |
| Moment of Inertia | I | mm^4 | 2.06×10^7 | 2.43×10^7 |
| Static Stiffness | k_{stat} | $\text{N}/\mu\text{m}$ | 18.06 | 21.3 |
| Dynamic Stiffness | k_{dyn} | $\text{N}/\mu\text{m}$ | 0.03 | 0.65 |
| Loss Factor - Theoretical | η_{theo} | | - | 0.0305 |
| Loss Factor - Experimental | η_{exper} | | 0.0018 | 0.0304 |

The following tables show the modal analysis results for the CMM beam in both directions. Each intersection of lines indicates a data point where an accelerometer reading was taken.

Table 5.6 First bending mode of the CMM beam in the X direction.

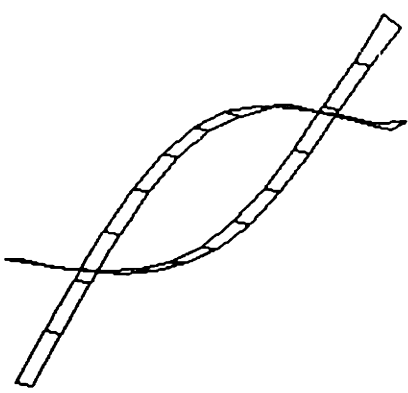
| | | | |
|---|----------|---------------|--------|
|  | | ω (Hz) | η |
| | Undamped | 1596 | .0018 |
| | Damped | 1597 | .0304 |

Table 5.7 Significant bending and plate modes of the CMM beam in the y direction.

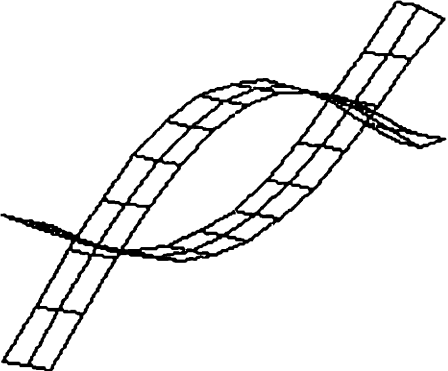
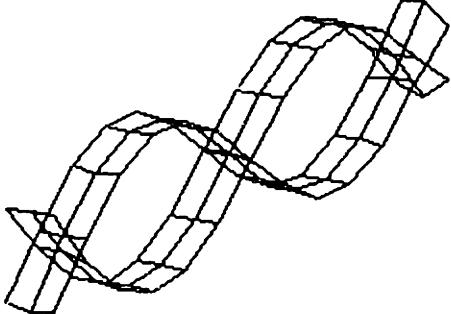
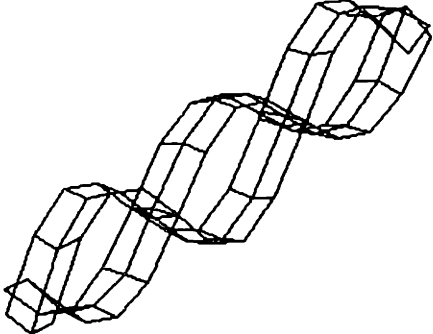
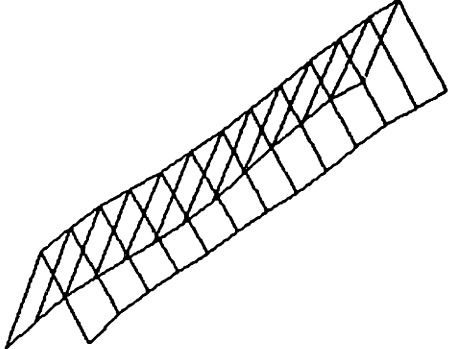
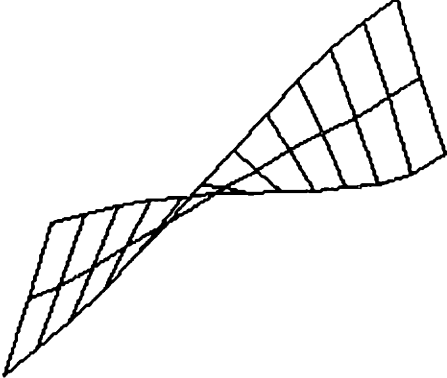
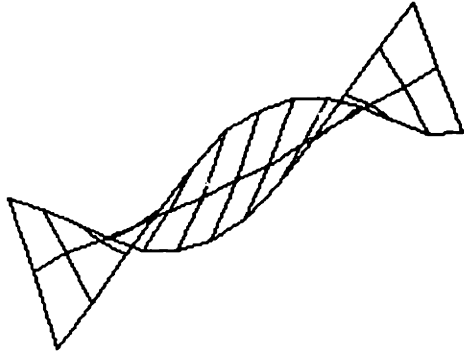
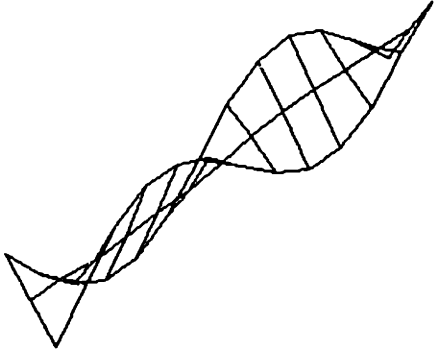
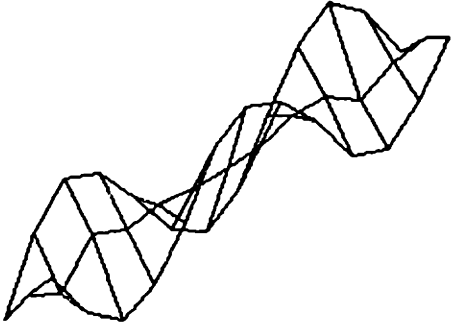
| | | | |
|---|-------------------------------|---|--|
| <p><u>First Bending Mode:</u></p>  | <p>Undamped</p> <p>Damped</p> | <p>ω (Hz)</p> <p>557</p> <p>520</p> | <p>η</p> <p>.0066</p> <p>.0104</p> |
| <p><u>Second Bending Mode:</u></p>  | <p>Undamped</p> <p>Damped</p> | <p>ω (Hz)</p> <p>1463</p> <p>1352</p> | <p>η</p> <p>.0022</p> <p>.0102</p> |
| <p><u>Third Bending Mode:</u></p>  | <p>Undamped</p> <p>Damped</p> | <p>ω (Hz)</p> <p>3088</p> <p>2451</p> | <p>η</p> <p>.003</p> <p>.0082</p> |
| <p><u>First Plate Mode:</u></p>  | <p>Undamped</p> <p>Damped</p> | <p>ω (Hz)</p> <p>3156</p> <p>3076</p> | <p>η</p> <p>.0058</p> <p>.0066</p> |

Table 5.8 Torsional modes of the CMM beam in the 0-4 kHz region.

| | | | |
|--|----------------------------|--|---|
| <p><u>First Torsional Mode:</u></p>  | <p>Undamped Damped</p> | <p>ω (Hz)</p> <p>1152 993</p> | <p>η</p> <p>.0046 .0088</p> |
| <p><u>Second Torsional Mode:</u></p>  | <p>Undamped Damped</p> | <p>ω (Hz)</p> <p>1796 1593</p> | <p>η</p> <p>.0034 .0076</p> |
| <p><u>Third Torsional Mode:</u></p>  | <p>Undamped Damped</p> | <p>ω (Hz)</p> <p>2388 2148</p> | <p>η</p> <p>.0032 .0132</p> |
| <p><u>Fourth Torsional Mode:</u></p>  | <p>Undamped Damped</p> | <p>ω (Hz)</p> <p>3089 2928</p> | <p>η</p> <p>.0024 .0064</p> |

5.5 - Conclusions

ShearDamping for ceramic beams can be summarized as follows. First, a properly designed ShearDamper component can increase the loss factor by a factor of 15-20. The weight increase using typical design has been about 25-50%. Furthermore, the recent results indicate that finite element modeling of the ShearDamping technique appears to be an accurate method for predicting the performance.

The design of the damped structures should maximize the internal damper stiffness, maximize the relative motion between the structure and the dampers, and select the proper shear modulus of the damping layer.

5.6 - Future Work

As with many research projects, these initial studies in ShearDamping ceramic structures are useful for future design work. The next set of ShearDamping prototypes will build upon the experience of those presented in this report.

Three significant changes will be made in next set of prototypes. First, the material for the inserts will be changed to a higher stiffness ceramic (Aluminum Oxide - 99.5% pure) in order to improve the stiffness ratio presented in Equation 2. The higher purity Aluminum Oxide has a modulus of elasticity which is 20% higher than that of the external beam but is still economical and readily available. Second, the viscoelastic layer will be more precisely tuned with finite element studies in order to determine the most effective shear modulus for the shear layer. Figure 5.2 is an example of such optimization which can have a significant effect on the damping performance of the structure. Third, further optimization can be done on the shape of the inserts in order to improve the stiffness and displacement from the neutral axis without significantly increasing the weight of the structure.

Designs have also been proposed for ceramic beams with multiple internal cells. Since many precision machines are designed with rectangular cross section beams, designs for implementing ShearDamper technology into these designs have been developed. Figure 5.16 is a configuration for a three cell beam with ceramic inserts.

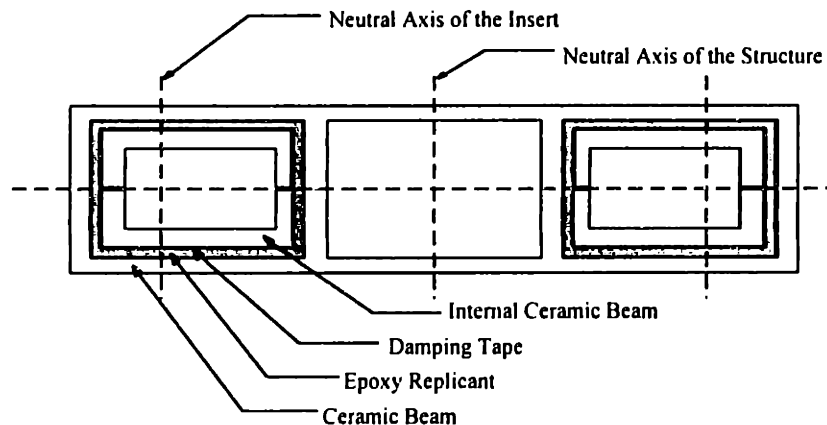


Figure 5.16 Next generation ShearDamper configuration in a three cell beam.

The beam has been designed to increase the damping of the beam such that the loss factor will be approximately 0.2. Since the calculated damping from equation 5.2 represents the maximum damping for a given configuration, the beam is designed with a loss factor which is slightly higher than the intended value for the prototype. Table III shows the main damping parameters of the beam.

Table 5.9 Predicted damping parameters of a ShearDamped three cell ceramic beam.

| Property | Symbol | Unit | Undamped | Damped |
|--|-------------------|-----------------|--------------------|--------------------|
| Mass | m_{insert} | kg | 18.5 | 26 |
| Moment of Inertia Stiff Direction | I | mm ⁴ | 2.06×10^7 | 2.12×10^7 |
| Moment of Inertia Weak Direction | I | mm ⁴ | 1.85×10^6 | 1.89×10^6 |
| Static Stiffness | k_{stat} | N/ μ m | 18.06 | 18.63 |
| Loss Factor - Predicted Stiff Direction | $\eta_{theo,max}$ | | - | 0.245 |
| Loss Factor - Predicted Weak Direction | $\eta_{theo,max}$ | | - | 0.052 |

5.7 - References

- [1] A. Nashif, D. Jones, and J. Henderson, Vibration Damping, John Wiley & Sons, New York, 1985.
- [2] Marsh, E.R., "An Integrated Approach to Structural Damping", Ph.D. Thesis, Massachusetts Institute of Technology, 1994.
- [3] A.H. Slocum, E.R. Marsh, and D.H. Smith, "A New Damper for Machine Tool Structures: the Replicated Internal Viscous Damper", Journal of Precision Engineering, Vol. 16, No. 3, 1994, 174-183.
- [4] C. Johnson, and D. Kienholz, "Finite Element Prediction of Damping in Structures with Constrained Viscoelastic Layers", American Institute of Aeronautics and Astronautics, Vol. 20, No. 9, 1982, 1284-1290.

CHAPTER 6

DESIGN OF AN INDUSTRIAL PRECISION CERAMIC GRINDING MACHINE

The following chapter describes the design of a precision grinding machine built at the Precision Products Group at Wilbanks International. The Wilbanks Precision Grinding Machine (WPGM) was designed for use as a production machine at Wilbanks and as a test bed for the ideas discussed in the previous chapters of this thesis.

The machine was initially proposed by Reg Maas¹, and involved nearly every member of the Precision Products Group at Wilbanks. The design evolved from September 1993 through September 1995 (even as the structure was being assembled). The principle designers of this machine are Paul Scagnetti, Reg Maas, and Prof. Alex Slocum.

The sections of this chapter focus on the design of particular systems within the precision grinding machine. The design process for this machine was iterative. The design of one system intimately effected the design of another in most cases. It is hoped that this description will serve as an example for machine tool engineers who are considering alternative technologies for next generation machines.

¹ Reg Maas, senior engineer for the Precision Products Group for over 7 years, was a critical part of the development of the Wilbanks Precision Grinding Machine. Reg also developed the multiple cell ceramic beam discussed in chapter 2 of this thesis.

6.1 - Introduction

Wilbanks first considered building a precision grinding machine for large ceramic beams because this machine configuration is not produced by major machine tool manufacturers. The general goals of this machine development project are summarized in Table 6.1.

Table 6.1 General goals for the Precision Ceramic Grinding Machine development project at Wilbanks International.

| Goal | Description |
|--|---|
| Current Production | Replace a machine tool which is worn out and difficult to replace since major machine tool manufacturers do not make a similar configuration at a reasonable price. |
| Marketing Precision Ceramic Structures | Demonstrate to machine tool manufacturers that ceramic materials can be successfully used in precision machine tools. |
| Improve current state of ceramic grinding machines | Improve grinding machine durability because their conventional machines often wear down within 1 year. This design will lead to future designs for other machine tools at Wilbanks and Coors Ceramics in general. |

The goals of this project can be summarized as follows: Wilbanks fulfilled their requirement for a specific machine tool and utilized the opportunity to study a method for solving their current problems with ceramic grinding machines.

The current endgrinding machine is an Elb machine which was designed for a different grinding process. The machine has required serious rework over the last 10 years. Figure 6.1 is a photograph of the current endgrinder.



Figure 6.1 The current endgrinder at Wilbanks International.

There were four main influences for the design of the WPGM.

- The history and experience gained from using the current endgrinder machine.
- The ideas and prototypes mentioned in the previous chapters of this thesis.
- Production requirements (such as part size and range of motion).
- Production and assembly limitations of the plant.

Each of these influences are described in the following sections.

6.1.1 - Previous Experience

The design of the present endgrinder was a major influence in the design of the WPGM. Although the machine was far from perfect, it has served as a production machine for 20 years. Therefore, many attributes of the current machine were successful and can be used in the design of the WPGM.

The configuration of the current machine is the most sensible for an endgrinding machine. The machine grinds the ends of long beams. Therefore, a T based configuration is very sensible for this type of grinding process. Figure 6.2 is a overview diagram of an endgrinding machine.

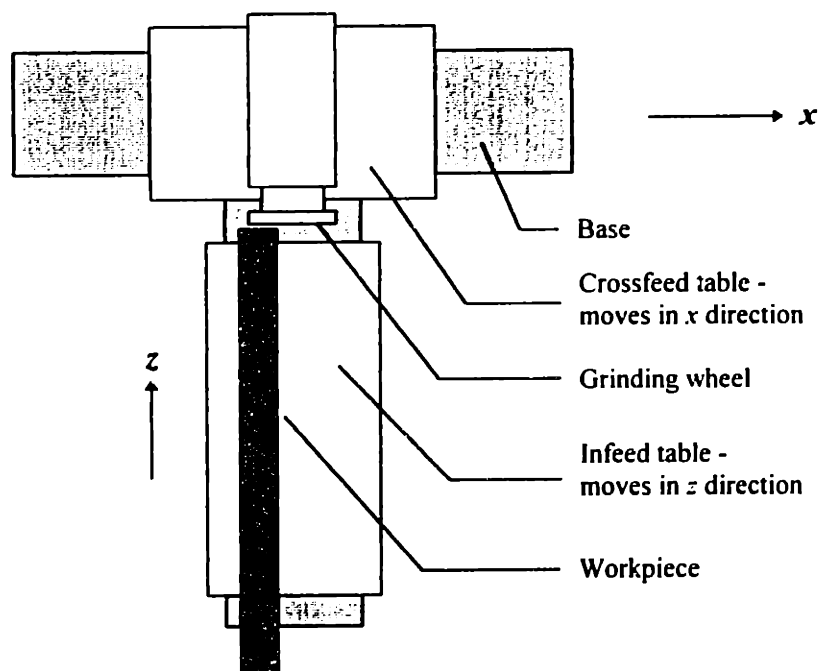


Figure 6.2 Overview diagram for a grinding machine for the ends of long beams.

Perhaps the most important lesson learned from the current endgrinder is that the part is too long to be traversed in the x direction across the grinding wheel. The grinding accuracy of the current machine is effected by the part rotating about the y . The new endgrinder moves the grinding wheel rather than the long part.

The next most important lesson from the existing endgrinder is that the infeed table should be long enough to clamp the parts securely and accurately. The infeed table on the

current endgrinder is only 30" long in the z direction. For 120" parts, less than one quarter of the part is clamped to the table. It is impractical for production space reasons to have the table be 120", but longer is better.

The most significant lessons learned are listed in table 6.2. This list is separate from the general list of machine tool requirements discussed in chapter 1 in that it relates only to the information gained from this particular machine.

Table 6.2 Lessons learned from the current endgrinding machine at Wilbanks which influenced the design of the WPGM.

| Issue | Lesson Learned |
|----------------------|--|
| Coolant guards | Grinding area should be enclosed to avoid spraying coolant mist in shop area. |
| Table length | Table should be long enough too rigidly clamp 120" parts.. |
| Fixturing | Workpiece table should have threaded holes every 4" for toggle clamps in order to hold parts securely. |
| Workpiece squareness | A fixture should be included on the infeed table for quickly aligning long parts square to the grinding wheel. |

6.1.2 - New Machine Tool Technologies

The new endgrinder was conceived with the goals mentioned in chapter 1. Namely, (1) increased stiffness and damping in the bearings and structure, (2) improved thermal stability, (3) increased motion resolution in the infeed axis, and (4) improved straightness in the crossfeed (sensitive axis). Since the technologies had not been used in previous designs, there was no easy way to budget for the amount of machine errors, although there was precedent from prototypes. The following goals in table 6.3 were qualitative rules (goals) during the design process.

Table 6.3 Error estimates for the Wilbanks Precision Grinding Machine.

| Error Type | Estimate |
|--------------------------------------|---|
| Straightness of motion | 1 micron per meter of motion. |
| Stiffness of bearings | 3 Mlbs/in. in sensitive directions. |
| Dynamic stiffness of structural loop | Minimum stiffness of 100 N/ μ m. |
| Thermal stability | Machine should be maintained within 2° F. |
| Motion resolution | Infeed motion of 5 μ m. in the sensitive direction. |

6.1.3 - Production Requirements for the WPGM

Additionally, there were specific production requirements which effected the design. These requirements included issues such as maximum part size, range of infeed motion, and traverse speed for the grinding wheel. These requirements had a significant effect on the final design of the machine. Table 6.4 is a list of production requirements and the areas of design which they affected.

Table 6.4 Production requirements for the WPGM.

| Production Requirement | Description | Design Issues for the Grinding Machine |
|-------------------------------|--|---|
| Part size | 30" wide by 10" thick by 120" long | <ul style="list-style-type: none"> • Table size and design • Grinding wheel size (and therefore spindle size) • Range of traverse travel |
| Infeed range of motion | At least 2" | <ul style="list-style-type: none"> • Ballscrew length • Length of structure and infeed rails |
| Traverse speed | Capable of 1 ft./sec. | <ul style="list-style-type: none"> • Bearing design • Actuator choice for traverse motion |
| Load Capacity | 2,000 lbs | <ul style="list-style-type: none"> • Bearing design • Structural design |

6.1.4 - Manufacturing Capabilities

The capability of the manufacturing plant strongly influenced the design decisions. Since the machine was intended for production at Wilbanks, the limitations of the production facility were critical to the design. The Precision Products Group at Wilbanks produces high accuracy ceramic beams for the coordinate measuring machine industry. The limitations mainly effected the design of the structure (which is ceramic). In general, the capabilities of the Precision Products Group were extremely well suited to building this type of machine. Table 6.5 is a summary of the main capability issues which effected the design of the WPGM.

Table 6.5 Wilbanks capabilities which influenced the design of the WPGM.

| Issue | Description | Design Issues |
|--------------|--|--|
| Material | Types of ceramic material available and frequently fired at Wilbanks | Used 96% Aluminum Oxide which is the most commonly used and economical ceramic |
| Densifying | Methods available for bringing ceramic powder to density | Designed parts to be isostatically pressed |

| | | |
|------------------|---|---|
| Press tooling | New press tooling often requires significant development and is expensive | Designed structural components around existing tooling (see chart in chapter 2) |
| Size limitations | Machines and kilns are limited in terms of width, height, and length. | Designed components to be smaller than 24" x 24" x 120" until the final assembly process. |

6.1.5 - Existing Components

Since the WPGM was built to serve as a production machine, it was initiated as a capital equipment project. The budget for the machine was established based on the market value of a similar machine, and the projected costs. The cost analysis assumed the use of components already at Wilbanks including an Elb spindle, and several ceramic beams. The design of the WPGM assumed that these components would be part of the final design in order to meet budget goals.

The spindle which was allocated for the WPGM had been used on a machine at Wilbanks for 20 years. The design of the WPGM assumed that this spindle would be modified and reconditioned.

This spindle was intended to serve during the initial use of the endgrinder until a water-hydrostatic spindle was completed and tested. Prof. Slocum initiated a separate research program for the development of a water-hydrostatic spindle which is planned for implementation on the WPGM by May 1996. Thus, the design of the WPGM accounts for the immediate use of the Elb spindle and eventual use of a water-hydrostatic spindle.

The base structure of the WPGM was built entirely out of beams which had been rejected for customer use due to minor aesthetic blemishes. The beams were an assumed part of the design of the WPGM. However, they would have been chosen for the base structure even if they were not available from the manufacturing recycling bin.

6.2 - Design Overview for the Wilbanks International Precision Ceramic Grinding Machine

6.2.1 - Historical Overview

An initial design concept was developed to meet all of the production and manufacturing requirements while benefiting from previous experience and new machine tool technologies. The production requirements and manufacturing capabilities were constraints upon the design whereas the new machine tool technologies and previous experience were design tools.

Over several months, the initial concept of the endgrinder was developed then reviewed then refined. Reg Maas finished the initial concept for the machine in September 1993. The machine concept was reviewed at M.I.T. by Reg Maas, Alex Slocum, Paul Scagnetti, and Christoph Brunner. For another 6 months, the initial work was done separately at Wilbanks International and M.I.T. During this time, the structural

design concept was revised (close to the final design) and the hydrostatic bearing pads were design and analyzed at M.I.T.

In June of 1994, Paul Scagnetti moved to Oregon to work with Reg on the design and oversee the production. Over the next year, the concept was detailed and developed into production drawings and procedures. Since a typical production cycle for the main ceramic components was about 5 months, the design was roughly finalized in four stages; (1) the design of the base, (2) the design of the hydrostatic bearings and tables, (3) the hydrostatic bearing pump system, and (4) the electrical system.

It is important to note that Wilbanks is not a machine tool manufacturer. Therefore, the design cycle and methods were not standard. Component drawings were finalized based on available production capacity, and lead time. The machine was not fully designed then released for production. Design changes were occasionally made after parts were in production. This machine represents the work of approximately 25 people. However, no engineers or production staff were officially 100% dedicated to the endgrinder project at Wilbanks.

The production, assembly, and debugging of the machine lasted until March of 1996. Though modifications will likely be made after that time depending upon the initial production results and comments.

6.2.2 - Concept of the WPGM

Section 6.1 discussed the goals, requirements, and constraints which guided the design of the WPGM. Figure 6.3 shows the endgrinder design concept. It incorporates water-hydrostatic bearings, and a ceramic structure which are the principle research issues of the machine. The section 6.3 will describe the design in more detail.

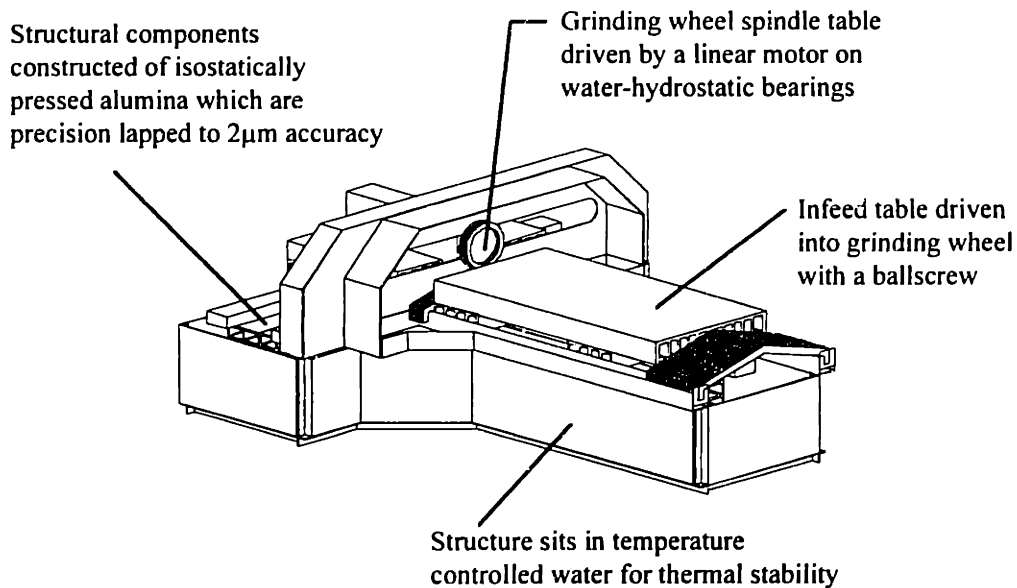


Figure 6.3 Diagram of the WPGM (minus the support equipment).

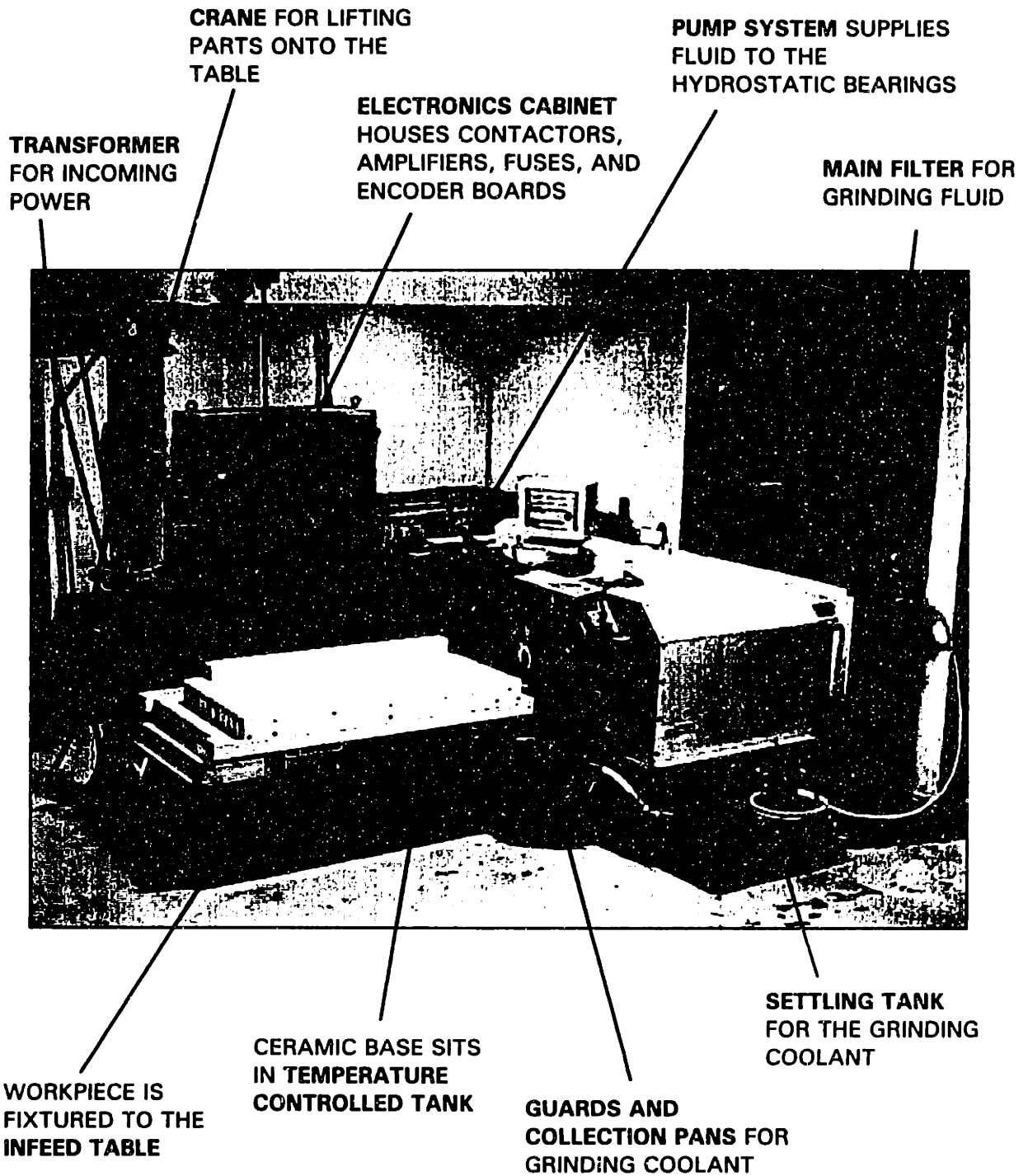


Figure 6.4 Photograph of the WPGM.

The next section describes the design of the systems and structure of the WPGM. The description is organized into the following sections:

- Base structure
- Tables - crossfeed and infeed
- Linear hydrostatic bearing design
- Crossfeed overconstraint system
- Design for thermal stability
- Actuator and electronic systems
- Hydrostatic bearing pump system
- Coolant and cover guard design

6.3 Structural Design Description of the WPGM

6.3.1 - Base structure design

The base structure is constructed of the largest production ceramic beam made by Wilbanks. As mentioned in section 6.1, the shape of the base is a T because of the type of grinding process. In order to increase the stiffness and size capacity of the machine, 4 of these beams were bonded together to create a large prismatic beam. The cross-section of this bonded beam is shown in Figure 6.5. The cross-section size was restricted by the size capacity of the production equipment at Wilbanks.

The moments of inertia of the beam are 2909in^4 about the horizontal axis and 3018in^4 about the vertical axis.

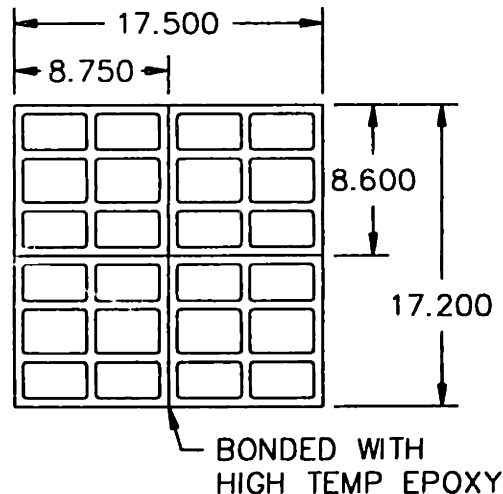


Figure 6.5 Cross-section of the beam used in the base structure of the WPGM base.

The WPGM base consists of 2 beams with this cross-section joined in a T configuration. The length of each of the legs of this T were determined by the desired size capacity of the machine. Figure 6.6 is one of the production drawings of the WPGM base.

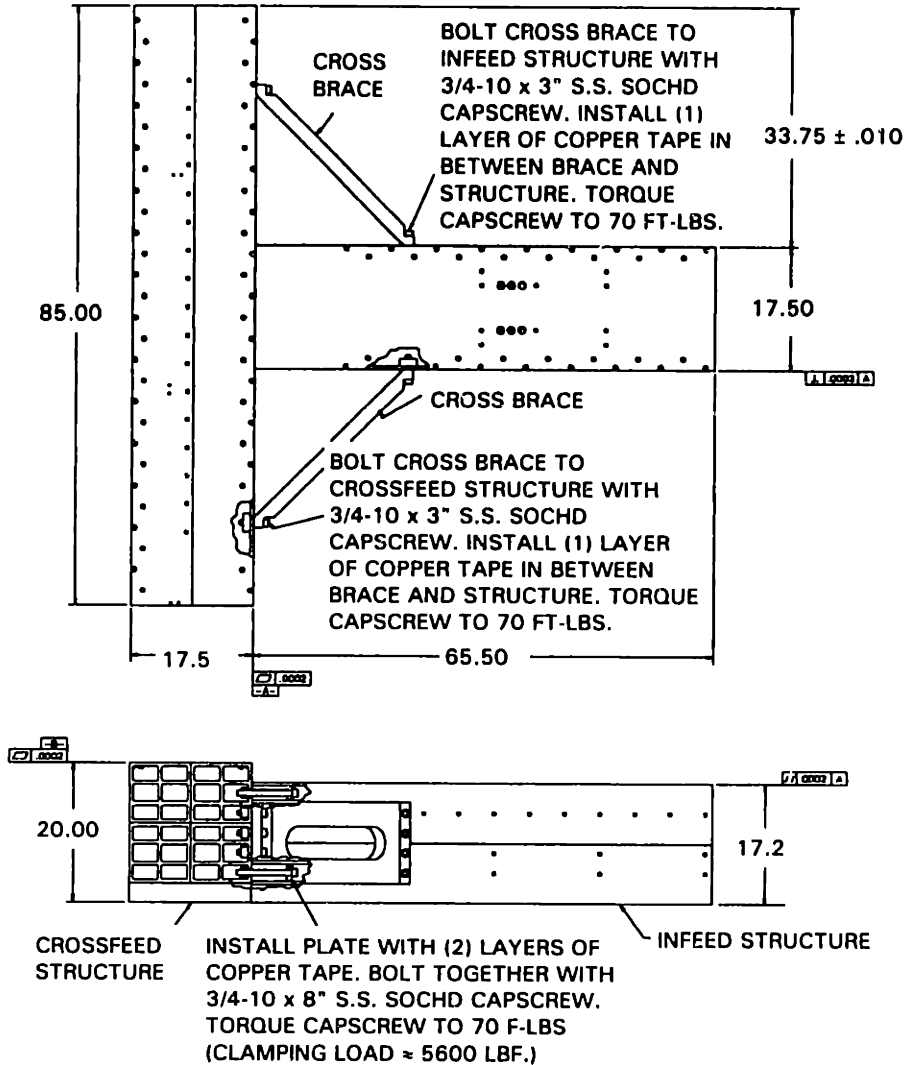


Figure 6.6 Production drawing for the base of the WPGM.

Figure 6.6 indicates how several design issues were addressed. First, the joinery of the infeed and crossfeed structures was accomplished with drawback plates and 3/4" bolts. Drawback plates are bonded into the infeed structure, then used as shear plates for drawback plates. Second, the cross braces were added to increase the stiffness of the structure at joint (particularly the rotational stiffness of the joint).

Figure 6.7 is a photograph of the completed WPGM base. The photograph shows the base without the thermal bath which maintains the constant temperature. The photograph also shows how the precision rails are positioned onto the base. In the background (upper left of photo) is the infeed table which will be discussed in the next section.

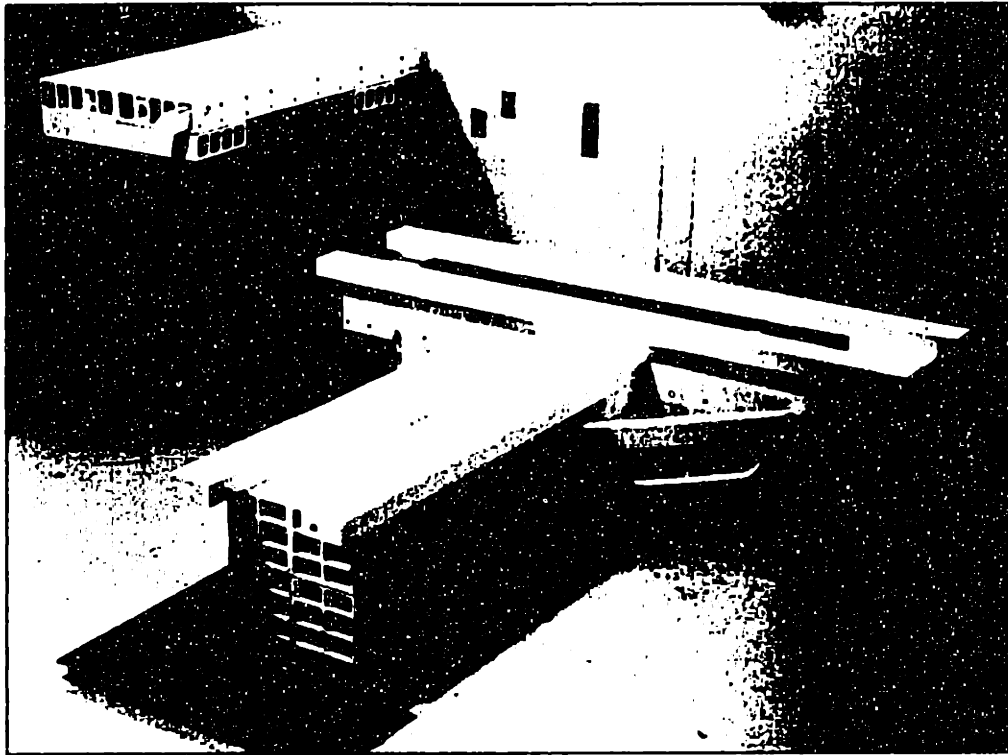


Figure 6.7 Photograph of the WPGM base structure with rails.

6.3.2 - Infeed and Crossfeed Tables

The infeed and crossfeed tables were also designed to be constructed of standard beams. The infeed table was designed as a simple workpiece holding surface which would have hardware for fixturing components. The crossfeed table was designed to hold the spindle. The production drawings for the infeed table are shown in Figure 6.8.

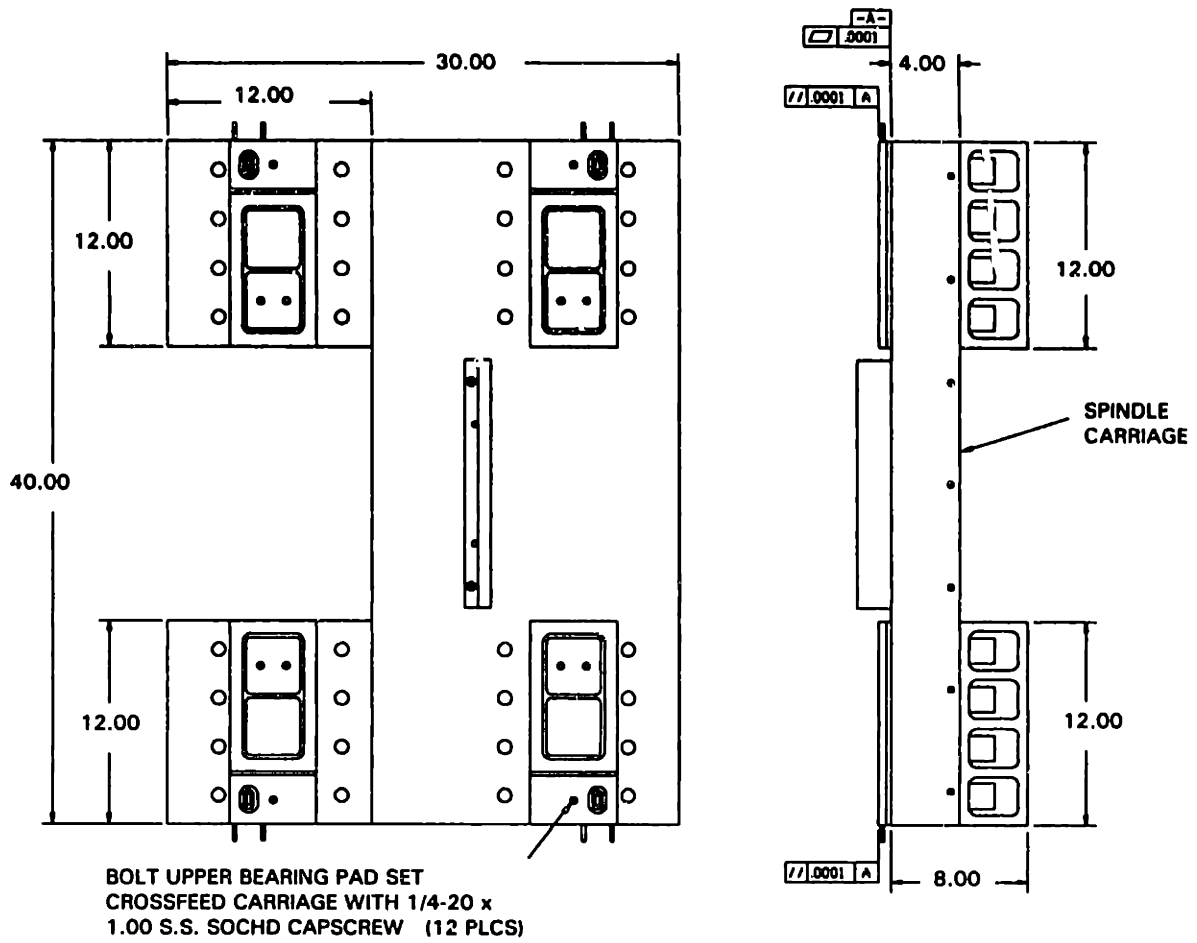


Figure 6.8 Production drawing of the crossfeed table of the WPGM.

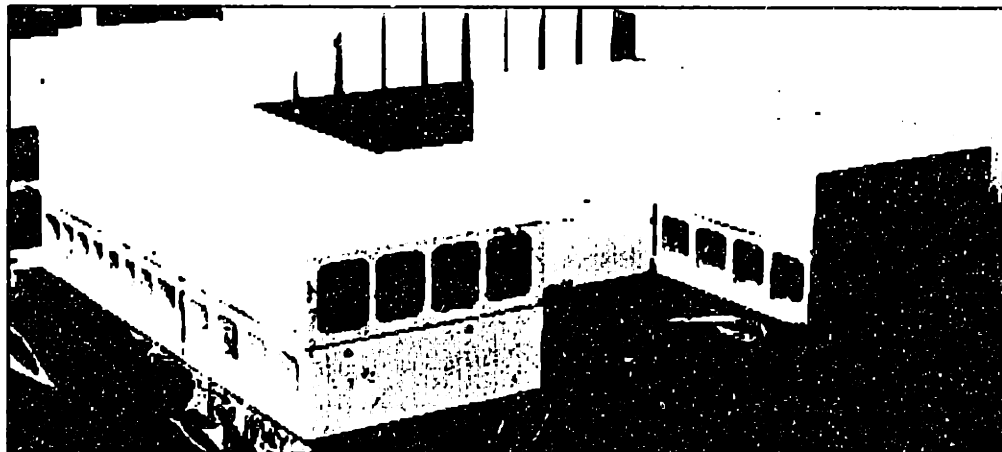


Figure 6.9 Photograph of the crossfeed table of the WPGM.

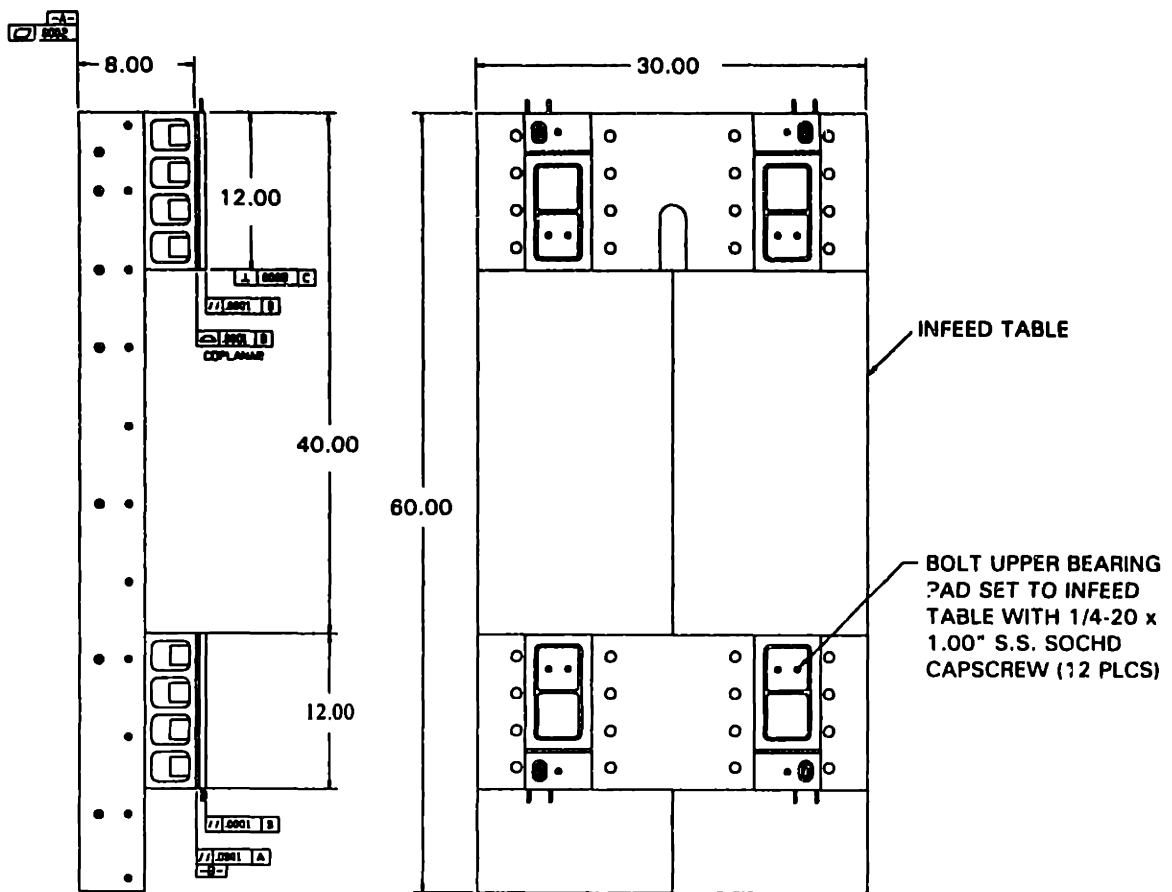


Figure 6.10 Production drawing of the WPGM infeed table.

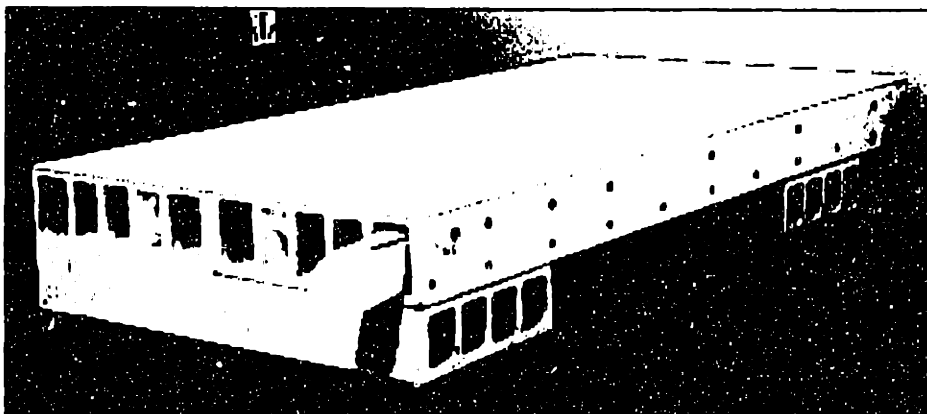


Figure 6.11 Photograph of the WPGM infeed table.

6.3.3 - Precision Rails

The rails have a significant effect on the accuracy of the machine. The straightness of the rails is critical to the straightness of the carriage system travel. The main design issues for the rails are:

- Bolting the rails down to the base structure.
- Tolerances for matching the dimensions of the rails to one another.
- Tolerances for flatness and parallelism of both rails.

There are two distinct design configurations for bolting the rails to the base. Figures 6.12, 6.13, and 6.14 are diagrams of a rail bolted to the structure. This technique makes the assembly process difficult, but results in a rail which is perfect for hydrostatic bearing systems.

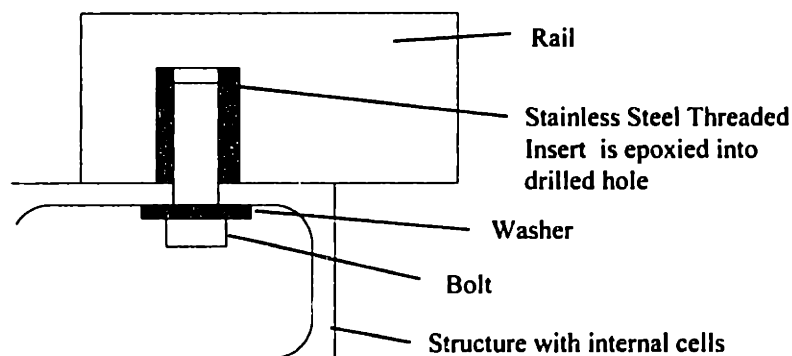


Figure 6.12 Diagram of bolting rail to the structure from inside the structure.

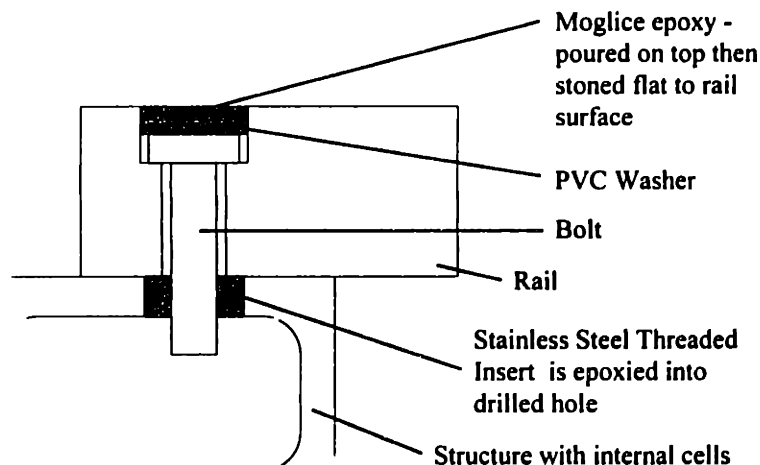


Figure 6.13 Diagram of bolting rail to structure from top of rail.

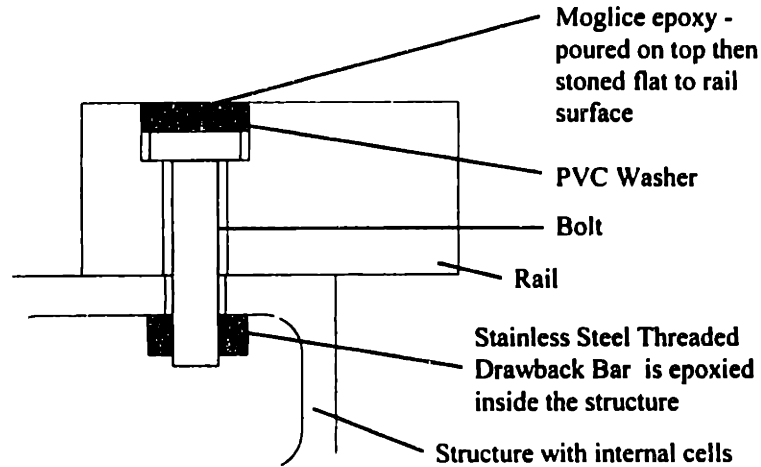


Figure 6.14 Diagram of bolting rail from top into a drawback bar.

There are advantages and disadvantages to each of these configurations. Table 6.6 summarizes the advantages and disadvantages of each configuration. In general, Figure 6.14 was the most successful configuration and the most suitable for production applications. Future machine tool builders considering ceramic bases and rails will certainly confront this issue on each design. Most likely, they will find that there is little advantage to the configuration in Figure 6.13 except for the reduced expense. Figure 6.12 provides a perfect bearing surface but is difficult to assemble on larger machines. In this configuration, the bolts have to be torqued from the inside which requires an air ratchet (which is not as accurate in setting the torque on the rail), special fixtures, and is time consuming.

Table 6.6 Analysis of the three proposed techniques for bolting the rails to the base.

| | Figure 6.12 | Figure 6.13 | Figure 6.14 |
|---|--|---|---|
| Assembly Issues | Difficult to torque the bolts into the rails. | Easy to install bolts. However, top surface must be stoned flat. | Easy to install bolts. But top surface must be stoned flat. |
| Potential Problems | Inserts are held in with epoxy which is limited by shear strength, could pull out of rail. | Inserts are held in with epoxy which is limited by shear strength, could crack base. | |
| Performance of Rail for Hydrostatic Bearings | Ideal. All surfaces are lapped ceramic. | Moglice covers could cause problems, but have performed well in current applications. | Moglice covers could cause problems, but have performed well in current applications. |

The rails for the WPGM were designed for the configuration shown in Figure 6.14. They have counter bored holes which accommodate the bolt head (3/8"-16) and have enough depth to allow for the PVC washer and the cover of Moglice. The PVC washer was made to the exact diameter of the counterbore (and about 0.200" in depth), then pressed into the rail. It is primarily installed so that if the rail needs to be disassembled, the epoxy can be easily removed. The Moglice layer (approximately 0.100" in depth) is poured on top of the PVC washer then stoned flat to within 0.0001". Figures 6.15 and 6.16 are photographs of the rails for the WPGM.

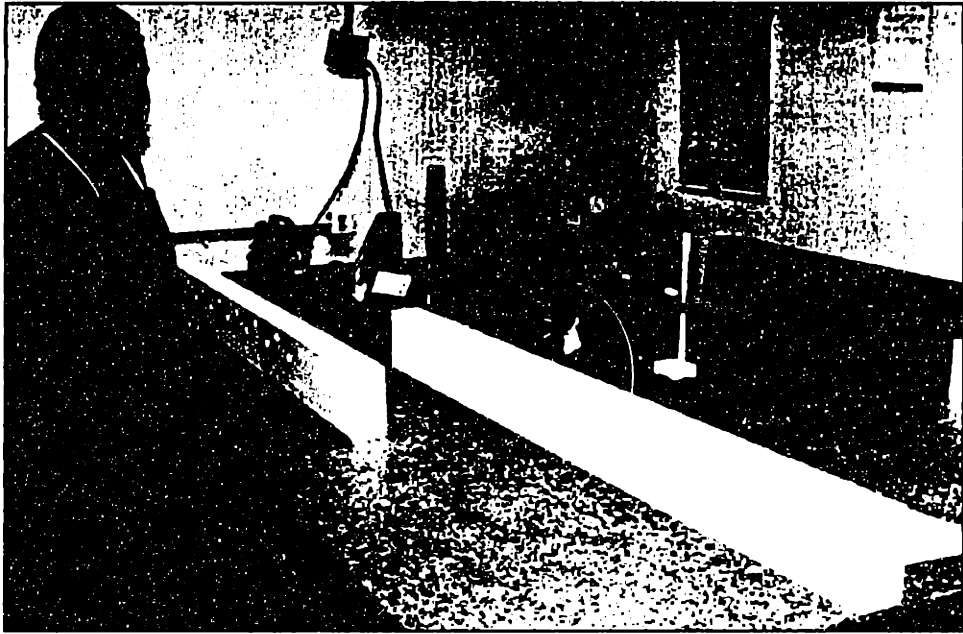
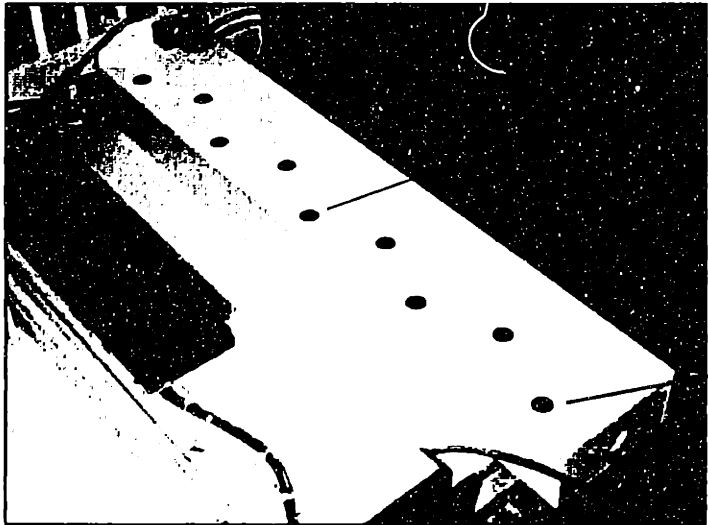


Figure 6.15 Rails for the WPGM are lapped and inspected for flatness and parallelism. The rails are matched to one another within 0.000080".



Staggered bolt pattern for tilt stiffness.

Bolts covered with PVC plug and epoxy. Epoxy is stoned flat to rail surface.

Figure 6.16 Rail installed on the WPGM and bolt holes covered with epoxy.

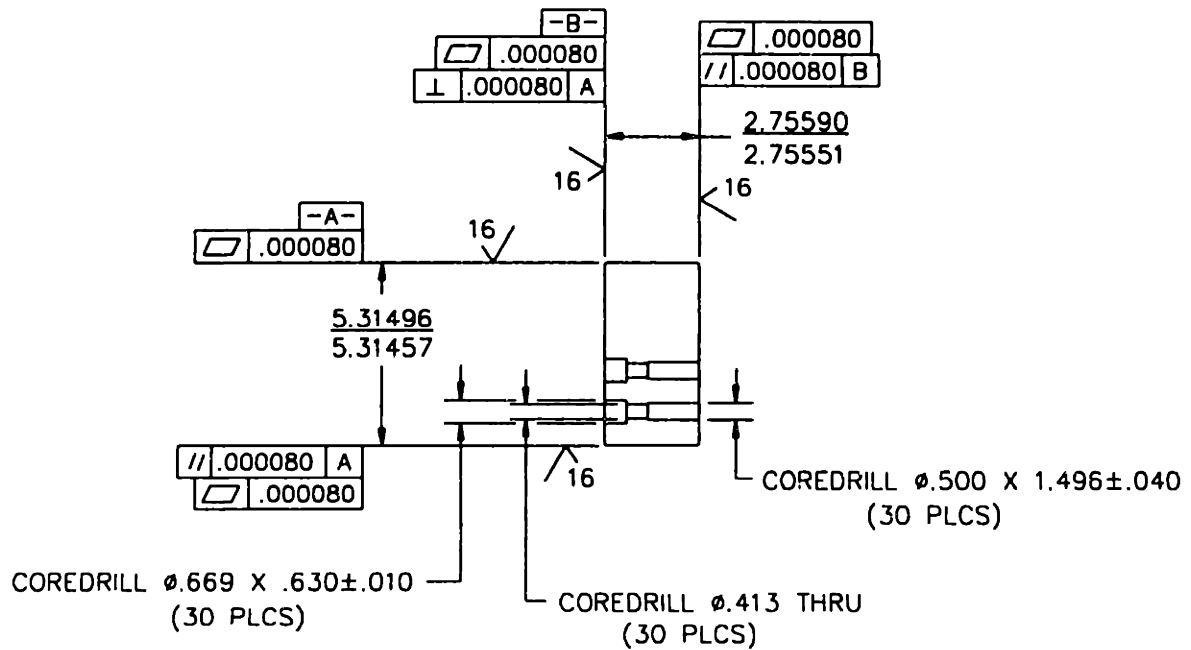


Figure 6.17 End view (from production drawing) of the rails for the WPGM. The drawing shows the tolerances on a typical rail for hydrostatic bearings.

6.4 - Hydrostatic Linear Bearing System Design

The bearings for the WPGM were designed with spreadsheet analysis tools and the knowledge gained from the prototypes described in section 3.6. The configuration was similar to the ceramic machine tool axis prototype built at M.I.T. except that the horizontal bearings use both rails rather than one.

6.4.1 - Bearing Configuration

Figure 6.17 shows an end view diagram of the configuration for the hydrostatic bearings. The configuration utilizes two significant design principles; (1) symmetrical loading on the base from the bearing pressure, (2) ceramic-on-ceramic contact between each pair of hydrostatic bearings, and (3) bolted connections rather than bonded to allow for possible disassembly. The first principle guarantees that the base will not be distorted or twisted by eccentric loading. The second principle guarantees that the gap will be held consistent. The prototype axis used epoxy to hold the bearings in place which is successful as long as the epoxy is thermally stable, stiff, and used in a thin layer. The third principle was significant for maintenance reasons. While the prototype could afford a design which would be impossible to disassemble without damage, the WPGM had to allow for possible maintenance. The upper and horizontal bearings are bolted directly to the table. The lower bearings are bolted to the table through the spacer block.

The accuracy of the spacer blocks is a critical part of the hydrostatic bearing performance. The spacer blocks are match lapped (thus all 4 spacer blocks have the same height) within 0.000060". Since the nominal bearing gap is 0.0015", the variation in the gap is 4%. The gap was adjusted by inserting a stainless steel shim material in between the table and the spacer block.

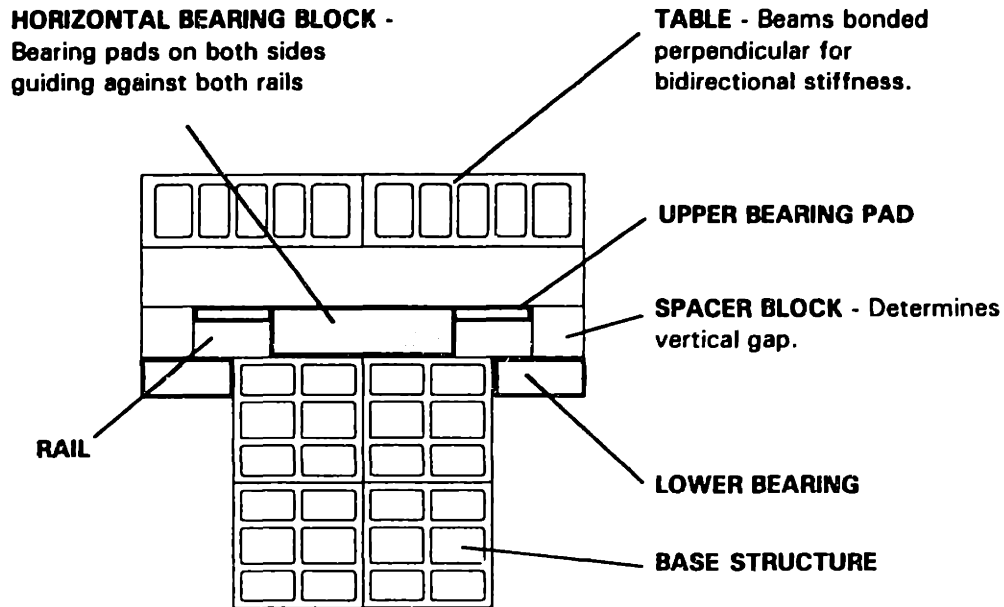


Figure 6.17 Diagram of the configuration for the hydrostatic bearings on both axes of the WPGM. The gray areas are the bearing blocks.

6.4.2 - Bearing Pad Design

The bearing pad design utilized the spreadsheet design tool developed by the Precision Engineering Research Group at M.I.T.² Once the overall geometry of the bearings is decided, the bearing pad configuration can be iteratively designed using spreadsheets as shown in Tables 6.6 and 6.7. The spreadsheet input is the bearing pad geometry and the output is the system performance.

² Nathan Kane of the Precision Engineering Research Group at M.I.T. developed the most recent set of spreadsheets for water-hydrostatic bearings. The spreadsheets were used in the design of this system.

Table 6.6 Input to the spreadsheet for the WPGM hydrostatic bearings.

| Bearing Gap, Supply Pressure, Initial Load | | | | | |
|---|--------|--------------------------|-----------|------------------|----------|
| Name | Symbol | Units | (SI) | (English) | |
| Fluid dynamic viscosity | mu | Ns/m ² | 0.001 | | |
| Fluid density | rho | kg/m ³ | 1000 | | |
| Nominal gap | hn | um, 0.001 in | 26.4 | 1.04 | |
| Supply Pressure | Ps | Pa, psi | 565,370 | 82 | |
| Initial load on the pad pair | Fi | N, lb | 289 | 65 | |
| Max. % reduction of hn | pred | (%) | 20% | 20% | |
| Dimensions | | Upper, Lower Pads | | Side Pads | |
| | | Upper Pad | Lower Pad | Right Pad | Left Pad |
| Name | Symbol | (mm) | (mm) | (mm) | (mm) |
| Chamfer width | | 0.76 | 0.76 | 0.76 | 0.76 |
| x pad length | xpad | 304.80 | 304.80 | 304.80 | 304.80 |
| y pad width | ypad | 129.54 | 64.26 | 63.50 | 63.50 |
| x leakage land length 1 | xll1 | 16.13 | 15.24 | 14.48 | 14.48 |
| x leakage land length 2 | xll2 | 16.89 | 16.00 | 15.24 | 15.24 |
| y leakage land length 1 | yll1 | 14.61 | 18.39 | 18.42 | 18.42 |
| y leakage land length 2 | yll2 | 86.72 | 17.66 | 16.87 | 16.87 |
| supply groove width | sg | 5.51 | 5.51 | 5.51 | 5.51 |
| x restrictor land length 1 | xrl1 | 5.08 | 5.08 | 5.08 | 5.08 |
| x restrictor land length 2 | xrl2 | 5.08 | 5.08 | 5.08 | 5.08 |
| y restrictor land length 1 | yrl1 | 5.08 | 5.08 | 5.08 | 5.08 |
| y restrictor land length 2 | yrl2 | 5.08 | 5.08 | 5.08 | 5.08 |
| x collector groove length | xcg | 18.97 | 30.91 | 22.78 | 22.78 |
| y collector groove width | ycg | 5.51 | 5.51 | 5.51 | 5.51 |
| drainage groove width | dg | 6.10 | 6.10 | 5.51 | 5.51 |
| x bearing land length 1 | xbll1 | 19.05 | 19.43 | 17.55 | 17.55 |
| x bearing land length 2 | xbll2 | 18.29 | 18.67 | 16.79 | 16.79 |
| y bearing land length 1 | ybl1 | 18.29 | 19.81 | 19.05 | 19.05 |
| y bearing land length 2 | ybl2 | 18.29 | 19.81 | 18.29 | 18.29 |
| radius of pocket | rpk | 6.35 | 6.35 | 6.35 | 6.35 |
| x pocket length | xpk | 186.66 | 175.74 | 189.74 | 189.74 |
| y pocket width | ypk | 91.44 | 23.12 | 24.64 | 24.64 |

As the results in section 7.5 demonstrate, the agreement between the spreadsheets and the actual performance is usually within 10%. For most design purposes, agreement within 10% for stiffness and flow prediction is sufficient. It would be difficult, given the tolerances and measurement uncertainty to develop a design tool which would more accurate than the current models.

Table 6.7 Output of the spreadsheets. This is the predicted performance of the linear bearing system.

| Performance | Upper, Lower bearings | | Side Bearings | |
|---|-----------------------|------------|---------------|------------|
| | Delta | (SI) | Delta | (SI) |
| Maximum Forces | Delta (um) | (N) | Delta (um) | (N) |
| Fmax down | 5.28 | 7741 | 5.28 | 2423 |
| Fmax up | -5.28 | -734 | -5.28 | -2423 |
| Fmax ext d = (Fmaxdown - Fi) | 5.28 | 7452 | 5.28 | 2134 |
| Fmax ext u = (Fmaxup - Fi) | -5.28 | -1023 | -5.28 | -2712 |
| Stiffness | Delta (um) | (N/um) | Delta (um) | (N/um) |
| Stiffness (F=Fmaxdown) | 5.28 | 809 | 5.28 | 395 |
| Stiffness (F=Fi) | -3.66 | 681 | 0.59 | 491 |
| Stiffness (F=0) | -4.09 | 654 | 0.00 | 492 |
| Stiffness (F=Fmaxup) | -5.28 | 578 | -5.2832 | 395 |
| Flow | Delta (um) | (lit./min) | Delta (um) | (lit./min) |
| Total Flow (F=Fmaxdown) | 5.28 | 1.87 | 5.28 | 1.77 |
| Total Flow (F=Fi) | -3.66 | 1.72 | 0.59 | 1.82 |
| Total Flow (F=0) | -4.09 | 1.71 | 0.00 | 1.82 |
| Total Flow (F=Fmaxup) | -5.28 | 1.67 | -5.28 | 1.77 |
| Pump Power | Delta (um) | (W) | Delta (um) | (W) |
| Pump Power (F=Fmaxdown) | 5.28 | 17.6 | 5.28 | 16.7 |
| Pump Power (F=Fi) | -3.66 | 16.3 | 0.59 | 17.1 |
| Pump Power (F=0) | -4.09 | 16.1 | 0.00 | 17.1 |
| Pump Power (F=Fmaxup) | -5.28 | 15.7 | -5.28 | 16.7 |
| Max. Allowable Carriage Velocity | | (m/min.) | | (m/min.) |
| (=1/2 minimum fluid velocity) | | 9.7 | | 10.8 |

The overall shape of the restrictors and bearing pockets is similar to the prototype. The restrictors are oval in shape and the bearing pockets have damping lands in the middle to increase the squeeze film damping. Figures 6.18 and 6.19 are photographs of the upper and horizontal bearings. The bearings, similar to the other components of the WPGM, were constructed of 96% aluminum oxide (isostatically pressed). The restrictor and bearing pad features were milled into the pads before firing ("green machined"). Then, the faces were ground and lapped parallel and matched in thickness.

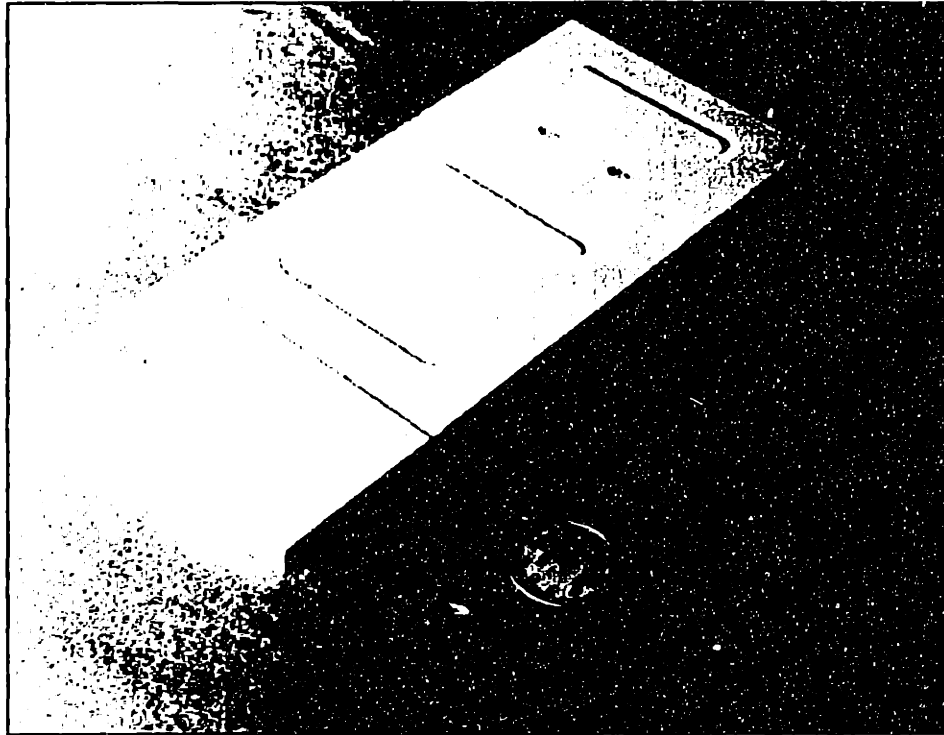


Figure 6.18 Photograph of an upper hydrostatic bearing pad of the WPGM.

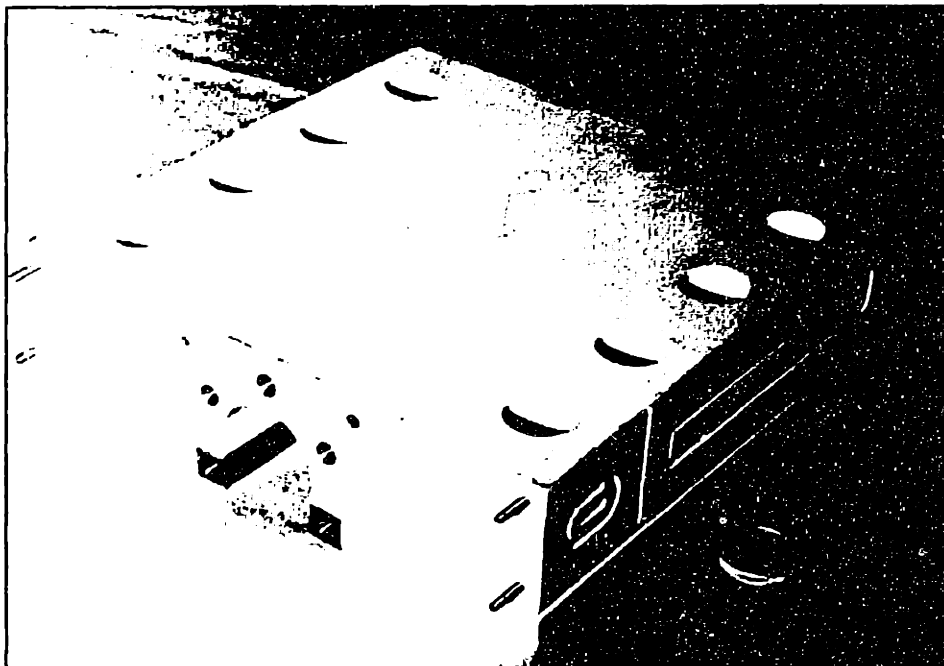


Figure 6.19 Photograph of a horizontal bearing pad for the WPGM.

6.5 - Hydrostatic Bearing Pump System Design

The pump system was designed based upon the principles developed in chapter 4. The main goals of the pump system are to supply pressurized water to the bearings at about 200psi. and filtered to 1.0 μ m with minimal pressure fluctuations.

The temperature control aspect of the fluid was not addressed by the hydrostatic bearing system. Using a temperature controller after a high pressure pump complicates the design and increases the cost dramatically. Instead, a separate temperature controller was implemented in the tank for the structure of the machine. The critical issue for the temperature control of the machine is that the base remains at a constant temperature. Therefore, the fluid in the tank can be controlled separately and recirculated with a smaller pump.

Figure 6.20 is a schematic of the pressure supply system which shows the major components and their relative position.

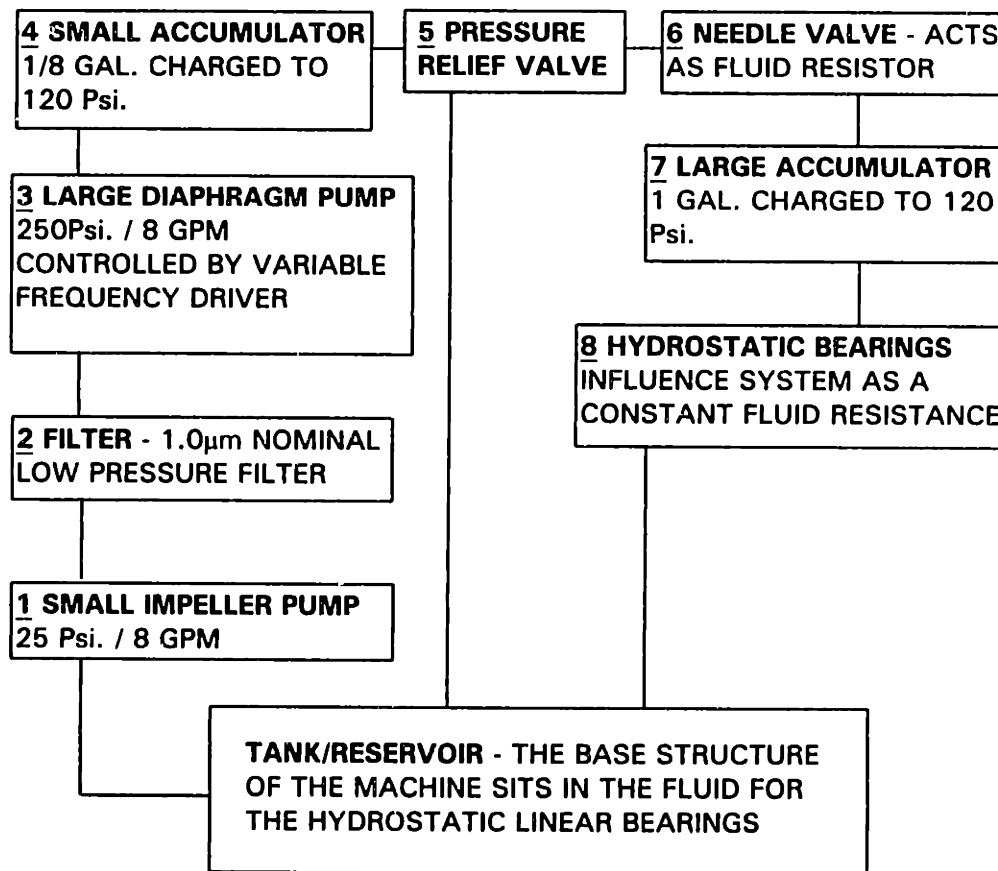


Figure 6.20 Schematic of the hydrostatic bearing system fluid supply system (the underlined numbers will be referenced in Figures 6.21 and 6.22).

As Figures 6.21 and 6.22 demonstrate, the placement of these components is mainly governed by ergonomics. In particular, an acoustic box was constructed to shield the operators from the noise of the large pump. The placement of the other components was determined by the noise reduction simulations and the available space.

7 LARGE ACCUMULATOR

2 FILTER

1 SMALL IMPELLER PUMP

ACCOUSTIC BOX FOR
LARGE PUMP



Figure 6.21 Photograph of hydrostatic bearing pump system with the acoustic box closed.

ACCOUSTIC FOAM

3 LARGE DIAPHRAGM
PUMP

6 NEEDLE VALVE

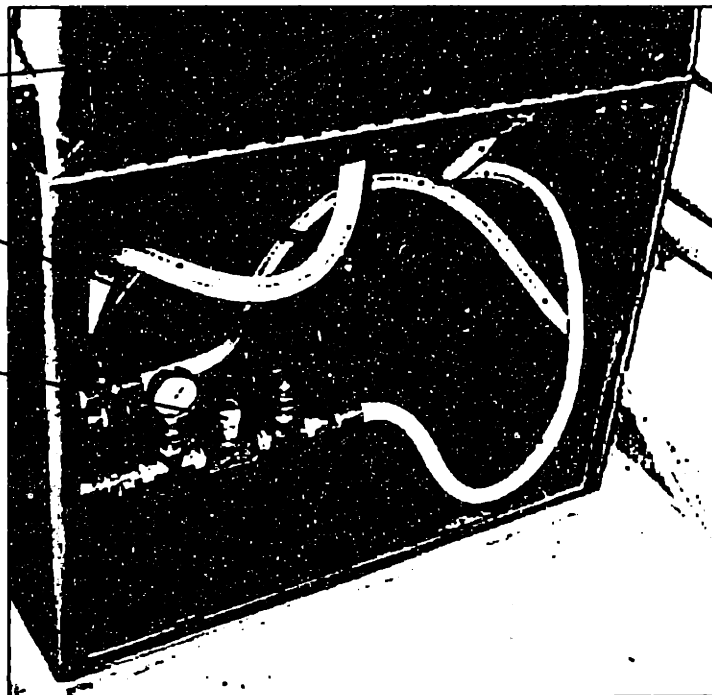


Figure 6.22 Photograph of large pump inside the acoustic shielding box.

6.6 - Crossfeed Overtravel Stops

Since the base of the machine is ceramic, it is critical not to apply tensile loads. One particular case where this is critical is the stopping system for possible overtravel of the crossfeed table. For example, if power to the crossfeed table is suddenly halted, the table needs to be brought to rest without damaging the base or the table. In order to prevent possible problems, a system was designed involving rods through the structure and shock absorbers mounted in the crossfeed table. Figures 6.23 and 6.24 are a schematic and photograph (respectively) of this system (without the bearings). It is not possible to force tension on the base structure even when large dynamic loads are applied.

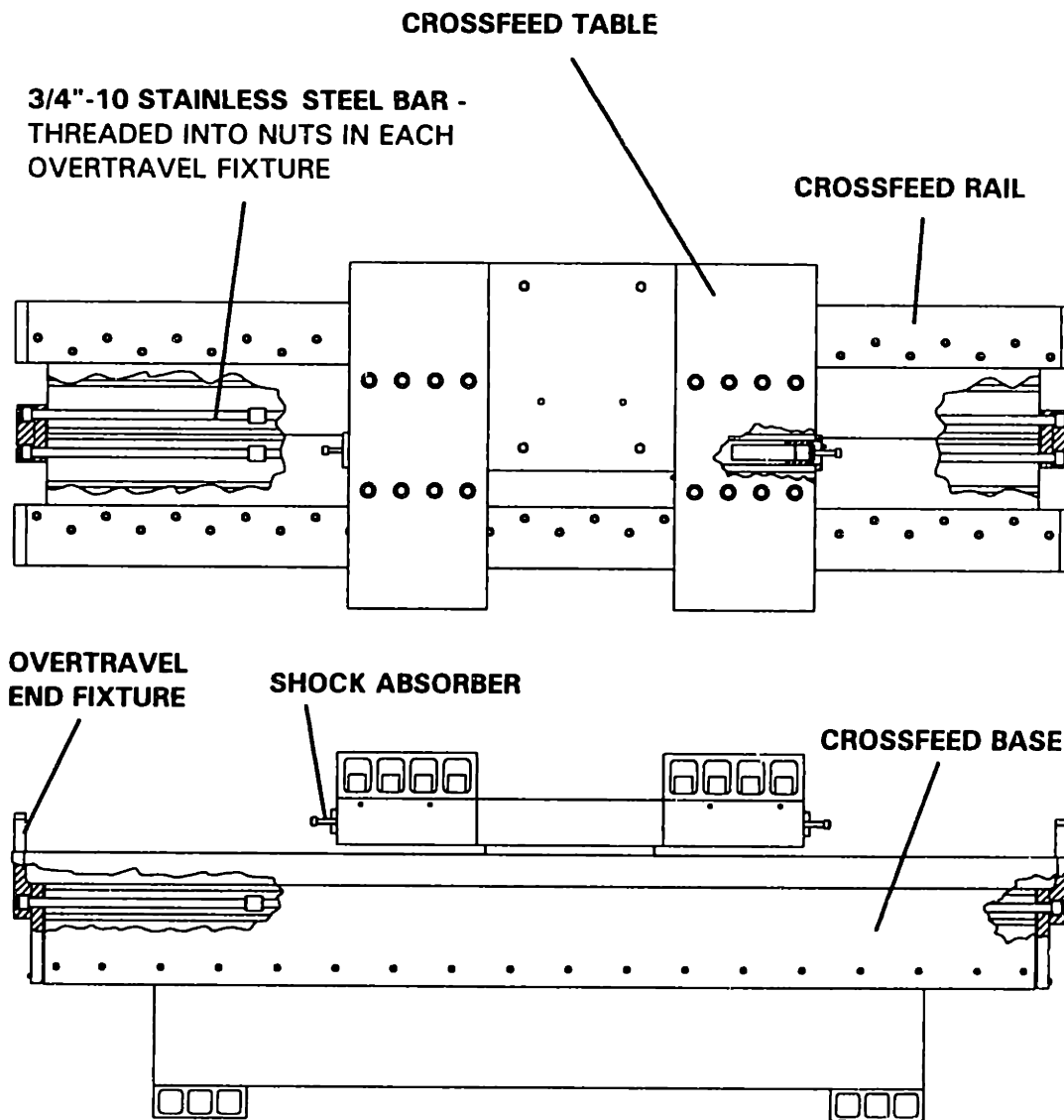


Figure 6.23 Schematic of the crossfeed overtravel system.

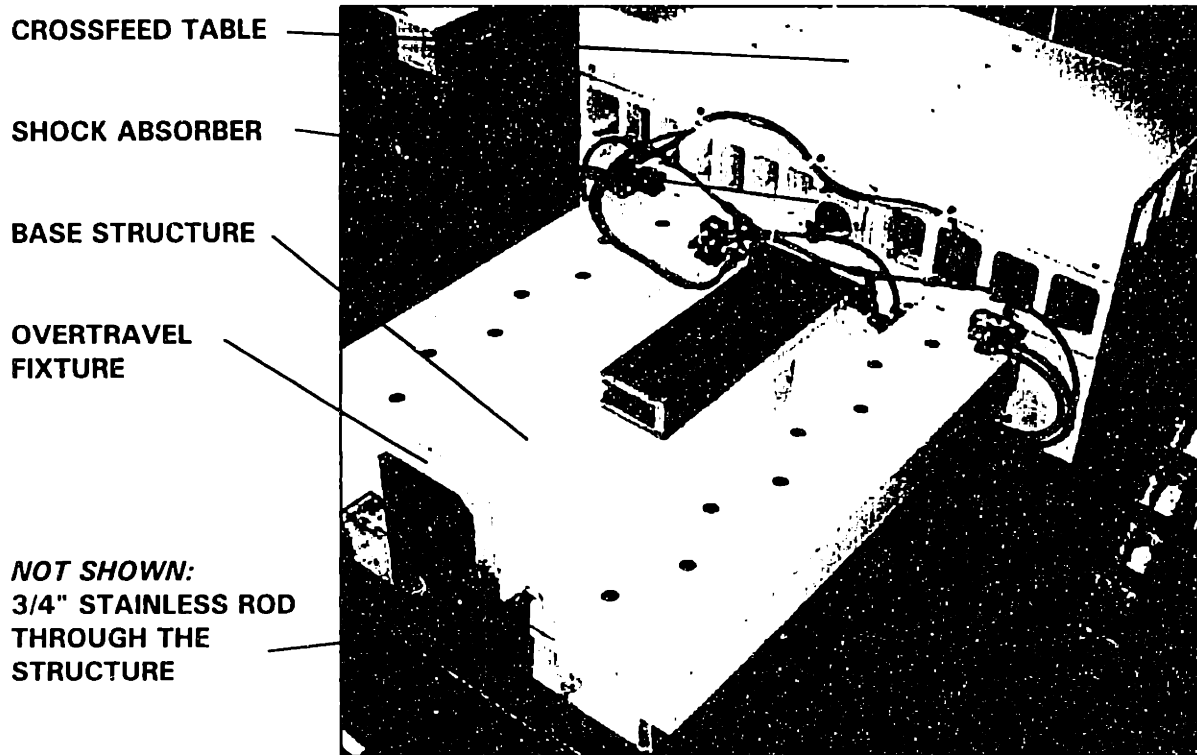


Figure 6.24 Photograph of the main components in the crossfeed overtravel stop system.

When the table travels to the end, the shock absorber hits the overtravel fixture. The energy of the collision is absorbed by; (1) the shock absorber, (2) the elastic energy of the overtravel fixture, and (3) elastic stretching of the stainless rods in the structure. The table, which weighs 1000lbs., could hit the overstop at 2 ft./sec. without causing damage. Since the table will be run at less than 1 ft./sec. in production, the system has a sufficient safety factor.

6.7 - Temperature Control System

Thermal errors are often as significant as geometric errors in machine tools. A constant temperature system for the structure of the machine was designed to offset the heat sources. In the WPGM, heat is introduced by the motors, the bearings, and surrounding environment. Although the machine sits in a temperature controlled room (which maintains temperature constant to within $\pm 3^\circ$ F.), a thermal bath was designed to further control this temperature within $\pm 0.5^\circ$ F. The bath uses a recirculating pump and chiller to pull the water from the tank and remove added heat. Figure 6.25 shows the machine base in the tank. The chiller can remove 2100W of heat. The hydrostatic bearings and linear motor could add as much as 2500W, though not all will be transferred to the base. Through the first 3 months in operation the chiller operated at only 50% capacity. Therefore, the chiller has sufficient heat removing capacity.

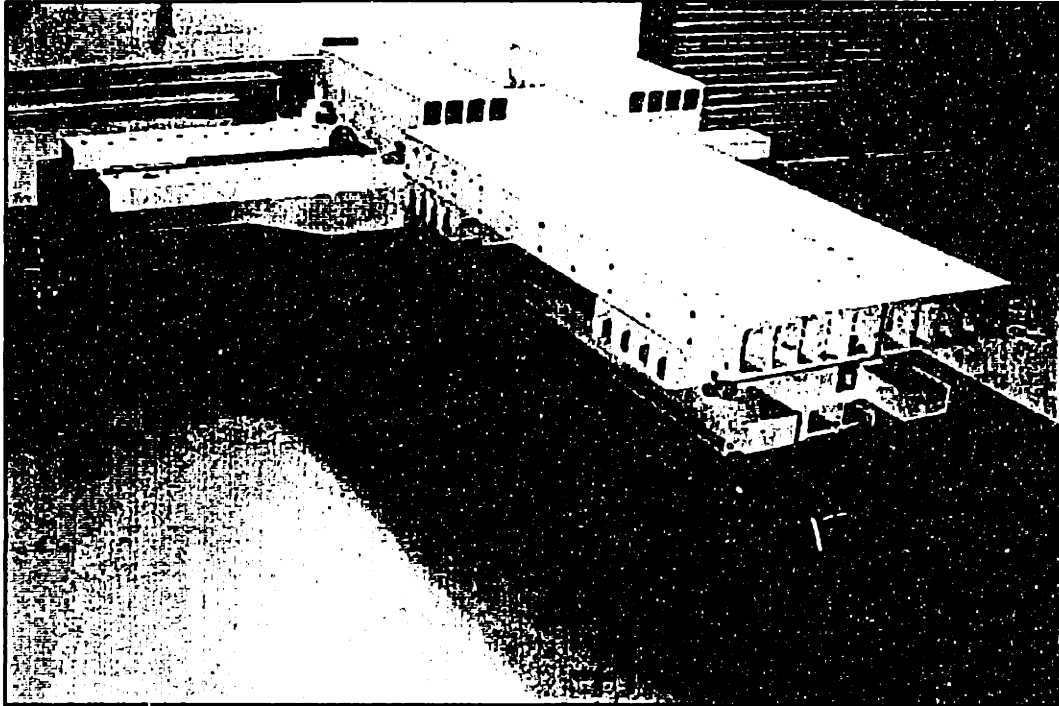


Figure 6.25 Photograph of the base and tables of the WPGM sitting in the temperature controlled tank. This tank serves as both a reservoir for the hydrostatic bearing fluid and a constant temperature "bath" for the machine structure. The water is pulled from the tank on the right side and dispensed within the tank at the three outermost points of the T.

6.8 - Drive Systems and Electronics

There are two linear actuators on the WPGM. A linear motor drives the crossfeed table and a ballscrew drives the infeed motion. The actuators were chosen to fulfill the unique requirements of each axis.

6.8.1 - Linear Motor for the Crossfeed Table

The crossfeed table is driven by a linear motor². The motor has a force capacity of 450lbs peak. The motor consists of a magnet track (attached to the base), and a moving coil (attached to the underside of the crossfeed table). The motor has 3 phases which are sinusoidally commutated. Each phase uses about 3.0amps continuously, and 10amps peak. Figure 6.26 shows the main components of the linear motor system.

² The linear motor was a LM-410, produced by Trilogy Systems. Tel: (713) 338-2739.

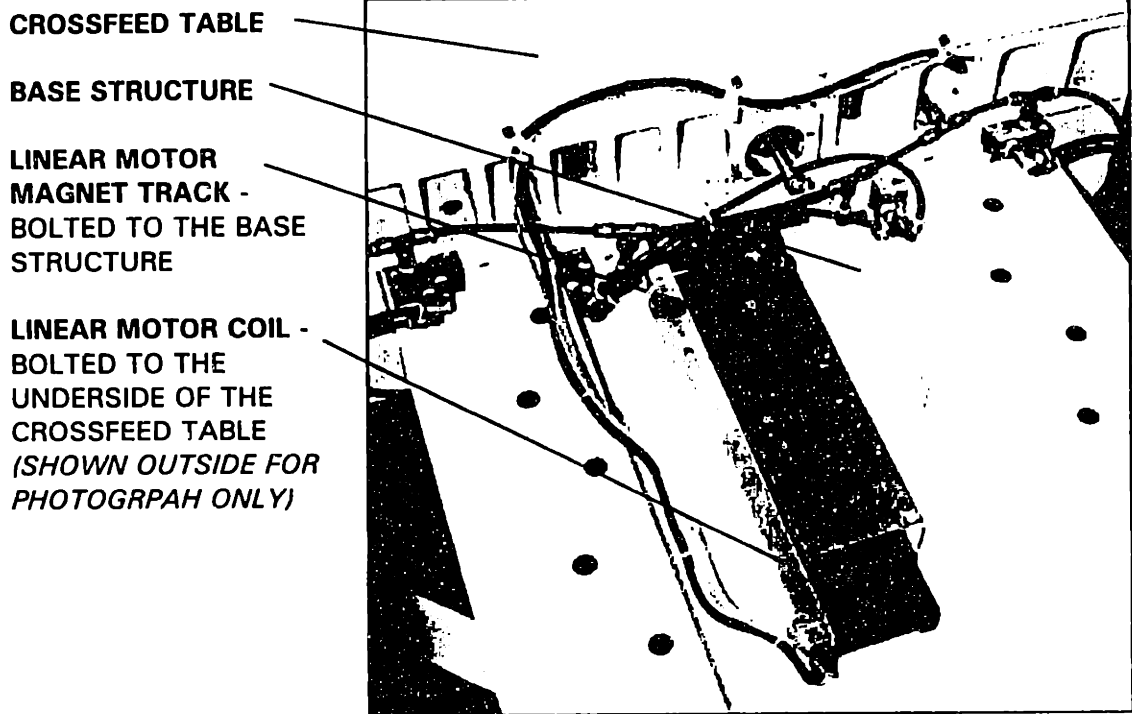


Figure 6.26 Photograph of the linear motor components in place on the WPGM. The coil consists of copper wires. The magnet track is a row of permanent magnets on top and bottom.

6.8.2 - Servomotor/Ballscrew Infeed Actuator³

The infeed actuator must deliver high axial stiffness and fine motion resolution. Typical infeed motions for the WPGM will be 0.001" and the stiffness goal is 1.0lbs/ μ in. A ballscrew actuator with 5 threads per inch was chosen since the infeed velocity can be less than 0.010 in./sec. The diameter of the ballscrew is 1.378" which was as large as possible for the configuration. The ballscrew nut is bolted to the front horizontal bearing block on the infeed table. The ballscrew is attached to the base of the machine. In order to maintain high axial stiffness, the ballscrew is grounded to the base with 2 tapered high precision roller bearings. Figure 6.27 is a photograph of the components of the infeed actuator excluding the hydrostatic bearing block. Figure 6.28 is a schematic of the complete system

³ The servomotor, amplifier, and power supply were produced by Kollmorgen. The ballscrew was produced by Thomson Saginaw (Saginaw, MI): Tel: (517) 776-4123.

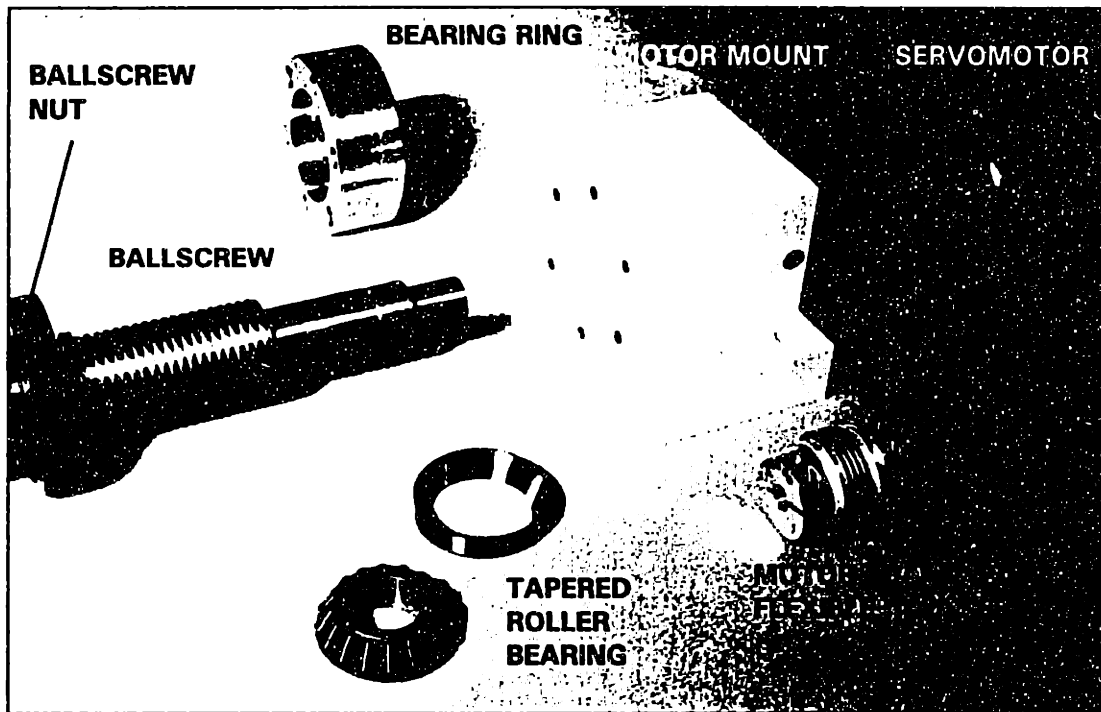


Figure 6.27 Infeed actuator components before assembly. The full assembly includes another set of tapered roller bearings and several socket head cap screws.

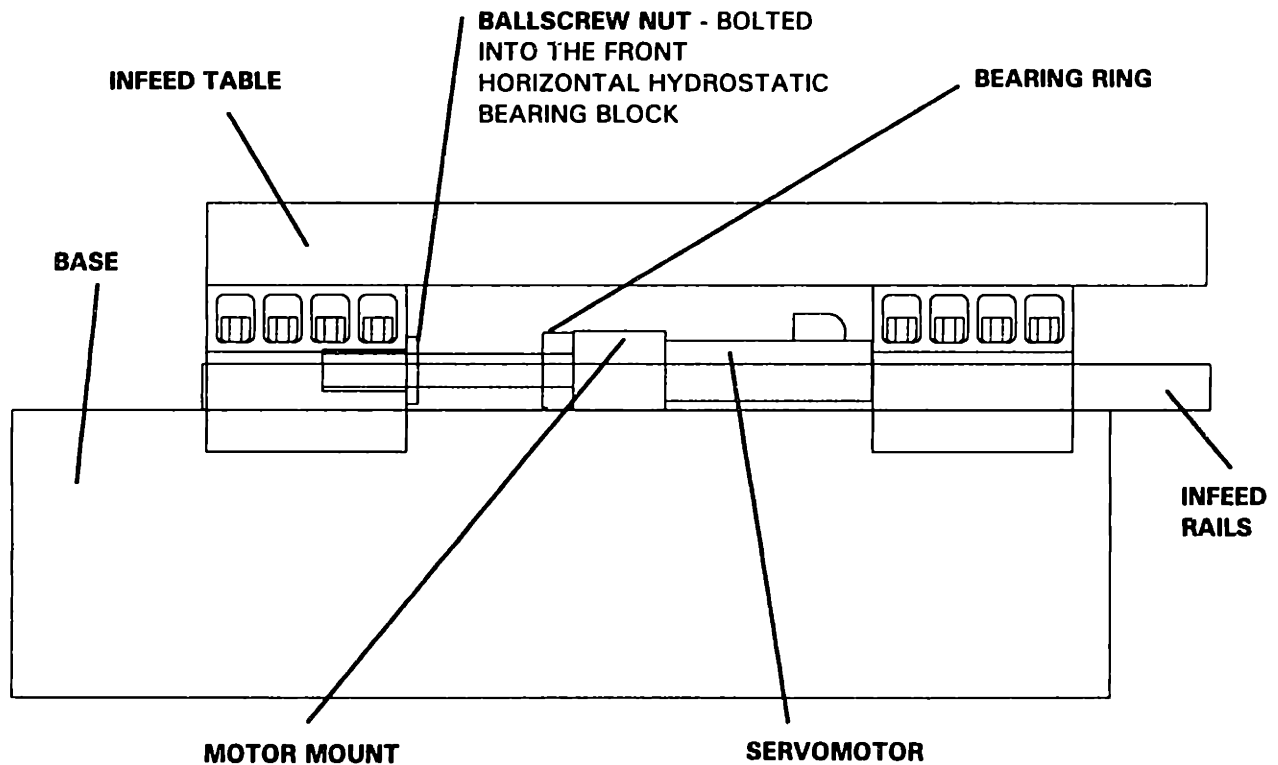


Figure 6.28 Schematic of the infeed actuator assembly.

6.8.3 - WPGM Electronics

The electronics and power supplies are maintained in an electrical cabinet near the WPGM. The main controller for the machine is a PMAC-Lite³ controller card which is inserted into a personal computer. The card can control as many as 4 axes (however any motor commutated by PMAC requires 2 axes), plus optical switches and analog outputs and inputs. For the WPGM, the PMAC is used to commutate the linear motor and control the ballscrew (which is commutated by a separate controller).

The electronics cabinet (shown in Figure 6.29) contains the contactors, fuses, transformers, power supplies, and encoder cards for both axes. The power is brought from the main supply of the plant and transformed down to 240V. The contactors are used as off/on switches for components of the machine such as the hydrostatic bearing pump, the coolant pump, the power supplies for the motors, and the spindle. The fuses prevent large surges of current to any of the components. The power supplies and amplifiers are responsible for sending the current to each phase of both motors.

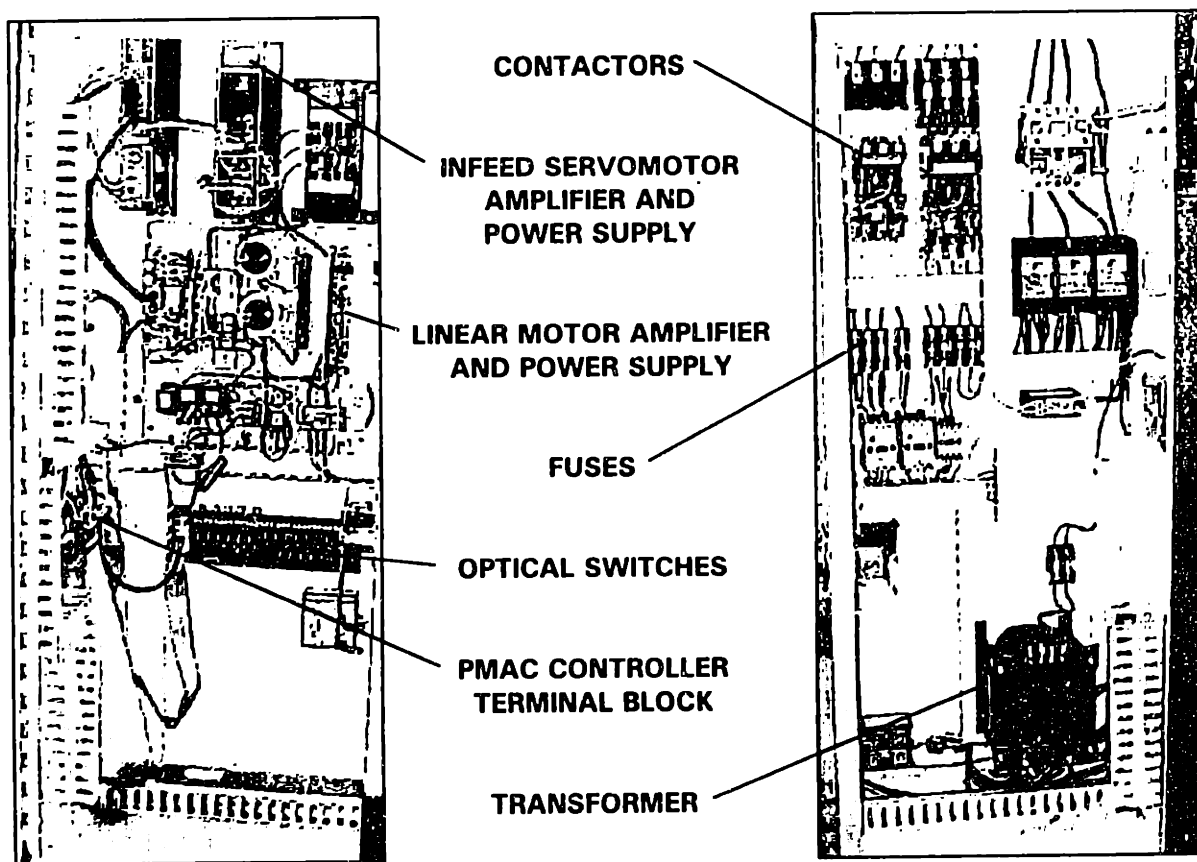


Figure 6.29 Photographs of the left and right sides of the electrical cabinet.

³ PMAC is Produced by Delta Tau Data Systems. Northridge, CA. Tel: (818) 998-2095

6.9 Coolant Supply and Cover Guards

The coolant supply system for the WPGM has three critical specifications; (1) the fluid velocity leaving the nozzle at the grinding wheel must be faster than the surface speed of the wheel, (2) the coolant must be filtered (to less than $1.0\mu\text{m}$ nominal) so that ceramic particles are not pumped back into the grinding process, and (3) the coolant must settle long enough to return to the ambient temperature. The system, shown in Figure 6.30, is significantly different than coolant systems on most ceramic grinding machines.

The WPGM system uses 2 tanks and 2 pumps; one as a settling tank and one as a storage tank. Conventional grinding machines at Wilbanks use one settling tank which accumulates ceramic particles on the bottom. Using this set-up, the particles are usually pumped back into the grinding area along with the coolant. The only way to filter particles with a one tank system is to use a filter after the pump which reduces the velocity of the fluid.

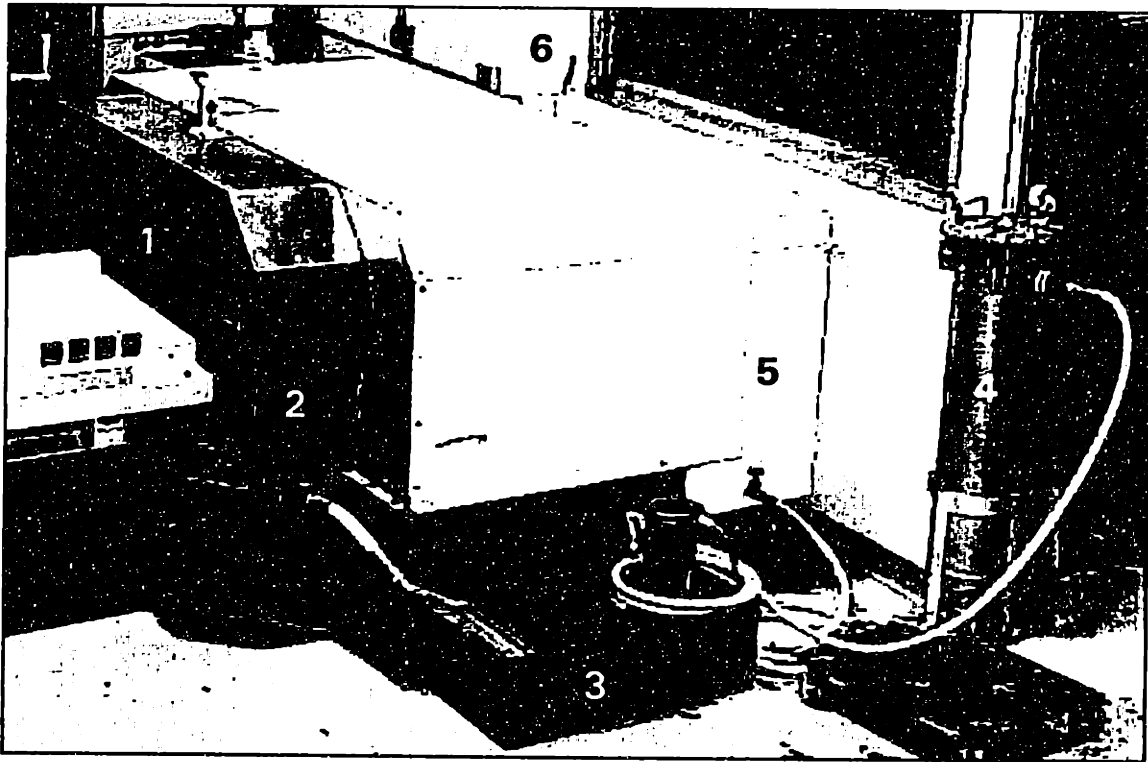


Figure 6.30 Photograph of the coolant system for the WPGM. The numbers indicate important components of the system.

Referring to the numbers in Figure 6.30. The fluid is pumped into the grinding area (point # 1) through a fan nozzle which increases the velocity of the fluid. The fluid collects in the collection pans (point # 2) and drains into the settling tank (point # 3). This tank, which has baffles to increase settling, includes a pump to send the coolant through the filter (point # 4). Filtering the coolant is therefore a two step process; (1) settling to remove the larger ($> 0.020''$) particles, and (2) filtering with a $0.5\mu\text{m}$ nominal bag type

filter. This configuration has a maintenance advantage as well, in that the small tank and bag filter are easy to change, whereas larger tanks are time consuming to drain and clean. The clean fluid then moves into the storage tank where the average cycle time for the fluid is about 8 minutes⁴. After settling in the storage tank (point # 5), the fluid is pumped back into grinding process by a large pump (point # 6).

⁴ Cycle time refers to the volume of the storage time divided by the volume flow rate of the coolant. In order to allow the coolant to settle to the ambient temperature of the environment, it should have a cycle time of greater than 5 minutes (though this depends upon the shape and position of the coolant tank).

CHAPTER 7

EXPERIMENTAL CHARACTERIZATION OF THE WILBANKS PRECISION GRINDING MACHINE

This chapter describes a series of non-grinding experiments run on the Wilbanks Precision Grinding Machine (WPGM) in order to characterize the machine. The critical characteristics are accuracy, stiffness, noise level, and the flow rate and pressures of the hydrostatic bearings, and bandwidths. The three most important measurements are straightness of travel, stiffness, and modal analysis.

This results indicate that the WPGM is an excellent platform for grinding ceramic materials. The straightness of the hydrostatic bearing table is $0.75\mu\text{m}$ (over 1.2 meters of travel). The stiffness of the structural loop (without the conventional spindle) is between $1.0\text{lbs./}\mu\text{in}$ (maximum with the infeed bearings off) and $0.5\text{lbs./}\mu\text{in}$ (minimum with the infeed bearings on and the ballscrew infeeding). The modal analysis indicates that there are no significant modes associated with the structure or the hydrostatic bearings. The noise measurements demonstrate that bearing supply pressure fluctuations can be reduced to less than 0.03psi . (when the supply pressure is 200psi).

7.1 - Straightness of Motion

For linear bearing systems, straightness refers to the amount of motion transverse to the principle axis. Depending upon the configuration, the measurement captures either pure transverse motion, rotational motion, or both.

For this system, there are two linear axes of motion. Some error motions effect the machine performance. Figure 7.1 is a diagram of the error motions for the linear axes. The error motions are described in tables 7.1 and 7.2. An error motion which directly effects the accuracy of the machine tool performance is referred to as *sensitive*. An error occurring in a direction which does not effect the accuracy of a machine tool is referred to as *insensitive*.

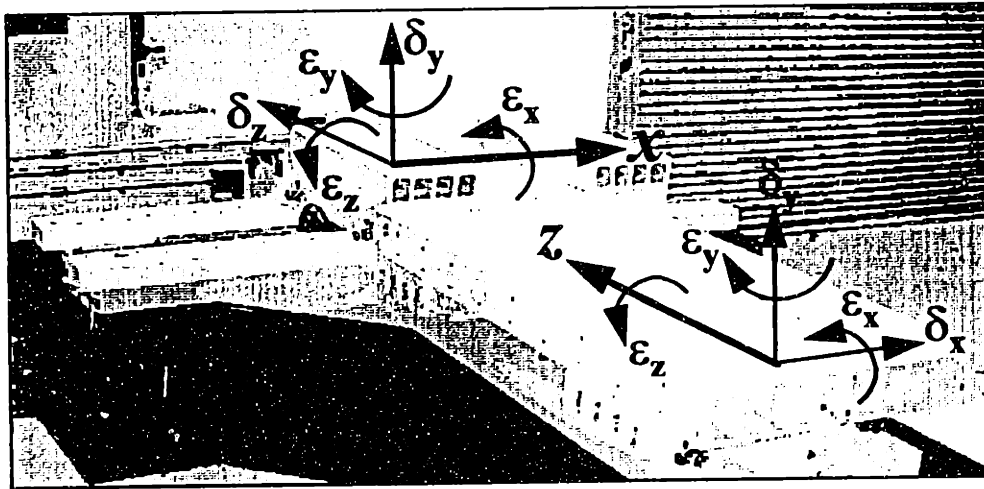


Figure 7.1 Definition of error motions for the WPGM. The large X indicates the direction of motion for the crossfeed table (the table in the back), and Z indicates the direction of motion for the infeed table (the closest table). The linear error motions are denoted by δ (with a subscript indicating the direction of the error motion), and the rolling error motions by ϵ (with a subscript denoting the axis about which the table is rolling).

Table 7.1 Description of error motions for the crossfeed table of the WPGM.

| Error Motion | Description | Sensitive / Insensitive |
|----------------------------------|--|-------------------------|
| $\delta_{z, \text{crossfeed}}$ | Straightness of the table in the z direction | Sensitive |
| $\delta_{y, \text{crossfeed}}$ | Straightness of the table in the y direction | Insensitive |
| $\epsilon_{x, \text{crossfeed}}$ | Rolling motion of the table about the x axis | Sensitive |
| $\epsilon_{y, \text{crossfeed}}$ | Yaw motion of the table about the y axis | Sensitive |
| $\epsilon_{z, \text{crossfeed}}$ | Pitch motion of the table about the z axis | Insensitive |

Table 7.2 Description of error motions for the infeed table of the WPGM.

| Error Motion | Description | Sensitive / Insensitive |
|-------------------------------|--|-------------------------|
| $\delta_{x, \text{infeed}}$ | Straightness of the table in the x direction | Insensitive |
| $\delta_{y, \text{infeed}}$ | Straightness of the table in the y direction | Insensitive |
| $\epsilon_{x, \text{infeed}}$ | Pitch motion of the table about the x axis | Sensitive |
| $\epsilon_{y, \text{infeed}}$ | Yaw motion of the table about the y axis | Sensitive |
| $\epsilon_{z, \text{infeed}}$ | Rolling motion of the table about the z axis | Insensitive |

For the WPGM, there are a total of 5 sensitive error motions. Since the infeed motions are typically small during the grinding process, the $\epsilon_{x, \text{infeed}}$ and the $\epsilon_{y, \text{infeed}}$ are less critical to the performance of the machine. The most critical error motions are $\delta_{z, \text{crossfeed}}$, $\epsilon_{x, \text{crossfeed}}$, and $\epsilon_{y, \text{crossfeed}}$. These can be measured separately or as a combined error motion at the point where the grinding wheel moves. In other words, a straightness measurement recorded with the gage head in the same position as the grinding wheel would capture a combination of these errors. This measurement would capture the most critical errors for the grinding process.

It is important to note that the machine performance is not equally effected by each of these error motions. The most critical of these error motions is the linear error motion $\delta_{z, \text{crossfeed}}$. The other two significant errors, which are angular roll errors, depend upon the distance from the roll point to the edge of the grinding wheel. Figure 7.2 is a diagram of the effect of $\epsilon_{y, \text{crossfeed}}$ and $\delta_{z, \text{crossfeed}}$ on the grinding wheel error.

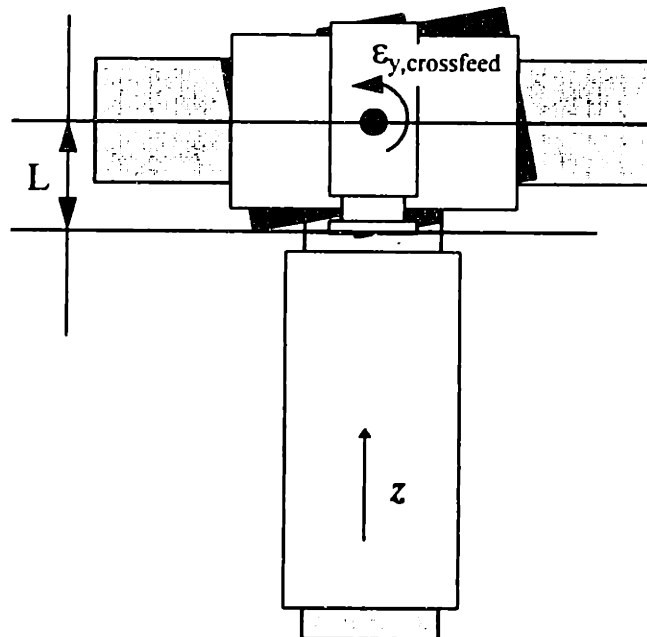


Figure 7.2 Diagram of the effect of a table roll error about the vertical axis, $\epsilon_{y, \text{crossfeed}}$.

As the table rotates, the middle of the grinding wheel will move in the z direction according to the expression:

$$\delta_{z,\epsilon_y} = 2L \sin^2 \frac{\epsilon_{y,\text{crossfeed}}}{2} \quad (7.2)$$

Since the L distance in the WPGM is approximately 0.4 meters, an angular rotation of 1 degree would cause an error in the z direction of approximately 0.6mm. However, it is extremely unlikely that such a large rotation would occur. Typical error motions for industrial machines are on the order of .0002 degrees (1 arc seconds) which would cause an error of about .1 μ m. Therefore, these errors are not as directly significant as the linear error motions. Roll errors about the x axis have a similar effect as shown in Figure 7.3

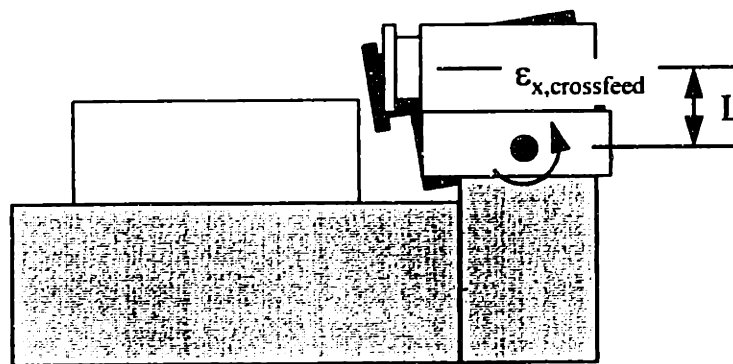


Figure 7.3 Diagram of the effect of a table roll error about the x axis, $\epsilon_{x,\text{crossfeed}}$.

As the table rotates, the middle of the grinding wheel will move in the z direction according to the expression:

$$\delta_{z,\epsilon_x} = 2L \sin^2 \frac{\epsilon_{x,\text{crossfeed}}}{2} \quad (7.2)$$

As mentioned previously, a measurement can be arranged such that the three most significant error motions are captured collectively. Figure 7.4 and 7.5 are diagrams and photographs of such an experiment for the WPGM. In order to separate the effects of the imperfections of the artifact (straight edge) and the error motions of the machine, the reversal technique is employed. This technique involves taking two measurements, with the artifact reversed in between measurements. The average of these two readings indicates the artifact error, while the deviation from this average is the error of the machine. In order to verify that this technique worked properly, the artifact was also measured on a Moore # 5 measurement machine with a Federal Gage Head.

The straight edge, which is a lapped ceramic artifact was straight to within .25 μ m over 1.3 meters. Both the reversal measurements and the Moore # 5 results confirmed this accuracy. Figure 7.6 shows the two traces for the straightness measurement (the bottom is the reversed measurement). The traces indicate that the maximum straightness error is 0.75 μ m over 1.2 meters of travel

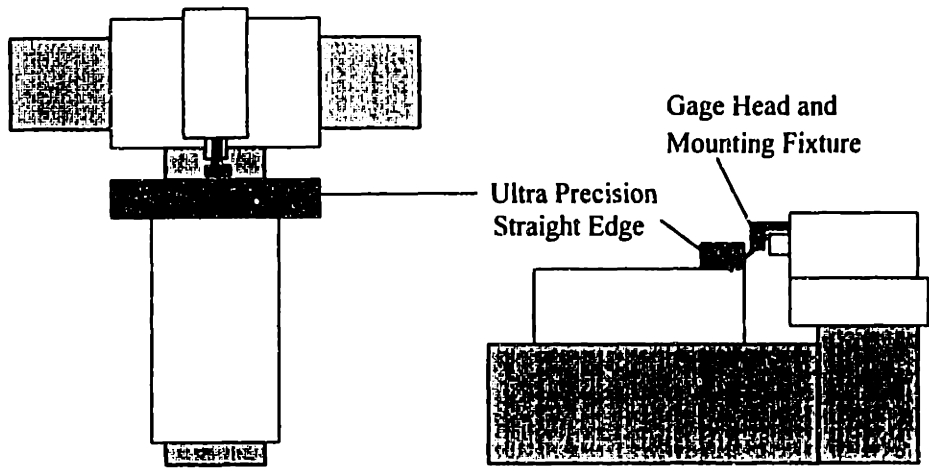


Figure 7.4 Diagram of measurement set-up for capturing the three most significant error motions of the crossfeed table on the WPGM.

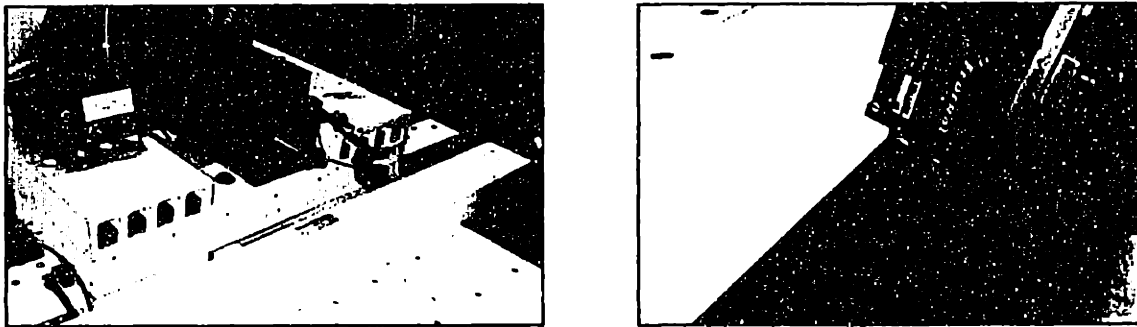


Figure 7.5 Photograph of measurement set-up for capturing the three most significant error motions of the crossfeed table on the WPGM.

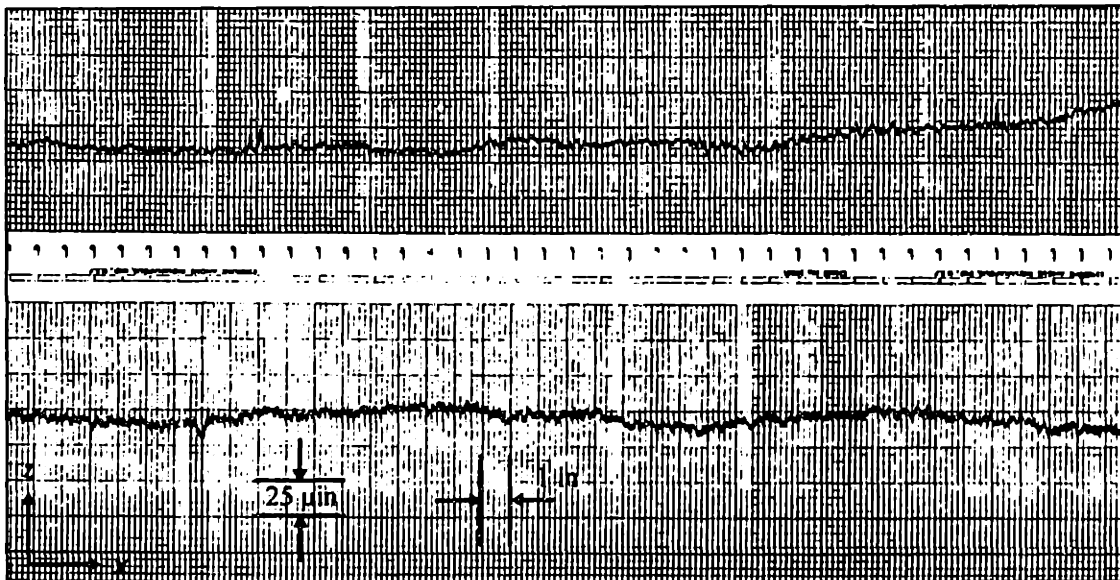


Figure 7.6 Straightness and reversed straightness measurement for the crossfeed table over 1.2 meters of travel in the horizontal direction.

7.2 - Modal Analysis

Modal analysis is a method for testing a system response to a dynamic force. For machine tools, modal analysis is an important test for examining how much the machine will vibrate during grinding operations. Since vibrations are undesirable for grinding operations, modal analysis is useful in determining what type of motion is occurring at various frequencies of interest.

When a machine does vibrate during grinding, it is often apparent to the touch. However, this information is not sufficient to remedy the problem. One must know where the vibration is occurring as well as the type of vibration. For example, knowing that the spindle table has a bending mode at a particular frequency might lead an engineer to reinforce the table in order to increase the natural frequency.

Modal analysis is often performed by exciting the machine with an impulse hammer (which contains a piezo-electric force transducer for measuring the force) then measuring the response in several locations with an accelerometer (which also contains a piezo-electric element). Figure 7.6 is a photograph of a typical testing set-up for modal analysis of a machine tool.

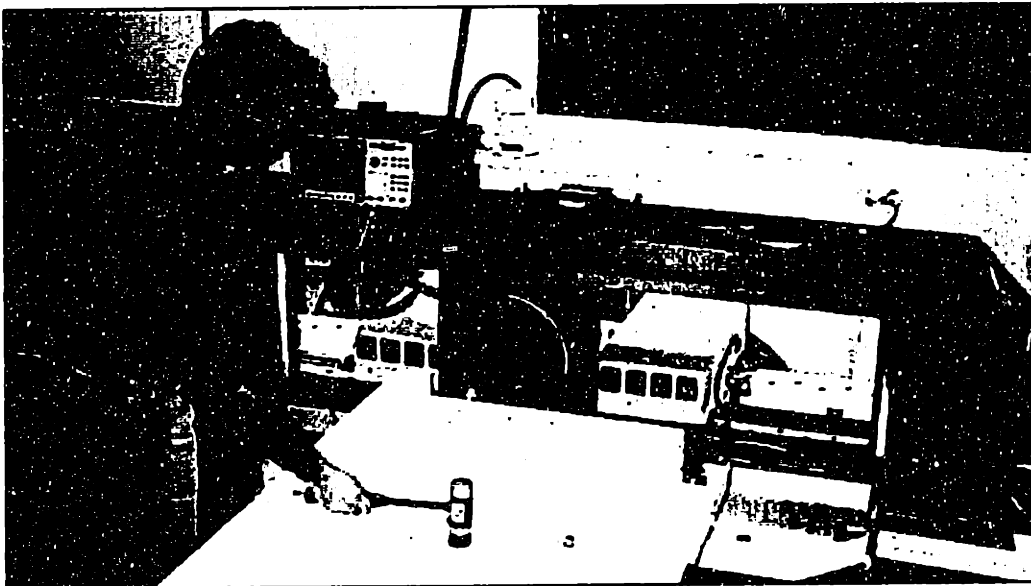


Figure 7.6 Modal analysis set-up. The operator inputs a measured force into the WPGM with an impulse hammer, then measures the response with an accelerometer. The fourier transformations are performed by a signal analyzer.

The dynamic compliance of a machine tool component is described as a complex number. The most important quantity for machine tool applications is the magnitude of the real and imaginary parts. It is important to note that an accelerometer reading captures all acceleration at the measurement point. Some of the motion is due to machine compliance, and some is due to vibrations in the floor. Therefore in order to capture the dynamic compliance of the machine tool, readings must be taken in different locations and subtracted (subtraction must be done with both parts of the complex number).

7.2.1 - Modal Analysis of the Crossfeed Hydrostatic Bearing System

Figure 7.7 is a diagram of the measurement locations for determining the vertical compliance of the crossfeed table on the WPGM. Twelve measurements were taken and analyzed using Star Modal Analysis Software. The difference in measurements at points 1 and 9 (shown in Figure 7.8) indicates the vertical dynamic compliance of the hydrostatic bearing system and table.

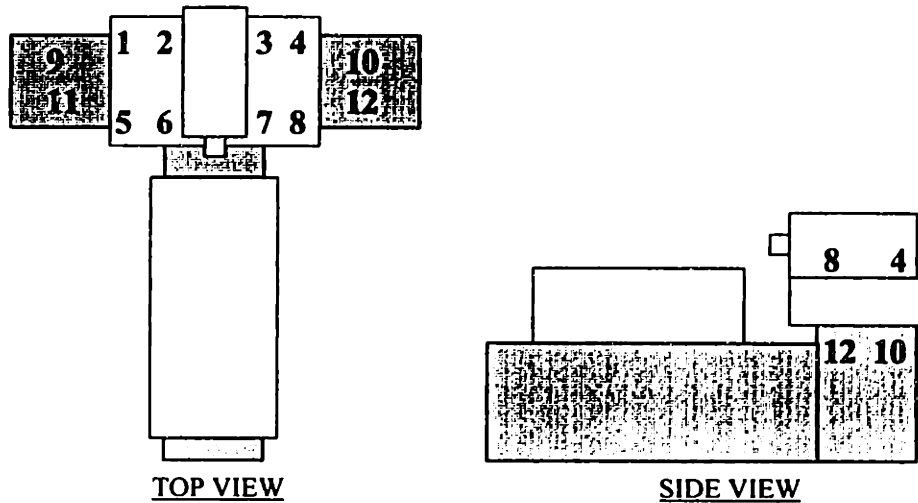


Figure 7.7 Location of measurement points used to describe the dynamic performance of the hydrostatic bearings. Point # 1 is drive point and the first measurement.

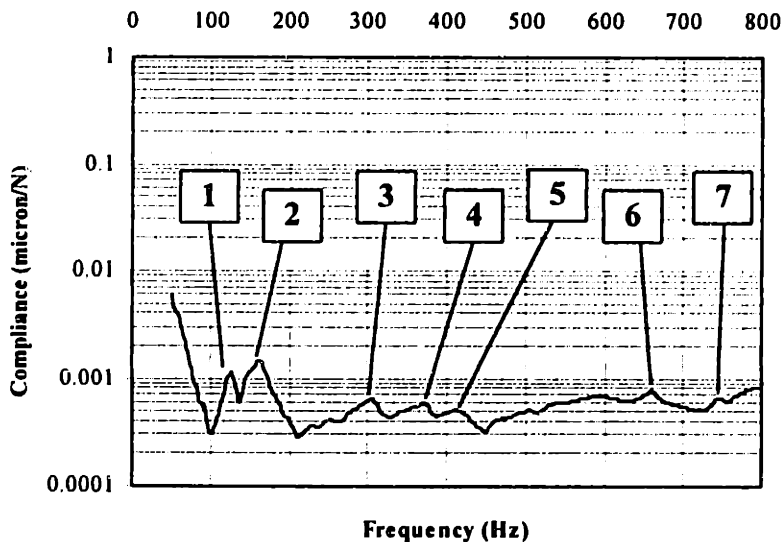


Figure 7.8 Vertical dynamic compliance of the crossfeed hydrostatic bearing table. The bearing performance can be characterized by subtracting the response measurement from a point on the table with a point on the base. The hydrostatic bearing supply pressure was 200 psi. The numbers correspond to modes which will be examined with modal analysis software.

The individual modes of the table motion can be animated using modal analysis software. The software computes the magnitude and phase of motion at each point. Figure 7.9 illustrates the significant motion of the table. All of the modes numbered in Figure 7.8 are rotational modes in which the base and the table rotate about the x axis. Therefore, there is not a direct mode in which the table moves vertically away from the base.

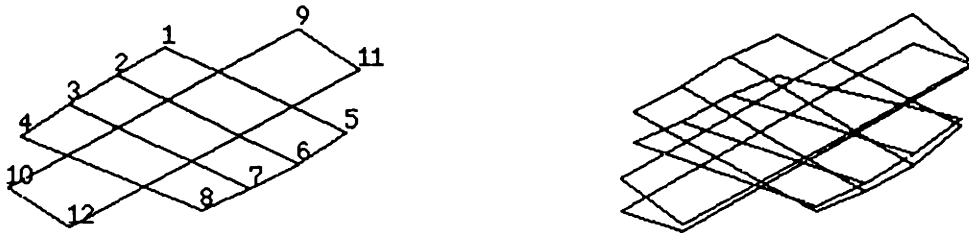


Figure 7.9 Diagram of the measurement points (left) and the motion of the table and base system (right). This motion was common for most of the modes shown in Figure 7.8. The motion is a rotation about the x axis.

The modal analysis results indicate that the bearing system does not have the clear compliance mode in which the table moves vertical to the base. Rather, all modes are rotational. These modes are significant for the performance of the grinding because they do cause motions in the sensitive direction.

7.2.2 - Modal Analysis of the Structural Grinding Loop

The most critical information about the grinding machine performance is the vibrations around the structural loop between the grinding wheel and the workpiece. This loop determines how well the machine will grind parts. Figure 7.10 is a diagram of the structural loop and a schematic of the various compliances around the loop.

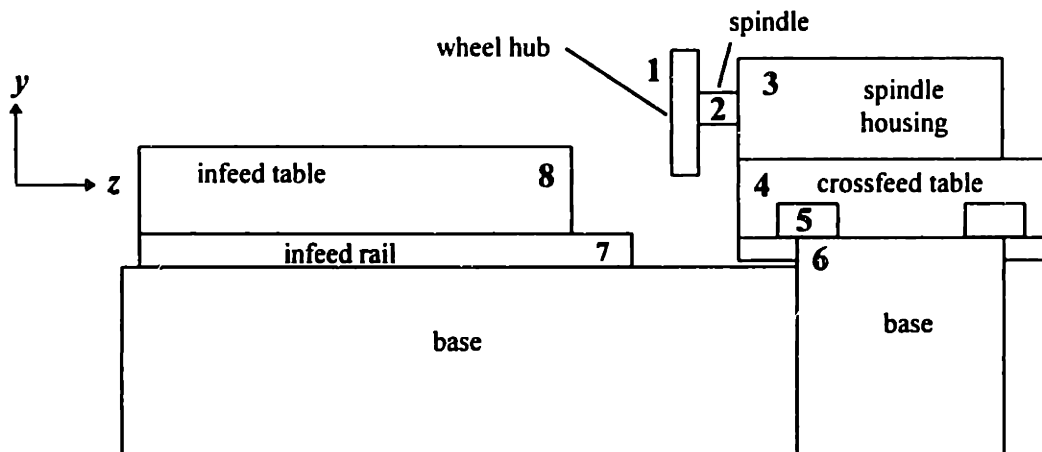


Figure 7.10 Diagram of the positions around the structural loop compliances.

Table 7.3 Table of compliances around the structural loop. The compliances are denoted as the difference in motion per unit force between two points.

| Points | Name | Description |
|--------|-------------------------------|---|
| 1-2 | Wheel hub | Compliance of wheel hub relative to the spindle housing. |
| 2-3 | Spindle | Compliance of spindle relative to the spindle housing. |
| 3-4 | Spindle mounting | Compliance of the spindle mounting to the table. Spindle is bolted to the table in the front and bolted with bellville washers in the back to allow for thermal expansion. |
| 4-5 | Crossfeed hydrostatic bearing | Compliance of the hydrostatic bearing in the horizontal direction. This is mainly the compliance of the horizontal bearings, but also the rotation stiffness of the table about the x axis. |
| 5-6 | Crossfeed rail to base | Compliance of crossfeed rail relative to the base. This compliance should be very low since the rails are bolted down to the base at 3" intervals. |
| 6-7 | Base to infeed rail | Compliance of the infeed rails relative to the base. This compliance should be very low since the rails are bolted down to the base at 3" intervals. |
| 7-8 | Infeed rail to infeed table | Compliance of the table relative to the rails. When the hydrostatic bearings are turned on, the main compliance is the ballscrew, when the bearings are off, the friction of the table weight on the rails is the main stiffness. |

The results indicate that the main compliance in this structural loop is the wheel hub and the spindle. In other words, between points 4 and 8, there is not considerable motion compared to the motion of points 1 through 4. Figure 7.11 is a plot of the compliance between points 1 and 4. The two most important modes are at 90 Hz and at 130 Hz. The mode at 90 Hz is a linear movement of the spindle in the z direction. The mode at 130 Hz is a rotation of the spindle about the x axis.

The compliance of the spindle is primarily due to the stiffness of the bearings and the geometry of the wheel and spindle rotor. The bearings used in the spindle are tapered roller bearings at both ends of the spindle shaft. Such bearings will always have a finite compliance which accounts for the mode at 90 Hz. The mode at 130 Hz is primarily due to the ratio of the spindle diameter compared with the diameter of the wheel hub. The spindle diameter is 3.2" while the wheel hub is 14" in diameter and 3" thick. The wheel hub was designed to be as stiff as possible. However, the thickness of the wheel hub

which acts to increase the stiffness also increases the weight. The weight of the wheel hub is 130 lbs, which has a significant effect on the natural frequency of the spindle and wheel hub modes.

The modal analysis clearly demonstrates that the spindle and wheel hub design are now the most significant issues for the next generation of grinding machines when stiff structures and linear bearings are used.

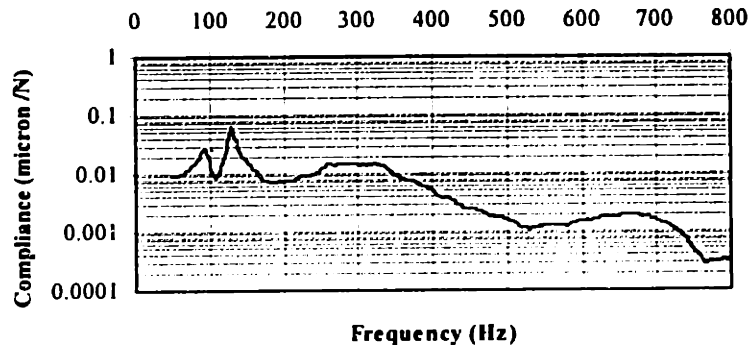


Figure 7.11 Plot of compliance as a function of frequency for the spindle and wheel hub. The compliance in this plot accounts for the motion between points 1 and 4 in Figure 7.10. The amplification at resonance (or Q' factor) is 10.

The motion between points 4 and 8 indicate the stiffness of the system aside from the spindle motion. By subtracting the frequency response from point 4 with the frequency response on the infeed table (point # 8 in Figure 7.10), the compliance of the bearings, the base, and the infeed table in the z direction are grouped together. It is important to note that viewing these components as simple springs can lead to misinterpretations about the dynamic compliance. Each point represents 6 degrees of freedom with respect to the next point. Therefore, the motion between 2 points includes rotational and linear compliances. Figure 7.12 is a plot of the dynamic compliance between the crossfeed table and the workpiece of the WPGM.

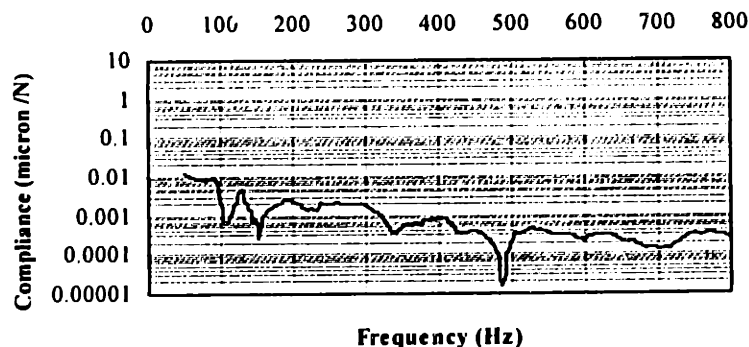


Figure 7.12 Plot of compliance as a function of frequency for the linear bearings and the base of the WPGM. The compliance in this plot accounts for the motion between points 4 and 8 in Figure 7.10. The Q factor is 1.1.

¹ The "Q" factor for a system is the amplification at resonance. It is equivalent to the maximum compliance (at the resonant frequency) divided by the static compliance of the system.

The main mode for the structure is at 130Hz and is linear motion of the tables relative to one another. The worst case compliance according to these measurements is $.004\mu\text{m}/\text{N}$ which corresponds to a stiffness of $250 \text{ N}/\mu\text{m}$ (approximately 1.5Mlbs/in.). This stiffness is more than an order of magnitude greater than the wheel hub and spindle.

Thus, the compliance of the entire loop (shown in Figure 7.13) is dominated by the spindle and wheel hub. The plot is almost identical to Figure 7.11. The most noticeable difference is the increase in stiffness at approximately 70Hz which occurs because two of the springs in the structural loop are cancelling one another out and the motion of this frequency is significantly lower. However, the performance of the machine is dominated by the resonances which occur at the same frequencies as in Figure 7.11.

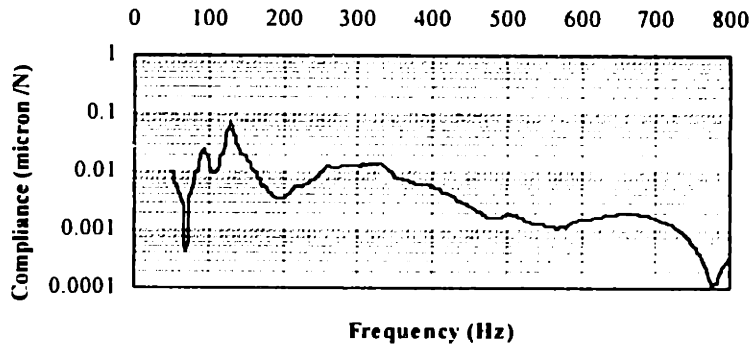


Figure 7.13 Plot of compliance as a function of frequency for the grinding structural loop of the WPGM. The compliance in this plot accounts for the motion between points 1 and 8 in Figure 7.10

As a comparison to this loop stiffness, the frequency response of a conventional machine was also sampled. Since the spindle on the WPGM dominates the compliance (the weakest link dominates the performance), the performance of the entire structural loop will be only somewhat better than the performance of a conventional machine. The plots in Figure 7.14 indicate that in the most critical region for grinding, from 50 Hz to 250 Hz, the WPGM has significantly higher stiffness, even though the wheel and the spindle are the dominate compliances in the loop

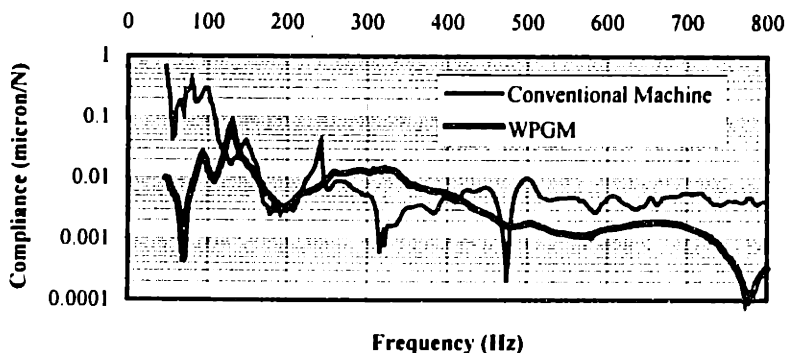


Figure 7.14 Plot of compliance as a function of frequency for the grinding structural loop of the WPGM and a comparable conventional grinding machine.

7.3 - Noise Measurements

In order to maintain constant supply pressure and reduce system vibrations, the pump system for the WPGM included accumulators as described in chapter 6 (and discussed in a more general manner in chapter 4). This brief section confirms the effectiveness of accumulators, when tuned correctly to reduce pressure fluctuations in the hydrostatic bearings. Figure 7.15 is a block diagram of the system

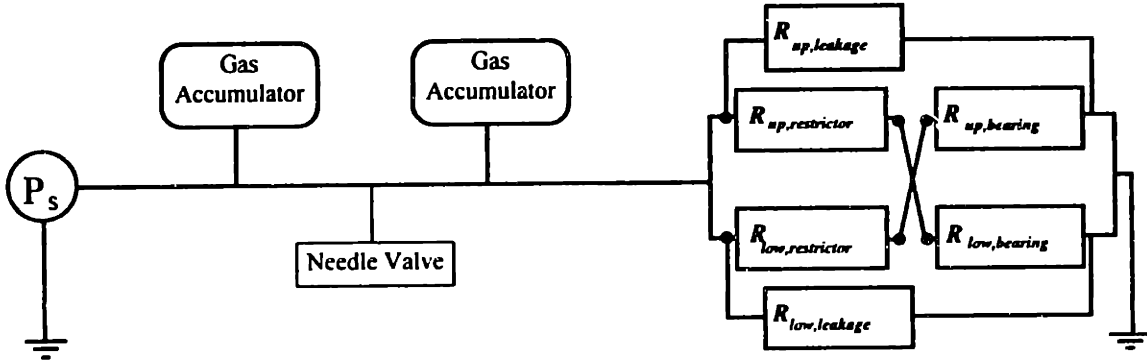


Figure 7.15 Block diagram of the fluid path of a self-compensated, hydrostatic bearing system. The restrictors and bearing lands are represented as fluid resistances.

Figure 7.16 is a power spectrum of the pressure (measured immediately before entering one of the hydrostatic bearing pads) without tuning any of the accumulators. The plot indicates that the bearings have significant noise at the frequency of the pump. The largest fluctuation is approximately 0.05% of the supply pressure. This fluctuation is not significant compared with other systems. In particular, the long rubber hoses which are used in the system have sufficient capacitance to reduce the supply fluctuations.

However, in order to tune the system so that the fluctuations are completely insignificant, the accumulators are charged with nitrogen when the system is turned off. Their initial value is approximately 60% of the supply pressure. This value was chosen from previous experience and seems to yield good noise reduction results.

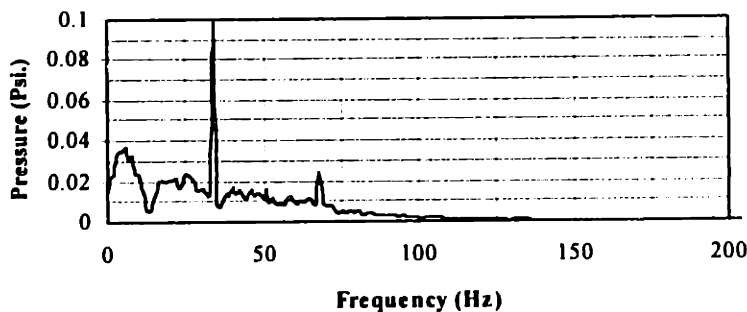
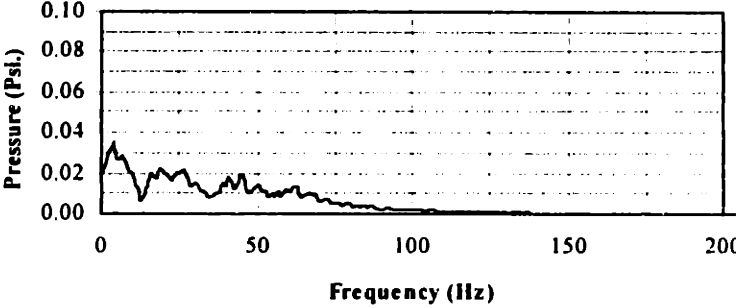
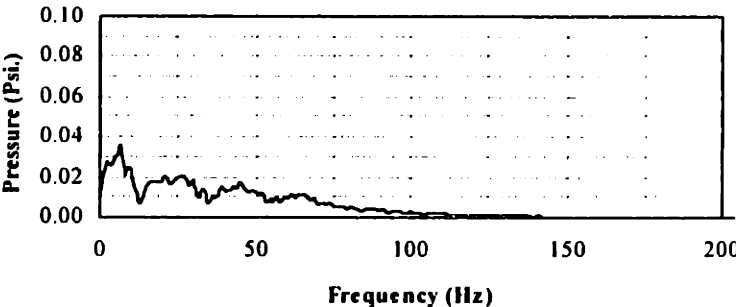
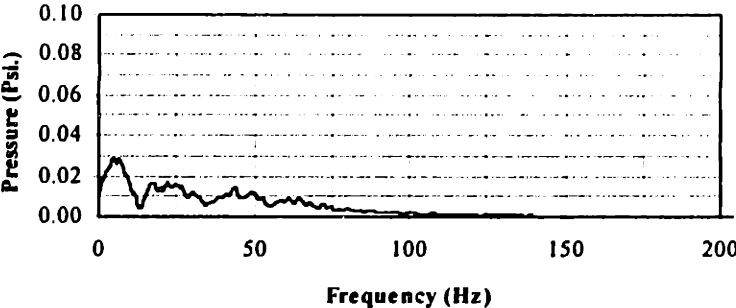


Figure 7.16 Linear power spectrum for the hydrostatic bearing pressure measured at the inlet to the hydrostatic bearing pad. The accumulators are not charged and the needle valve is open. The nominal supply pressure is 200psi.

In tuning the accumulators, it is recommended that the accumulator be reduced in 5 psi. increments. At each interval, the power spectrum indicates the change in pressure fluctuations. Table 7.4 indicates how effectively the pressure fluctuations can be reduced.

Table 7.4 Table of pressure variations in the supply pressure as a function of frequency for various accumulator and needle valve settings. In all cases, the supply pressure is 200 psi.

| Description | Measurement |
|--|--|
| <p>Figure 7.17</p> <p>First Accumulator: 100 psi. Second Accumulator: 100 psi. Needle Valve: open</p> |  |
| <p>Figure 7.18</p> <p>First Accumulator: 50 psi. Second Accumulator: 50 psi. Needle Valve: open</p> |  |
| <p>Figure 7.19</p> <p>First Accumulator: 50 psi. Second Accumulator: 50 psi. Needle Valve: 30 psi. drop @ 3.7 gal./min.</p> |  |

7.4 - Stiffness Measurements

This section is an analysis of the loop stiffness of the WPGM. The loop stiffness (as discussed in section 1.2.2) measures the machine deflection between the grinding wheel and the workpiece. It is a measurement of how much the machine will deflect during grinding processes. Additionally, loop stiffness experiments are conducted to determine which components in the structural loop are the most compliant.

Machine tool stiffness is one of the most important performance measurements. Stiffness has a direct impact on the accuracy of the components and the production rate. As mentioned in chapter 1, there is a distinction between static stiffness and dynamic stiffness. Whereas modal analysis measures dynamic stiffness, force-displacement experiments analyze the static stiffness of a machine tool. There are two components required for measuring static stiffness; (1) a repeatable force and force measurement, and (2) a high accuracy measurement of displacement.

The force is generally provided by a hydraulic piston or piezo-electric actuator. For stiff machines, the hydraulic actuator is preferable because it can generate larger forces (well over 1000 lbs.). The piezo-electric actuators are preferable for lower forces (0-100 lbs.) because they have higher force resolution and repeatability. Measuring the force is generally done with a load cell. Load cells are produced in a variety of load capacities, and repeat well for static forces.

Displacement can be measured by numerous sensors. Capacitance probes and laser interferometer measurements provide the highest resolution, but are difficult to use in some geometries. LVDT probes are a fast method of measuring sub-micron displacement, and can be used in almost any geometry.

For the WPGM, an experiment was conducted using a hydraulic piston (with a load cell) and 2 LVDT probes to measure the displacement of each portion of the structural loop. Figure 7.20 is a photograph of a typical set-up for measuring static stiffness of the WPGM. The set-up was varied throughout the loop stiffness experiments in order to analyze different components within the loop.

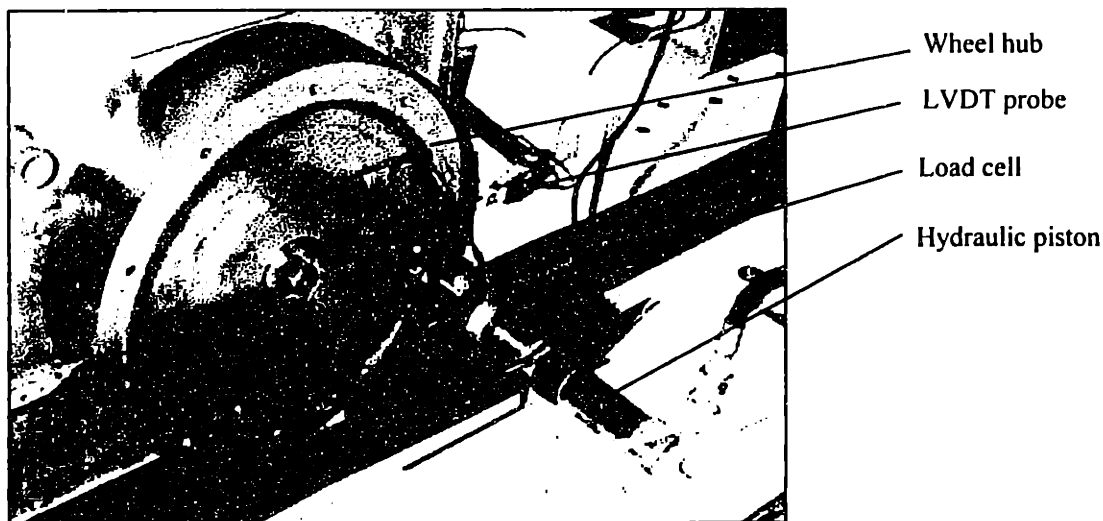


Figure 7.20 Experimental set-up for measuring static stiffness of the WPGM.

In the WPGM, there are 4 significant compliances in the structural loop which could effect the performance of the machine; (1) the spindle, (2) the crossfeed linear bearings in the z direction, (3) the base structure between the crossfeed table and the infeed table, and (4) the ballscrew of the infeed table. Each of these compliances has the most significant effect on the stiffness in the z direction. Referring to figure 7.20, the individual compliances are the same as those for the modal analysis. However, based on the information gained from the modal analysis, the number of compliances has been simplified from 7 to 4.

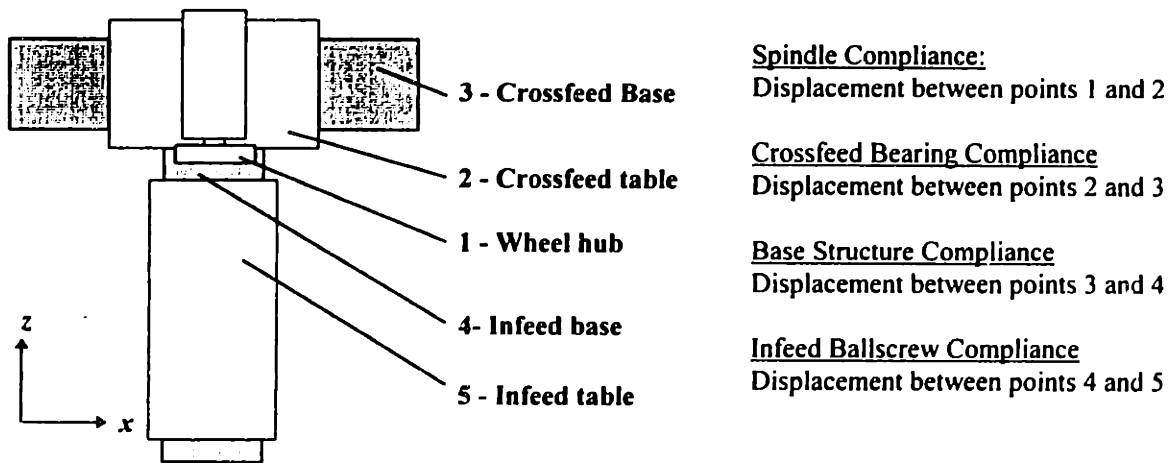


Figure 7.21 Measurement points and important compliances of the WPGM.

The static stiffness measurements indicate that the spindle is the most compliant part of the structural loop by an order of magnitude. Figure 7.22 shows the total compliance of the spindle compared with the compliance of the structural loop. The stiffness of the loop without the spindle is approximately 0.5lbs./ μ in with the infeed table bearings on, and 1.0lbs./ μ in with the bearings off. During grinding operations, the infeed bearings will be on until the final dwell grinding (or "spark-out"). The spindle has a total compliance of approximately 0.12lbs./ μ in. This spindle compliance is measured by applying a force to the outer perimeter of the wheel hub. This type of loading reflects the grinding forces as the wheel begins to grind a component. It indicates the maximum compliance for the wheel hub/spindle. The spindle stiffness is comparable to high quality conventional spindles of similar size. The compliance is expected since the spindle rotor diameter is 2.7". Therefore, it is rotationally compliant towards the large moments which are exerted when forces are applied 7.0" (the edge of the wheel hub) from the center.

The spindle compliance has three main components; (1) axial stiffness of the rotor in the z direction, (2) rotational stiffness of the rotor about the y axis, and (3) elasticity of the wheel hub. Figure 7.23 illustrates these compliances. Figure 7.24 is a plot of the displacement of the rotational and elastic components of the spindle stiffness. Figure 7.25 is a plot of the spindle axial displacement which indicates the axial stiffness is approximately 1.2lbs./ μ in.

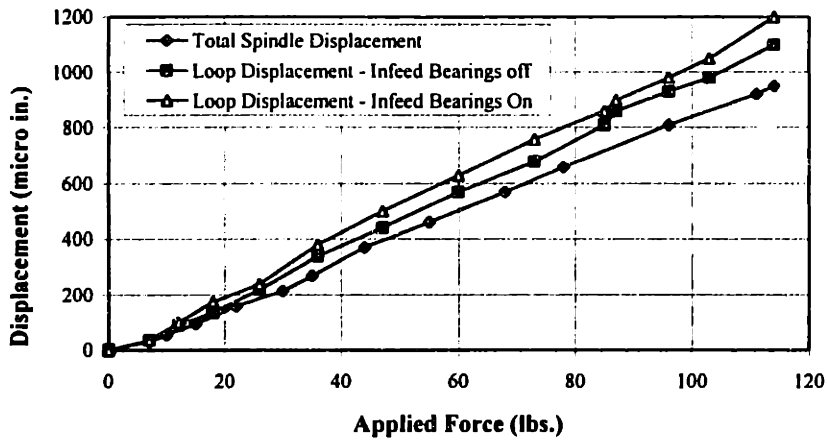


Figure 7.22 Plot of displacement versus applied force for the spindle, the structural loop with the infeed table bearings off, and the structural loop with the infeed table bearings on. The measurements were taken with a set-up similar to figure 7.19 in which a force is applied at the outer edge of the wheel hub and the displacement is measured by LVDT probes.

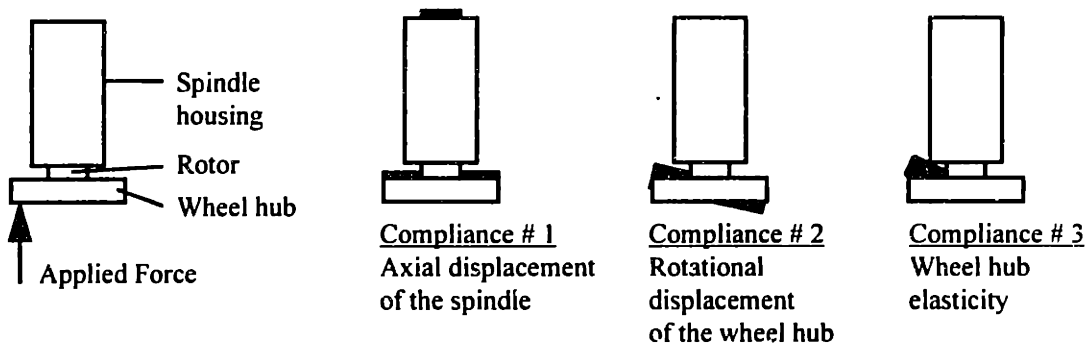


Figure 7.23 Diagram of the three types of compliance in the wheel hub and spindle.

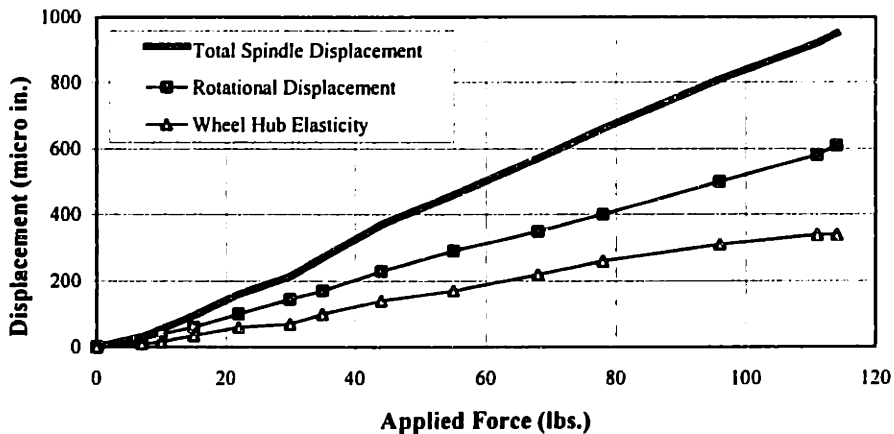


Figure 7.24 Plot of displacement versus applied force for the spindle rotation and the wheel hub elasticity.

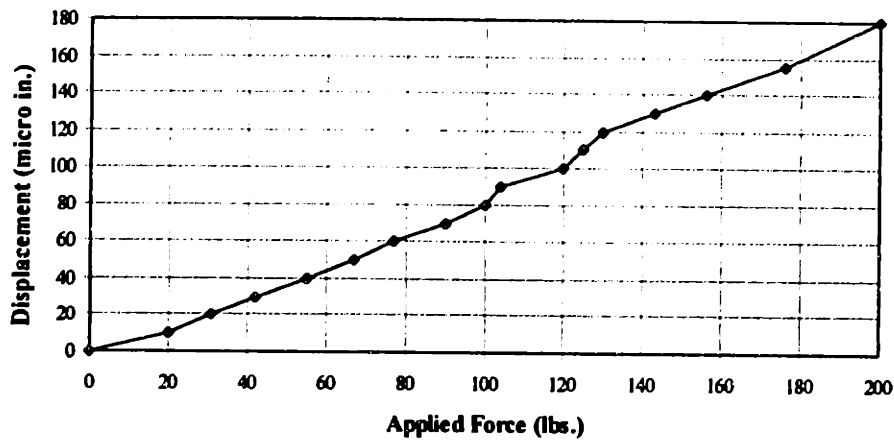


Figure 7.25 Plot of axial displacement versus applied force for the spindle. The force and displacement were applied and measured on the centerline of the spindle rotor. The plot indicates that the axial stiffness of the spindle is 1.2lbs./ μ in

The other compliances in the structural loop were also measured independently to confirm the results of Figure 7.22. The compliance of the crossfeed table in the horizontal direction was tested and shown in Figure 7.26. The plot indicates the bearing stiffness (for one set of bearing pads) is approximately 3.0lbs./ μ in when the supply pressure is 100psi and 4.0lbs./ μ in when the supply pressure is 200 psi. Since the table has 2 sets of bearing pads, the stiffness of the table during grinding will be higher. A stiffness test with the force applied in the center of the wheel hub and displacements measured on the corners of the crossfeed table indicated that the combined stiffness is approximately 8.0lbs./ μ in.

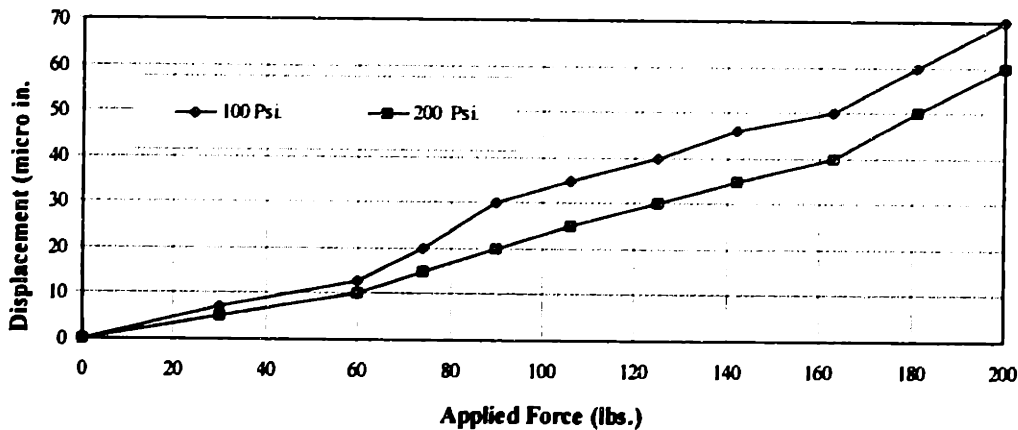


Figure 7.26 Displacement of the crossfeed table in the horizontal direction as a function of applied load. The force and displacement were applied and measured on the corner of the table. A second probe on the other side was used to confirm that only one set of bearings pads was being displaced from the nominal position.

The infeed table ballscrew is another critical part of the structural loop. When the table is infeeding during grinding operations, the ballscrew stiffness directly effects the grinding process. The stiffness test (shown in Figure 7.27) for the ballscrew indicates that the stiffness is approximately 1.40lbs./ μ in. During the dwell cycle at the end of each grinding process, the hydrostatic bearings which support the infeed table are collapsed in order to increase the loop stiffness. The friction between the table and the rails then dominates the stiffness in this part of the loop. Immediately after the bearings are turned off, the axial stiffness of the infeed table increases to approximately 14.0lbs./ μ in.

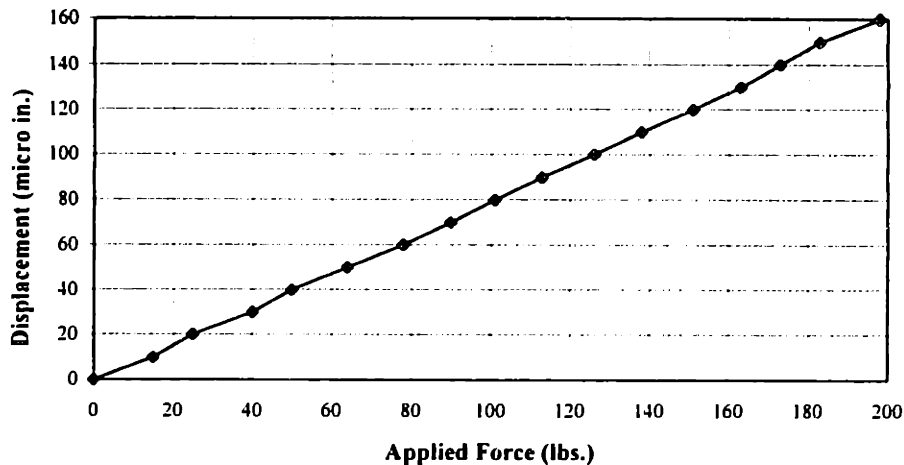


Figure 7.27 Plot of displacement versus applied load for the z direction of the infeed table. The plot indicates that the stiffness is approximately 1.40lbs./ μ in..

Finally, the base structure has a stiffness of at least 20.0lbs./ μ in. A test for the base structure displacement indicated that the base (between points 3 and 4 on Figure 7.21) did not displace more than 10.0 μ in. under 200lbs. of applied force. The displacement measurement is close to the repeatability of the LVDT probe (which is about 5 μ in. depending upon the ambient vibration and thermal conditions). This compliance does not have a significant effect upon the grinding process in which forces usually less than 50lbs. A repeatable measurement for the base stiffness would require forces of 1000lbs. which could potentially damage part of the system.

In conclusion, the results indicate that the spindle is the most compliant part of the structural loop by an order of magnitude. Figure 7.22 demonstrates that the displacement of the wheel hub with respect to the workpiece is dominated by the wheel hub and spindle compliances. The modal analysis (section 7.2) also indicated that the spindle compliance is substantially larger than the bearings or structure. Table 7.5 summarizes the significant compliances of the WPGM.

Table 7.5 Compliances in the structural loop of the WPGM.

| Description | Measurement # (from Figure 7.20) | Stiffness |
|---|-------------------------------------|--|
| Spindle and wheel hub loaded on outer edge | Point 1 to 2 | 0.12lbs./ μ in. |
| Crossfeed table bearings (one pair of bearings) | Point 2 to 3 | 3.0lbs./ μ in. @ 100 psi. 4.0lbs./ μ in. @ 200 psi. |
| Base Structure | Point 3 to 4 | over 20.0lbs./ μ in. |
| Infeed table with hydrostatic bearings on | Point 4 to 5 | 1.20lbs./ μ in. |
| Infeed table with hydrostatic bearings off | Point 4 to 5 | 14.0lbs./ μ in. |

7.5 - Hydrostatic Bearing Flows and Pressures

This section describes the flow rates and bearing pocket pressures for the crossfeed table. The resistances, flow rates, and pocket pressures can be predicted by the spreadsheet design tools. Therefore, the experimental results can be compared to the spreadsheet values to test their accuracy. Since these measurements are made to check the machine against theory (and are not direct performance characterizations), extremely accurate gauges are not required. Flow measurements were made with a rotometer flow meter which has an accuracy of ± 0.03 gal./min.. Pressure readings were made with a needle pressure gauge with accuracy of ± 3.0 psi.

7.5.1 - Horizontal Bearings on the Crossfeed Table

Figure 7.28 describes the pressure and flow reading from one of the horizontal bearing pad sets on the crossfeed table.

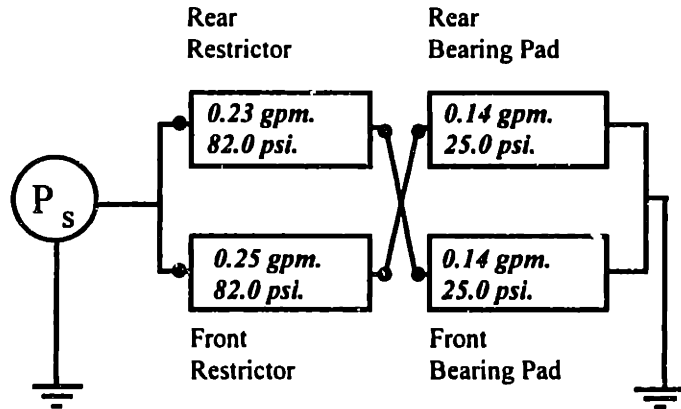


Figure 7.28 Pressure and flow measurements on one horizontal bearing of the crossfeed table. The readings indicate the flow into each labeled area.

Comparing spreadsheet values to experimental values is challenging because the bearing gap has a strong influence on the predicted values. Therefore, measured values must be used to adjust the nominal gap. The nominal gap on the WPGM was set with shim material. The actual gap will be larger than the shim stock (often 0.0005" larger). Therefore, the shim stock used to set the gap should be thinner than the desired nominal gap. On horizontal bearings, measuring the nominal gap is also difficult because the table can't generally be moved to both front and rear extreme positions. The measurements on the horizontal bearing pads of the WPGM indicate a bearing gap of 0.002" total. However, it is possible that there is ± 0.0002 " error in this measurement.

The following procedure has been used to test the accuracy of the spreadsheets relative to the experimental values. First, the supply pressure and geometry of the bearing pads is entered into the spreadsheets. Second, the nominal gap is adjusted from the measured value until the flow rate matches the experimental value. Third, the stiffness and bearing pocket pressures can be compared to check the correlation. Table 7.6 is a comparison of the spreadsheet and experimental values for the horizontal bearings on the crossfeed table of the WPGM.

Table 7.6 Comparison of experimental and spreadsheet values for the horizontal bearing pads of the WPGM. Note that the spreadsheet value for the nominal gap is adjusted in order to match the spreadsheet flow rate with the experimental value. Additionally, the experimental value for the nominal gap has a possible error of ± 0.0002 ".

| Characteristic | Spreadsheet Value | Experimental Value | Difference |
|-------------------------|---------------------|---------------------|------------|
| Nominal Gap | 0.00104" | 0.0008" | 22 % |
| Flow Rate | 0.48 gpm | 0.48 gpm | - |
| Stiffness | 2.81 lbs./ μ in | 3.00 lbs./ μ in | 7 % |
| Bearing Pocket Pressure | 27.2 psi. | 25.0 psi. | 8 % |

7.5.2 - Vertical Bearings on the Crossfeed Table

Measurements were also made on the upper and lower bearing pads. The flow and pressure measurements are summarized in Figure 7.29. Since the vertical pads bear the weight of the carriage, the spreadsheets must accurately account for the initial load. In the vertical direction, the bearing gap measurement will be more accurate. Since the bearing gap is determined by the spacer blocks, the spreadsheet gap values match more closely with the experimental value. The designed nominal gap (0.00075") matches the experimental value within 2%. Nevertheless, the same procedure will be used to compare the values. Table 7.7 compares the spreadsheet values to the experimental values.

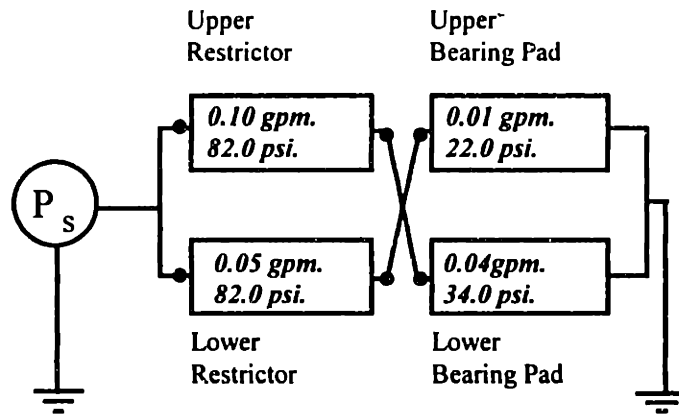


Figure 7.29 Pressure and flow measurements on one vertical bearing of the crossfeed table. The readings indicate the flow into the labeled area.

Table 7.7 Comparison of experimental and spreadsheet values for the vertical bearing pads of the WPGM. Note that the spreadsheet value for the nominal gap is adjusted in order to match the spreadsheet flow rate with the experimental value. Additionally, the experimental value for the nominal gap has possible error of ± 0.0001 ".

| Characteristic | Spreadsheet Value | Experimental Value | Difference |
|-------------------------------|--------------------|--------------------|------------|
| Nominal Gap | 0.00072" | 0.00075" | 4 % |
| Flow Rate | 0.15 gpm | 0.15 gpm | - |
| Stiffness | 6.1 lbs./ μ in | 6.7 lbs./ μ in | 8 % |
| Upper Bearing Pocket Pressure | 18.9 psi. | 22.0 psi. | 13 % |
| Lower Bearing Pocket Pressure | 39.3 psi. | 34.0 psi. | 13 % |

Since the nominal gap is close to the design value in this case, it is informative to look at the spreadsheets from the perspective of the design engineer. If the spreadsheets are run with the measured gap (which is the same as the designed gap), the table indicates how closely the system performance can be predicted before assembly. Table 7.8 indicates that the spreadsheets are effective for predicting the system performance within approximately 12%. Note that the experimental values have accuracy limitations. Additionally, some variation would be expected since the bearings have tolerances and the rails are not perfectly straight.

Table 7.8 Comparison of experimental and spreadsheet values for the vertical bearing pads of the WPGM. Note that the spreadsheet value for the nominal gap matches the experimental value.

| Characteristic | Spreadsheet Value | Experimental Value | Difference |
|-------------------------------|--------------------------|---------------------------|-------------------|
| Nominal Gap | 0.00075" | 0.00075" | - |
| Flow Rate | 0.17 gpm | 0.15 gpm | 12 % |
| Stiffness | 5.9lbs./ μ in | 6.7 lbs./ μ in | 12 % |
| Upper Bearing Pocket Pressure | 18.2 psi. | 22.0 psi. | 14 % |
| Lower Bearing Pocket Pressure | 39.0 psi. | 34.0 psi. | 12 % |

7.6 - Conclusions

This chapter has demonstrated that the WPGM is an excellent platform for grinding ceramic materials. The straightness of the hydrostatic bearing table is $0.75\mu\text{m}$ over 1.2 meters of travel. The stiffness of the structural loop (without the conventional spindle) is between 1.0 lbs./ μ in (maximum with the infeed bearings off) and 0.5 lbs./ μ in (minimum with the infeed bearings on and the ballscrew infeeding). The modal analysis also indicated that there no significant modes associated with the structure or the hydrostatic bearings. The noise measurements demonstrated that (with proper tuning of the accumulators) the bearing supply pressure fluctuations can be reduced to less than 0.03 psi. even when the supply pressure is 200 psi.

However, it is equally significant to note that the experiments demonstrate that one weak compliance in the system degrades system stiffness directly. Since the compliances of the structural loop act like springs in series, the performance of the system is dominated by the least stiff component.

Finally, the results indicate that the spreadsheets used to design the hydrostatic bearings, effectively predict the bearing performance within approximately 10%. The critical parameter is the nominal gap. When the nominal gap is carefully controlled (section 7.5.2), the spreadsheets can be used to directly predict the stiffness, flow rate, and bearing pocket pressure. In cases where the nominal gap cannot be carefully measured and assembled (section 7.5.1), the spreadsheets can be matched to the experimental values by adjusting the nominal gap to equate the flow rate and supply pressure. The results indicate that the shim material used to set the nominal gap should be about 0.0005" less than the desired nominal gap.

CHAPTER 8

GRINDING EXPERIMENTS ON THE WPGM

This chapter describes the initial grinding tests run on the WPGM to characterize the grinding performance of the machine under standard operating conditions. The grinding machine will be used for grinding structural ceramic components. Therefore, the typical material removal rates are approximately $0.5\text{in}^3/\text{min}$. (depending upon the specific component).

Grinding results depend upon many factors other than the machine. In chapter 1, the main parameters of the grinding process were described. A good machine tool is necessary, but not sufficient for good grinding results. Therefore, one must be careful to make conclusions about a machine solely from grinding experiments.

There are four important metrics for the grinding performance of the machine; (1) straightness of the ground component, (2) surface finish, (3) material removal rate, and (4) the modulus of rupture of the component (which is highly dependent upon the fracture induced by the grinding process).

Three grinding experiments were conducted. First, a solid plate of aluminum oxide (96% isostatically pressed) was ground at three different material removal rates on the WPGM. For each material removal rate, the straightness, and surface finish were measured. Second, the end of a multiple cell ceramic beam was ground on the WPGM. These will be the main products ground on this machine. Third, modulus of rupture (M.O.R.) bars were ground on the WPGM and three other machines. The modulus was experimentally determined using a four point bending test.

8.1 - Grinding Set-Up

Tests on the WPGM were run under the following conditions:

- The grinding wheel is a resin bonded diamond grit cup wheel (the diamond grit is 120 and the concentration is 75). The wheel outside diameter is 8".
- The wheel RPM is 1450.
- The coolant is water-based, with a water soluble oil lubricant.
- 10 dwell passes for each grind cycle.

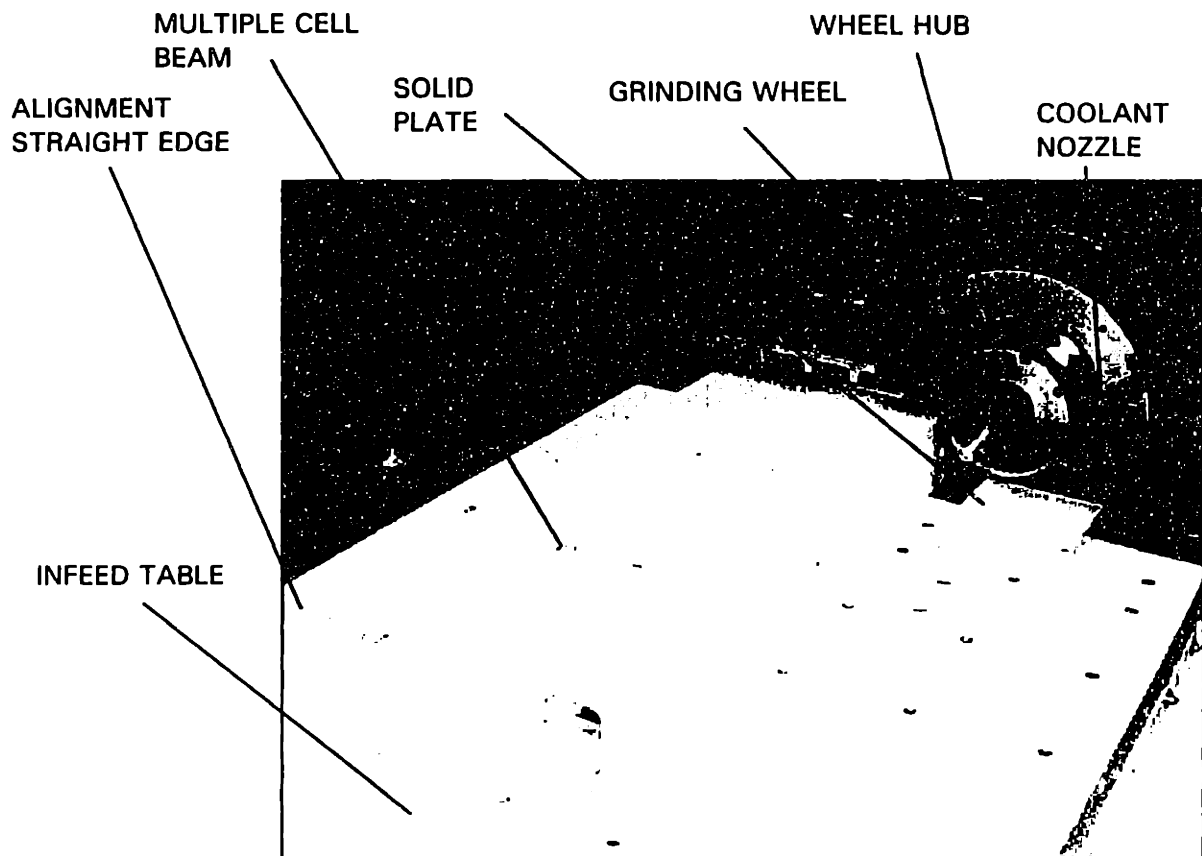


Figure 8.1 Photograph of the grinding set-up for a multiple cell beam or a solid plate. The clamping hardware is not shown.

8.2 - Straightness Performance

The components ground on the WPGM in the initial grinding characterization test were straight within $2\mu\text{m}$ (0.000080" micro inches) over the entire surface. The first set of grinding tests were run on a solid plate of ceramic. Three 1.5" thick edges (on a square part 6" x 6" x 1.5") were ground at removal rates of 0.36, 0.72, 1.08 in³/min. The straightness and surface finish results are summarized in Table 8.1. Table 8.2 is a comparison of these results to grinding results achieved on conventional grinding

machines. Figures 8.2 are the straightness plots for the plate ground on the WPGM. The plots indicate the difference in surface finish at higher material removal rates.

Table 8.1 Straightness and surface finish results for the WPGM.

| Material Removal Rate (in ³ /min) | Feed Rate (in./sec.) | Depth of Cut (in.) | Straightness (in. over 6") | Surface Finish (μin.) |
|--|----------------------|--------------------|----------------------------|-----------------------|
| 0.36 | 8 | 0.0005" | 0.000080" | 16 |
| 0.72 | 8 | 0.0010" | 0.000080" | 18 |
| 1.08 | 8 | 0.0015" | 0.000085" | 22 |

Table 8.2 Comparison of grinding results for similar material removal rates of 0.36in³/min. The results are obtained with slightly different wheel configuration and grit. The straightness was measured over 12".

| Machine | Wheel Grit | Straightness | Surface Finish |
|--------------------|------------|--------------|----------------|
| WPGM | 120 | 0.000080" | 16 |
| Surface Grinder | 200 | 0.000250" | 16 |
| Current Endgrinder | 120 | 0.000760" | 22 |

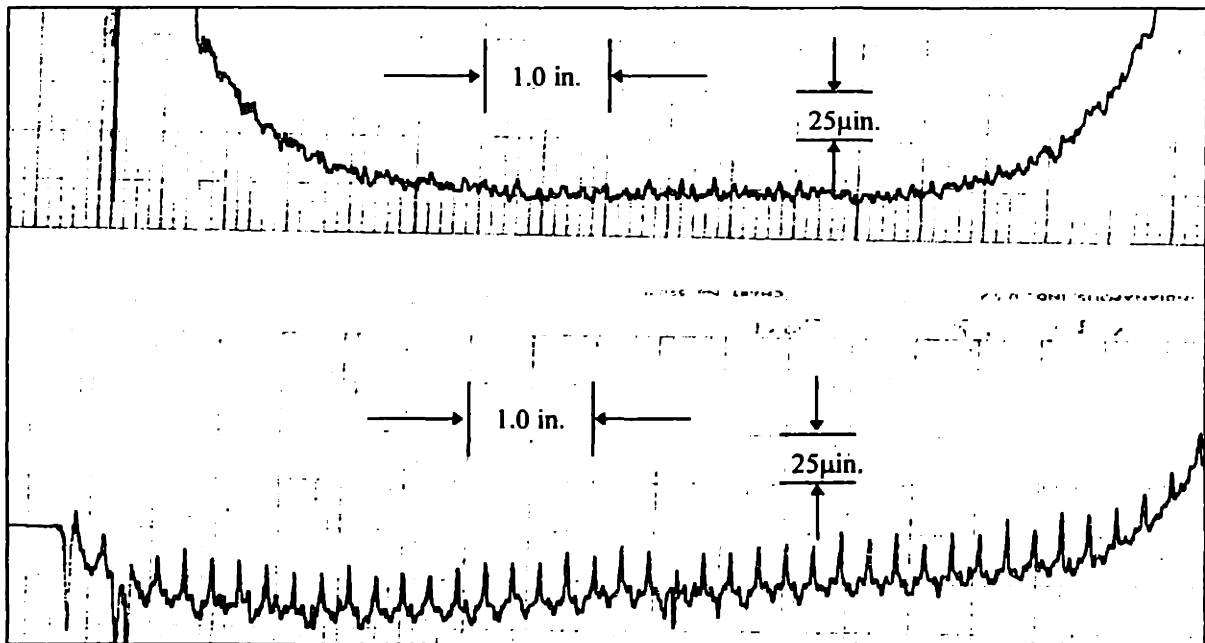


Figure 8.2 Straightness plots for the 6" x 6" x 1.5" plate ground on the WPGM. The top plot was ground at a material removal rate of 0.36in³/min., the bottom plot was 1.08in³/min..

The multiple cell beam was ground on the WPGM (1 end) and the current endgrinder in order to compare the difference in straightness. The grinding indicates that the straightness error of the WPGM, is an order of magnitude better than the conventional machine. Figure 8.3 shows the plots from the two ends of the beam. The small humps on the WPGM end correspond with the webs of the beam.

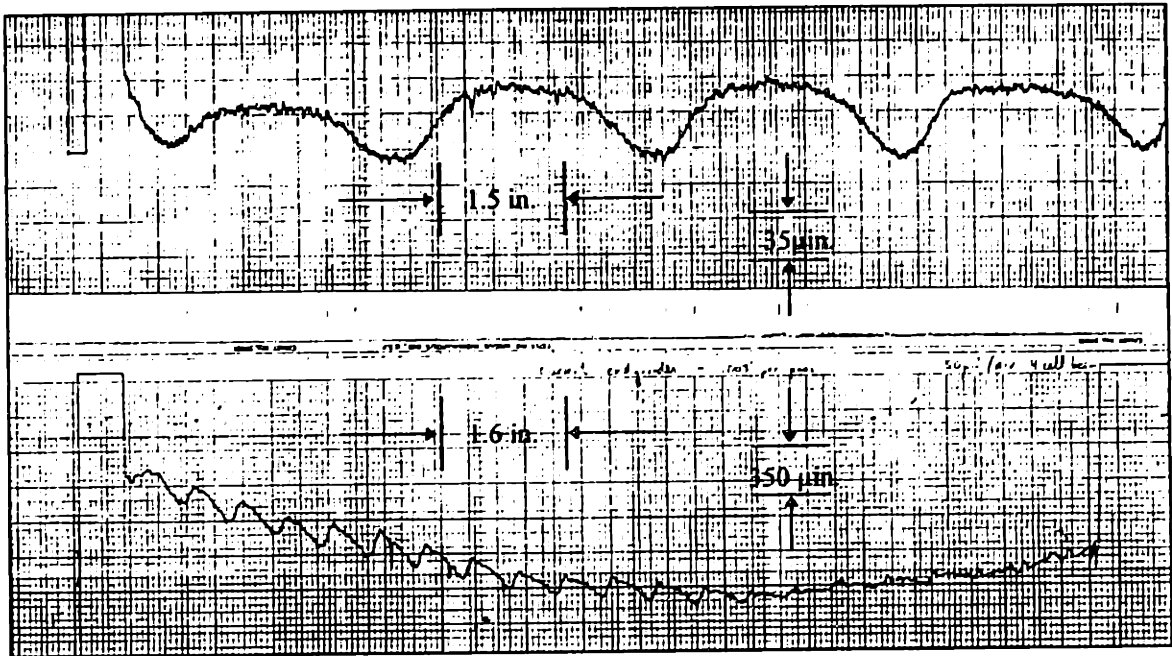


Figure 8.3 Straightness plots for a beam ground on the WPGM (top) and a conventional machine (bottom). It is important to note that the scale is $50\mu\text{m}$ on the bottom and $5\mu\text{m}$ per division. The overall straightness error is $0.000060''$ on the WPGM and $0.00080''$ for the conventional machine.

8.3 - Modulus of Rupture Experiment

Modulus of rupture is related to the surface finish of a part. Therefore, parts ground on different machines will have different modulus of rupture. To test this characteristic, small rectangular bars ($0.15'' \times 0.25'' \times 2.00''$, 96% pure dry pressed aluminum oxide) are ground then broken in a four point bending test. The modulus of rupture is calculated with geometry and load information (described in chapter 2).

An experiment was run to compare the modulus of rupture on the WPGM, a Blanchard grinding machine, and a standard surface grinding machine. For each machine, 20 small bars were ground then experimentally tested. It is important to note that wheel grit and fixturing configuration will be significant in the results and cannot be made identical on each machine. The premise of this experiment was to grind the bars on each machine at the same material removal rate, then examine the effect on strength. Such a test favors machines with higher wheel surface speeds and finer grit wheels. Table 8.3 summarizes the characteristics of each grinding machine for this experiment.

Table 8.3 Grinding parameters for the machines used in the modulus of rupture experiment. The material removal rate ($0.36\text{in}^3/\text{min}$) and the number of dwell passes (10 passes) was the same for each machine.

| Machine | Wheel Diameter | Wheel Surface Speed | Wheel Grit | Infeed per Pass | Traverse Speed |
|--------------------|----------------|---------------------|------------|-----------------|----------------|
| WPGM | 8" | 2930ft./min. | 120 | 0.0005" | 10in./sec. |
| Surface Grinder | 20" | 6150ft./min. | 180 | 0.0003" | 12in./sec. |
| Blanchard | 14" | 5650ft./min. | 120 | 0.0003" | 40rev./min. |
| Current Endgrinder | 14" | 5650ft./min. | 120 | 0.0005" | 10in./sec. |

Table 8.4 and Figure 8.4 summarize the results. The WPGM was shown to have the smallest standard deviation between samples. The blanchard style, with higher surface speed, provided the highest average modulus of rupture of the ground samples. The surface grinder measurements were lower because the grinding marks were parallel to the fracture direction. Therefore, the marks had a more significant effect on the strength of the parts.

Table 8.4 Modulus of rupture experimental results. 20 samples were ground for each machine.

| Machine | M.O.R. Average (kPsi.) | M.O.R. Standard Deviation (kPsi.) | Weibull Modulus |
|--------------------|------------------------|-----------------------------------|-----------------|
| Polished* | 46200 | 4000 | 14.00 |
| WPGM | 40508 | 3027 | 10.48 |
| Surface Grinder | 24463 | 3912 | 14.76 |
| Blanchard | 43994 | 4501 | 8.61 |
| Current Endgrinder | 44385 | 5306 | 8.20 |

* Polished values are taken from a Coors Ceramics catalogue as a reference value to compare with the ground samples. Measurements were not produced in the same experiment as the ground samples.

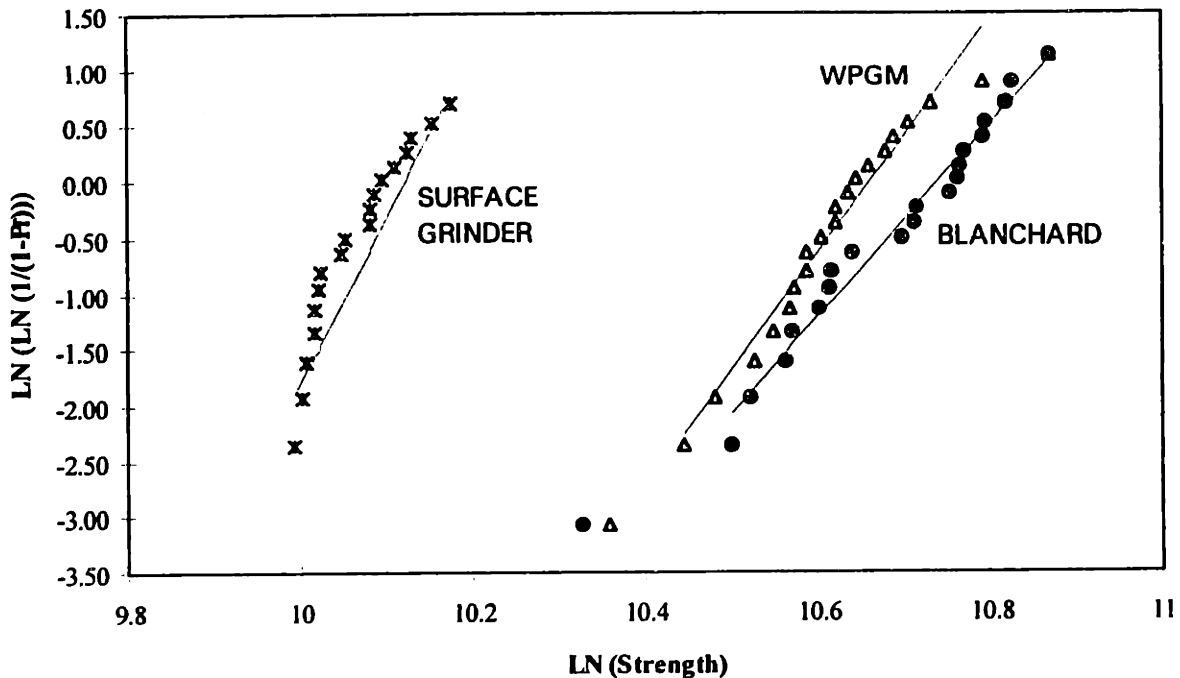


Figure 8.4 Weibull modulus plot for the samples ground on the WPGM, the Blanchard, and Surface Grinding Machines.

8.4 - Summary of Grinding Results

The grinding results indicate that the WPGM produces excellent straightness relative to the other machines tested. Conventional machines produced straightness results of 0.00025" over a 12" surface. The WPGM produced surfaces straight within 0.000080" over 12".

The WPGM has achieved material removal rates higher than conventional surface grinders. The WPGM has achieved removal rates of 1.75in³/min. and will be increased after the completion of this thesis. The goal will be to remove at least 2.00in³/min. and optimistically 3.00in³/min..

The surface finish is highly dependent upon the type of wheel used on the machine. The surface finish achieved with a 180 grit was 5μin. and 16μin. with a 120 grit wheel. This is similar to the surface finishes achieved on other machines such as the Blanchard.

The modulus of rupture experiment demonstrated that the WPGM exhibited higher repeatability than the Blanchard grinding machine. These results were influenced by the different configurations of each machine. An important influence is the direction of the grinding marks from each machine. The surface grinder created grinding marks perpendicular to the length of the MOR bars which reduced the strength results substantially. The other machines produced marks at the angle (approximately 45 degrees) which influences the results. Therefore, these results are intended to give qualitative result as to the effect of the grinding on the strength.

CHAPTER 9

CONCLUSIONS

The ceramic industry needs machine tools with improved durability and accuracy in order to reduce the cost of ceramic components. Machine tool companies, which supply the ceramic factories, have largely avoided the idea of building an entirely new class of machines even though there are potential performance advantages. Developing a new machine design (especially one which is radically different) requires several costly iterations and years of reliability testing. The thesis starts the machine tool and ceramic industries down the path toward better machines.

This dissertation presented a new grinding machine specifically for finishing ceramic components. The most significant result of this thesis is the Wilbanks Precision Grinding Machine (WPGM). The significant novel design features of this machine are:

1. The first production grinding machine with an all ceramic base structure, rails, and main components. The structure has higher stiffness than conventional machines, and was lapped to an accuracy far better than conventional cast iron machine bases. The base demonstrates that there is significant potential in using ceramic components in machine tools.
2. The first production grinding machine (along with the new machine from Weldon Machine Tool) to feature hydrostatic linear bearings on all axes. The bearings (along with the accurately lapped ceramic rails) demonstrated straightness results of 0.000030" (over more than 3 feet of travel). Furthermore, the stiffness tests, and frequency response indicated that they have higher static and dynamic stiffness than conventional roller bearings (about 4.0lbs./ μ in.).
3. The initial grinding results indicate that this machine has the potential to out-perform conventional machines in terms of straightness and material removal rates.

Aside from the grinding machine built at Wilbanks, the thesis also presented original work in the area of hydrostatic bearings. The following work on hydrostatic bearings was part of this thesis project.

1. A dynamic model of hydrostatic bearings for predicting dynamic performance, and designing fluid circuits which remove the pressure fluctuations inherent in any high pressure system. The bond graph developed is useful for sizing and positioning accumulators, and choosing the length and diameters of supply lines for the hydrostatic bearings.
2. Characterization of two prototypes before the grinding machine was designed. These prototypes were critical to the design of the Wilbanks and Weldon machines because they proved that the concept was solid. The straightness and stiffness results on these prototypes were the reason that the work was taken beyond the laboratory stage.
3. A comparison of the spreadsheet design tools and the experimental performance of the bearings (along with Nathan Kane, a colleague from the Precision Engineering Research Group). The comparison will be important for future projects involving hydrostatic bearings because designers will be able to rely on the simple analysis performed within minutes on a spreadsheet.

The thesis also presented research which extended the concept of ShearDamping (developed by Eric Marsh and Alex Slocum, and described in chapter 5) to ceramic structures. The relatively high specific stiffness of ceramic structures makes them difficult to damp. However, by tuning the parameters of the ShearDamped composite structure, the loss factor was increased by 20X while the weight only increase by 50%.

Finally, this thesis presented a design manual for engineers considering the use of ceramic structures in precision machine design projects. The manual describes the process of manufacturing large ceramic structures and the issues involved in designing with ceramic. Table 9.1 has been included as a summary.

Table 9.1 Lessons learned during the completion of this project.

| Issue | Date | Technical | Non-Technical |
|-----------------------------------|-----------------------|--|--|
| Component Manufacture / Purchase | June 1994 - June 1995 | <ol style="list-style-type: none"> 1. Firing problems 2. Designing ceramic components 3. Tolerances for ceramic components | <ol style="list-style-type: none"> 1. Leadtimes required for various items 2. Hidden cost of development projects for small manufacturing plants |
| Initial Assembly - Main Structure | June - September | <ol style="list-style-type: none"> 4. Issues with bolted connections (cracking) 5. Thermal issues for assembly (allowing structure to settle) | <ol style="list-style-type: none"> 3. Organizing large efforts such as moving structures 4. Managing budget 5. Managing my time and others 6. Budgeting time (multiply estimate by 3.....at least) |
| Hydrostatic bearing | September - November | <ol style="list-style-type: none"> 6. Hydroscopic growth of non-ceramic components | <ol style="list-style-type: none"> 7. Dealing with unexpected problems |
| Electronics | August- January '96 | <ol style="list-style-type: none"> 7. What's a contactor?? 8. Specifying components 9. Arranging and integrating components 10. Debugging shorts, etc. | <ol style="list-style-type: none"> 8. Bringing different talents together to get the job done... 9. Hiring consultants to "fill in the gaps" |